Imperial College London
Department of Civil and Environmental Engineering

Nonlinear Analysis of Composite Shells with Application to Glass Structures

Yating Liang

October 2015

Submitted in fulfilment of the requirements for the degree of Doctor of Philosophy
in Civil and Environmental Engineering of Imperial College London
and the Diploma of Imperial College London

Declaration of Originality

I confirm that this thesis is my own work and that any material from published or unpublished work from others is appropriately referenced.

Copyright Declaration

Abstract

Laminated glass is a special composite material, which is characterised by an alternating stiff/soft lay-up owing to the significant stiffness mismatch between glass and PVB. This work is motivated by the need for an efficient and accurate nonlinear model for the analysis of laminated glass structures, which describes well the through-thickness variation of displacement fields and the transverse shear strains and enables large displacement analysis.

An efficient lamination model is proposed for the analysis of laminated composites with an alternating stiff/soft lay-up, where the zigzag variation of planar displacements is taken into account by adding to the Reissner-Mindlin formulation a specific set of zigzag functions. Furthermore, a piecewise linear through-thickness distribution of the material transverse shear strain is assumed, which agrees well with the real distribution, yet it avoids layer coupling by not imposing continuity constraints on transverse shear stresses.

Local formulations of curved multi-layer shell elements are established employing the proposed lamination model, which are framed within local co-rotational systems to allow large displacement analysis for small-strain problems. In order to eliminate the locking phenomenon for the shell elements, an assumed strain method is employed and improved, which readily addresses shear locking, membrane locking, and distortion locking for each constitutive layer. Furthermore, a local shell system is proposed for the direct definition of the additional zigzag displacement fields and associated parameters, which allows the additional displacement variables to be coupled directly between adjacent elements without being subject to the large displacement co-rotational transformations.

The developed multi-layer shell elements are employed in this work for typical laminated glass problems, including double glazing systems for which a novel volume-pressure control algorithm is proposed. Several case studies are finally presented to illustrate the effectiveness and efficiency of the proposed modelling approach for the nonlinear analysis of glass structures.

Acknowledgements

The work presented in this thesis has been carried out under the supervision of Prof. Bassam A. Izzuddin, to whom I would like to express my deepest gratitude for his continuous guidance, support, and encouragement throughout the three years of my PhD study. I am also grateful to him for providing valuable feedback and constructive comments on the full draft.

I am also in debt to Mr Franklin Lancaster in Eckersley O'Callaghan for providing practical case studies for this work, and to Dr Lorenzo Macorini for his constructive suggestions during this research work. In addition, the financial supports provided by the Rector's Scholarship Fund at Imperial College and the Dixon Scholarship Fund in the Department of Civil and Environmental Engineering are both acknowledged.

Furthermore, I wish to thank my parents, Guodong Liang and Ping Lu, for their consistent care and unconditional support, which has always been an enormous source of inspiration and strength for me. I also wish to thank my boyfriend, Ou Zhao, for his love, company, and continuous encouragements.

Last but not least, I am quite thankful to my colleagues and friends whom I have worked with in room 317A, in Skempton Building, and at the South Kensington Campus over the years for their kind suggestions and company.

Contents

List of Tables

List of Figures

Notation

All symbols used in this thesis are defined where they first appear. For the reader‘s convenience, the principal meanings of the commonly used notations are contained in the list below. The reader is cautioned that some symbols denote more than one quantity; in such cases the meaning should be clear when read in context.

Abbreviations

1D,2D,3D	One-dimensional, two-dimensional, and three dimensional, respectively
AG	Annealed glass
CLT	Classical lamination theory
CNF6	6-noded conforming shell element
CNF9	9-noded conforming shell element
DOF	Degree of freedom
EDN	Equivalent single layer model with the application of the principle of virtual displacements
EDZN	EDN models enriched with Murakami’s zigzag function
EDZN*	EDZN models with further simplifications
EMCN	Equivalent single layer models with the application of Reissner’s mixed variational theorem
EMZCN	Equivalent single layer models, enriched with Murakami’s zigzag

	function, with the application of Reissner's mixed variational theorem
ESL	Equivalent single layer
FCSR	Face-to-core stiffness ratio
FSDT	First-order shear deformation theory
HnCm	m-noded corrective strain element with n^{th} order hierarchic modes
HnOm	m-noded objective strain element with n^{th} order hierarchic modes
HSDT	Higher-order shear deformation theory
LDN	Layer-wise model with the application of the principle of virtual displacements
LG	Laminated glass
Ln-H3O6	n-layer 6-noded laminated shell element with the application of the H3O6 optimisation to each layer
Ln-H3O9	Proposed n-layer 9-noded laminated shell element with the application of the H3O9 optimisation to each layer
LW	Layer-wise
LWT	Layer-wise theory
MITC	Mixed Interpolation of Tensorial Component
MITC6	6-noded degenerated shell element using MITC method
MITC6*	6-noded co-rotational shell element using the MITC6 strain mapping between covariant strains fixed at element centre and local generalised strains
MITC9	9-noded degenerated shell element using MITC method

MITC9* 9-noded co-rotational shell element using the MITC9 strain mapping between covariant strains and local generalised strains

MITC9is* 9-noded co-rotational shell element using the MITC9 strain mapping between covariant strains fixed at element centre and local generalised strains

MZZF Murakami's zigzag function

MZZFi A beam model where the MZZF is added to the 1D HSDT model with an i^{th}-order z expansion for the whole beam thickness.

PVB Polyvinyl butyral

PVD The principle of virtual displacements

RMVT Reissner's mixed variational theorem

TSDT Third-order shear deformation theory

VRT Vlasov-Reddy theory

WLF Williams-Landell-Ferry equation

ZZT Zigzag theory

Roman Symbols

$\mathbf{B}_m^{(k)}, \mathbf{B}_b^{(k)}, \mathbf{B}_s^{(k)}$ First derivatives of the generalised strains at layer (k) with respect to pseudo parameters $\mathbf{U}^{(k)}$ (conforming formulation)

$\hat{\mathbf{B}}_m^{(k)}, \hat{\mathbf{B}}_b^{(k)}, \hat{\mathbf{B}}_s^{(k)}$ First derivatives of the generalised strains at layer (k) with respect to pseudo parameters $\mathbf{U}^{(k)}$ (hierarchic optimisation approach with objective assumed strains)

$\tilde{\mathbf{B}}_m^{(k)}, \tilde{\mathbf{B}}_b^{(k)}, \tilde{\mathbf{B}}_s^{(k)}$ First derivatives of the generalised strains at layer (k) with respect to pseudo parameters $\mathbf{U}^{(k)}$ (hierarchic optimisation approach with corrective assumed strains)

$\mathbf{c}_r^o, \mathbf{c}_s^o$ Unit vectors for local shell coordinate system at initial configuration

$\mathbf{c}_r, \mathbf{c}_s$ Unit vectors for local shell coordinate system at current configuration

$\mathbf{c}_x, \mathbf{c}_y, \mathbf{c}_z$ Unit vectors for local element coordinate system at current configuration

C_1, C_2 WLF parameters

$\mathbf{C}_p^{(k)}$ Material constitutive matrix of layer (k) for planar stresses/strains

$\mathbf{C}_s^{(k)}$ Material constitutive matrix of layer (k) for transverse shear stresses/strains

$\mathbf{C}_{v,p}^{n+1}$ Viscoelastic constitutive matrices for planar stresses/strains at time t_{n+1}

$\mathbf{C}_{v,s}^{n+1}$ Viscoelastic constitutive matrices for transverse shear stresses/strains at time t_{n+1}

$\mathbf{D}_b^{(k)}$ Constitutive matrix for generalised bending stresses/strains at layer (k)

$\mathbf{D}_m^{(k)}$ Constitutive matrix for generalised membrane stresses/strains at layer (k)

$\mathbf{D}_s^{(k)}$ Constitutive matrix for generalised transverse shear stresses/strains at layer (k)

$\mathbf{d}_i$ Global translational displacements of node *i*

$\mathbf{f}_A$ Resistance forces with respect to additional zigzag parameters $\mathbf{U}_A$

$\mathbf{f}_C$ Resistance forces with respect to basic local parameters $\mathbf{U}_C$

$\mathbf{f}_G$ Resistance forces with respect to basic global parameters $\mathbf{U}_G$

$\mathbf{f}^{(k)}$	Vector of pseudo nodal forces at layer (k)
$\mathbf{F}^{(k)}$	Generalised membrane stress at layer (k)
G_0	Instantaneous shear modulus
G_j	Shear modulus of j^{th} Maxwell element
G_∞	Long-time plateau shear modulus.
h	Thickness of plate/shell
h_e	Nominal element length
h_-, h_+	Values of z at the bottom and top of the cross-section, respectively
h_k	Thickness of layer (k)
h_{k-}, h_{k+}	Values of z at the bottom and top of layer (k), respectively
$\mathbf{J}$	Jacobian matrix
$\mathbf{J}_C$	Jacobian matrix evaluated at element centre
(k)	Layer (k)
K	Bulk modulus
$\mathbf{k}^{(k)}$	Local stiffness matrix of layer (k)
$\mathbf{k}_C$, $\mathbf{k}_A$, $\mathbf{k}_{CA}$, $\mathbf{k}_{AC}$	Local stiffness matrices of multi-layer shell elements
$\mathbf{k}_G, \mathbf{k}_{GA}, \mathbf{k}_{AG}$	Global stiffness matrices of multi-layer shell elements
L_1, L_2, L_3	Area coordinates
$\mathbf{M}_C$	Local consistent mass matrix

$\mathbf{M}_G$	Global consistent mass matrix
$\mathbf{M}^{(k)}$	Generalised bending stresses at layer (k)
$\mathbf{n}_i$	Normal vector at node *i*
N_c	Number of soft layers in the lamination
N_e	Number of element nodes
N_i	Shape function of node *i*
N_l	Number of constitutive layers in the lamination
N_M	Number of Maxwell elements
p_E^0	Gas pressure in the enclosure at the initial undeformed configuration
p_E^{n+1}	Gas pressure in the enclosure at the current deformed configuration
$\mathbf{Q}_{AS}^{(k)}$	Generalised transverse shear stresses at layer (k)
r,s	2D curvilinear shell coordinates
$\bar{\mathbf{r}}_i$	Components of the normal vector along the local x- and y-axes at node *i*
$\ddot{\bar{\mathbf{r}}}_i$	Local rotational accelerations of node *i*
$\mathbf{R}^o$, $\mathbf{R}$	Orientation matrices of the local co-rotational framework at the initial and current configurations, respectively
$\mathbf{T}_A^{(k)}$	Transformation matrix from additional zigzag displacement parameters of element to pseudo displacement parameters of layer (k)
$\mathbf{T}_C^{(k)}$	Transformation matrix from local displacement parameters of element to pseudo displacement parameters of layer (k)
$\mathbf{t}_i$	Local translational displacements of node *i*

$\ddot{\mathbf{t}}_i$	Local translational accelerations of node *i*
u_{x0}, u_{y0}, u_{z0}	x, y, and z planar displacement fields evaluated on the middle surface, respectively
$\mathbf{U}_{Ai}$	Vector of additional nodal parameters at node *i*
$\mathbf{U}_{Ci}$	Vector of local translational and rotational nodal parameters at node *i*
$\mathbf{U}_{Gi}$	Vector of global translational and rotational nodal parameters at node *i*
$\mathbf{U}_i^{(k)}$	Vector of pseudo nodal parameters of layer (k) at node *i*
$\mathbf{v}_{ij}^o, \mathbf{v}_{ij}$	Vectors connecting node *i* to node *j* in the initial and current element configuration, respectively
V_E^0	Enclosed gas volume at the initial undeformed configuration (t = 0s)
V_E^n	Enclosed gas volume at the previous deformed configuration (t = t_n)
V_E^{n+1}	Enclosed gas volume at the current deformed configuration (t = t_{n+1})
$\overline{V}_E^{n+1}$	Approximate enclosed gas volume at the current deformed configuration (t = t_{n+1})
x,y,z	Local element coordinates
X,Y,Z	Global coordinates
$\mathbf{x}_i^o$	Local coordinates of node *i*
z_0	Offset of the shell mid-surface along the z-axis
$z^{(k)}$	z value extracted on the middle surface of layer (k)

Greek Symbols

$\alpha^{(k)}$	Angle from the shell directional vector $\mathbf{c}_r^o$ to the material fibre direction at layer (k)
β	Rotation from $\mathbf{c}_r$ in shell system to $\mathbf{c}_x$ in local element coordinate system
$\boldsymbol{\varepsilon}$	Conforming strains
$\tilde{\boldsymbol{\varepsilon}}$	Enhanced strains adopting the corrective fields
$\hat{\boldsymbol{\varepsilon}}$	Enhanced strains adopting the objective fields
$\boldsymbol{\varepsilon}_b, \boldsymbol{\varepsilon}_m, \boldsymbol{\varepsilon}_s$	Bending generalised strains, membrane strains, and transverse shear strains
$\boldsymbol{\varepsilon}_b^{(k)}, \boldsymbol{\varepsilon}_m^{(k)}, \boldsymbol{\varepsilon}_s^{(k)}$	Bending generalised strains, membrane strains, and transverse shear strains at layer (k) for laminations
$\boldsymbol{\varepsilon}^h$	Hierarchic corrective strains
$\boldsymbol{\varepsilon}^o$	Objective strains
$\boldsymbol{\varepsilon}_p^{(k)}$	Planar material strains of layer (k)
$\boldsymbol{\varepsilon}_s$	Transverse shear strains
$\boldsymbol{\varepsilon}_{s,AS}^{(k)}$	Assumed transverse shear strains of layer (k)
$\varphi^{(k)}$	Angle from the local element x-axis to the material fibre direction at layer (k)
ξ, η, ζ	Natural coordinates
ν	Poisson's ratio
θ_x, θ_y	Components of the normal vector along the x- or y-axis

$\vartheta_x^j, \vartheta_y^j$	Additional fields associated with the jth proposed zigzag function along the x and y axes of the local element system, respectively
$\vartheta_r^j, \vartheta_s^j$	Additional fields associated with the jth proposed zigzag function along the r and s axes of the local shell system, respectively
ρ	Density
$\boldsymbol{\sigma}_p^{(k)}$	Planar material stresses of layer (k)
$\boldsymbol{\sigma}_{s,AS}^{(k)}$	Assumed transverse shear stresses of layer (k)
τ_j	A relaxation time parameter of the j^{th} Maxwell element
ΔV_E^{n+1}	Volume change of the enclosure during the current time step Δt^{n+1}
$\Delta \bar{V}_E^{n+1}$	Approximate volume change of the enclosure during the current time step Δt^{n+1}
$\Delta V_{E,i}^{n+1}$	Contribution from element i to the enclosure volume change during the current time step Δt^{n+1}
$\tilde{\mathbf{T}}$	Transformation matrix from conforming strains to corrective strains
$\hat{\mathbf{T}}$	Transformation matrix from conforming strains to objective strains
Ω^e	Element domain
Ω_E^n	Enclosed surface at time t_n
$\boldsymbol{\Psi}^h$	Hierarchic strain-inducing modes
$\boldsymbol{\Psi}^o$	Objective strain-inducing modes
$\bar{\boldsymbol{\Psi}}_\Delta^h$	Hierarchic strain-inducing modes for three edge strains of triangular shell element
$\boldsymbol{\Psi}_\Delta^o$	Objective strain-inducing modes for three edge strains of triangular shell

element

$\boldsymbol{\Psi}_b^h, \boldsymbol{\Psi}_m^h, \boldsymbol{\Psi}_s^h$ Hierarchic corrective modes for bending generalised strains, membrane strains, and transverse shear strains, respectively

$\bar{\boldsymbol{\Psi}}_b^h, \bar{\boldsymbol{\Psi}}_m^h, \bar{\boldsymbol{\Psi}}_s^h$ Modified hierarchic bending, membrane and transverse shear strain modes, respectively

$\boldsymbol{\Psi}_b^o, \boldsymbol{\Psi}_m^o, \boldsymbol{\Psi}_s^o$ Objective modes for bending generalised strains, membrane strains, and transverse shear strains, respectively

Chapter 1

Introduction

Laminated glass (LG) has been widely used in many applications of engineering, including for example in architectural glazed façades (Figure 1.1) owing to its transparency, aesthetic appearance and safety characteristics. It is composed of one or more polymer layers sandwiched between layers of glass plies (Figure 1.2). Polyvinyl butyral (PVB) is the most commonly used interlayer, which can go through large deformation prior to rupture, hence providing good energy-absorbing capability. In the event of fracture of the glass, PVB retains glass debris in place, withstands further loadings, and absorbs more energy. Therefore, LG mitigates injury to occupants in buildings subject to extreme loading conditions, and is thus increasingly being utilised for structures that are vulnerable to blast and earthquakes.

Figure 1.1: The Shard, London. (www.shardldn.com)

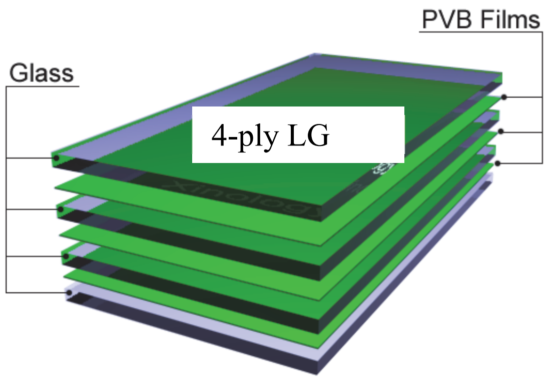

Figure 1.2: Composition of LG (xinology.com).

Even though the safety advantage of LG over annealed glass is apparent, there is a lack of design codes to guide the design of LG structures. Current design codes related to LG only provide a coarse estimation of the resistance for secondary structural components. For instance, the ASTM (2012) E1300-12a states that it only applies to vertical and sloped glazing in buildings for which the specified design loads consist of wind load, snow load and self-weight with a total combined magnitude less than or equal to 15kPa. Accordingly, this code is not applicable to the design of structural glass members. The reason behind the lack of design guidance is that the mechanical behaviour of LG is quite complicated even prior to fracture, which involves significant zigzag displacements and complex stress fields, sensitivity to loading rates and temperature, as well as significant geometric nonlinearity under moderate loading. These factors make it difficult to describe the behaviour of LG units with one set of codified formulae.

Therefore, reliable numerical modelling tools are required to facilitate the design and assessment of LG structures. An advanced approach in modelling the LG should balance the need for accuracy and the computational demand. To achieve this goal it is essential to have a full understanding of the characteristics of LG structures.

1.1 Features of laminated glass structures

The behaviour of LG is characterised by several distinctive features as follows:

(1) Material mismatch. There is a significant stiffness variation through the glass laminate thickness, where the glass-to-PVB stiffness ratio falls into the range from 10^3 to 10^6,

which is much larger than the stiffness variation in laminations where the change of material properties is achieved by changing the orientation of constitutive layers. This material mismatch leads to a significant zigzag effect in displacements and complex stress fields in the thickness direction.

(2) Stacking sequence. The LG composition follows an alternating stiff/soft lay-up scheme due to the inclusion of soft PVB layers between relatively stiff glass plies. This stacking sequence is different from usually encountered sandwich structures where all soft cores are layered together and sandwiched by stiff sheets.

(3) Large slenderness. Most LG components can be regarded as two-dimensional structures due to the relatively small thickness compared to length and width, which induces large deflections under transverse loading. For an accurate modelling of such structures, a suitable geometric nonlinear analysis capability is required to solve large displacement problems.

(4) Sensitivity to loading duration and temperature. PVB is a viscoelastic material, the mechanical properties of which vary with different loading rates and temperature, hence leading to varying effective sectional modulus of the glass laminate.

(5) Fracture of glass. The strength of glass has a wide statistical variation due to random Griffith flaws as a result of both the manufacturing process and service conditions. The development of cracks is also complicated since the crack pattern is influenced by the glass fracture strength, the size of the pre-existing flaws, and the interaction between PVB and glass.

(6) Nonlinear material properties of PVB. After fragmentation of glass plies, PVB layer undergoes large deformation. Experiments have shown that in the large strain range this material exhibits a highly nonlinear viscoelastic response.

1.2 Aims and scope

It is apparent from the previous discussion that the full nonlinear analysis of LG is quite an involved task, requiring complete understanding of all the aforementioned characteristics.

However, it is important to note that features (1)-(4) exist throughout the loading history in all LG problems, whereas features (5)-(6) are manifested in the post-cracking phases, where large strains are induced in PVB.

This research focuses on features (1)-(4), and gives new insights into the behaviour of LG structures prior to the initiation of glass cracking. The primary aim is to raise an efficient lamination model which captures the characteristics of LG and provides reliable estimations on its structural response. The outcome of this research may facilitate LG design and assessment by providing a reliable and efficient numerical modelling tool, and it may also serve as a basis upon which the features (5)-(6) can be investigated and considered in future.

Given the topic under consideration, the forthcoming chapters of this thesis mainly address the following objectives:

(1) Formulation of lock-free monolithic shell finite elements. Low-order Reissner-Mindlin shell elements are associated with the issue of locking, where the element exhibits over-stiff response due to the existence of polluting higher-order strain terms. Part of this research aims at eliminating the locking phenomenon in quadrilateral and triangular elements with the use and enhancement of an assumed strain method.

(2) Adoption of a co-rotational framework for a simple incorporation of lamination models in geometric nonlinear analysis. As discussed previously, most LG problems are associated with large displacements and finite rotations due to the slenderness of the structures. Part of this research aims at incorporating local shell element formulations into available co-rotational frameworks, which filter out rigid body modes, thereby allowing the upgrading of linear local element formulations of different sophistication to geometric nonlinear analysis with relative ease.

(3) Establishment of efficient and accurate lamination model. An extensive amount of research effort has been devoted to lamination theories, most of which are nevertheless aimed at general applications. With regard to the distinct characteristics of the glass laminate, a narrowing-down of the scope to laminations with an

alternating stiff/soft lay-up may yield simpler lamination models associated with a reduced computational demand.

(4) Incorporation of lamination models in finite element formulations. The employment of a co-rotational framework allows simple incorporation of lamination models within local shell element formulations. One aim of this research is to seek ways for minimising the required co-rotational transformations in multi-layer shell element formulations.

(5) Selection of appropriate material models. Considering that the scope of the present work is focused on the pre-cracking stage of LG, a linear elastic material model will be used for glass. However, in view of the temperature and time dependency of PVB material, this research aims at selecting and developing an appropriate material model to capture the viscoelastic characteristics of PVB.

(6) Illustrative numerical problems for demonstration of possible applications. Finally, this research aims at applying the proposed numerical modelling capabilities to several case studies on LG structures, which may be used to illustrate the wide applications of the proposed multi-layer shell elements in solving LG problems.

1.3 Outline of thesis

This thesis is composed of nine chapters. This chapter introduces the research topic and its aims and objectives. Chapter 2 provides a systematic literature review relevant to the research topic. An overview of experimental investigations and numerical modelling tools in LG problems is first given, followed by the introduction of available lamination theories. Numerical issues relevant to nonlinear shell element formulations are also reviewed in this chapter.

In Chapter 3, the formulations of monolithic quadrilateral and triangular shell elements are presented. An effective locking-elimination approach, which is employed and improved in this research, is first reviewed and then followed by the description of two efficient co-rotational coordinate systems. Subsequently, formulations of curved quadrilateral and triangular elements are presented, both of which employ the co-rotational systems and address locking via the adoption of the improved assumed strain method. In order to allow dynamic analysis, a consistent mass matrix is also derived for both elements. Numerical verifications of both elements are provided in Chapter 4.

In Chapter 5, a three-layer sandwich model is first developed, where a novel zigzag function is proposed, which is equivalent to an existing zigzag function for symmetrically laminated sandwich structures but yields much better accuracy when asymmetric cross-sections are considered. Besides, a piecewise linear transverse shear strain distribution is assumed, which reproduces the real distribution without imposing stress constraints at laminar interfaces. Based on this sandwich model, a generalised model with an alternating stiff/soft lay-up is further developed, where a set of zigzag modes specific to the considered lamination is proposed, and an assumed piecewise linear variation of transverse shear strains is employed. The accuracy and efficiency of the lamination model is illustrated with a 1D beam problem.

Chapter 6 presents the incorporation of the proposed lamination model into co-rotational shell elements. For further computational efficiency, a 2D 'shell' coordinate system is proposed in this research for the direct definition of the additional zigzag variables, which effectively minimises the required co-rotational transformations. The generalisation of the consistent mass matrices of monolithic elements to allow for multi-layer cases is also presented, thus enabling the analysis of laminated shell structures under dynamic loading. At the end of this chapter, linear and nonlinear numerical examples are presented to verify the laminated shell elements.

In Chapter 7, consideration is given to the application of the proposed laminated shell elements to LG. A viscoelastic material model for PVB is first presented, followed by verifying examples of LG panels subject to transverse loadings of different loading rates. In order to allow the analysis of insulated glazing, a volume-pressure control algorithm is presented to consider the effect of insulated air on the structural behaviour of double glazing units, which is verified with two numerical examples and is subsequently employed in Chapter 8 for the modelling of an insulated glazing system.

Several case studies are utilised in Chapter 8 to investigate the accuracy and efficiency of the developed capability for nonlinear analysis of LG. Buckling analysis, creep analysis and blast analysis of LG structures with different levels of sophistication are presented, where the efficiency and accuracy of the multi-layer shell modelling approach are discussed.

Finally, in Chapter 9, conclusions and achievements of this research are summarised, and recommendations for future work towards advanced LG modelling are provided.

Throughout this research, all finite element implementations and most of the numerical modelling are undertaken with the use of ADAPTIC (Izzuddin, 1991), a general finite element package for structural analysis. Part of the numerical modelling is also performed with the use of Maple v16.00 (Maple, 2012), a mathematical and analytical software, and ANSYS v14.5 (ANSYS, 2012), a commercial finite element software.

CHAPTER 2

Literature Review

2.1 Introduction

In this chapter, a literature review of the LG behaviour up to first cracking is provided. The experimental research on the pre-cracking behaviour of LG plates and beams as well as the characteristics of PVB is first reviewed, which provides valuable information for the validation of numerical modelling of glass structures. Subsequently, the relevant theoretical attempts in the modelling of LG are overviewed, which incorporate early mechanical models and numerical models. In finite element methods, models with three-dimensional (3D) solid elements, coincident elements, non-coincident elements connected by tie elements, and laminated shell elements are all briefly presented. With regard to available two-dimensional (2D) lamination theories, a review on the main categories is given, where the features and accuracy of each theory is briefly introduced. This chapter then proceeds with overviewing the material models for LG. The viscoelastic characteristic of PVB is explained, and the commonly used Maxwell mechanical models in describing viscoelastic materials are presented. The final part focuses on two aspects relating to the formulation of nonlinear shell finite elements, namely techniques dealing with element locking and available co-rotational approaches allowing large displacement analysis of shell structures.

2.2 Experimental investigations on laminated glass

2.2.1 Experiments on structural behaviour

A great many structural experiments were carried out in the last half of the 20^{th} century to investigate the flexural behaviour of LG up to first cracking. Hooper (1973) performed four-point bending tests on LG beams and examined the strain distribution through the beam thickness. Under sustained loading, the LG deformed as if the two glass plies were separated at a distance by a material of zero shear modulus, whereas under short-duration loading, the LG responded as a composite member having an interlayer shear modulus appropriate to its temperature. Hooper concluded accordingly that the degree of coupling between the two glass plies relies on the shear modulus of the interlayer, which in turn depends on the ambient temperature and the duration of loading.

Linden et al. (1984) and Vallabhan et al. (1987) conducted uniform pressure bending tests on LG, monolithic glass and layered glass units to establish the lower and upper bounds of the behaviour of LG under uniform pressure. By comparing experimental results of LG panels under uniform pressure with those of monolithic glass panels of the same rectangular dimensions and nominal thicknesses, Minor and Reznik (1990) concluded that the strength of LG is equal to the monolithic glass strength at room temperature, and Behr et al. (1993) established the analogy between the influence of increasing loading rate and the influence of decreasing the temperature on the behaviour of LG.

Bennison et al. (1999) carried out a series of biaxial flexural experiments on LG panels with various loading rates and temperatures and recorded the stress development and the sequence of glass-ply fracture. From the results they concluded that complex stress fields were developed in the LG due to the large modulus mismatch between glass and PVB. The location of the maximum biaxial stress was shifted from one glass ply to the other with various loading rates and/or temperatures, which resulted in different fracture sequences of the glass plies: high temperature and/or slow loading rates bias first cracking to the upper (loaded) ply, while low temperature and/or high loading rates promote lower (support) ply first cracking.

In the aforementioned experiments, transverse loadings were applied to the LG specimens, and the flexural strengths under various laboratory conditions were examined. There were also some experiments on LG specimens where in-plane flexural loading was applied. Biolzi et al. (2010) conducted three-point bending tests on the LG beams, where the point load was exerted parallel to the lamination beams to investigate the influence of interlayer stiffness on the structural performance and failure modes. They found that the interlayer plays a significant role in defining the planar response and the failure type.

There were also many experiments designated to investigate the post-cracking response of LG subjected to blast and impact loading (Timmel et al., 2007; Hooper et al., 2012; Nawar et al., 2014). However, since the scope of interest in this research is limited to the pre-cracking phase only, the details of these experiments are not presented.

2.2.2 Experiments on material behaviour

A large amount of experimental effort has been devoted to the material behaviour of PVB. Vallabhan et al. (1992) performed direct-shear tests on LG specimens at room temperature, where the lower glass ply was horizontally loaded at a low strain rate, while the upper glass ply was restrained by an electronic load cell recording the horizontal force transmitted through the PVB interlayer. The relative displacement of the two halves was also recorded. They plotted the average shear stress against the average shear strain, and concluded that under low strain rate and room temperature conditions, the initial stiffness of PVB was quite low, and it gradually increased with larger shear strains.

Biolzi et al. (2010) conducted uniaxial tensile tests on PVB coupons with a low displacement rate at room temperature, and plotted the material stress-strain curve, which showed that the material possesses a low modulus in the range of small strains and starts to exhibit material nonlinearity at finite-to-large strains.

Xu et al. (2011) carried out tension and uniaxial compression tests on PVB under respectively quasi-static and dynamic loading conditions. The corresponding material stress-strain curves all showed nonlinear behaviour in the large strain range. On the other hand, the discrepancy between the curves with different loading rates confirmed the viscoelastic characteristic of the material. Based on the stress-strain curve pattern, Xu et al. also classified the constitutive behaviour of PVB into three stages: the linear-elastic stage (small strain), the bi-exponent stage (moderate-to-large strain), and the failure stage (large strain).

The aforementioned tests on PVB all went through the large strain range of the material, which yielded a nonlinear stress-strain relationship. Bennison et al. (1999) , on the other hand, focused on the small-strain range where the stress-strain relationship can be regarded as linear. They conducted hydrostatic volumetric tests on PVB in a mercury-containing pressure cell at different temperatures, and found that the value of the bulk modulus K(t) was relatively unchanged with temperature and was fixed around 2.0GPa. They also performed a series of cyclic loading tests on PVB under different frequency and temperature conditions via the use of a dynamic mechanical analyser. The storage modulus E' and loss modulus E'' were determined by dynamic experiments, which were used for the determination of the shear relaxation modulus G(t).

2.3 Modelling of laminated glass

2.3.1 Mechanical models

Early theoretical research was mainly concentrated on the relationship between the behaviour of the LG and the behaviour of the monolithic glass having the same nominal geometry. Based on the experimental investigations by Linden et al. (1984), Vallabhan et al. (1987), Minor and Reznik (1990), and others, two experimentally defined bounds were proposed to describe the LG behaviour. The upper-bound model was a monolithic glass model having a thickness equal to the combined thicknesses of the glass plies in the LG. The lower-bound model corresponded to a layered glass model where two glass plies are layered up with no shear transfer.

Norville et al. (1998) pointed out the inaccuracy of the upper bound by emphasizing the contribution of the PVB thickness to the cross-sectional modulus, and then proposed an analytical model of the LG beam under uniform transverse loading. In the model, an equivalent section modulus was calculated, where the varying capability of PVB in transferring shear forces was taken into account with a factor q, the value of which was estimated based on the loading rate and temperature. Different distributions of the flexural stress were derived by assuming different values of the shear transfer factor q, as shown in Figure 2.1.

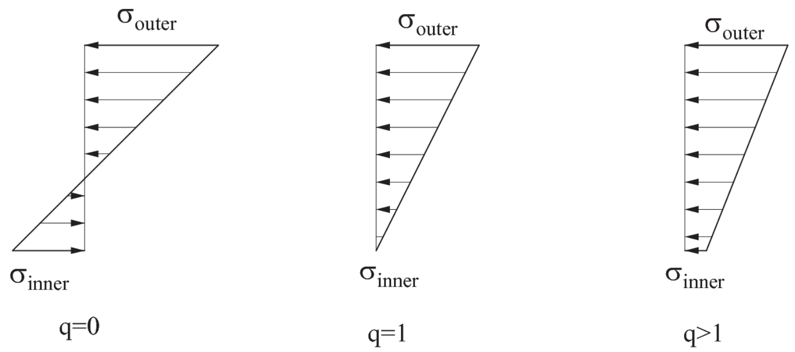

Figure 2.1: Distribution of flexural stress in single ply of LG beam (Norville et al., 1998).

2.3.2 Finite difference model

Vallabhan et al. (1993) used a mathematical model combined with a finite difference method to analyse LG units under uniformly distributed transverse loading. In order to predict the nonlinear behaviour of LG, von Karman's plate theory was used for two elastic plates, which were then connected by an infinitesimally thin elastic shear layer. This model took into account the cross-sectional distortion and geometric nonlinearity, and the effective shear modulus was calibrated against experimental results. A convergent solution of the derived nonlinear differential equations was obtained by using the finite difference method with an iterative technique. However, the application of this model to real problems incorporating complex geometric and loading conditions is likely to encounter massive storage requirements and computation time.

2.3.3 Finite element models

2.3.3.1 Three-dimensional solid element models

3D solid finite element models have been used by many researchers in simulating LG panels, including Bennison et al. (1999), Duser et al. (1999), and Wei et al. (2006), where several brick elements are usually employed through the out-of-plane direction for each ply to capture the structural response well. In order to take into account the time- and temperature-dependent effects of PVB, Bennison et al. (1999) and Wei et al. (2006) employed a linear viscoelastic material model for PVB. Although these solid models can provide accurate predictions for both displacements and stresses, the associated computational demands are often prohibitive, largely due to the numerous elements employed in both the planar and the out-of-plane directions.

2.3.3.2 Models with coincident elements

Sun et al. (2005) established a coincident shell/volume/shell model to predict the failure behaviour of windscreens, in which the PVB was modelled with solid elements while each glass ply was modelled with shell elements. Although this model may be appropriate for analysing sandwich structures where the core is much thicker than the face sheets, it seems unnecessary to use solid elements in modelling the PVB interlayer, which is so thin that the transverse normal strain is insignificant. Therefore, the use of solid elements for the PVB interlayer would result in higher computational demands with little improvement in accuracy.

In the simulation of impact problems, Du Bois et al. (2003) used two coincident elements through the thickness to model LG: one shell element for the two glass plies, and one membrane element for PVB. The use of one shell for the two glass plies was, however, based on the assumption that the through-thickness displacement variation is linear and that the PVB layer has negligible influence on the sectional modulus. It was also associated with the assumption that both glass plies fail at the same time, which led to the stiffness loss of both glass plies upon first cracking in either of them.

Timmel et al. (2007) improved the coincident shell-element model by letting one element represent one glass ply and the other represent the other glass ply plus the interlayer. For the latter element, material properties of the glass ply and the PVB interlayer were smeared throughout the element. With regard to the pre-cracking phase, the latter element with smeared material model still does not capture the local response of LG.

The employment of coincident element models greatly reduces the storage demand and computation time, compared with the 3D solid models. Nevertheless, the shell stiffness and density require adjustment prior to the analysis to maintain identical bending stiffness and total mass to the glass-PVB laminate.

2.3.3.3 Models with tie elements

Pyttel et al. (2011) proposed a model for simulating LG panels subjected to impact loading, where the two glass plies are modelled with two shells and the PVB layer is modelled with one membrane. Tie elements were employed for connection between nodes.

Peng et al. (2013) proposed a LG model in which the through-thickness direction was discretised using two shell elements with non-coincident nodes: one shell element represented the two glass sheets, which would be deleted when the failure criterion is reached, while the other shell element stood for the PVB interlayer. Tie elements were used to connect the non-coincident nodes. Similar to the model by Du Bois et al. (2003), the model automatically assumed the simultaneous failure of two glass plies.

The use of non-coincident elements linked with tie elements in the model is also more efficient than the 3D solid models. However, the continuity of displacements at layer interfaces is not preserved. The penalty based stiffness of the tie element should also be selected to balance solution accuracy with the violation of constraint conditions.

2.3.3.4 Multi-layered shell element models

There are also a few models with multi-layered shell elements, which further reduce the computational demand and alleviate the complexity in modelling laminated structures. Larcher et al. (2012) used layered shell elements to approximate the pre-cracking response of LG under blast loading. An elastic-plastic material model was used for PVB, and a failure criterion for the glass was set such that after numerical failure at an integration point of the glass ply stresses would be set to zero under tension while the material would still react to compression. However, the shell element is formulated based on the classical lamination theory assuming zero transverse shear strains and a linear variation of displacements through the plate thickness, which may result in accuracy for long-duration loadings, where the material properties change significantly in the thickness direction.

Seica et al. (2011) used a laminated shell model in the analysis of LG curtain wall systems under blast loading. The used layered shell element was based on the first-order shear deformation theory, which assumes a constant and a linear distribution of respectively the shear strain and the displacement through the plate thickness. The accuracy of this laminated shell element still yields inaccuracy if there is a noticeable stiffness mismatch through the thickness. In order to investigate the blast resistance of safety glass, Hooper et al. (2012) used two models to take account for the pre-cracking and post-cracking phases. A shell model exploiting multi-layered shell elements was adopted to predict the pre-cracking response with a maximum principle stress criterion. When the maximum principal stress in glass exceeded a limit value, the analysis would proceed with a post-cracking model, where an identical shell model was used for the post-cracking phase except that the Young's modulus of glass was set to zero. The layered shell element used in Hooper's model is still based on the first-order shear deformation theory.

In the study of the performance of double glazing systems under blast loading, Nawar et al. (2013) established a finite element model with layered shell elements employed for LG panes. Different material properties and layer thicknesses were given to the shell elements, and zigzag displacements and stresses through the shell thickness were considered by using many integration points in the thickness direction.

The layered shell models maintain the geometric continuity at layer interfaces and describe the lamination behaviour with fewer degrees of freedom (DOFs) than solid elements, which is very computationally efficient and does not require adjustment of the section modulus prior to the analysis. Nevertheless, in order to accurately capture the structural response, a proper lamination theory which accounts for cross-sectional warping ought to be embedded in the layered element formulation. In the next section, a systematic review of lamination theories is presented.

2.4 Lamination theories

Numerous research works can be found in the literature on 2D lamination theories. In terms of the employed variational principles, lamination models can be grouped into two main categories: displacement-based approaches, and mixed approaches with independently assumed displacement and stress fields. Although there are also a few stress-based approaches (Lekhnitskii, 1935), these tend to have significant shortcomings in relation to the treatment of geometric and material nonlinearity, and as such they are not discussed here.

2.4.1 Displacement approaches

The displacement approaches make assumptions on displacement fields only, based on which strains and stresses can be derived via the compatibility and constitutive relationships. The principle of virtual displacements (PVD) is employed to establish the governing equations. In terms of displacement descriptions, there are mainly two categories of displacement approaches (Carrera, 2003; Carrera & Demasi, 2002). Equivalent Single Layer (ESL) descriptions postulate base functions at the multi-layer level, and the associated displacement variables are defined for the whole lamination. Layer-wise (LW) descriptions, on the other hand, make assumptions for displacements at the layer level, so that each layer is regarded as an independent plate with ESL descriptions.

The accuracy of a lamination model is usually dependent on the suitability of the assumptions made for the displacement and stress distributions in the thickness direction. Therefore in the following, lamination models with the ESL and LW descriptions are briefly reviewed.

2.4.1.1 Equivalent Single Layer (ESL) description

The ESL models usually assume through-thickness displacement modes at the multi-layer level, which leads to the independence of the number of displacement variables from the number of constitutive layers.

The classical lamination theory (CLT) is an extension of the Kirchhoff plate theory to laminated composites, which assumes that the transverse normal of the plate before deformation remains straight and perpendicular to the mid-surface after deformation (Figure 2.2). The displacement fields are thus given as:

$$u_\alpha(x,y,z) = u_{\alpha 0}(x,y) - z\frac{\partial u_{z0}(x,y)}{\partial \alpha} \quad (\alpha = x,y) \tag{2.1}$$

$$u_z(x,y,z) = u_{z0}(x,y) \tag{2.2}$$

where $u_{x0}, u_{y0}, \text{and } u_{z0}$ denote the displacements evaluated at the middle surface. It is evident the assumed displacements result in zero transverse shear deformation, which is incorrect for moderately thick to thick applications.

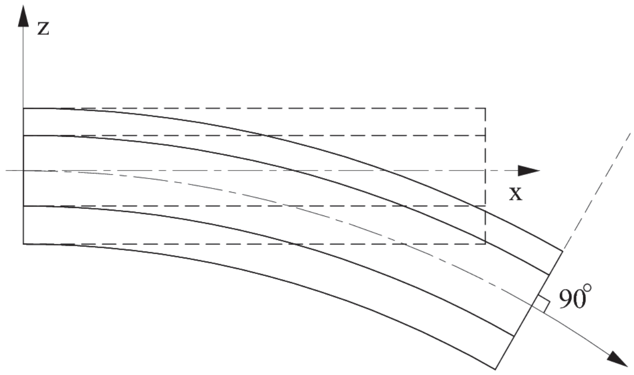

Figure 2.2: Classical lamination theory.

First-order shear deformation theory (FSDT), as depicted in Figure 2.3, extends the Reissner-Mindlin plate theory to a multi-layer case and assumes the following displacement fields:

$$u_{\alpha}(x,y,z) = u_{\alpha 0}(x,y) + z\theta_{\alpha}(x,y) \quad (\alpha = x, y) \tag{2.3}$$

$$u_{z}(x,y,z) = u_{z0}(x,y) \tag{2.4}$$

where θ_{α} denotes the rotation of the cross-section. As a result, constant shear strains are derived at each layer, which is different from the real shear strain distribution and hence leads to inaccuracy in the solution.

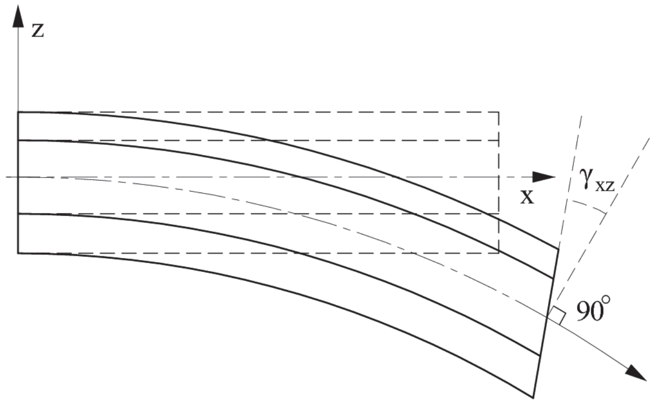

Figure 2.3: First-order shear deformation theory.

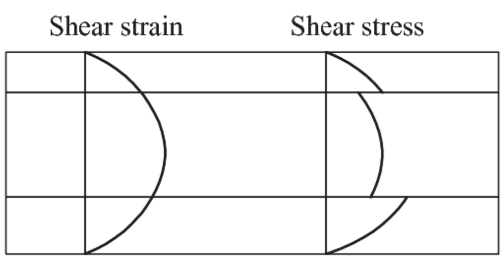

Figure 2.4: Distribution of transverse shear stress and strain in Vlasov-Reddy theory (Carrera, 2002).

The Vlasov-Reddy theory (VRT) (Reddy, 2004) modifies the Reissner-Mindlin type theories by enriching planar displacement fields with third-order terms with respect to z without introducing more variables, which results in a parabolic distribution of the transverse shear strain and achieves stress-free boundary conditions (Figure 2.4). The displacement fields are given as:

$$u_\alpha(x,y,z) = u_{\alpha 0} + (z - \frac{4}{3h^2} z^3)\theta_\alpha - \frac{4}{3h^2} z^3 \frac{\partial u_z}{\partial \alpha} \quad (\alpha = x, y) \tag{2.5}$$

$$u_z(x,y,z) = u_{z0} \tag{2.6}$$

The VRT is an improved shear deformation theory over the FSDT, which preserves the number of variables of FSDT and provides a more accurate prediction of displacements and stresses. However, the VRT is associated with a continuous distribution of the transverse shear strain through the plate thickness, while in fact it is the transverse shear stress that should be continuous through the lamination thickness

Higher-order shear deformation theories (HSDTs) introduce to displacement fields additional variables associated with higher-order z expansions to enrich the distribution of the transverse shear strains (Reddy, 2004). A generalised expression of HSDTs is given by:

$$u_i(x,y,z) = u_{i0} + z\,u_{i1} + z^2\,u_{i2} + \cdots + z^{N_i}\,u_{iN_i} \quad (i = x, y, z) \tag{2.7}$$

where N_i is the highest order of expansion used for the displacement u_i. Note that although HSDTs improve the accuracy of the global response with higher-order out-of-plane z expansions of the displacement fields, these z expansions, which are defined at the multi-layer level, cannot describe the zigzag-type discontinuity associated with the variation of mechanical properties through the thickness.

In order to allow a zigzag description of displacements, Murakami (1986) improved FSDT and HSDTs by introducing a piecewise linear zigzag function (Figure 2.5), which is defined as:

$$f(z) = (-1)^k \frac{2(z - z^{(k)})}{h_k}, \quad z \in [h_{k-}, h_{k+}] \tag{2.8}$$

where h_k is the thickness of layer (k); h_{k-} and h_{k+} refer to the values of z at the bottom and top of layer (k), respectively; and $z^{(k)}$ is the extracted value of z on the middle surface of layer (k).

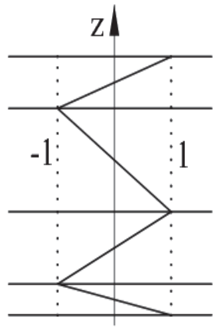

Figure 2.5: Murakami's zigzag function.

A generalised expression of the inclusion of Murakami's zigzag function (MZZF) within HSDTs is hence given as (Figure 2.6):

$$u_i(x, y, z) = u_{i0} + z\,u_{i1} + z^2\,u_{i2} + \cdots + z^{N_i}\,u_{iN_i} + f(z)\,u_{iZ} \quad (i = x, y, z) \tag{2.9}$$

where u_{iZ} represents the displacements associated with the Murakami type zigzag mode. These models are denoted by acronyms EDZN, where N denotes the highest order of z expansions employed (Carrera, 2003).

In the aforementioned ESL models, the number of displacement variables is independent of the number of layers because the base functions are defined at the multi-layer level and used by all constitutive layers. However, the displacement variables defined at the multi-layer level in turn lead to their insensitivity to constitutive layers. The inclusion of MZZF within HSDTs greatly improves the predictions, but a LW description is still necessary if accurate estimation of local effects is required. It is noted that MZZF may not the best zigzag function in some lamination lay-ups, unless it is coupled with the use of mixed assumption (Carrera, 2001).

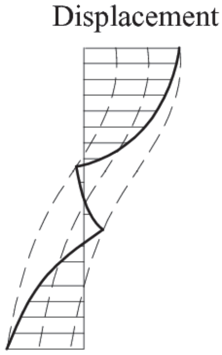

Figure 2.6: Schematic representation of the EDZN model (Carrera, 2003).

2.4.1.2 Layer-wise (LW) description

In the LW description, base functions are assumed at the layer level, and compatibility conditions at layer interfaces are imposed to fulfil the continuity requirements on inter-laminar displacements (Figure 2.7). Each layer of the laminate is regarded as an independent plate or shell and is solved with any of the ESL theories, such that the zigzag effect of the lamination can be well reflected. (Reddy, 2004)

At each layer, the displacements are generally expressed as:

$$u_i^{(k)}(x,y,z) = u_{i0}^{(k)} + z\,u_{i1}^{(k)} + z^2\,u_{i2}^{(k)} + \cdots + z^{N_i}\,u_{iN_i}^{(k)} \quad (i = x, y, z) \tag{2.10}$$

where $u_{i0}^{(k)} \rightarrow u_{iN_i}^{(k)}$ are displacement variables defined at layer (k).

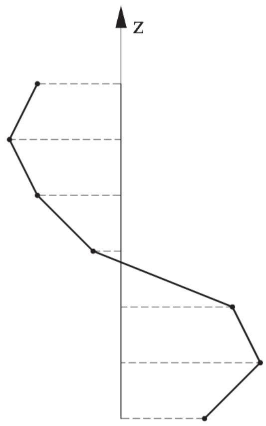

Figure 2.7: Layer-wise description of displacement (a linear field).

These displacement-based LW models are denoted by the acronyms LDN (Carrera, 2003). Owing to the definition of displacement variables at the layer level, the LW models capture both global and local response of laminations. Nevertheless, this leads to the dependence of DOFs on the number of constitutive layers, where some layer displacement variables are owned by one layer and some other displacement variables are shared by adjacent layers. Another shortcoming of LW models is the violation of continuity of shear stress at interfaces.

There are also a few displacement-based LW models which impose inter-laminar continuity constraints on both displacement fields and transverse stress fields (Pandit et al., 2008; Pandit et al., 2009; Kapuria & Achary, 2004). By fulfilling continuity requirements on both transverse stresses, the number of displacement parameters can be reduced, which in turn results in highly coupled constitutive layers.

2.4.2 Mixed approaches

In the mixed approaches, not only displacement variables but also stress and/or strain variables are used in the formulation, and mixed variational principles are employed to relate the displacement variables with stress and/or strain variables.

In the modelling of a multi-layer plate, Murakami (1986) introduced the MZZF within FSDT and assumed a piecewise quadratic continuous distribution of transverse shear stresses. Then, by employing Reissner's mixed variational theorem (RMVT), stress unknowns were expressed in terms of displacement unknowns, and governing equations were derived. Later, the mixed formulation was extended to higher-order planar displacement fields by Toledano and Murakami (1987).

A generalization of RMVT to develop ESL and LW plate/shell theories, as well as finite element applications, has been provided by Carrera (1997). Both sets of the RMVT models are reviewed in the following.

2.4.2.1 ESL description with RMVT applications

In the RMVT-based formulations with the ESL description, the displacement variables are defined at the multi-layer level, which is the same as PVD-based formulations employing the ESL description. On the other hand, the continuity requirement of transverse stresses at laminar interfaces calls for a LW description for transverse stresses. Subsequently, the displacement and transverse stress fields for these models can be expressed as (Carrera, 1997):

$$\mathbf{u} = F_0\mathbf{u}_0 + F_1\mathbf{u}_1 + F_r\mathbf{u}_r \quad (r = 2 \to N) \tag{2.11}$$

$$\boldsymbol{\sigma}_n^{(k)} = F_t\boldsymbol{\sigma}_{nt}^{(k)} + F_b\boldsymbol{\sigma}_{nb}^{(k)} + F_r\boldsymbol{\sigma}_{nr}^{(k)} \quad (r = 2 \to N) \tag{2.12}$$

where $\mathbf{u} = \left\langle u_x, u_y, u_z \right\rangle^T$ and $\boldsymbol{\sigma}_n^{(k)} = \left\langle \sigma_{xz}^{(k)}, \sigma_{yz}^{(k)}, \sigma_z^{(k)} \right\rangle^T$ are the assumed displacement fields and transverse stress fields, respectively; the through-thickness functions F_r are higher-order z polynomials, which are defined at the multi-layer level for displacements and at the layer level for stresses; F_t is a linear function of z defined at the layer level, which has a value of 1 at the top of layer (k) and reduces linearly to 0 at the bottom of layer (k); and F_b is similarly defined except that it equates to 1 at the bottom and 0 at the top of layer (k). To fulfil the continuity requirement of transverse stresses, the following constraints are imposed at each laminar interface:

$$\boldsymbol{\sigma}_{nt}^{(k)} = \boldsymbol{\sigma}_{nb}^{(k+1)} \quad (k = 1 \to N_l - 1) \tag{2.13}$$

where N_l is the number of layers.

The boundary conditions are also satisfied via the following equations:

$$\boldsymbol{\sigma}_{nb}^{(1)} = \overline{\boldsymbol{\sigma}}_{nb}, \quad \boldsymbol{\sigma}_{nt}^{(N_l)} = \overline{\boldsymbol{\sigma}}_{nt} \tag{2.14}$$

These ESL models with the application of RMVT are denoted by the acronyms EMCN.

Better accuracy can be achieved via the inclusion of MZZF in such models (Figure 2.8), which leads to the following sets of assumed displacements (Carrera, 1997):

$$\mathbf{u} = F_0\mathbf{u}_0 + F_1\mathbf{u}_1 + f(z)\mathbf{u}_Z + F_r\mathbf{u}_r \quad (r = 2 \to N) \tag{2.15}$$

The expressions of transverse stresses are the same as (2.12). These EMCN models enriched with the MZZF are denoted as EMZCN, the performance of which is improved by capturing the zigzag effect. The EMZCN models provide a convenient tool to consider the lamination effects in terms of accuracy versus the required computational efforts, and they have also been employed in finite element formulations to analyse sandwich and lamination problems involving geometric nonlinearity (Carrera, 1998; Carrera & Krause, 1998; Carrera & Parisch, 1997; Carrera, 1997).

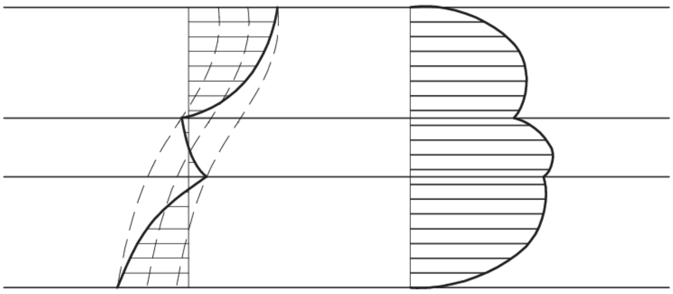

Figure 2.8: Schematic representation of the EMZCN model (Carrera, 2003).

2.4.2.2 LW description with RMVT applications

The LW models with the employment of RMVT assume displacements and transverse stresses both at the layer level, with the expressions for layer displacements given as:

$$\mathbf{u}^{(k)} = F_t \mathbf{u}_t^{(k)} + F_b \mathbf{u}_b^{(k)} + F_r \mathbf{u}_r^{(k)} \quad (r = 2 \rightarrow N) \tag{2.16}$$

The expressions of transverse stresses are the same as (2.12).

Inter-laminar constraints are imposed on both displacements and transverse stresses, so these models can capture well the zigzag effect of displacements and transverse stresses (Figure 2.9).

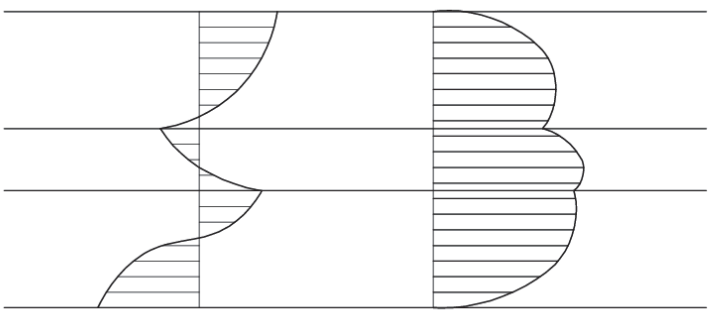

Figure 2.9: Schematic representation of displacements and transverse stresses in RMVT (Carrera, 2003).

2.5 Material modelling

2.5.1 General

Structural glass is a brittle material, the strength of which has a wide statistical variation due to the embedded Griffith flaws (Bennison et al., 1999). However, in the pre-cracking phase, it can be regarded as an isotropic material with well-defined Young's modulus and Poisson's ratio. Therefore, in this research, an isotropic material model is employed for glass.

On the other hand, the stress-strain curve of PVB is nonlinear in the finite-to-large strain range. Based on experimental data, Xu et al. (2011) proposed nonlinear tension and compression constitutive models for both quasi-static and dynamic loading conditions, with the parameters in the model determined through curve fitting. These material models can be used for impact analysis where the localised strains in PVB are too large to ignore the material nonlinearity.

By restricting the concentration on the pre-cracking phase where the deformation of the PVB is within small-strain range, a linear stress-strain relationship can be regarded for this material. There are several works in the literature that employ linear viscoelastic material models in the analysis of LG under both pseudo-static and dynamic loadings (Wei et al., 2006; Bennison et al., 1999; Duser et al., 1999). Therefore, in the following, the features of viscoelastic materials are provided, and linear viscoelastic material models are reviewed.

2.5.2 Viscoelastic materials

Polymers are composed of large molecules, which are formed via polymerisation of many small monomers. They are viscoelastic materials, with the material properties dependent on both temperature and time (Shaw & MacKnight, 2005). Figure 2.10 depicts the schematic modulus-temperature curve for typical viscoelastic materials, where the stress relaxation modulus E is obtained at a given time (say 10 sec).

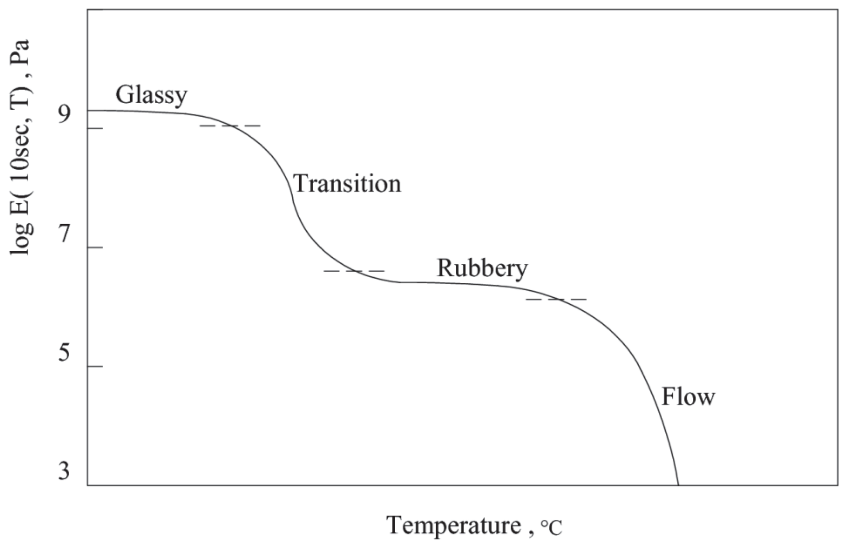

Figure 2.10: Schematic modulus-temperature curve for viscoelastic materials (Shaw & MacKnight, 2005).

The effect of the temperature on viscoelastic material properties can be explained at the molecular level. Evident from the curve, the glassy region corresponds to the low temperature range, where the polymer shows high stiffness owing to insufficient thermal energy for allowing segment motions of polymer molecules. In the transition region, elevated temperature results in increased thermal energy that initiates the movement of molecular segments, which induces an abrupt decrease in the material modulus. As the temperature increases, the modulus reaches another plateau region, called the rubbery plateau region. For further increase in temperature, the modulus undergoes a second abrupt decrease due to the increased thermal energy allowing translation of whole polymer molecules (Shaw & MacKnight, 2005).

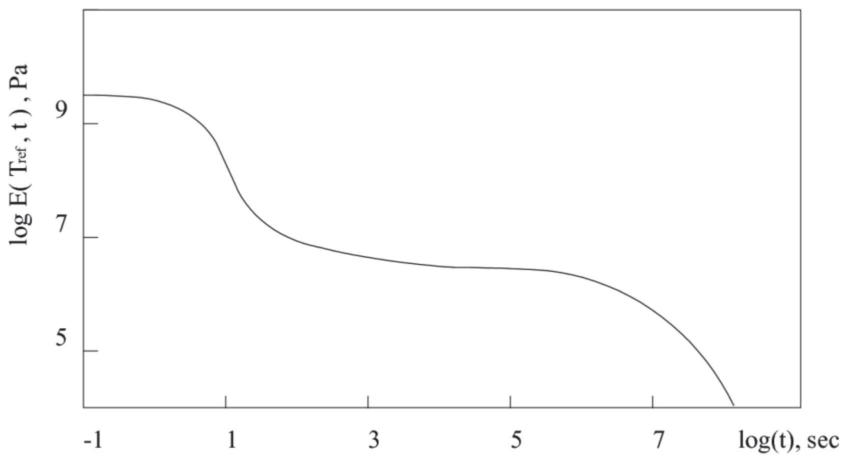

Figure 2.11: Schematic master curve of stress relaxation modulus (Shaw & MacKnight, 2005).

Figure 2.11 depicts the modulus-time curve for viscoelastic materials at a reference temperature. Here again, the time-dependent effect is explained at the molecular level. A high modulus is observed upon load application, owing to the insufficient time for the polymer molecules to reorient and relieve local strains. As time passes the glass transition process is observed, where the modulus decreases significantly due to segmental reorientation. After extensive chain reorientation has taken place, the distortion in chains has been alleviated, and the polymer behaves like a rubber. As time increases much further, the chains can move past one another, resulting in complete relaxation, which accounts for the second rapid decrease in the modulus (Shaw & MacKnight, 2005).

2.5.3 Mechanical models for viscoelastic materials

The time-temperature correspondence principle states that the effect of changing temperature is the same as applying a multiplicative factor to the time scale, which can be expressed as follows (Shaw & MacKnight, 2005):

$$E(T,t) = E(T_0, t/a_T) \tag{2.17}$$

where T_0 is the reference temperature, and T is an arbitrary temperature. Equation (2.17) states that if the material modulus-time curve at a reference temperature T_0 is known, the modulus-time curve at an arbitrary temperature T can be obtained from the known curve by multiplying the time scale with a factor $1/a_T$.

The Williams-Landell-Ferry (WLF) equation gives the relationship between a_T and the change in temperature $(T-T_0)$ (Ferry, 1980):

$$\log_{10} a_T = -\frac{C_1(T-T_0)}{C_2 + T - T_0} \tag{2.18}$$

in which C_1 and C_2 are constants that vary from polymer to polymer.

With the employment of (2.17)-(2.18), the master curve (i.e. the modulus-time curve) of a polymer at an arbitrary temperature can be obtained from the master curve constructed at a reference temperature.

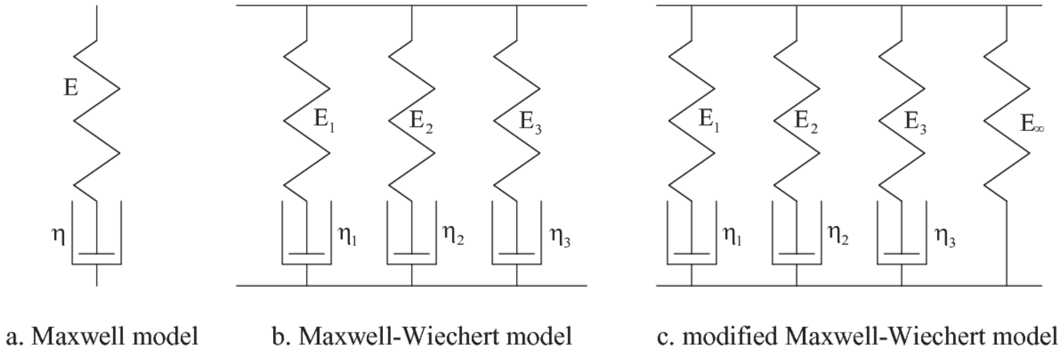

Figure 2.12: Mechanical viscoelastic material models (Shaw & MacKnight, 2005).

Many mechanical models have been proposed to reproduce the linear viscoelastic response of real systems. The Maxwell model is a series combination of a spring element and a dashpot element, as shown in Figure 2.12.a, where the Hooke spring represents the pure elastic response, and the dashpot element represents the pure viscous response (Shaw & MacKnight, 2005). The Maxwell-Wiechert model is a generalised model consisting of an arbitrary number of Maxwell elements connected in parallel, as shown in Figure 2.12.b (Shaw & MacKnight, 2005). This model is usually used to obtain the stress relaxation modulus. The stress relaxation modulus resulting from this model is given as (Shaw & MacKnight, 2005):

$$E(t) = \sum_{j=1}^{N_M} E_j e^{-t/\tau_j} \tag{2.19}$$

where N_M is the number of Maxwell elements employed in the Maxwell-Wiechert model; τ_j is a relaxation time parameter of the j^{th} Maxwell element.

It is possible to replace one of the Maxwell elements in the Maxwell-Wiechert model with a spring, as shown in Figure 2.12.c. In this manner, the stress would decay to a finite value rather than zero, thus (2.19) is modified to the following form (Bennison et al., 1999):

$$E(t) = E_\infty + \sum_{j=1}^{N_M} E_j e^{-t/\tau_j} \tag{2.20}$$

where E_∞ is the long-time plateau modulus.

The relationship between the stress and the strain can be expressed as:

$$\sigma(t) = \int_0^t E(t-s)\frac{\partial \varepsilon(s)}{\partial s}ds \tag{2.21}$$

The use of this generalised Maxwell series for representing the shear modulus of viscoelastic materials automatically accounts for time-dependent effects. On the other hand, the temperature-dependent effects on the variation in shear modulus can be considered by using the WLF equation to shift the time dependent shear modulus curve to a different temperature. The incorporation of both time- and temperature-dependent effects in the viscoelastic material model makes it possible for analysing problems with a wide range of temperature and loading rates.

2.6 Locking elimination techniques

Ever since the emergence of the displacement-based finite element method, a most serious problem that has influenced its application in linear and nonlinear structural analysis has been related to the locking phenomenon, in which the element exhibits an over-stiff response resulting from its inability to correctly model lower-order modes. The significance of this phenomenon is determined by several factors, including the type of structural analysis problem, the theory underlying the associated mathematical model, as well as the element shape and order. Early forms of locking were observed in the modelling of plate bending problems using the Reissner-Mindlin hypothesis (Zienkiewicz & Taylor, 2000), where the inability of a mesh of conforming elements to bend without inducing transverse shear strains leads to deteriorating performance as the plate thickness is reduced, a phenomenon referred to as shear locking. Other forms of locking can also arise with conforming elements, such as membrane locking when using curved shell elements, and distortion locking when employing isoparametric mapping with irregular element shapes.

Whilst locking phenomena may be viewed from several different perspectives depending on the context of element application, a common feature is the degradation in the approximation of various strains over the element domain, principally due to polluting higher-order strains. Numerous research efforts have been devoted to addressing this issue over the past few decades, which can be grouped under distinct strands, as briefly reviewed in the following.

Uniform reduced integration (Zienkiewicz et al., 1971; Pugh et al., 1978; Stolarski & Belytschko, 1982) addresses element locking by filtering out higher-order stiffness terms via the employment of a reduced number of integration points, which in turn suffers from rank deficiency leading to spurious mechanisms. Selective reduced integration (Hughes et al., 1977; Doherty et al., 1969; Malkus & Hughes, 1978) improves the shear locking performance of Reissner-Mindlin plate bending elements by employing reduced integration for only the transverse shear strain terms while utilising full integration on the remaining terms, which effectively addresses the rank deficiency issue. However, such a technique is restricted to plates with uncoupled flexural and transvers shear actions, and accordingly it cannot be employed for modelling the nonlinear elasto-plastic material response.

There are a few enhanced displacement methods in the literature (Tessler & Hughes, 1985; Tessler & Hughes, 1983; Izzuddin & Lloyd Smith, 2003), which generally eliminate shear locking by introducing extra displacement parameters, which, however, leads to an enlarged stiffness matrix with more DOFs.

The enhanced assumed strain methods (Simo et al., 1993; Simo & Rifai, 1990) address locking by enriching the element with enhanced strain fields, where the enhanced strain parameters are condensed out using the Hu-Washizu variational principle. Later, Korelc and Wriggers (1997) used a Taylor series expansion of strains with respect to natural coordinates in improving the behaviour of distorted elements and relieving the coupling of enhanced modes.

Another group of assumed strain methods eliminates polluting higher-order strains by sampling and interpolating strain components at selected locations (Jang & Pinsky, 1987; Huang & Hinton, 1984; Macneal, 1982; Panasz & Wisniewski, 2008; Bathe & Dvorkin, 1986). The components to be sampled, the locations of the sampling points, and the interpolation functions vary in the literature. The family of elements using the Mixed Interpolation of Tensorial Components (MITC) method (Lee & Bathe, 2010; Bathe et al., 2003; Bucalem & Bathe, 1993; Bathe & Dvorkin, 1986), as a specific group of two-level approximation methods, performs sampling and mapping in a covariant coordinate system before transformation to a Cartesian coordinate system. Nevertheless, the performance of these strain mapping elements relies strongly on the locations of sampled strains for the assumed interpolation, which can lead to degradation of accuracy for irregular element shapes. To extend the ability of elements based on strain mapping method to highly irregular element shapes, Wisniewski and Panasz (2013) used corrected shape functions in the element formulation, which addresses the sensitivity to mesh distortions, though nonlinear equations must be solved for determining the additional parameters describing the element distortion.

The hierarchic optimisation approach (Izzuddin, 2007), also as an assumed strain method, eliminates the polluting strain terms by performing mathematical optimisation on a combination of the conforming strains with assumed hierarchic higher-order strain terms towards an objective strain distribution. In this respect, the objective strains follow the distribution afforded by the original element DOFs in terms of real (physical) coordinates, while the hierarchic modes are used solely for the purpose of optimisation of the strain fields and are eliminated via the optimisation procedure. This method not only alleviates shear and membrane locking, but also addresses locking arising from element distortion.

2.7 Co-rotational approach

In formulating large displacement finite elements for small strain problems, the relationship between the strain and displacement fields is highly nonlinear and complex if the displacement fields are referred to a fixed coordinate system, where the nonlinear strain terms arise mainly from the element rigid body rotations. The co-rotational approach, which decomposes the element motion into rigid body and strain-inducing parts via the use of a local co-rotational system, offers exceptional benefits for large displacement structural analysis problems with deformations of the bending type, particularly when accounting for arbitrarily large rigid body rotations. By choosing an element-specific co-rotational reference system which follows the element current deformed configuration, rigid body rotations of the element are removed, and low-order, even linear, relationships between the strain and local displacement fields may be employed. Therefore, the co-rotational approach shifts the focus of large displacement modelling from relating the strain and displacement fields to establishing transformations between local co-rotational and global nodal entities, hence effectively decoupling the large displacement issues from the local element discretization of the continuum response. In this respect, the co-rotational approach has the potential to be applied as an element independent procedure (Crisfield & Moita, 1996; Rankin & Brogan, 1986), upgrading linear local element formulations of different sophistication to geometric nonlinear analysis with relative ease.

A principal issue in any co-rotational approach is associated with the specific choice of the local reference system in relation to the current deformed element configuration. Depending on the specific definition of the local co-rotational system, the resulting co-rotational approach may be element independent but restricted to elements of a specific shape and order, or it may be more generally applied to elements of a particular shape regardless of order.

Rankin and Brogan (1986) defined two co-rotational systems for 3-noded triangular and 4-noded quadrilateral elements, respectively, where in both cases one of the local system axes was effectively aligned to one of the element edges. These definitions of the co-rotational system were used by Li et al. (Li & Vu-Quoc, 2007; Li et al., 2015) in 6-noded triangular elements for problems involving geometric and material nonlinearity, and by Jiang and Chernuka (1994) in a 4-noded quadrilateral element for large displacement analysis. Norachan et al. (2012) employed a co-rotational system for an 8-noded degenerated shell element, utilising the enhanced assumed strain and advanced natural strain concepts for the treatment of locking (Kim et al., 2005; Eberlein & Wriggers, 1999), where one of the local system axes was aligned with one of the planar covariant base vectors. Alves de Sousa et al. (2006) also considered a co-rotational approach for a degenerated shell element, though the co-rotational transformations were applied at the constitutive integration point level, thus losing the desirable characteristics of element independence and decoupling between the co-rotational transformations and the local element formulation.

Whilst an arbitrary definition that simply requires the local co-rotational system to closely follow the current element configuration, as in the above definitions, may not significantly affect the large displacement response predictions for small strain problems, this often leads to local system definitions which are not invariant to the specified order of the element nodes. Besides the errors that could arise with such definitions when elements in the same mesh are defined using different nodal ordering, it has also been argued that the invariance characteristic would be desirable for extending the co-rotational approach to large strain problems (Crisfield & Moita, 1996) and for identifying the bifurcation points of perfectly symmetric structures (Battini & Pacoste, 2004).

Towards this end, several approaches were previously proposed to achieve the invariance of the local system to nodal ordering. Kebari and Cassell (1992) defined the co-rotational system for a 9-noded quadrilateral shell element by locating the two planar axes symmetrically with respect to the two planar curvilinear coordinates at each integration point. Kim and co-workers (Kim & Lomboy, 2006; Kim et al., 2003; Kim et al., 2007) employed this definition of the co-rotational system in the formulation of 4-noded and 8-noded monolithic and laminated shell elements for analysis of both elastic and elasto-plastic problems, but the alignment of the planar axes was performed at the element centroid only rather than at all integration points. Crisfield and Moita (1996) proposed a co-rotational system that enforced zero local spin at the element centroid using polar decomposition, which they employed for 2D/3D continuum elements as well as shell elements. A common feature of these definitions is their reliance on the local element displacement fields, which restricts their application in each instance to elements of the same shape and order; in this respect, these definitions are only partially element independent. It is also worth noting that Crisfield and Moita (1996) indicated that their approach leads to an asymmetric geometric stiffness matrix, which is obviously undesirable from a computational perspective. In reality, the geometric stiffness matrix, which is directly related to the second derivatives of local with respect to global nodal displacements, cannot be asymmetric when the local co-rotational system is uniquely defined in terms of global nodal displacements.

There are a few other definitions of the local co-rotational system which not only possess the invariance characteristic to nodal ordering but are also defined in terms of only nodal position variables, thus making them potentially independent of the local element formulation and its order. Rankin (1998) defined a co-rotational system by minimising the square of Euclidean norm of nodal local displacements, where the local system orientation was determined through an iterative procedure. This definition was adopted by Eriksson and Pacoste (2002) and later refined by Battini and Pacoste (Battini & Pacoste, 2004) for a 3-noded triangular shell element where the need for iteration was overcome with explicit expressions for the orientation of the local system. Importantly, Battini and Pacoste (2004) developed similar expressions for the 3-noded triangular element considering also the zero spin definition (Crisfield & Moita, 1996), and they noted that both alternative definitions may be directly used for elements of higher order. Whilst achieving considerable simplification over the previous approaches (Crisfield & Moita, 1996; Rankin & Brogan, 1986), the approach developed by Battini and Pacoste (2004) employs two stages, where in the first stage local entities are determined for a local system that follows one of the element edges, and this is then subjected to a spin rotation in a second stage to determine its final orientation. A simpler bisector definition was proposed by Izzuddin (2005) for quadrilateral elements, where the local planar axes are defined as the bisectors of interior angles formed by the intersection of the two element diagonals. This co-rotational system was subsequently employed by Li et al. (Li et al., 2013; Li et al., 2011; Li et al., 2008) in the formulation of a 9-noded shell element applied to multi-layered shell problems and elasto-plastic analysis. Later, Izzuddin (2006) extended the bisector definition to triangular elements by aligning the bisectors of the angle that has changed most from the undeformed configuration, which still possesses all the desirable characteristics. Meanwhile, he also proposed an alternative and equally simple definition, the zero-macrospin definition (Izzuddin, 2006), which is based on zero-spin at the macro element level, thus reducing the material spin in an aggregate sense over the element domain. Not only do both definitions of the local co-rotational system achieve nodal invariance as well as independence of the local element formulation and order, but they are also easily and directly determined from global nodal position variables.

2.8 Concluding remarks

This chapter presents experiments on LG beams and panels, where the features of LG have been pointed out, including the zigzag displacement variation through the LG thickness and the dependence of results on loading rates and temperatures. Subsequently, various numerical modelling approaches, along with their advantages and disadvantages, have been presented. The benefits of laminated shell models over other alternatives have been discussed with respect to the computational demand and the accuracy, though an adequate through-thickness description of the lamination is required.

An extensive review of existing 2D lamination theories is subsequently presented, where the benefits and disadvantages of displacement-based models and mixed models with either ESL descriptions or LW descriptions have been discussed. Although a great many lamination theories have been developed, there is a lack of lamination models that consider laminated composites with significant stiffness mismatch and an alternating stiff/soft lay-up, such as the considered LG profiles, which are associatred with huge glass-to-PVB modulus ratios. The special stiffness mismatch and stacking sequence ought to induce different through-thickness characteristics, which may be utilised to obtain simpler and accurate lamination models.

Furthermore, the interpretation of the viscoelastic characteristic of PVB is presented, and several mechanical models for representing linear viscoelastic materials are overviewed. The generalised Maxwell model captures well the characteristic of PVB, which enables the dependence of PVB material properties to the loading rate and temperature.

In the perspective of shell element formulations, available lock-elimination approaches are overviewed, and their advantages and shortcomings are discussed. Although a lot of effort has been devoted to overcoming the locking phenomenon, it remains difficult for shell elements with either regular or distorted shape to possess an optimal convergence rate, which implies room for enhancement of current methods. Finally, the benefits and desirable characteristics of the co-rotational approach, as well as the existing alternative definitions of the co-rotational system, are presented. It is worth noting that a more targeted review of the literature is also undertaken in subsequent chapters, at the point of presenting new developments.

CHAPTER 3

Monolithic Quadrilateral and Triangular Shell Elements

3.1 Introduction

In accordance with the research aims described in Chapter 1, the objective of this chapter is to provide efficient monolithic shell element formulations allowing large displacement analysis. These will later be employed as the basis for developing geometrically nonlinear formulations of laminated shells, with the inclusion of an appropriate through-thickness description of the displacements and stresses.

As reviewed in Chapter 2, the locking phenomenon exists in lower-order plate and shell elements based on the Reissner-Mindlin hypothesis, which is associated with an over-stiff element response resulting from its inability to correctly model lower-order strain modes. The hierarchic optimisation approach proposed by Izzuddin (2007), as an assumed strain method, not only alleviates shear and membrane locking, but also addresses locking arising from element distortion. In this chapter, this method is reviewed and elaborated, and it is subsequently employed throughout this research.

As mentioned before, the employment of the co-rotational approach for large-displacement small-strain problems can upgrade linear local element formulations of different sophistication to geometric nonlinear analysis with relative ease. The exclusion of rotational rigid-body modes from the local element formulation also enables the optimal mapping between assumed and conforming strains to be established only once for an element at the start of incremental nonlinear analysis. Furthermore, in the consideration of laminations, the co-rotational approach allows the inclusion of a constant through-thickness description of local displacements and stresses into the local element formulation, which will be elaborated in Chapter 6. Therefore, the two simple and efficient definitions of the co-rotational approach, the bisector and the zero-macrospin definitions proposed by Izzuddin (2006), are also reviewed and elaborated in this chapter, and these are subsequently utilised in this research work.

Following the review of the hierarchic optimisation approach and the two co-rotational systems, co-rotational formulations of monolithic 9-noded and 6-noded shell elements are presented, where the 9-noded element was previously developed by Izzuddin and co-workers (Izzuddin & Li, 2004; Li et al., 2008) and modified for the strain mappings in this work, while the 6-noded element is fully developed in the present research work. Consistent mass matrices for both elements are also derived, which allows the dynamic analysis of the considered shell elements.

3.2 Hierarchic optimisation approach

The hierarchic optimisation approach was originally proposed by Izzuddin (2007) for nonlinear shell finite elements, and it not only alleviates shear and membrane locking, but also addresses locking arising from element distortion. This approach can be regarded as an assumed strain method, but it has three distinct features.

Firstly, it introduces the notion of *objective* strain modes, defined in the physical coordinate system, which act as the target strain modes for the conforming strain modes enhanced with *corrective* strain modes. The objective and corrective strain parameters are obtained from mathematical optimisation, and this leads to two alternative families of element, denoted by acronym keys O and C, in which assumed strains based respectively on the objective or corrective strain fields are directly mapped at the element level to the conforming strains. Secondly, the corrective strain modes are established from hierarchic displacement modes defined in the natural coordinate system, where modes up to any hierarchic order m can be considered in the element optimisation process for both the O and C element families.

Importantly, these hierarchic modes are used solely for the purpose of optimisation of the objective and corrective strain fields, and as such do not influence the number of element DOFs. Thirdly, geometric nonlinearity is considered within a co-rotational framework (Li et al., 2008; Izzuddin, 2007), which provides accurate nonlinear predictions with the Reissner-Mindlin hypothesis for the local shell element response, and which enables the optimal mapping between assumed and conforming strains to be established for an element from the solution of a linear system of equations. In this respect, the optimal mapping for individual elements need only be established once, at the start of incremental nonlinear analysis, and further computational benefits arise from uncoupled mappings of the planar, bending and transverse shear strains, which can be applied even to elements with local geometric nonlinearity.

The concept of the hierarchic optimisation approach is to employ hierarchic strain parameters, associated with higher-order shape functions beyond those used in the conforming element formulation, such that the combination of the conforming strains $\boldsymbol{\varepsilon}$ and the hierarchic *corrective* strains $\boldsymbol{\varepsilon}^{\mathrm{h}}$ offers a close approximation of the highest-order strain distribution $\boldsymbol{\varepsilon}^{\mathrm{o}}$ afforded by the original element DOFs in terms of real (physical) coordinates. In this respect, the *objective* strain vector $\boldsymbol{\varepsilon}^{\mathrm{o}}$ combines contributions from various strain-inducing modes $\boldsymbol{\Psi}^{\mathrm{o}}$ associated with the strain field under consideration, where the number of such modes depends on the associated DOFs of the conforming element. Accordingly, $\boldsymbol{\varepsilon}$ is enhanced with $\boldsymbol{\varepsilon}^{\mathrm{h}}$ towards $\boldsymbol{\varepsilon}^{\mathrm{o}}$ (Izzuddin, 2007):

$$\boldsymbol{\varepsilon}+\boldsymbol{\varepsilon}^{\mathrm{h}} \approx \boldsymbol{\varepsilon}^{\mathrm{o}}, \quad \boldsymbol{\varepsilon}^{\mathrm{h}} = \boldsymbol{\Psi}^{\mathrm{h}}\boldsymbol{\alpha}^{\mathrm{h}}, \quad \boldsymbol{\varepsilon}^{\mathrm{o}} = \boldsymbol{\Psi}^{\mathrm{o}}\boldsymbol{\alpha}^{\mathrm{o}} \tag{3.1}$$

where $\boldsymbol{\Psi}^{\mathrm{h}}$ and $\boldsymbol{\Psi}^{\mathrm{o}}$ represent the hierarchic corrective and objective strain-inducing modes, respectively, while $\boldsymbol{\alpha}^{\mathrm{h}}$ and $\boldsymbol{\alpha}^{\mathrm{o}}$ are the respective associated strain parameters.

The employment of mathematical optimisation leads to a minimisation of the error between the corrective strain field $\boldsymbol{\varepsilon}+\boldsymbol{\varepsilon}^{\mathrm{h}}$ and objective strain field $\boldsymbol{\varepsilon}^{\mathrm{o}}$. Considering the target of optimisation to be a functional integrating the square of this error over the element domain, the strain parameters $\boldsymbol{\alpha}^{\mathrm{h}}$ and $\boldsymbol{\alpha}^{\mathrm{o}}$ are easily obtained for a given set of conforming strains $\boldsymbol{\varepsilon}$ from the solution of the following linear system of equations (Izzuddin, 2007):

$$\left(\int_{\Omega^e} \left[\begin{array}{c|c} \boldsymbol{\Psi}^{hT}\boldsymbol{\Psi}^{h} & -\boldsymbol{\Psi}^{hT}\boldsymbol{\Psi}^{o} \\ \hline -\boldsymbol{\Psi}^{oT}\boldsymbol{\Psi}^{h} & \boldsymbol{\Psi}^{oT}\boldsymbol{\Psi}^{o} \end{array} \right] d\Omega^e \right) \left\{ \begin{array}{c} \boldsymbol{\alpha}^{h} \\ \hline \boldsymbol{\alpha}^{o} \end{array} \right\} = \int_{\Omega^e} \left[\begin{array}{c} -\boldsymbol{\Psi}^{hT} \\ \hline \boldsymbol{\Psi}^{oT} \end{array} \right] \boldsymbol{\varepsilon}\, d\Omega^e \tag{3.2}$$

in which Ω^e is the element domain.

Accordingly, the elimination of the strain parameters at the element level preserves the computational efficiency, and the conforming strains are enhanced with hierarchic higher-order corrective strains towards the objective strains. The enhanced strains can be expressed in either the corrective or the objective form, where the difference between the two alternative approaches reduces with mesh refinement (Izzuddin, 2007):

$$\tilde{\boldsymbol{\varepsilon}} = \boldsymbol{\varepsilon} + \boldsymbol{\Psi}^{h}\boldsymbol{\alpha}^{h} \quad \text{(Corrective)} \tag{3.3}$$

$$\hat{\boldsymbol{\varepsilon}} = \boldsymbol{\Psi}^{o}\boldsymbol{\alpha}^{o} \quad \text{(Objective)} \tag{3.4}$$

Unlike previous enhanced assumed strain approaches (Korelc & Wriggers, 1997; Simo et al., 1993; Simo & Rifai, 1990), the hierarchic optimisation approach leads to two variant element families, depending on whether the corrective (C) or objective (O) fields is adopted for the assumed strains. Furthermore, while the corrective strain field $\boldsymbol{\varepsilon}^{h}$ resembles the enhanced assumed strain in previous approaches, its approximation order is not capped to a prescribed distribution but can attain any hierarchic order *m*. On the other hand, the additionally introduced objective strain field $\boldsymbol{\varepsilon}^{o}$ for a specific *n*-noded element is comprised of all low-order modes afforded by the original element DOFs in terms of real (physical) coordinates, which provides a natural remedy for distortion locking.

Noting the above distinct features, the resulting families of hierarchically optimised elements are denoted by acronyms H*m*O*n* and H*m*C*n*, corresponding respectively to the objective (O) and corrective (C) assumed strain families, where *m* is the order of hierarchic displacement fields used for the corrective strain modes, and *n* refers to the number of element nodes. Thus for example, H3O9 refers to a quadrilateral 9-noded Reissner-Mindlin shell element, with quadratic Lagrangian shape functions and cubic hierarchic displacement modes (*m*=3) for the corrective strains, and with the assumed strains based on the objective (O) strain modes.

For isoparametric elements, the integration is most effectively carried out with Gaussian quadrature, and hence the solution for $\boldsymbol{\alpha}^{\mathrm{h}}$ and $\boldsymbol{\alpha}^{\mathrm{o}}$ can be related to the strains $\boldsymbol{\varepsilon}_{(\mathrm{i})}$ at Gauss points as:

$$\boldsymbol{\alpha}^{\mathrm{h}} = \boldsymbol{\Gamma}^{\mathrm{h}} \begin{Bmatrix} \boldsymbol{\varepsilon}_{(1)} \\ \vdots \\ \boldsymbol{\varepsilon}_{(\mathrm{i})} \\ \vdots \end{Bmatrix}, \quad \boldsymbol{\alpha}^{\mathrm{o}} = \boldsymbol{\Gamma}^{\mathrm{o}} \begin{Bmatrix} \boldsymbol{\varepsilon}_{(1)} \\ \vdots \\ \boldsymbol{\varepsilon}_{(\mathrm{i})} \\ \vdots \end{Bmatrix} \tag{3.5}$$

in which the subscript (i) represents the Gauss point number.

Therefore, the enhanced strains at the Gauss points can be determined as follows depending on the alternative approach (Izzuddin, 2007):

$$\begin{Bmatrix} \tilde{\boldsymbol{\varepsilon}}_{(1)} \\ \vdots \\ \tilde{\boldsymbol{\varepsilon}}_{(\mathrm{i})} \\ \vdots \end{Bmatrix} = \tilde{\mathbf{T}} \begin{Bmatrix} \boldsymbol{\varepsilon}_{(1)} \\ \vdots \\ \boldsymbol{\varepsilon}_{(\mathrm{i})} \\ \vdots \end{Bmatrix}, \quad \tilde{\mathbf{T}} = \mathbf{I} + \begin{bmatrix} \boldsymbol{\Psi}^{\mathrm{h}}_{(1)} \\ \vdots \\ \boldsymbol{\Psi}^{\mathrm{h}}_{(\mathrm{i})} \\ \vdots \end{bmatrix} \boldsymbol{\Gamma}^{\mathrm{h}} \quad \text{(Corrective)} \tag{3.6}$$

$$\begin{Bmatrix} \hat{\boldsymbol{\varepsilon}}_{(1)} \\ \vdots \\ \hat{\boldsymbol{\varepsilon}}_{(\mathrm{i})} \\ \vdots \end{Bmatrix} = \hat{\mathbf{T}} \begin{Bmatrix} \boldsymbol{\varepsilon}_{(1)} \\ \vdots \\ \boldsymbol{\varepsilon}_{(\mathrm{i})} \\ \vdots \end{Bmatrix}, \quad \hat{\mathbf{T}} = \begin{bmatrix} \boldsymbol{\Psi}^{\mathrm{o}}_{(1)} \\ \vdots \\ \boldsymbol{\Psi}^{\mathrm{o}}_{(\mathrm{i})} \\ \vdots \end{bmatrix} \boldsymbol{\Gamma}^{\mathrm{o}} \quad \text{(Objective)} \tag{3.7}$$

in which $\tilde{\mathbf{T}}$ and $\hat{\mathbf{T}}$ are transformation matrices that transform conforming strains to respectively corrective strains and objective strains at the Gauss points.

For geometrically linear elements, the assumed strains $\tilde{\boldsymbol{\varepsilon}}$ or $\hat{\boldsymbol{\varepsilon}}$ can be directly related to the original displacement parameters via a respective strain operator $\tilde{\mathbf{B}}$ or $\hat{\mathbf{B}}$, since $\boldsymbol{\varepsilon}$ is readily related to such parameters through the conventional conforming $\mathbf{B}$ matrix. For geometrically nonlinear elements, however, it is more effective to determine the conforming strains and then transform these to assumed strains according to (3.6) or (3.7).

3.3 Co-rotational coordinate systems

In the following, the bisector and the zero-macrospin definitions of the co-rotational approach proposed by Izzuddin (2006) are reviewed, both of which are applicable to quadrilateral and triangular elements of different orders.

3.3.1 Bisector definitions

3.3.1.1 Quadrilateral element

The bisector co-rotational system for a 4-noded shell element is depicted in Figure 3.1, where the local x and y axes are chosen as the bisectors of the two diagonals of the undeformed element, and rigid body rotations are extracted by orienting these local planar axes so as to also bisect the element diagonals in the current deformed configuration. Clearly, this simple definition automatically satisfies the orthogonality requirement for the two planar axes, and leads to a relative local orientation of the deformed to the undeformed configuration which is invariant to nodal ordering. On the latter point, it is true that starting from a different node leads to different local axes; however, the eight possible sets of axes represent permutations over three specific orthogonal directions relative to the global system, which always leads to the same global element forces and tangent stiffness matrix regardless of the element nodal ordering. This bisector definition implies that the local rotations of the element diagonals, from the undeformed to the deformed configuration, are minimised, as can be observed from the right inset of Figure 3.1.

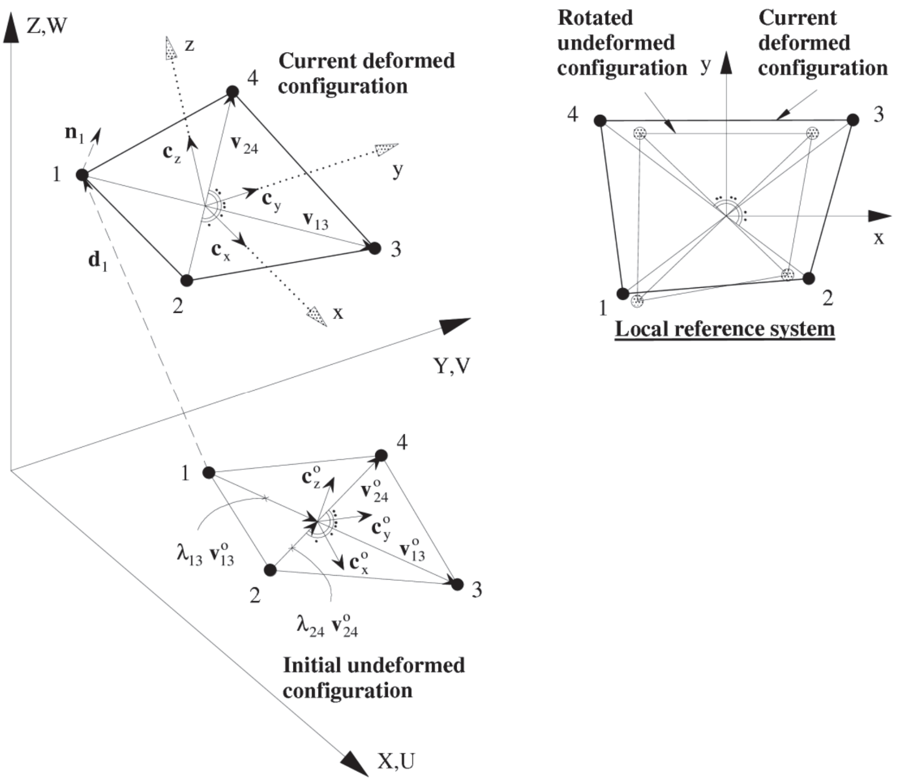

Figure 3.1: Bisector local co-rotational system and global nodal parameters for a 4-noded quadrilateral element (Izzuddin, 2006).

With reference to Figure 3.1, the triad ($\mathbf{c}_x, \mathbf{c}_y, \mathbf{c}_z$) defining the current orientation of the local co-rotational system relative to the global system is simply obtained as (Izzuddin, 2006):

$$\mathbf{c}_x = \frac{\mathbf{c}_{13} - \mathbf{c}_{24}}{\left|\mathbf{c}_{13} - \mathbf{c}_{24}\right|}, \quad \mathbf{c}_y = \frac{\mathbf{c}_{13} + \mathbf{c}_{24}}{\left|\mathbf{c}_{13} + \mathbf{c}_{24}\right|}, \quad \mathbf{c}_z = \mathbf{c}_x \times \mathbf{c}_y \tag{3.8}$$

with:

$$\mathbf{c}_{ij} = \frac{\mathbf{v}_{ij}}{\left|\mathbf{v}_{ij}\right|}, \quad \mathbf{v}_{ij} = \mathbf{v}_{ij}^{o} + \mathbf{d}_j - \mathbf{d}_i \tag{3.9}$$

where $\mathbf{v}_{ij}^{o}$ is the vector connecting node *i* to node *j* in the initial element configuration, and $\mathbf{d}_i = \left\langle U_{X,i}, U_{Y,i}, U_{Z,i} \right\rangle^T$ represents the global translational displacements of node *i*.

3.3.1.2 Triangular element

A bisector definition of the local co-rotational system for the triangular element becomes slightly more involved than for the quadrilateral element, particularly when the property of invariance to nodal ordering is to be achieved. In this respect, Izzuddin (2006) proposed that the invariance characteristic can be attained by considering the three internal angles (α, β, γ), subtended by the three lines connecting the triangle vertices to its centroid O, and aligning the bisectors of the angle that has changed most from the undeformed configuration (say angle $\delta\alpha$), as illustrated in the right inset of Figure 3.2 for alignment of the bisectors of α. Clearly, such a definition leads again to a relative local orientation of the deformed to the undeformed configuration which is invariant to nodal ordering, ensuring further that the local rotations of the three centroidal lines, from the undeformed to the deformed configuration, are minimised. The determination of the co-rotational triad is provided elsewhere (Izzuddin, 2006; Izzuddin & Liang, 2015).

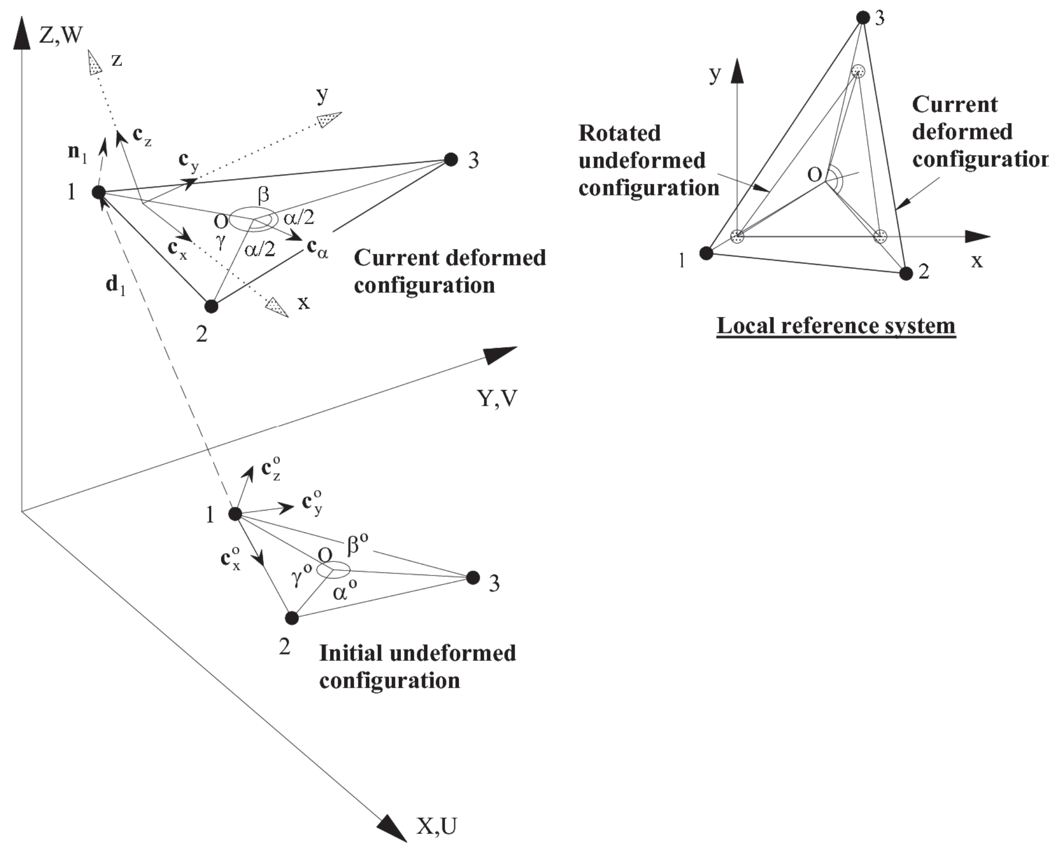

Figure 3.2: Bisector local co-rotational system and global nodal parameters for a 3-noded triangular element (Izzuddin, 2006).

It is important to note the alteration of the selected angle *during iteration* can lead in rare cases to oscillations between two angles, thus causing convergence difficulties, particularly when any two values of $(\delta\alpha, \delta\beta, \delta\gamma)$ are very close. In this respect, the selection of the specific angle to be bisected is fixed during an incremental step according to relative values of $(\delta\alpha, \delta\beta, \delta\gamma)$ at the last known equilibrium configuration.

3.3.2 Zero-macrospin definitions

The optimal orientation of the local reference system provides a rotated undeformed configuration such that the relative spin of the material in the current deformed configuration is zero. An equivalent condition is that the material strains are obtained from the rotated undeformed configuration using 'stretch' operations only, which cannot be fulfilled at all material points within an element that is subject to general strain variations when a single local reference system is used. The zero-macrospin definitions proposed by Izzuddin (2006) are based on zero-spin at the macro element level, which reduce the material spin in an aggregate sense over the element domain.

To introduce the zero-macrospin definitions of the local co-rotational system, consider a unit square area, defined by orthogonal unit vectors $\mathbf{c}_x = \langle 1\ 0 \rangle^T$ and $\mathbf{c}_y = \langle 0\ 1 \rangle^T$, which is subjected to a uniform planar 'stretch' operation in any two orthogonal directions leading to transformed vectors $\mathbf{c}'_x$ and $\mathbf{c}'_y$, as shown in Figure 3.3. It can be shown that $\mathbf{c}_x$ is always obtained as the normalised sum of $\mathbf{c}'_x$ and $\mathbf{c}'^n_y$, where $\mathbf{c}'^n_y$ is a planar rotation of $\mathbf{c}'_y$ by $-\pi/2$. $\mathbf{c}_y$ is similarly obtained as the normalised sum of $\mathbf{c}'_y$ and $\mathbf{c}'^n_x$, where $\mathbf{c}'^n_x$ is a planar rotation of $\mathbf{c}'_x$ by $+\pi/2$. Accordingly, if $\mathbf{c}_z$ is known, the remaining vectors of the triad are easily obtained from the stretched vectors as (Izzuddin, 2006):

$$\mathbf{c}_x = \frac{\mathbf{c}'_x + \mathbf{c}'^n_y}{\left|\mathbf{c}'_x + \mathbf{c}'^n_y\right|}, \quad \mathbf{c}'^n_y = \mathbf{c}'_y \times \mathbf{c}_z, \quad \mathbf{c}_y = \mathbf{c}_z \times \mathbf{c}_x \tag{3.10}$$

The use of this inverse transformation at the finite element level rather than at a specific material point can ensure zero-macrospin at the overall element level without the need for iteration.

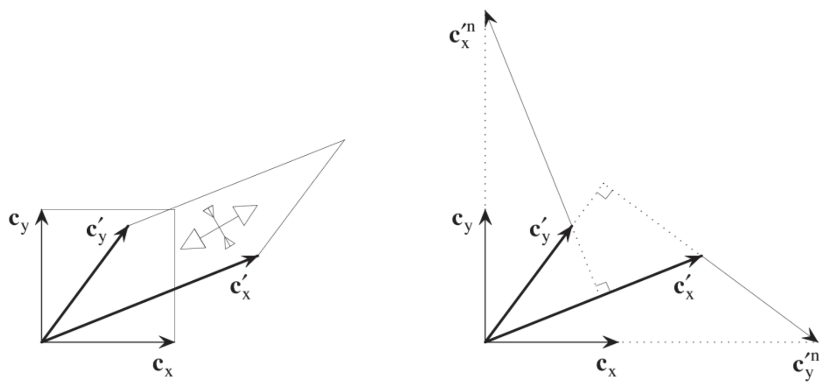

Figure 3.3: Influence of a uniform 'stretch' operation on a unit square area (Izzuddin, 2006).

3.3.2.1 Triangular element

With reference to Figure 3.4, in the initial undeformed configuration, the orthogonal unit vectors $\mathbf{c}_x^o$ and $\mathbf{c}_y^o$ are defined such that $\mathbf{c}_x^o$ is aligned with edge 1-2, and these are expressed in terms of the initial element vectors $\mathbf{v}_{12}^o$ and $\mathbf{v}_{23}^o$ as (Izzuddin, 2006):

$$\mathbf{c}_x^o = a_{x1}\mathbf{v}_{12}^o + a_{x2}\mathbf{v}_{23}^o, \quad \mathbf{c}_y^o = a_{y1}\mathbf{v}_{12}^o + a_{y2}\mathbf{v}_{23}^o \tag{3.11}$$

with the constants a_{x1}, a_{x2}, a_{y1}, and a_{y2} determined as:

$$a_{x1} = \frac{1}{\left|\mathbf{v}_{12}^o\right|}, \quad a_{x2} = 0, \quad a_{y1} = -\frac{\mathbf{c}_{12}^{o\,T}\mathbf{c}_{23}^o}{\left|\mathbf{v}_{12}^o\right|\sqrt{1-\left(\mathbf{c}_{12}^{o\,T}\mathbf{c}_{23}^o\right)^2}}, \quad a_{y2} = \frac{1}{\left|\mathbf{v}_{23}^o\right|\sqrt{1-\left(\mathbf{c}_{12}^{o\,T}\mathbf{c}_{23}^o\right)^2}} \tag{3.12}$$

$$\mathbf{c}_{ij}^o = \frac{\mathbf{v}_{ij}^o}{\left|\mathbf{v}_{ij}^o\right|} \tag{3.13}$$

In the current deformed configuration, the stretched vectors $\mathbf{c}'_x$ and $\mathbf{c}'_y$ are linked to $\mathbf{v}_{12}$ and $\mathbf{v}_{23}$ by the same geometric relationship (Izzuddin, 2006):

$$\mathbf{c}'_x = a_{x1}\mathbf{v}_{12} + a_{x2}\mathbf{v}_{23}, \quad \mathbf{c}'_y = a_{y1}\mathbf{v}_{12} + a_{y2}\mathbf{v}_{23} \tag{3.14}$$

where the constants a_{x1}, a_{x2}, a_{y1}, and a_{y2} are as given by (3.12).

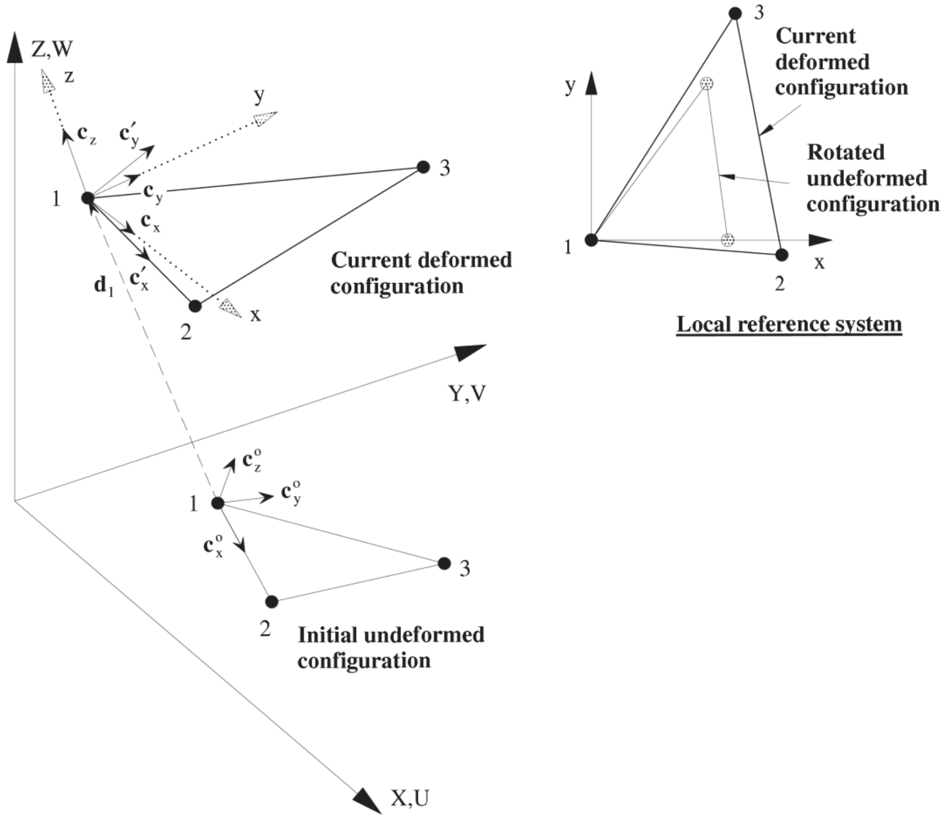

Figure 3.4: Zero-macrospin local co-rotational system for a 3-noded triangular element (Izzuddin, 2006).

With the stretched vectors $\mathbf{c}'_x$ and $\mathbf{c}'_y$ obtained according to (3.14), the rotated unit vectors $\mathbf{c}_x$ and $\mathbf{c}_y$, defining the current orientation of the local co-rotational system, are established from the inverse 'stretch' operation given by (3.10), taking $\mathbf{c}_z$ as the unit normal vector in the current deformed configuration, which is expressed as:

$$\mathbf{c}_z = \frac{\mathbf{v}_{12} \times \mathbf{v}_{23}}{\left|\mathbf{v}_{12} \times \mathbf{v}_{23}\right|} \tag{3.15}$$

It is noted that the orientation of an undeformed triangle can always be uniquely determined so that a corresponding triangle of any deformed shape may be obtained using a uniform 'stretch' operation. Therefore, the zero-macrospin definition for triangular elements is invariant to nodal numbering, since the relative orientation between the rotated undeformed and the current deformed configuration is uniquely defined.

3.3.2.2 Quadrilateral element

Unlike the triangular shape, it is not possible to obtain an arbitrarily deformed quadrilateral shape using a single uniform 'stretch' operation, regardless of the orientation of the undeformed quadrilateral. This can be easily appreciated from the fact that each of the component triangles in the quadrilateral shape may require a different orientation of the undeformed configuration to obtain the corresponding deformed shape from a 'stretch' operation. Therefore, the application of the zero-macrospin condition to the quadrilateral element could lead to different relative orientations of the current undeformed and deformed configurations, depending on which three nodes are attached to the stretched planar vectors, thus violating invariance to nodal ordering. Izzuddin (2006) addressed this potential shortcoming by linking the stretched planar vectors to all four nodes via the two diagonals, which is elaborated elsewhere (Izzuddin, 2006; Izzuddin & Liang, 2015). Via the use of diagonals in the establishment of the co-rotational coordinates, this zero-macrospin definition of the local co-rotational system for quadrilateral elements also provides invariance to nodal ordering.

3.4 9-noded quadrilateral shell element

A 9-noded monolithic shell element is elaborated in this research, which was originally developed by Izzuddin and Li (2004) as a conforming co-rotational element employing the bisector definition and later improved by Izzuddin (2007) using the hierarchic optimisation approach for overcoming locking. In this research, further modifications of the hierarchic optimisation approach are proposed to enable the element to pass the patch tests. In the following, the local element formulation of the 9-noded shell element is presented, and its incorporation within a co-rotational framework for large displacement analysis is briefly described.

3.4.1 Local element kinematics

Figure 3.5 presents three different coordinate systems for the element which undergoes large displacements. The local co-rotational coordinate system is denoted by (x,y,z). The 9-noded Reissner-Mindlin shell element utilises five local displacement parameters (three translations and two rotations) at each node. The local element geometry and displacement fields for the quadrilateral element are interpolated as follows:

$$\mathbf{x}^{o} = \begin{Bmatrix} x \\ y \\ z_0 \end{Bmatrix} = \sum_{i=1}^{N_e} N_i(\xi, \eta)\mathbf{x}_i^{o} \tag{3.16}$$

$$\mathbf{t} = \begin{Bmatrix} u_{x0} \\ u_{y0} \\ u_{z0} \end{Bmatrix} = \sum_{i=1}^{N_e} N_i(\xi, \eta)\mathbf{t}_i, \quad \overline{\mathbf{r}} = \begin{Bmatrix} \theta_x \\ \theta_y \end{Bmatrix} = \sum_{i=1}^{N_e} N_i(\xi, \eta)\overline{\mathbf{r}}_i \tag{3.17}$$

where z_0 represents the offset of the shell mid-surface along the z-axis, thus generalising the kinematics of flat plates to shallow shells; $\mathbf{x}_i^{o} = \langle x_i, y_i, z_{0i} \rangle^T$ denotes local coordinates of node *i*; $\mathbf{t}_i = \langle u_{x0,i}, u_{y0,i}, u_{z0,i} \rangle^T$ represents the local translational displacements of node *i*; $\overline{\mathbf{r}}_i = \langle \theta_{x,i}, \theta_{y,i} \rangle^T$ represents the components of the normal vector along the x- and y-axes at node *i*; and N_e is the number of element nodes, in this case 9.

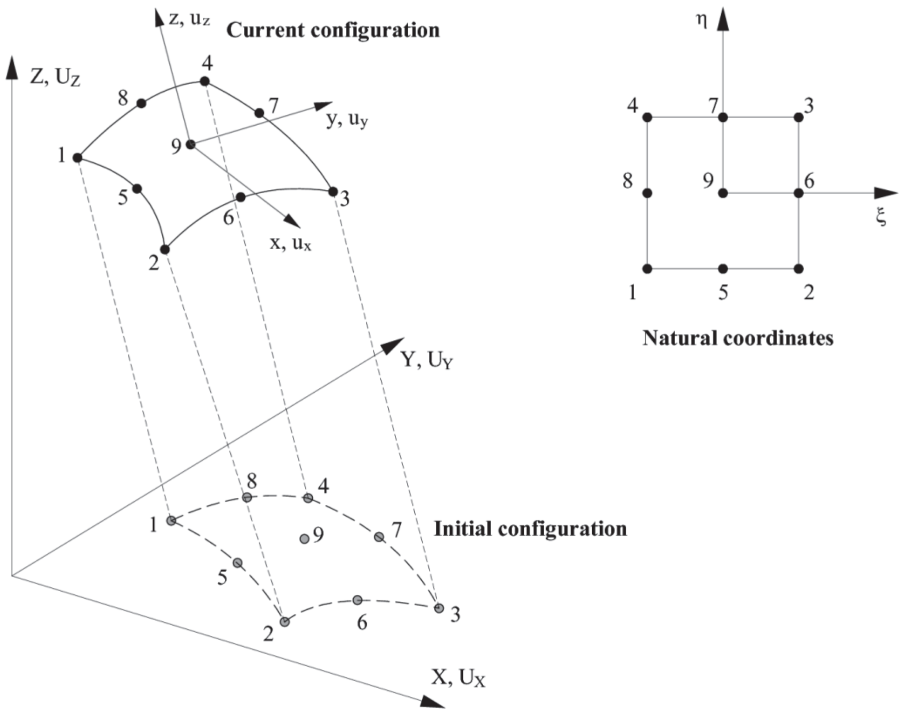

Figure 3.5: Global, local and natural coordinates for 9-noded shell element (Izzuddin, 2007).

The shape functions for the 9-noded element are expressed in terms of 2D natural coordinates (ξ, η):

$$N_i(\xi, \eta) = \frac{(\xi - \xi_i')(\xi - \xi_i'')}{(\xi_i - \xi_i')(\xi_i - \xi_i'')} \cdot \frac{(\eta - \eta_i')(\eta - \eta_i'')}{(\eta_i - \eta_i')(\eta_i - \eta_i'')} \quad (i = 1 \rightarrow 9) \tag{3.18}$$

with (ξ_i, η_i) representing the natural coordinates of node *i*, $(\xi_i \neq \xi_i' \neq \xi_i'') = -1, 0, 1$ and $(\eta_i \neq \eta_i' \neq \eta_i'') = -1, 0, 1$.

The element strain state is fully determined by membrane strains $\boldsymbol{\varepsilon}_m$, bending generalised strains $\boldsymbol{\varepsilon}_b$, and transverse shear strains $\boldsymbol{\varepsilon}_s$. Local geometric nonlinearity is addressed through quadratic approximation of the membrane strains, while the influence of large displacements is accounted for through transformations between the local co-rotational system and the global system, as presented later in Section 3.4.3. Accordingly, the various conforming generalised strains are obtained as follows:

$$\boldsymbol{\varepsilon}_m = \begin{Bmatrix} \varepsilon_x \\ \varepsilon_y \\ \gamma_{xy} \end{Bmatrix} = \begin{Bmatrix} \dfrac{\partial u_{x0}}{\partial x} \\ \dfrac{\partial u_{y0}}{\partial y} \\ \dfrac{\partial u_{x0}}{\partial y} + \dfrac{\partial u_{y0}}{\partial x} \end{Bmatrix} + \begin{Bmatrix} \dfrac{1}{2}\left(\dfrac{\partial z_0}{\partial x} + \dfrac{\partial u_{z0}}{\partial x}\right)^2 - \dfrac{1}{2}\left(\dfrac{\partial z_0}{\partial x}\right)^2 \\ \dfrac{1}{2}\left(\dfrac{\partial z_0}{\partial y} + \dfrac{\partial u_{z0}}{\partial y}\right)^2 - \dfrac{1}{2}\left(\dfrac{\partial z_0}{\partial y}\right)^2 \\ \left(\dfrac{\partial z_0}{\partial x} + \dfrac{\partial u_{z0}}{\partial x}\right)\left(\dfrac{\partial z_0}{\partial y} + \dfrac{\partial u_{z0}}{\partial y}\right) - \left(\dfrac{\partial z_0}{\partial x}\right)\left(\dfrac{\partial z_0}{\partial y}\right) \end{Bmatrix} \tag{3.19}$$

$$\boldsymbol{\varepsilon}_b = \begin{Bmatrix} \kappa_x \\ \kappa_y \\ \kappa_{xy} \end{Bmatrix} = \begin{Bmatrix} \dfrac{\partial \theta_x}{\partial x} \\ \dfrac{\partial \theta_y}{\partial y} \\ \dfrac{\partial \theta_x}{\partial y} + \dfrac{\partial \theta_y}{\partial x} \end{Bmatrix} \tag{3.20}$$

$$\boldsymbol{\varepsilon}_s = \begin{Bmatrix} \gamma_{xz} \\ \gamma_{yz} \end{Bmatrix} = \begin{Bmatrix} \theta_x + \dfrac{\partial u_{z0}}{\partial x} \\ \theta_y + \dfrac{\partial u_{z0}}{\partial y} \end{Bmatrix} \tag{3.21}$$

3.4.2 Hierarchic optimisation of 9-noded shell element

The hierarchic optimisation approach aims at restoring the lower-order strain fields by enhancing the conforming strains towards a set of prescribed objective strain modes which are of lower-order in terms of real coordinates and as afforded by the element DOFs. It is important to note that the objective strain modes are selected in terms of real coordinates rather than natural coordinates, so that the element is less sensitive to distortion. In the following, a complete set of lower-order strain modes specific to the 9-noded shell element is presented (Izzuddin, 2007), based on which the hierarchic optimisation approach is performed separately for the generalised membrane, bending and transverse shear strains to eliminate locking.

3.4.2.1 Objective strain modes

The planar displacement fields (u_{x0}, u_{y0}) for a 9-noded shell element can generate three rigid body modes and fifteen membrane strain-inducing modes. Therefore, fifteen low-order objective planar modes can be afforded by this element, for which the corresponding membrane strains are expressed as:

$$\mathbf{\Psi}_m^o = \begin{bmatrix} \frac{\partial}{\partial x} & 0 \\ 0 & \frac{\partial}{\partial y} \\ \frac{\partial}{\partial y} & \frac{\partial}{\partial x} \end{bmatrix} \mathbf{\Phi}_m^o \tag{3.22}$$

where $\mathbf{\Phi}_m^o$ are objective planar strain-inducing modes given by:

$$\mathbf{\Phi}_m^o = \left[\begin{array}{ccc:c:c} x & y & 0 & {}^2\mathbf{\Phi}^o & \mathbf{0} \\ 0 & x & y & \mathbf{0} & {}^2\mathbf{\Phi}^o \end{array}\right] \tag{3.23}$$

with ${}^2\mathbf{\Phi}^o$ representing six bi-quadratic modes for each of the two planar displacement fields:

$${}^2\mathbf{\Phi}^o = \left\langle x^2 \;\; xy \;\; y^2 \;\; x^2y \;\; xy^2 \;\; x^2y^2 \right\rangle \tag{3.24}$$

The transverse displacement field u_{z0} for a 9-noded shell element can generate one rigid body mode and eight transverse shear strain modes. Therefore, eight low-order objective transverse modes can be afforded by this element, for which the corresponding transverse shear strains are expressed as:

$$\mathbf{\Psi}_{s,z}^{o} = \begin{Bmatrix} \dfrac{\partial}{\partial x} \\ \dfrac{\partial}{\partial y} \end{Bmatrix} \mathbf{\Phi}_{s,z}^{o} \tag{3.25}$$

where $\mathbf{\Phi}_{s,z}^{o}$ are objective transverse strain-inducing modes given by:

$$\mathbf{\Phi}_{s,z}^{o} = \left\langle x \;\; y \;\; x^2 \;\; xy \;\; y^2 \;\; x^2y \;\; xy^2 \;\; x^2y^2 \right\rangle \tag{3.26}$$

The rotational fields (θ_x, θ_y) of a 9-noded element can generate fifteen curvature-inducing modes, with the objective curvature modes being the same as the above membrane strain modes:

$$\mathbf{\Psi}_{b}^{o} = \mathbf{\Psi}_{m}^{o} \tag{3.27}$$

With four rigid body modes already accounted for in relation to the planar and transverse displacement field, the remaining two rigid body modes are generated by combining the two constant rotation modes with a linear distribution of the transverse displacement. This leaves one rotational mode that generates no curvatures but a linear transverse shear strain mode $\mathbf{\Psi}_{s,\theta}^{o} = \left\langle -y, x \right\rangle^T$ which is not included in (3.25); furthermore, this represents an elaboration of the original approach of Izzuddin (2007), which did not include this specific mode. Therefore, a complete objective set of transverse shear strain modes is given by:

$$\mathbf{\Psi}_{s}^{o} = \left[\mathbf{\Psi}_{s,z}^{o} \,\middle|\, \mathbf{\Psi}_{s,\theta}^{o} \right] \tag{3.28}$$

Accordingly, there are in total 39 objective strain modes for the 9-noded shell element (15 membrane $\mathbf{\Psi}_{m}^{o}$, 15 curvature $\mathbf{\Psi}_{b}^{o}$, 9 transverse shear $\mathbf{\Psi}_{s}^{o}$), which ensure the correct rank of the element stiffness matrix. In the following sub-sections, the hierarchic optimisation approach is employed to address shear, membrane and distortion locking in the local element formulation with the employment of the above objective strain modes $\boldsymbol{\Psi}_m^o$, $\boldsymbol{\Psi}_b^o$, and $\boldsymbol{\Psi}_s^o$.

3.4.2.2 Shear locking

With reference to (3.21), the conforming element cannot bend in any arbitrary mode (θ_x, θ_y), as allowed by its rotational DOFs, without polluting $(\gamma_{xz}, \gamma_{yz})$ with second-order terms. Although the transverse displacement field (u_{z0}) via the associated translational DOFs, offers an effective first-order approximation of $(\gamma_{xz}, \gamma_{yz})$, the polluting terms from (θ_x, θ_y) can lead to a significant overestimation of the transverse shear strain energy, hence causing shear locking. These polluting terms can be filtered out by introducing hierarchic transverse displacement fields, with the aim of achieving the first-order approximation of $(\gamma_{xz}, \gamma_{yz})$ afforded by the element, as given by the objective strain modes $\boldsymbol{\Psi}_s^o$.

The hierarchic transverse displacement modes, which are used to establish corrective strains, are defined in terms of natural coordinates. The hierarchic optimisation approach can utilise hierarchic modes up to any order, where complete cubic and quartic displacement modes are considered below:

$$u_{z0}^h(\xi, \eta) = \boldsymbol{\Phi}_s^h \boldsymbol{\alpha}_s^h, \quad \boldsymbol{\Phi}_s^h = \left\langle {}^3\boldsymbol{\Phi}^h \,\middle|\, {}^4\boldsymbol{\Phi}^h \,\middle|\, \cdots \right\rangle \tag{3.29}$$

$${}^3\boldsymbol{\Phi}^h = \left\langle \chi(\xi) \;\; \chi(\eta) \;\; \eta\chi(\xi) \;\; \xi\chi(\eta) \;\; \eta^2\chi(\xi) \;\; \xi^2\chi(\eta) \;\; \chi(\xi)\chi(\eta) \right\rangle \tag{3.30}$$

$${}^4\boldsymbol{\Phi}^h = \left\langle \omega(\xi) \;\; \omega(\eta) \;\; \eta\omega(\xi) \;\; \xi\omega(\eta) \;\; \eta^2\omega(\xi) \;\; \xi^2\omega(\eta) \;\; \eta^3\omega(\xi) \;\; \xi^3\omega(\eta) \;\; \omega(\xi)\omega(\eta) \right\rangle \tag{3.31}$$

with:

$$\chi(\delta) = \delta(\delta^2 - 1), \quad \omega(\delta) = \delta^2(\delta^2 - 1) \tag{3.32}$$

The corresponding hierarchic shear strains are therefore obtained from:

$$\boldsymbol{\varepsilon}_s^h = \begin{Bmatrix} \gamma_{xz}^h \\ \gamma_{yz}^h \end{Bmatrix} = \begin{Bmatrix} \dfrac{\partial}{\partial x} \\ \dfrac{\partial}{\partial y} \end{Bmatrix} u_{z0}^h = \boldsymbol{\Psi}_s^h \boldsymbol{\alpha}_s^h, \quad \boldsymbol{\Psi}_s^h = \begin{Bmatrix} \dfrac{\partial}{\partial x} \\ \dfrac{\partial}{\partial y} \end{Bmatrix} \boldsymbol{\Phi}_s^h \tag{3.33}$$

where $\boldsymbol{\Psi}_s^h$ represents the corrective hierarchic shear strain modes, and $\boldsymbol{\alpha}_s^h$ are associated hierarchic strain parameters.

The objective shear strain field is, on the other hand, defined as:

$$\boldsymbol{\varepsilon}_s^o = \begin{Bmatrix} \gamma_{xz}^o \\ \gamma_{yz}^o \end{Bmatrix} = \boldsymbol{\Psi}_s^o \, \boldsymbol{\alpha}_s^o \tag{3.34}$$

where $\boldsymbol{\Psi}_s^o$ is given in (3.28), and $\boldsymbol{\alpha}_s^o$ are the associated objective strain parameters.

With $\boldsymbol{\Psi}_s^o$ and $\boldsymbol{\Psi}_s^h$ selected, the assumed transverse shear strains can be obtained from the corresponding conforming shear strains in accordance with the hierarchic optimisation approach via (3.2)-(3.7). In addition to the corrective (C) and objective (O) alternative approaches, the optimisation procedure can be applied with hierarchic modes up to any complete polynomial order ($n = 3, 4, \cdots$), where the minimum number of sampling Gauss points is $(n+1)^2$. Depending on the alternative approach, this leads to variant 9-noded elements characterised by acronym keys, such as H3O9 and H4C9 for an objective strain element with 3rd order hierarchic modes and a corrective strain element with 4th order hierarchic modes, respectively. It is even possible for the optimisation to be undertaken without hierarchic correction modes, in which case the assumed strains are the objective strains which are a best fit of the conforming strains, leading to an element denoted by H2O9.

3.4.2.3 Membrane locking

From (3.19) it is apparent that a curved shell element cannot deform in any arbitrary transverse mode (u_{z0}), as allowed by its translational DOFs, without polluting $(\varepsilon_x, \varepsilon_y, \gamma_{xy})$ with higher-order terms. Although the planar displacement fields (u_{x0}, u_{y0}), via the associated translational DOFs, offer an effective first-order approximation of $(\varepsilon_x, \varepsilon_y, \gamma_{xy})$, the polluting terms from (u_{z0}) can lead to a significant overestimation of the membrane strain energy. In addressing membrane locking, hierarchic planar translational parameters can be introduced to filter out the higher-order terms and achieve the first-order approximation of $(\varepsilon_x, \varepsilon_y, \gamma_{xy})$ afforded by the element, as given by the objective strain modes $\boldsymbol{\Psi}_m^o$.

The hierarchic planar displacements, which are used to establish the corrective membrane strains, are defined in terms of natural coordinates. Again, the hierarchic optimisation approach can utilise hierarchic modes up to any order, where complete cubic and quartic modes are provided below:

$$\begin{Bmatrix} u_{x0}^{h}(x, y) \\ u_{y0}^{h}(x, y) \end{Bmatrix} = \mathbf{\Phi}_{m}^{h}\, \boldsymbol{\alpha}_{m}^{h}, \quad \mathbf{\Phi}_{m}^{h} = \left[\begin{array}{cc:cc:c} {}^{3}\mathbf{\Phi}^{h} & \mathbf{0} & {}^{4}\mathbf{\Phi}^{h} & \mathbf{0} & \cdots \\ \mathbf{0} & {}^{3}\mathbf{\Phi}^{h} & \mathbf{0} & {}^{4}\mathbf{\Phi}^{h} & \cdots \end{array}\right] \tag{3.35}$$

where ${}^{3}\mathbf{\Phi}^{h}$ and ${}^{4}\mathbf{\Phi}^{h}$ are defined in (3.30) and (3.31), respectively.

The corresponding hierarchic membrane strains are then obtained from:

$$\boldsymbol{\varepsilon}_{m}^{h} = \begin{Bmatrix} \varepsilon_{x}^{h} \\ \varepsilon_{y}^{h} \\ \gamma_{xy}^{h} \end{Bmatrix} = \begin{bmatrix} \dfrac{\partial}{\partial x} & 0 \\ 0 & \dfrac{\partial}{\partial y} \\ \dfrac{\partial}{\partial y} & \dfrac{\partial}{\partial x} \end{bmatrix} \begin{Bmatrix} u_{x0}^{h} \\ u_{y0}^{h} \end{Bmatrix} = \mathbf{\Psi}_{m}^{h}\, \boldsymbol{\alpha}_{m}^{h}, \quad \mathbf{\Psi}_{m}^{h} = \begin{bmatrix} \dfrac{\partial}{\partial x} & 0 \\ 0 & \dfrac{\partial}{\partial y} \\ \dfrac{\partial}{\partial y} & \dfrac{\partial}{\partial x} \end{bmatrix} \mathbf{\Phi}_{m}^{h} \tag{3.36}$$

where $\mathbf{\Psi}_{m}^{h}$ represents the hierarchic membrane strain modes, and $\boldsymbol{\alpha}_{m}^{h}$ are corresponding strain parameters.

The objective membrane strain fields are given as:

$$\boldsymbol{\varepsilon}_{m}^{o} = \begin{Bmatrix} \varepsilon_{x}^{o} \\ \varepsilon_{y}^{o} \\ \gamma_{xy}^{o} \end{Bmatrix} = \mathbf{\Psi}_{m}^{o}\, \boldsymbol{\alpha}_{m}^{o} \tag{3.37}$$

where $\mathbf{\Psi}_{m}^{o}$ is given by (3.22)-(3.23), and $\boldsymbol{\alpha}_{m}^{o}$ are associated strain parameters.

Similar to optimisation for shear locking, the assumed strains can now be obtained in accordance with Section 2, where similar alternative approaches and levels of hierarchic optimisation may be employed.

3.4.2.4 Distortion locking

The use of objective shear and membrane strain modes consisting of complete polynomials in terms of real instead of natural coordinates readily addresses locking due to polluting higher-order terms as a result of distortion in the isoparametric element shape. For a complete treatment of distortion locking, however, it may also be necessary to filter out the polluting bending strains. In this respect, the transformation of the conforming to assumed bending strains can be shown to be identical to that relating the conforming and assumed membrane strains, as detailed previously in Section 3.4.2.3.

3.4.2.5 Modification of hierarchic strains

The aforementioned optimised formulations of the 9-noded shell element work well in the elimination of membrane and shear locking. Nevertheless, the element variants do not pass the constant strain patch tests if the edge nodes are not located at the middle of each element edge, which is a desirable characteristic for all finite element formulations so as to ensure convergence with mesh refinement regardless of element geometric irregularity. In order to ensure the optimised elements pass the constant mode patch tests, all hierarchic strain modes require zero mean values throughout the element domain (Simo et al., 1993). Therefore, in this research, a modification of the original hierarchic strain modes (Izzuddin, 2007) is proposed to enforce zero mean constraints on each strain mode, which is achieved as follows via integration over the real element domain Ω^e :

$$\bar{\boldsymbol{\Psi}}_m^h[i,j] = \boldsymbol{\Psi}_m^h[i,j] - \frac{\int_{\Omega^e} \boldsymbol{\Psi}_m^h[i,j]\,d\Omega^e}{\Omega^e}, \quad \bar{\boldsymbol{\Psi}}_b^h[i,j] = \bar{\boldsymbol{\Psi}}_m^h[i,j] \quad (i = 1 \to 3,\ j = 1 \to N_m^h) \tag{3.38}$$

$$\bar{\boldsymbol{\Psi}}_s^h[i,j] = \boldsymbol{\Psi}_s^h[i,j] - \frac{\int_{\Omega^e} \boldsymbol{\Psi}_s^h[i,j]\,d\Omega^e}{\Omega^e} \quad (i = 1 \to 2,\ j = 1 \to N_s^h) \tag{3.39}$$

where N_m^h and N_s^h represent the number of hierarchic membrane/curvature and transverse shear modes, respectively.

Accordingly, in this work, the modified hierarchic strain modes $\bar{\boldsymbol{\Psi}}_m^h$, $\bar{\boldsymbol{\Psi}}_b^h$, and $\bar{\boldsymbol{\Psi}}_s^h$ replace the original modes $\boldsymbol{\Psi}_m^h$, $\boldsymbol{\Psi}_b^h$, and $\boldsymbol{\Psi}_s^h$ in performing the hierarchic optimisation, thus replacing (3.2) with:

$$\left(\int_{\Omega^e}\left[\begin{array}{c|c}\bar{\boldsymbol{\Psi}}^{hT}\bar{\boldsymbol{\Psi}}^h & -\bar{\boldsymbol{\Psi}}^{hT}\boldsymbol{\Psi}^o \\ \hline -\boldsymbol{\Psi}^{oT}\bar{\boldsymbol{\Psi}}^h & \boldsymbol{\Psi}^{oT}\boldsymbol{\Psi}^o\end{array}\right]d\Omega^e\right)\left\{\begin{array}{c}\boldsymbol{\alpha}^h \\ \hline \boldsymbol{\alpha}^o\end{array}\right\}=\int_{\Omega^e}\left[\begin{array}{c}-\bar{\boldsymbol{\Psi}}^{hT} \\ \hline \boldsymbol{\Psi}^{oT}\end{array}\right]\boldsymbol{\varepsilon}\,d\Omega^e \tag{3.40}$$

3.4.3 Co-rotational system

The bisector co-rotational system definition is employed for the 9-noded shell element, where the x- and y-axes always coincide with the bisectors of the diagonal vectors generated from the four corner nodes while the z-axis is orthogonal to the xy-plane, as expressed by (3.8). The local nodal translations $\mathbf{t}_i$ are established by rotating the initial undeformed configuration about the origin of ($\mathbf{c}_x^o, \mathbf{c}_y^o, \mathbf{c}_z^o$) to the current local system orientation, as defined by ($\mathbf{c}_x, \mathbf{c}_y, \mathbf{c}_z$), and then measuring the translations from the rotated undeformed configuration. On the other hand, the local nodal rotations are determined as the projection of the nodal normals on the rotated local reference system ($\mathbf{c}_x, \mathbf{c}_y, \mathbf{c}_z$). Accordingly, in the co-rotational system, the five local nodal parameters are expressed as:

$$\mathbf{U}_{Ci}=\left\langle \mathbf{t}_i^T \ \ \bar{\mathbf{r}}_i^T \right\rangle^T \tag{3.41}$$

where $\mathbf{t}_i$ and $\bar{\mathbf{r}}_i$ are respectively the three translations and two rotations at node *i* as defined in Section 3.4.1.

For smooth surfaces where normals are uniquely defined over the domain, only two global rotational DOFs are required for each node. Therefore, the two smallest components of each nodal normal are directly used as global rotational DOFs when dealing with finite rotations of the normal (Izzuddin, 2005), resulting in five global parameters per node:

$$\mathbf{U}_{Gi}=\left\langle \mathbf{d}_i^T \ \ \bar{\mathbf{n}}_i^T \right\rangle^T \tag{3.42}$$

where: $\mathbf{d}_\mathrm{i}$ represents the global translational displacements of node *i*, as defined in Section 3.3.1; $\mathbf{n}_\mathrm{i}$ is the normal vector at node *i*, and $\bar{\mathbf{n}}_\mathrm{i} = \left\langle \mathbf{n}_{\mathrm{i},\alpha_\mathrm{i}} \;\; \mathbf{n}_{\mathrm{i},\beta_\mathrm{i}} \right\rangle^\mathrm{T}$ represents the two components of $\mathbf{n}_\mathrm{i}$ which are smallest in absolute terms, the third component $\mathbf{n}_{\mathrm{i},\gamma_\mathrm{i}}$ being determined by the constraint of a unit $\mathbf{n}_\mathrm{i}$. The indices α_i, β_i and γ_i are established from the following condition:

$$\left|\mathbf{n}^\mathrm{o}_{\mathrm{i},\alpha_\mathrm{i}}\right| \le \left|\mathbf{n}^\mathrm{o}_{\mathrm{i},\beta_\mathrm{i}}\right| \le \left|\mathbf{n}^\mathrm{o}_{\mathrm{i},\gamma_\mathrm{i}}\right| \tag{3.43}$$

where $\mathbf{n}^\mathrm{o}_\mathrm{i}$ is the normal vector of the last known equilibrium configuration. Therefore, the indices $\alpha_\mathrm{i}, \beta_\mathrm{i}$, and γ_i are revised at the beginning of each step.

Accordingly, the three components of the normal can be obtained from the two DOFs ($\mathbf{n}_{\mathrm{i},\alpha_\mathrm{i}}, \mathbf{n}_{\mathrm{i},\beta_\mathrm{i}}$) as:

$$\mathbf{n}_{\mathrm{i},\alpha_\mathrm{i}} = \bar{\mathbf{n}}_{\mathrm{i},1}, \quad \mathbf{n}_{\mathrm{i},\beta_\mathrm{i}} = \bar{\mathbf{n}}_{\mathrm{i},2}, \quad \mathbf{n}_{\mathrm{i},\gamma_\mathrm{i}} = \mathrm{sign}(\mathbf{n}^\mathrm{o}_{\mathrm{i},\gamma_\mathrm{i}})\sqrt{1 - \bar{\mathbf{n}}_\mathrm{i}^\mathrm{T}\bar{\mathbf{n}}_\mathrm{i}} \tag{3.44}$$

The transformation between global and local translational displacements is given as:

$$\mathbf{t}_\mathrm{i} = \mathbf{R}\mathbf{d}_\mathrm{i} + \left(\mathbf{R} - \mathbf{R}^\mathrm{o}\right)\mathbf{v}^\mathrm{o}_\mathrm{i}, \quad \mathbf{v}^\mathrm{o}_\mathrm{i} = \mathbf{X}^\mathrm{o}_\mathrm{i} - \mathbf{X}^\mathrm{o}_9 \tag{3.45}$$

where $\mathbf{X}^\mathrm{o}_\mathrm{i} = \left\langle \mathrm{X}_\mathrm{i}, \mathrm{Y}_\mathrm{i}, \mathrm{Z}_\mathrm{i} \right\rangle^\mathrm{T}$ denotes global coordinates of node *i*, while $\mathbf{R}^\mathrm{o}$ and $\mathbf{R}$ are the orientation matrices of the local co-rotational framework at the initial and current configurations, respectively, defined as:

$$\mathbf{R}^\mathrm{o} = \left[\mathbf{c}^\mathrm{o}_\mathrm{x} \;\; \mathbf{c}^\mathrm{o}_\mathrm{y} \;\; \mathbf{c}^\mathrm{o}_\mathrm{z}\right]^\mathrm{T}, \quad \mathbf{R} = \left[\mathbf{c}_\mathrm{x} \;\; \mathbf{c}_\mathrm{y} \;\; \mathbf{c}_\mathrm{z}\right]^\mathrm{T} \tag{3.46}$$

The transformation between global and local rotations is given as:

$$\bar{\mathbf{r}}_\mathrm{i} = \bar{\mathbf{R}}\,\mathbf{n}_\mathrm{i}, \quad \bar{\mathbf{R}} = \left[\mathbf{c}_\mathrm{x} \;\; \mathbf{c}_\mathrm{y}\right]^\mathrm{T} \tag{3.47}$$

The remaining transformations between the local co-rotational and global reference systems relate to the determination of the global nodal forces and tangent stiffness matrix from the corresponding local entities, requiring the first and second partial derivatives of local parameters with respect global parameters. These derivatives depend in turn on the first and second partial derivatives of ($\mathbf{c}_x, \mathbf{c}_y, \mathbf{c}_z$) with respect to global translational DOFs, where the first derivatives are provided elsewhere (Izzuddin & Liang, 2015), and the second derivatives can be similarly derived.

3.5 6-noded triangular shell element

In some practical problems involving complex geometry, the combination of both quadrilateral and triangular elements in a mesh is often required. Therefore, in this research work, a lock-free 6-noded triangular element is fully developed, which employs the hierarchic optimisation approach for the local response to overcome locking and embeds the local formulation within the zero-macrospin co-rotational system to allow large displacement analysis. The element kinematics, the application of the hierarchic optimisation approach, and the incorporation with the co-rotational system are presented in the following sections.

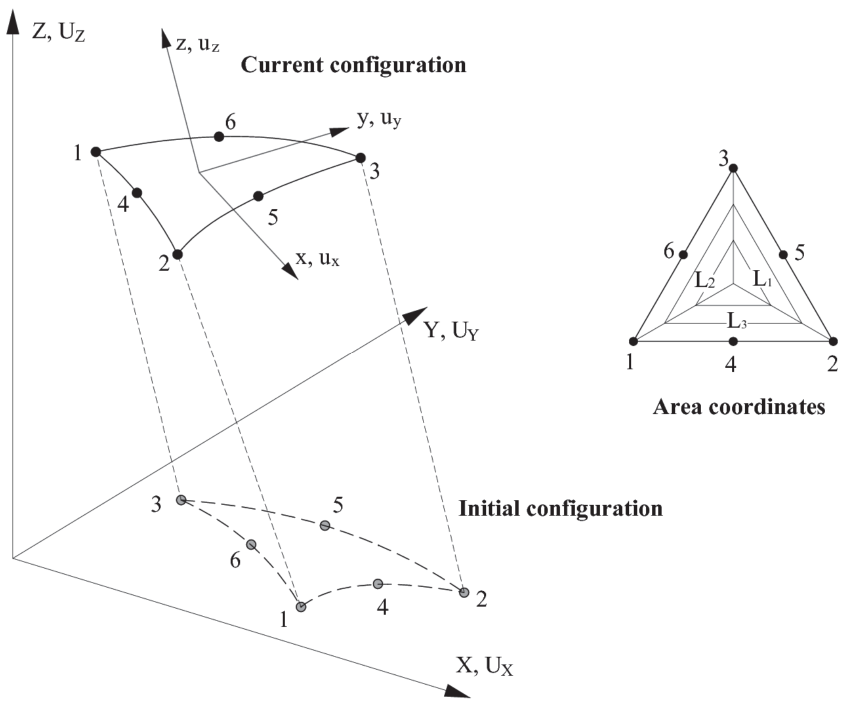

Figure 3.6: Global, local and area coordinates for 6-noded shell element.

3.5.1 Local element kinematics

Three different coordinate systems for the 6-noded element undergoing large displacements are depicted in Figure 3.6, where the local co-rotational coordinate system is denoted by (x,y,z). Similar to the previous 9-noded element, the local formulation of the 6-noded Reissner-Mindlin element utilises five local parameters (three translations and two rotations) at each node. The shape functions for the 6-noded element are expressed in terms of area coordinates (L_1, L_2, L_3) as follows:

$$N_i = L_i(2L_i - 1), \quad N_{i+3} = 4L_i L_{i+} \quad (i = 1 \to 3) \tag{3.48}$$

in which the area coordinate L_i equals 1 at node *i*, and linearly reduces to 0 at edge $i_- - i_+$; $i_+ = \mathrm{mod}(i,3)+1$; and $i_- = \mathrm{mod}(i_+,3)+1$. The shape functions can then be expressed in terms of Cartesian natural coordinates (ξ, η) by setting $L_1 = 1 - \xi - \eta$, $L_2 = \xi$, and $L_3 = \eta$, which are then employed in the interpolations of local element geometry and displacement fields for the triangular element, as given previously for the 9-noded element by (3.16)-(3.17) but with $N_e = 6$. The conforming strain-displacement relationships in the local system given by (3.19)-(3.21) for membrane strains $\boldsymbol{\varepsilon}_m$, bending generalised strains $\boldsymbol{\varepsilon}_b$, and transverse shear strains $\boldsymbol{\varepsilon}_s$ are also applicable to this 6-noded shell element.

3.5.2 Hierarchic optimisation of 6-noded shell element

The application of the hierarchic optimisation approach to the 6-noded shell element is developed here. In the following, a complete set of lower-order strain modes specific to the 6-noded shell element is presented, based on which the hierarchic optimisation approach is performed separately for the generalised membrane, bending, and transverse shear strains to eliminate locking. It is important to note that some further modifications of the hierarchic optimisation approach are made to allow its application to triangular elements, pass the constant strain patch tests, and satisfy the so-called 'spatial isotropy' requirements.

3.5.2.1 Objective strain modes

Similar to the 9-noded shell element, a preliminary selection of a complete set of low-order strain modes specific to the 6-noded shell element is provided, which are in terms of real coordinates to reduce sensitivity to element shape distortion.

The quadratic planar displacement fields (u_{x0}, u_{y0}) for a 6-noded shell element can generate three rigid body modes and nine membrane strain-inducing modes. Therefore, nine low-order objective membrane strain modes are expressed as in (3.22)-(3.23), but with the quadratic objective displacement modes ${}^{2}\mathbf{\Phi}^{o}$ now given by:

$$ {}^{2}\mathbf{\Phi}^{o} = \left\langle x^2 \;\; xy \;\; y^2 \right\rangle \tag{3.49} $$

The transverse displacement field (u_{z0}) for the 6-noded shell element can generate one rigid body mode and five transverse shear strain modes. Therefore, five low-order objective transverse shear strain modes are expressed as in (3.25), but with the quadratic objective transverse strain-inducing modes $\mathbf{\Phi}^{o}_{s,z}$ given by:

$$ \mathbf{\Phi}^{o}_{s,z} = \left\langle x \;\; y \;\; x^2 \;\; xy \;\; y^2 \right\rangle \tag{3.50} $$

The rotational displacement fields (θ_x, θ_y) of a 6-noded element can generate nine curvature-inducing modes, where the objective displacement modes and associated curvature modes are identical to those of the membrane strain-inducing modes, as expressed by (3.27).

Similar to the 9-noded element, the two rotational fields (θ_x, θ_y) for the 6-noded element also generate a linear transverse shear strain mode $\mathbf{\Psi}^{o}_{s,\theta} = \left\langle -y, x \right\rangle^{T}$, which is not included in $\mathbf{\Psi}^{o}_{s,z}$. Therefore, a complete objective set of transverse shear strain modes includes both $\mathbf{\Psi}^{o}_{s,z}$ and $\mathbf{\Psi}^{o}_{s,\theta}$, as expressed by (3.28).

There are in total 24 selected objective strain modes for the 6-noded shell element (9 membrane $\mathbf{\Psi}^{o}_{m}$, 9 curvature $\mathbf{\Psi}^{o}_{b}$, 6 transverse shear $\mathbf{\Psi}^{o}_{s}$), which ensure the correct rank of the element stiffness matrix. In the following sub-sections, the objective strain modes $\mathbf{\Psi}^{o}_{m}$, $\mathbf{\Psi}^{o}_{b}$, and $\mathbf{\Psi}^{o}_{s}$ are respectively used in the optimisation of the generalised membrane, bending, and transverse shear strains. Shear and membrane locking are relieved through separate optimisation procedures of $\boldsymbol{\varepsilon}_m$ and $\boldsymbol{\varepsilon}_s$, respectively, while distortion locking is relieved by expressing the three sets of objective strains in terms of real coordinates.

3.5.2.2 Shear locking

In addressing shear locking, the objective shear strain fields are obtained from (3.34) with the employment of the objective set of transverse shear strain modes $\mathbf{\Psi}^{o}_{s}$ defined in (3.28) and (3.50). The hierarchic optimisation approach can utilise hierarchic modes up to any order, with the hierarchic shear strain fields obtained from (3.33), but with cubic and quartic hierarchic displacement modes for the 6-noded shell element given by:

$$ {}^{3}\boldsymbol{\Phi}^{h} = \left\langle {}^{3}\Phi_{1}^{h},\ {}^{3}\Phi_{2}^{h},\ {}^{3}\Phi_{3}^{h},\ {}^{3}\Phi_{4}^{h} \right\rangle \tag{3.51} $$

$$ {}^{4}\boldsymbol{\Phi}^{h} = \left\langle \xi\,{}^{3}\Phi_{1}^{h},\ \xi\,{}^{3}\Phi_{2}^{h},\ \xi\,{}^{3}\Phi_{3}^{h} + \eta\,{}^{3}\Phi_{2}^{h},\ \eta\,{}^{3}\Phi_{3}^{h},\ \eta\,{}^{3}\Phi_{4}^{h} \right\rangle \tag{3.52} $$

in which:

$$ {}^{3}\Phi_{1}^{h} = \xi^{3} - \frac{3}{2}\xi^{2} + \frac{1}{2}\xi, \quad {}^{3}\Phi_{2}^{h} = \xi^{2}\eta - \frac{1}{2}\xi\eta \tag{3.53} $$

$$ {}^{3}\Phi_{3}^{h} = \xi\eta^{2} - \frac{1}{2}\xi\eta, \quad {}^{3}\Phi_{4}^{h} = \eta^{3} - \frac{3}{2}\eta^{2} + \frac{1}{2}\eta \tag{3.54} $$

Similar to Section 3.4.2.5, in order for the element to pass the constant strain patch tests, the enforcement of zero mean values on all hierarchic modes $\boldsymbol{\Psi}_{s}^{h}$ is undertaken in accordance to (3.39). With $\boldsymbol{\Psi}_{s}^{o}$ and $\bar{\boldsymbol{\Psi}}_{s}^{h}$ obtained, the improved transverse shear strains, in either the objective (O) or corrective (C) form, can be obtained from the corresponding conforming strains via (3.40) and (3.3)-(3.7), which could alleviate, or even eliminate locking phenomena. Depending on the alternative approach, this leads to variant 6-noded elements characterised by acronym keys, such as H3C6 and H4O6 for a corrective strain element with 3rd order hierarchic modes and an objective strain element with 4th order hierarchic modes, respectively. It is also possible for the optimisation to be undertaken without hierarchic correction modes, in which case the assumed strains are the objective strains which are a best fit of the conforming strains, leading to an element denoted by H2O6.

3.5.2.3 Membrane locking

In addressing membrane locking, the objective strains $\boldsymbol{\varepsilon}_{m}^{o}$ are defined by (3.37) and (3.22)-(3.23) with ${}^{2}\boldsymbol{\Phi}^{o}$ given by (3.49). The hierarchic correction strains $\boldsymbol{\varepsilon}_{m}^{h}$ are defined by (3.35)-(3.36) with ${}^{3}\boldsymbol{\Phi}^{h}$ and ${}^{4}\boldsymbol{\Phi}^{h}$ expressed in (3.51)-(3.54), which are subsequently modified via (3.38) to allow the element pass constant strain patch tests. With $\boldsymbol{\Psi}_{m}^{o}$ and $\bar{\boldsymbol{\Psi}}_{m}^{h}$ obtained, the improved membrane strains, in either the objective or the corrective form, can be obtained from the corresponding conforming strains via (3.40) and (3.3)-(3.7).

3.5.2.4 Distortion locking

Distortion locking is addressed by using objective shear and membrane strain modes consisting of polynomials in terms of real instead of natural coordinates. For a complete treatment of distortion locking, however, it may also be necessary to filter out the polluting bending strains. In this respect, the transformation of the conforming to assumed bending strains is identical to that relating the conforming and assumed membrane strains.

3.5.2.5 Spatial isotropy

The optimisation approach improves the strain distribution via minimising the Euclidean norm of the strain residual, which is not spatially isotropic, as can be inferred from examining the strain tensor. The optimisation of transverse shear strains turns out to be isotropic, owing to the fact that these strain components transform spatially according to a first-order tensor transformation. However, the optimisation of either the membrane strains or curvature strains is not spatially isotropic, because these transform spatially according to a second-order tensor transformation. Since the associated objective function, which is the square of the error between objective and corrected strains, is not spatially invariant, in the sense that it varies when the same component strains are transformed to a different system, the outcome of the optimisation is not spatially isotropic. This means that the 6-noded element is no longer invariant to nodal ordering following optimisation, which is undesirable in practical applications (Lee & Bathe, 2004; Battini & Pacoste, 2004; Izzuddin & Liang, 2015).

In the application of the hierarchic optimisation approach to 9-noded quadrilateral elements, a bisector local system is used, which leads to identical directions of the local axes directions regardless of nodal ordering. In this respect, the outcome of the strain optimisation process remains invariant to nodal ordering. However, the local system triad used for the 6-noded triangular element varies with nodal ordering; hence the outcome of the strain optimisation process becomes dependent on nodal ordering, since the adopted objective function for the membrane and curvature strains is not spatially invariant.

In order to achieve nodal invariance for the optimised 6-noded triangular element, the optimisation of membrane and curvature strains is modified. For example, rather than enhancing the membrane strain components $(\varepsilon_x, \varepsilon_y, \gamma_{xy})$, the three membrane strains along the element edges $(\varepsilon_{12}, \varepsilon_{23}, \varepsilon_{31})$ are optimised, as illustrated in Figure 3.7. Accordingly, the objective function expressed in terms of these strains becomes invariant to nodal ordering, hence the outcome of the optimisation process achieves the same nodal invariance characteristic.

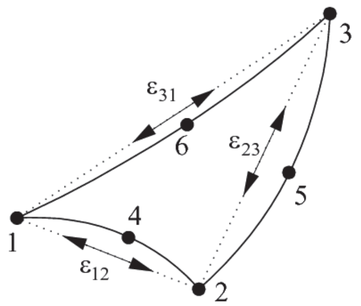

Figure 3.7: Three edge strains of the 6-noded triangular shell element.

Therefore, the following steps are employed to modify the hierarchic optimisation of membrane strains for the 6-noded shell element:

(i) Transform membrane strains $\boldsymbol{\varepsilon}^{m}$ to edge strains $(\varepsilon_{12}, \varepsilon_{23}, \varepsilon_{31})$:

$$\boldsymbol{\varepsilon}_{\Delta} = \begin{Bmatrix} \varepsilon_{12} \\ \varepsilon_{23} \\ \varepsilon_{31} \end{Bmatrix} = \mathbf{T}_{\Delta}\boldsymbol{\varepsilon}_{m}, \quad \mathbf{T}_{\Delta} = \begin{bmatrix} \hat{c}_1^2 & \hat{s}_1^2 & \hat{c}_1\hat{s}_1 \\ \hat{c}_2^2 & \hat{s}_2^2 & \hat{c}_2\hat{s}_2 \\ \hat{c}_3^2 & \hat{s}_3^2 & \hat{c}_3\hat{s}_3 \end{bmatrix} \tag{3.55}$$

where $\varepsilon_{i i_+}$ (i=1,2,3) is the edge strain along edge i-i_+; $\hat{c}_i$ and $\hat{s}_i$ are respectively the cosine and sine values of the angle from the x-axis to the edge i-i_+.

(ii) The hierarchic and objective strain modes for edge strains, $\boldsymbol{\Psi}_{\Delta}^{h}$ and $\boldsymbol{\Psi}_{\Delta}^{o}$, are obtained from the following transformation:

$$\bar{\boldsymbol{\Psi}}_{\Delta}^{h} = \mathbf{T}_{\Delta}\bar{\boldsymbol{\Psi}}_{m}^{h}, \quad \boldsymbol{\Psi}_{\Delta}^{o} = \mathbf{T}_{\Delta}\boldsymbol{\Psi}_{m}^{o} \tag{3.56}$$

(iii) Hierarchic optimisation is undertaken on the three edge strains:

$$\left(\int_{\Omega^e}\left[\begin{array}{c|c}\bar{\boldsymbol{\Psi}}_\Delta^{h\,T}\bar{\boldsymbol{\Psi}}_\Delta^h & -\bar{\boldsymbol{\Psi}}_\Delta^{h\,T}\boldsymbol{\Psi}_\Delta^o \\ \hline -\boldsymbol{\Psi}_\Delta^{o\,T}\bar{\boldsymbol{\Psi}}_\Delta^h & \boldsymbol{\Psi}_\Delta^{o\,T}\boldsymbol{\Psi}_\Delta^o\end{array}\right] d\Omega^e\right)\left\{\begin{array}{c}\boldsymbol{\alpha}_\Delta^h \\ \hline \boldsymbol{\alpha}_\Delta^o\end{array}\right\} = \int_{\Omega^e}\left[\begin{array}{c}-\bar{\boldsymbol{\Psi}}_\Delta^{h\,T}\mathbf{T}_\Delta \\ \hline \boldsymbol{\Psi}_\Delta^{o\,T}\mathbf{T}_\Delta\end{array}\right]\boldsymbol{\varepsilon}_m \, d\Omega^e \tag{3.57}$$

where $\boldsymbol{\alpha}_\Delta^h$ and $\boldsymbol{\alpha}_\Delta^o$ are associated strain parameters.

(iv) Parameters $\boldsymbol{\alpha}_\Delta^h$ and $\boldsymbol{\alpha}_\Delta^o$ are numerically solved using Gaussian quadrature in terms of the conforming strains component in the local x-y system:

$$\boldsymbol{\alpha}_\Delta^h = \boldsymbol{\Gamma}_\Delta^h \begin{Bmatrix}\boldsymbol{\varepsilon}_{m(1)} \\ \vdots \\ \boldsymbol{\varepsilon}_{m(i)} \\ \vdots\end{Bmatrix}, \quad \boldsymbol{\alpha}_\Delta^o = \boldsymbol{\Gamma}_\Delta^o \begin{Bmatrix}\boldsymbol{\varepsilon}_{m(1)} \\ \vdots \\ \boldsymbol{\varepsilon}_{m(i)} \\ \vdots\end{Bmatrix} \tag{3.58}$$

(v) The enhanced membrane strains at Gauss points are derived in either the corrective or the objective strain form:

$$\begin{Bmatrix}\tilde{\boldsymbol{\varepsilon}}_{m(1)} \\ \vdots \\ \tilde{\boldsymbol{\varepsilon}}_{m(i)} \\ \vdots\end{Bmatrix} = \tilde{\mathbf{T}}_m \begin{Bmatrix}\boldsymbol{\varepsilon}_{m(1)} \\ \vdots \\ \boldsymbol{\varepsilon}_{m(i)} \\ \vdots\end{Bmatrix}, \quad \tilde{\mathbf{T}}_m = \mathbf{I} + \begin{bmatrix}\bar{\boldsymbol{\Psi}}_{m(1)}^h \\ \vdots \\ \bar{\boldsymbol{\Psi}}_{m(i)}^h \\ \vdots\end{bmatrix}\boldsymbol{\Gamma}_\Delta^h \quad \text{(Corrective)} \tag{3.59}$$

$$\begin{Bmatrix}\hat{\boldsymbol{\varepsilon}}_{m(1)} \\ \vdots \\ \hat{\boldsymbol{\varepsilon}}_{m(i)} \\ \vdots\end{Bmatrix} = \hat{\mathbf{T}}_m \begin{Bmatrix}\boldsymbol{\varepsilon}_{m(1)} \\ \vdots \\ \boldsymbol{\varepsilon}_{m(i)} \\ \vdots\end{Bmatrix}, \quad \hat{\mathbf{T}}_m = \begin{bmatrix}\boldsymbol{\Psi}_{m(1)}^o \\ \vdots \\ \boldsymbol{\Psi}_{m(i)}^o \\ \vdots\end{bmatrix}\boldsymbol{\Gamma}_\Delta^o \quad \text{(Objective)} \tag{3.60}$$

The hierarchic optimisation of curvature strains follows the same steps. By modifying the optimisation procedure for membrane and curvature strains, whilst retaining the previous procedure for optimising transverse shear strains, the local formulation of an isotropic lock-free triangular element is obtained.

3.5.3 Co-rotational system

The local formulation of the 6-noded element is incorporated into a co-rotational framework based on the zero-macrospin definition, where the three corner nodes are utilised to obtain the local triad ($\mathbf{c}_x, \mathbf{c}_y, \mathbf{c}_z$) with reference to (3.10)-(3.15).

The transformation between global and local translational displacements is given as:

$$\mathbf{t}_i = \mathbf{R}\mathbf{d}_i + \left(\mathbf{R} - \mathbf{R}^o\right)\mathbf{v}_i^o, \quad \mathbf{v}_i^o = \mathbf{X}_i^o - \mathbf{X}_1^o \tag{3.61}$$

The transformation between global and local rotations is the same as given by (3.47). The remaining transformations between the local co-rotational and global reference systems relate to the determination of the global nodal forces and tangent stiffness matrix from the corresponding local entities, requiring the first and second partial derivatives of local DOFs with respect global DOFs. The first derivatives can be obtained through chain differentiation, and are presented in Appendix A, while the second derivatives can be similarly derived.

3.6 Consistent mass

The consistent mass matrices of monolithic quadratic shell elements are presented here, allowing the vibration and transient nonlinear dynamic analysis of plates and shells using the developed elements.

3.6.1 Local consistent mass

The same interpolation functions are employed for the local acceleration fields as those used for the local displacement fields:

$$\ddot{\mathbf{t}} = \begin{Bmatrix} \ddot{u}_{x0} \\ \ddot{u}_{y0} \\ \ddot{u}_{z0} \end{Bmatrix} = \sum_{i=1}^{N_e} N_i(\xi, \eta)\ddot{\mathbf{t}}_i, \quad \ddot{\mathbf{r}} = \begin{Bmatrix} \ddot{\theta}_x \\ \ddot{\theta}_y \end{Bmatrix} = \sum_{i=1}^{N_e} N_i(\xi, \eta)\ddot{\mathbf{r}}_i \tag{3.62}$$

where $\ddot{\mathbf{t}}$ and $\ddot{\mathbf{r}}$ are respectively the translational and rotational accelerations.

Defining $z = \frac{h}{2}\zeta$ and the density of the plate as ρ, the employment of the principle of virtual work leads to the following evaluation of local inertia forces:

$$\delta \mathbf{U}_C^T \mathbf{f}_C^I = \frac{\rho h}{2} \iint_{\Omega^e} \left(\int_{-1}^{1} (\ddot{u}_{x0}\delta u_{x0} + \ddot{u}_{y0}\delta u_{y0} + \ddot{u}_{z0}\delta u_{z0} + \frac{h^2}{4}\zeta^2 \ddot{\theta}_x \delta\theta_x + \frac{h^2}{4}\zeta^2 \ddot{\theta}_y \delta\theta_y) d\zeta \right) d\Omega^e \quad (3.63)$$

where the superscript 'I' indicates inertia force.

Further elaboration of (3.63) yields the following local mass matrix $\mathbf{M}_C$:

$$\mathbf{M}_C = \begin{bmatrix} \mathbf{M}_{11} & \mathbf{M}_{12} & \cdots & \mathbf{M}_{1N_e} \\ \mathbf{M}_{21} & \mathbf{M}_{22} & \cdots & \mathbf{M}_{2N_e} \\ \vdots & \vdots & \ddots & \vdots \\ \mathbf{M}_{N_e 1} & \mathbf{M}_{N_e 2} & \cdots & \mathbf{M}_{N_e N_e} \end{bmatrix}, \quad \mathbf{M}_{ij} = \begin{bmatrix} m_t & & & & \\ & m_t & & & \\ & & m_t & & \\ & & & m_r & \\ & & & & m_r \end{bmatrix} \mathbf{\Gamma}_{ij}^M \quad (3.64)$$

where:

$$\mathbf{\Gamma}_{ij}^M = \int_{-1}^{1}\int_{-1}^{1} N_i N_j \det(J) d\xi d\eta, \quad m_t = \rho h, \quad m_r = \frac{\rho h^3}{12} \quad (3.65)$$

with $\mathbf{J}$ denoting the Jacobian matrix:

$$\mathbf{J} = \begin{bmatrix} \frac{\partial x}{\partial \xi} & \frac{\partial x}{\partial \eta} & \frac{\partial x}{\partial \zeta} \\ \frac{\partial y}{\partial \xi} & \frac{\partial y}{\partial \eta} & \frac{\partial y}{\partial \zeta} \\ \frac{\partial z_0}{\partial \xi} & \frac{\partial z_0}{\partial \eta} & \frac{\partial z_0}{\partial \zeta} \end{bmatrix} \quad (3.66)$$

3.6.2 Global consistent mass

Although a co-rotational framework is conveniently adopted to determine the geometrically nonlinear element response, the consideration of such a system for determining consistent inertia forces is associated with significant complications (Le et al., 2014). Instead, the inertia forces are evaluated within an updated Lagrangian framework, which has been shown to be both practical and effective for co-rotational beam-column elements (Izzuddin, 1991).

In this context, denoting $\mathbf{T}^{\mathrm{o}}$ as the matrix that transforms incremental global to local nodal parameters based on the last known equilibrium configuration, as expressed by:

$$\mathbf{T}^{\mathrm{o}} = \frac{\partial \mathbf{U}_{\mathrm{C}}^{\mathrm{o}}}{\partial \mathbf{U}_{\mathrm{G}}^{\mathrm{o}}} \tag{3.67}$$

the global consistent mass matrix is readily obtained as:

$$\mathbf{M}_{\mathrm{G}} = \mathbf{T}^{\mathrm{o}\,\mathrm{T}} \mathbf{M}_{\mathrm{C}} \mathbf{T}^{\mathrm{o}} \tag{3.68}$$

3.7 Summary

In this chapter, formulations of lock-free monolithic quadrilateral and triangular shell elements are presented, which effectively overcome membrane, shear and distortion locking. With the further utilisation of a co-rotational approach, these formulations can be applied in geometrically nonlinear analysis while utilising only a second-order strain-displacement relationship in the local system; indeed, even a first-order strain-displacement relationship could be used, though at the expense of requiring a finer mesh for comparable accuracy in geometric nonlinear analysis.

The hierarchic optimisation approach is employed for eliminating locking, where the conforming strains are enhanced with hierarchic *corrective* strains, and mathematical optimisation is performed towards *objective* low-order strain fields, as afforded by the element DOFs. The utilisation of this optimisation approach within the local co-rotational system leads to a linear optimal mapping between assumed and conforming strains, which need only be established once at the start of incremental nonlinear analysis.

In applying the co-rotational approach for large displacement analysis, the bisector definition and the zero-macrospin definition of the local system are employed, both definitions satisfying the requirements of i) being simple to establish, ii) achieving nodal invariance, iii) reducing the spin of the element, and iv) providing a symmetric element tangent stiffness matrix (Izzuddin & Liang, 2015). The utilisation of the co-rotational systems also facilitates the application of the hierarchic optimisation approach and the later inclusion of through-thickness descriptions of displacements and stresses for laminated shells, as elaborated in Chapter 6.

The optimisation procedure for the 9-noded shell element, previously developed by Izzuddin (2007), is firstly modified through the introduction of an additional objective transverse shear strain mode, which is required to achieve the correct rank of the local stiffness. Secondly, a modification of the hierarchic strain modes is proposed to enable the 9-noded element to pass constant strain patch tests. In addition, the hierarchic optimisation approach is extended to a 6-noded triangular shell element, with the further consideration of the requirements of spatial isotropy. The local formulation of the 6-noded triangular shell element is framed within the zero-macrospin co-rotational system, which upgrades it to geometric nonlinear analysis with relative ease.

Finally, in order to enable vibration and transient nonlinear dynamic analysis of plates and shells, the consistent mass matrices are developed for both shell elements, utilising a practical updated Lagrangian approach.

The efficiency and effectiveness of the optimised variants of the 9-noded and 6-noded shell elements will be assessed next in Chapter 4 using zero energy mode tests, patch tests, isotropic element tests, convergence rate tests, as well as other linear and geometrically nonlinear numerical examples.

CHAPTER 4

Verification of Monolithic Shell Elements

4.1 Introduction

The modified 9-noded shell element and the newly developed 6-noded shell element, presented in previous chapter, have been implemented in ADAPTIC (Izzuddin, 1991) v2.14.2, which is used hereafter in several numerical examples to demonstrate the accuracy of both elements. For comparison purposes, also implemented in ADAPTIC are the 9-noded and 6-noded Reissner-Mindlin shell elements based on the MITC method (Bathe et al., 2003), for which the local formulations are provided in Appendix B. These MITC formulations are also incorporated within the same co-rotational approach as the developed formulations to enable large displacement analysis.

In presenting the results, variants of the 9-noded and 6-noded elements are denoted by element codes, as listed in Table 4.1.

Table 4.1: Variants of 9-noded and 6-noded shell elements considered.

Element code	Strain field	Hierarchic order	Sampling Gauss points
CNF9	Conforming	-	3×3
H2O9	Assumed, objective	-	3×3
H3O9	Assumed, objective	3	4×4
H4O9	Assumed, objective	4	5×5
H3C9	Assumed, corrective	3	4×4
H4C9	Assumed, corrective	4	5×5
MITC9*	Assumed, MITC9*	-	3×3
MITC9is*	Assumed, MITC9is*	-	3×3
CNF6	Conforming	-	13
H2O6	Assumed, objective	-	13
H3O6	Assumed, objective	3	13
H4O6	Assumed, objective	4	16
H3C6	Assumed, corrective	3	13
H4C6	Assumed, corrective	4	16
MITC6*	Assumed, MITC6*	-	13

4.2 Quadrilateral shell element

4.2.1 Zero energy mode test

In this test, the eigenvalues of the stiffness matrix of an unsupported shell element are calculated for each of the 9-noded element types, and the number of zero eigenvalues is counted. For an unsupported element with no spurious mechanisms, the number of zero eigenvalues should be exactly six. Both regular and irregular element shapes are considered in this test (Figure 4.1) to allow for more possibilities. All the considered element types (H2O9, H3O9, H4O9, H3C9, H4C9, MITC9* and MITC9is*) pass the zero energy mode test, i.e., all of them have exactly six zero eigenvalues of their element stiffness matrix.

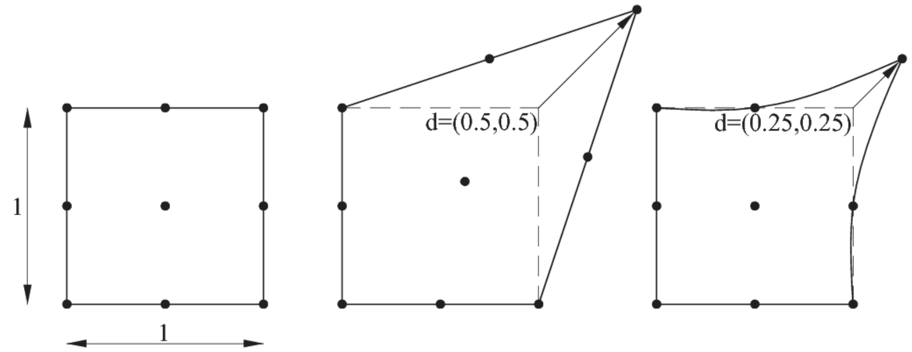

Figure 4.1: Various element shapes for the zero energy mode test of 9-noded shell element.

4.2.2 Patch tests

The five-element patch suggested by MacNeal and Harder (1985), as shown in Figure 4.2, is employed to illustrate the membrane and out-of-plane bending behaviour of the considered 9-noded shell elements. In the patch, edge nodes and internal nodes are placed at the middle positions. The geometric properties of the rectangular plate are: $L = 0.24$, $W = 0.12$, and $h = 0.001$. It has a Young's modulus of $E = 10^6$ and a Poisson's ratio of $\nu = 0.25$. In the membrane patch test, the boundary conditions at the external nodes are:

$$u_{x0} = 10^{-3}\left(x + \frac{1}{2}y\right), \quad u_{y0} = 10^{-3}\left(y + \frac{1}{2}x\right), \quad u_{z0} = \theta_x = \theta_y = 0$$

which correspond to a constant membrane strain state where $\varepsilon_x = \varepsilon_y = \gamma_{xy} = 0.001$.

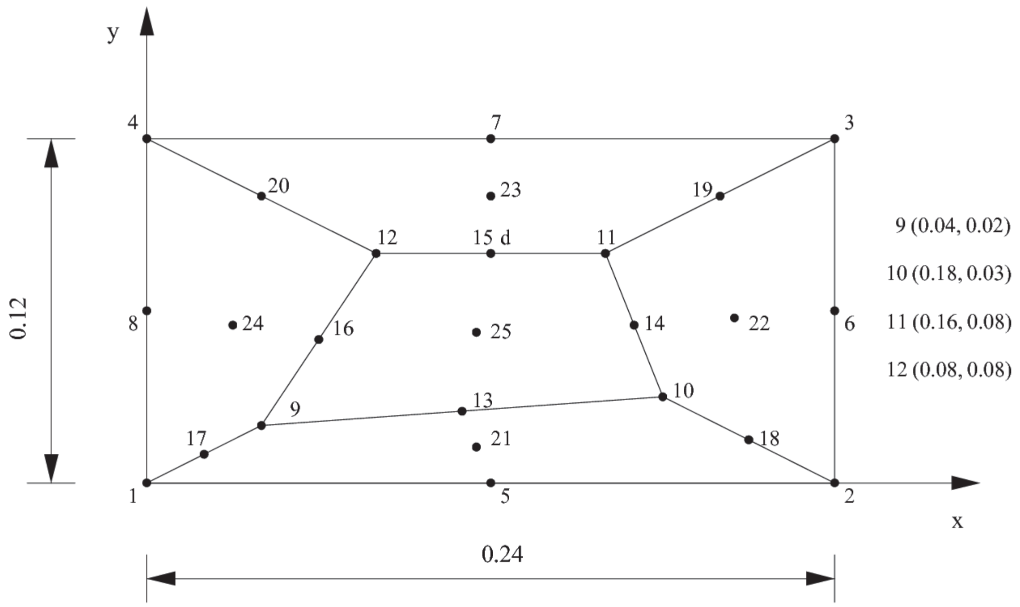

Figure 4.2: Five-element patch test.

In the out-of-plane bending patch test, the boundary conditions at the external nodes are:

$$u_{x0} = u_{y0} = 0, \quad u_{z0} = 10^{-3}\frac{\left(x^2 + xy + y^2\right)}{2}, \quad \theta_x = 10^{-3}\left(x + \frac{1}{2}y\right), \quad \theta_y = 10^{-3}\left(y + \frac{1}{2}x\right)$$

which correspond to a constant bending strain state where $\kappa_x = \kappa_y = \kappa_{xy} = 0.001$.

The patch tests are conducted on various quadrilateral element types, with the nodal displacements inside the patch and the strains evaluated at each element centre compared against reference values. The maximum relative errors in the nodal displacements and strain components are listed in Tables 4.2-4.3 for respectively the membrane and bending patch tests. Clearly, all the optimised 9-noded elements and the MITC9is* pass the patch tests. The results with MITC9*, however, yield small errors, as stated by Wisniewski and Panasz (2013).

Table 4.2: Relative error of displacements and strains in membrane patch test.

Element code	Maximum error in u_{x0}	Maximum error in u_{y0}	Maximum error in ε_x	Maximum error in ε_y	Maximum error in γ_{xy}
H2O9	0.000	0.000	0.000	0.000	0.000
H3O9	0.000	0.000	0.000	0.000	0.000
H4O9	0.000	0.000	0.000	0.000	0.000
H3C9	0.000	0.000	0.000	0.000	0.000
H4C9	0.000	0.000	0.000	0.000	0.000
MITC9*	0.054	0.031	0.010	0.015	0.022
MITC9is*	0.000	0.000	0.000	0.000	0.001

Table 4.3: Relative error of displacements and strains in bending patch test.

Element code	Maximum error in u_{z0}	Maximum error in θ_x	Maximum error in θ_y	Maximum error in κ_x	Maximum error in κ_y	Maximum error in κ_{xy}
H2O9	0.000	0.000	0.000	0.000	0.000	0.000
H3O9	0.000	0.000	0.000	0.000	0.000	0.000
H4O9	0.000	0.000	0.000	0.000	0.000	0.000
H3C9	0.000	0.000	0.000	0.000	0.000	0.000
H4C9	0.000	0.000	0.000	0.000	0.000	0.000
MITC9*	0.018	0.028	0.049	0.004	0.012	0.009
MITC9is*	0.000	0.000	0.000	0.000	0.000	0.000

A further step is taken to investigate the behaviour of the considered 9-noded elements in a more irregular mesh, where the original patch is distorted by shifting four edge nodes 13, 14, 15 and 16, either parallel or perpendicular to the edges, and moving the internal node 25 along the x-direction, as illustrated in Figure 4.3. All the shifts of nodal positions are of a magnitude d = 0.01. Results of the membrane patch test with this distorted mesh are given in Table 4.4. As expected, all the optimised 9-noded elements pass the test owing to the enforcement of zero mean on each hierarchic strain mode. The results with MITC9is* are also good, though small errors are generated in this case. However, MITC9* fails in the constant strain patch test, evident from the large relative errors in predicting displacements and strains.

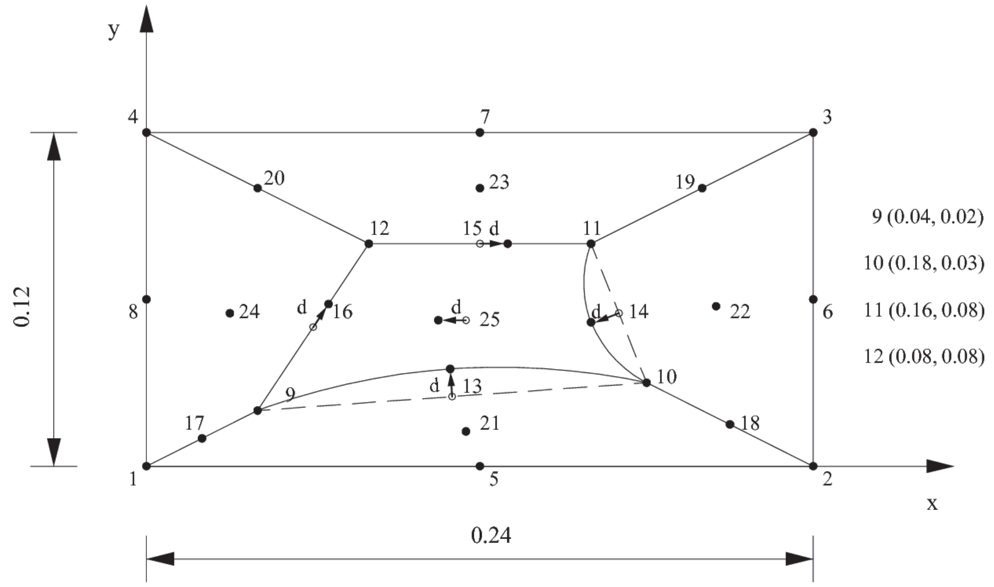

Figure 4.3: Five-element patch test (distorted mesh).

Table 4.4: Relative error of displacements and strains in membrane patch test (distorted mesh).

Element code	Maximum error in u_{x0}	Maximum error in u_{y0}	Maximum error in ε_x	Maximum error in ε_y	Maximum error in γ_{xy}
H2O9	0.000	0.000	0.000	0.000	0.000
H3O9	0.000	0.000	0.000	0.000	0.000
H4O9	0.000	0.000	0.000	0.000	0.000
H3C9	0.000	0.000	0.000	0.000	0.000
H4C9	0.000	0.000	0.000	0.000	0.000
MITC9*	0.212	0.112	0.040	0.435	0.210
MITC9is*	0.005	0.005	0.007	0.005	0.007

4.2.3 Convergence rate tests

4.2.3.1 Clamped square plate under uniform loading

The convergence rates of the optimised elements are investigated in this linear problem, where a $2\mathrm{L} \times 2\mathrm{L}$ square plate is clamped at all four edges and subjected to a uniformly distributed pressure, as shown in Figure 4.4. Soft boundary conditions are used along the four edges, and three thickness-to-length ratios (h/L) are considered to investigate the performance of various element formulations in addressing locking. The geometric and material parameters are given as: $\mathrm{L} = 1.0$, $\mathrm{E} = 1.7472 \times 10^7$, and $\nu = 0.3$. Due to symmetry, a quarter of the plate is modelled with 2×2, 4×4, 8×8, and 16×16 meshes of various 9-noded element types. The Jacobian matrix is constant in this example, which leads to identical results between the MITC9* and MITC9is* models. The convergence curves of the considered 9-noded elements are presented in Figure 4.5, with the relative error in the strain energy as a measure of accuracy:

$$\mathrm{RE} = \frac{\left|\mathrm{U}_{\mathrm{ref}} - \mathrm{U}\right|}{\mathrm{U}_{\mathrm{ref}}} \tag{4.1}$$

where U represents the total strain energy of a coarse mesh, and $\mathrm{U}_{\mathrm{ref}}$ represents the reference value, which is taken as the strain energy obtained from a fine mesh (128×128) of the H3O9 element. The results of the original MITC9 shell elements (Lee & Bathe, 2010) are also plotted in Figure 4.5 for comparison purposes, though employing a different accuracy measure:

$$\mathrm{RE} = \frac{\left\|\mathbf{u}_{\mathrm{ref}}^{\varepsilon} - \mathbf{u}^{\varepsilon}\right\|_{\mathrm{s}}^{2}}{\left\|\mathbf{u}_{\mathrm{ref}}^{\varepsilon}\right\|_{\mathrm{s}}^{2}} \tag{4.2}$$

where $\mathbf{u}_{\mathrm{ref}}^{\varepsilon}$ is the vector of reference nodal displacement values; $\mathbf{u}^{\varepsilon}$ is the finite element solution of nodal displacements; $\left\| \cdot \right\|_{\mathrm{s}}$ is the s-norm (Bathe et al., 2003). In linear elastic analysis with conforming element formulation, (4.1) and (4.2) are equivalent. Even though this equivalence does not strictly hold for hierarchic optimised formulations or mixed formulations, it can still be used for a general comparative assessment of the convergence rate. For both measures of accuracy, the optimal convergence rate is of a 4th order, with the discretisation error being $O(h_e^4)$ (h_e is the nominal element length), which is depicted in the figure with a solid straight line.

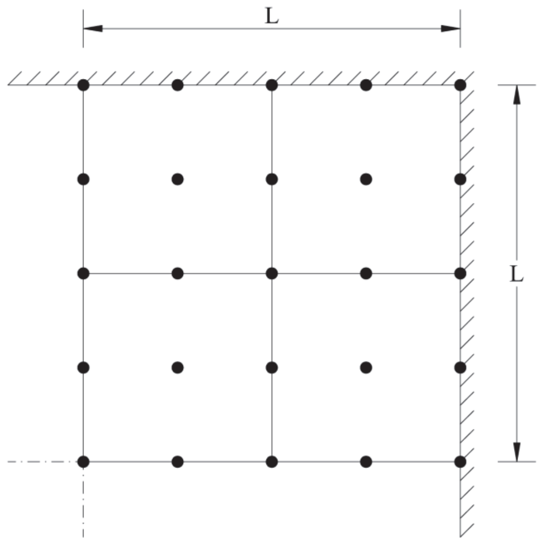

Figure 4.4: A quarter-model of a clamped square plate subjected to uniform pressure (9-noded shell element).

All the considered 9-noded elements show roughly optimal convergence rates with no significant upward shifting as the thickness is reduced (except for H3C9 and H4C9). In this problem, the MITC9* and the H2O9 elements seem to have marginally better accuracy, followed by the H3O9 and H4O9 elements. It is also observed that the results of the optimised elements with the objective alternative (H2O9, H3O9, and H4O9) are comparable to the MITC9 results (Lee & Bathe, 2010) in terms of both the convergence rate and accuracy, while the accuracy of the MITC9* element is even higher than the original MITC9 element, which may result from rounding errors, different accuracy measurement and the formulation differences, as can be found in Appendix B.

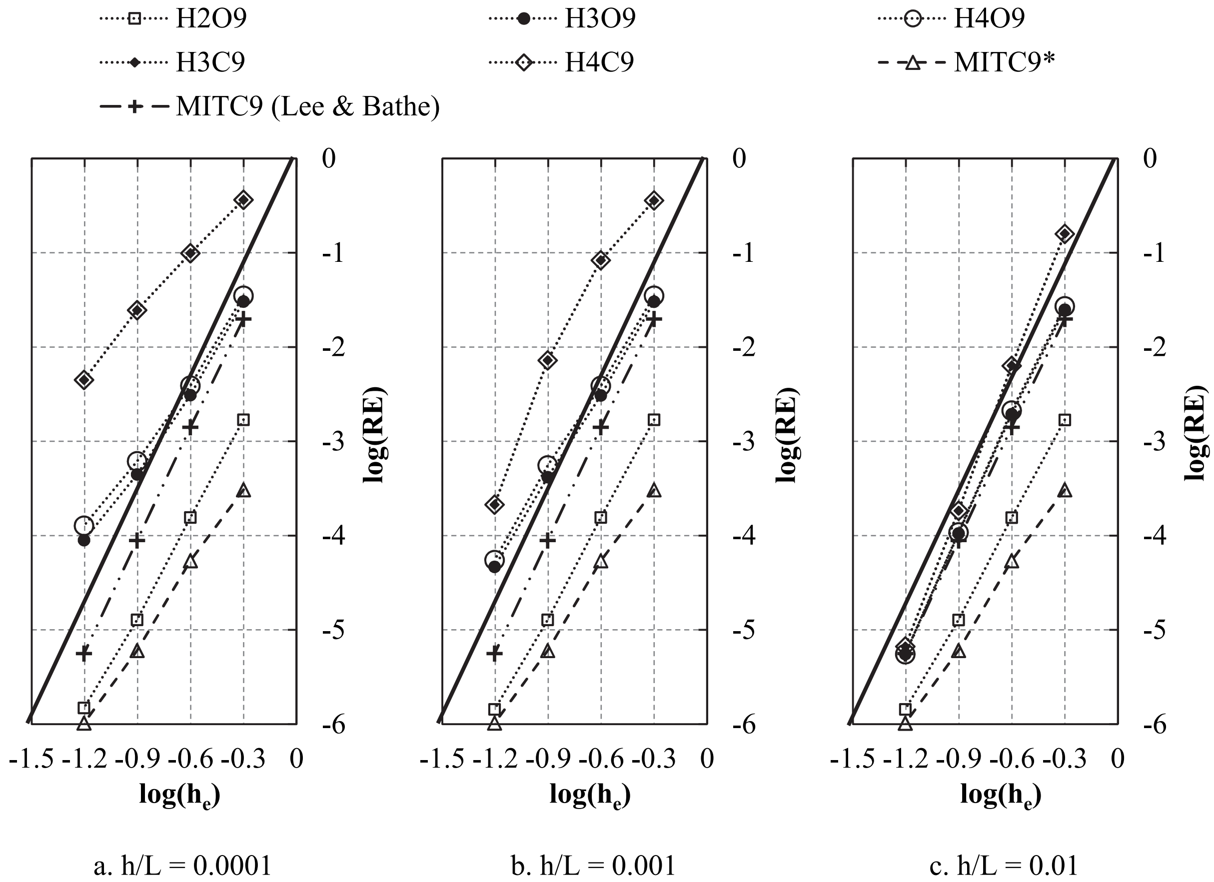

Figure 4.5: Convergence curves of various 9-noded elements for the clamped square plate problem.

4.2.3.2 Cylindrical shell under sinusoidal loading

A cylindrical shell, which has a length of 2L, a radius of R, and a constant thickness h, is subject to a periodic pressure $p(\theta) = p_0 \cos(2\theta)$. The geometric, material, and loading properties are given as: L = R = 1.0, E = 2.0×10^5, ν = 1/3, and $p_0 = 1.0$. Two boundary conditions at both curved ends are considered: a free boundary condition corresponding to a bending-dominant problem, and a fully clamped boundary condition corresponding to a membrane-dominant problem. Due to symmetry, a sixteenth of the model is analysed with a uniform mesh pattern, as shown in Figure 4.6.

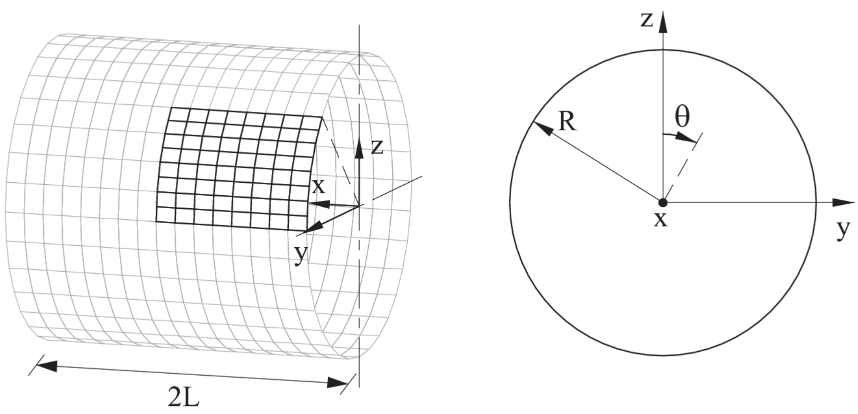

Figure 4.6: Cylindrical shell under periodical loading.

Figures 4.7-4.8 present the behaviour of various 9-noded optimised elements with respectively free and clamped boundary conditions. The relative error measure (4.1) is employed, and the optimal convergence rate is also depicted in the figures. In the bending-dominant problem, all the considered elements show comparable accuracy and good convergence rates, though not optimal. Furthermore, the convergence curves have no evidence of shifting upwards with thickness changes. These elements also perform generally well in the membrane-dominant problem. Figures 4.9-4.10 also provide the comparison of the H3O9 and MITC9* results against the MITC9 results (Bathe et al., 2000) with the same accuracy measure. The results show that the H3O9 and MITC9* have comparable convergence rates and accuracy. The MITC9 results have better accuracy in particular for a relatively large thickness-to-length ratio (h/L = 0.01), except for the free end case with a small thickness-to-length ratio (h/L = 0.0001) where the MITC9 element shows a significant degradation of the convergence rate.

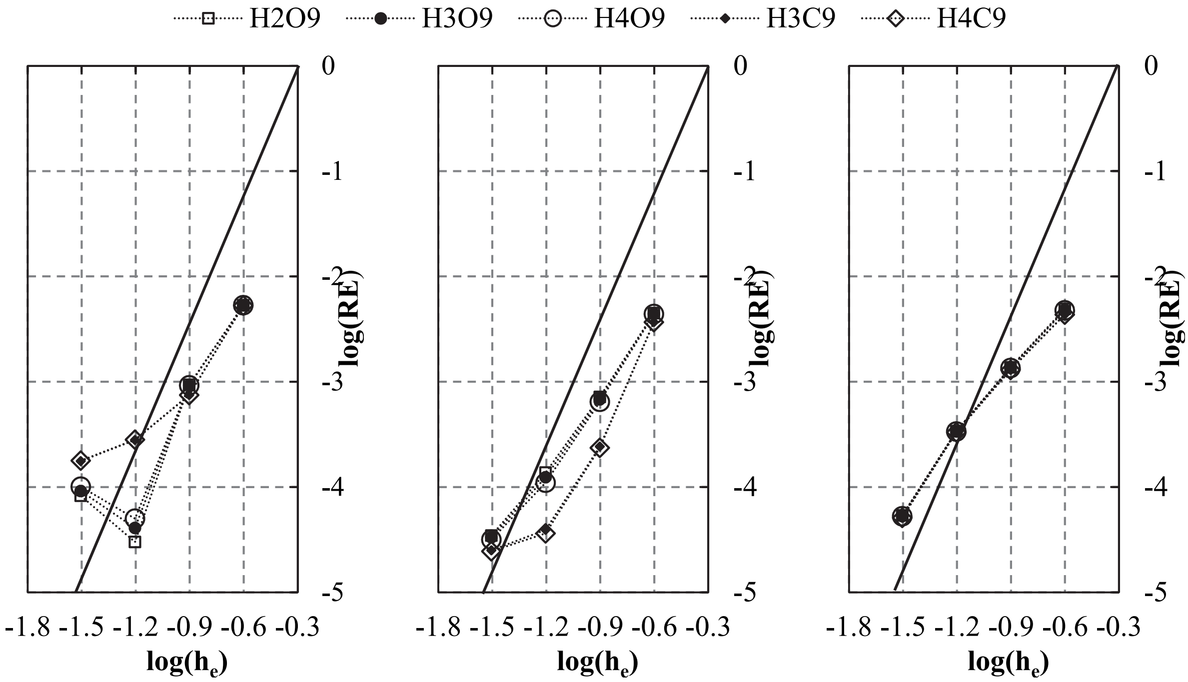

a. h/L = 0.0001 b. h/L = 0.001 c. h/L = 0.01

Figure 4.7: Convergence curves of various optimised 9-noded elements for the cylindrical shell problem (free boundary).

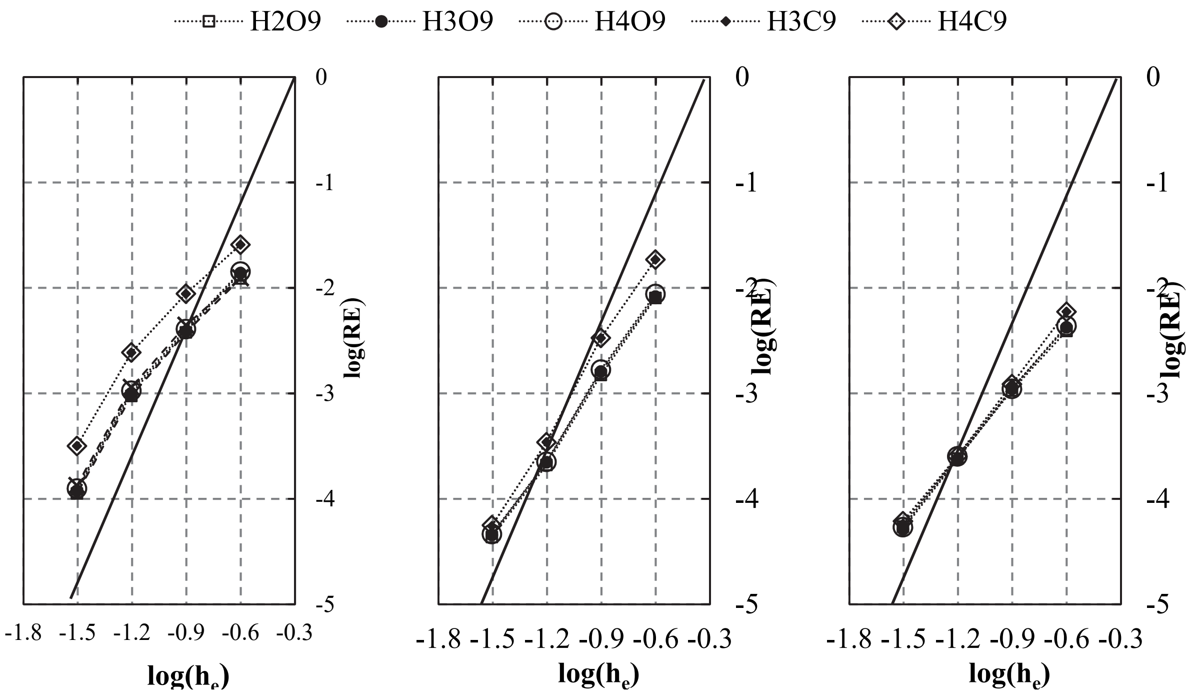

a. h/L = 0.0001 b. h/L = 0.001 c. h/L = 0.01

Figure 4.8: Convergence curves of various optimised 9-noded elements for the cylindrical shell problem (clamped boundary).

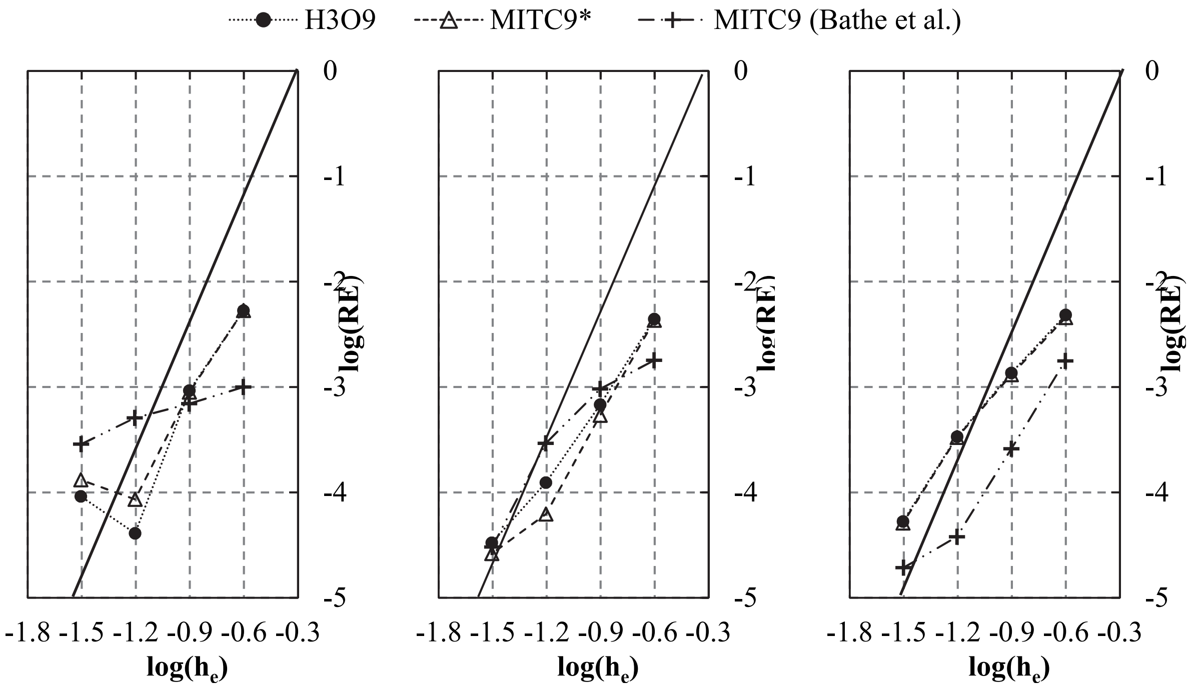

a. h/L = 0.0001 b. h/L = 0.001 c. h/L = 0.01

Figure 4.9: Convergence curves of H3O9, MITC9* and MITC9 elements for the cylindrical shell problem (free boundary).

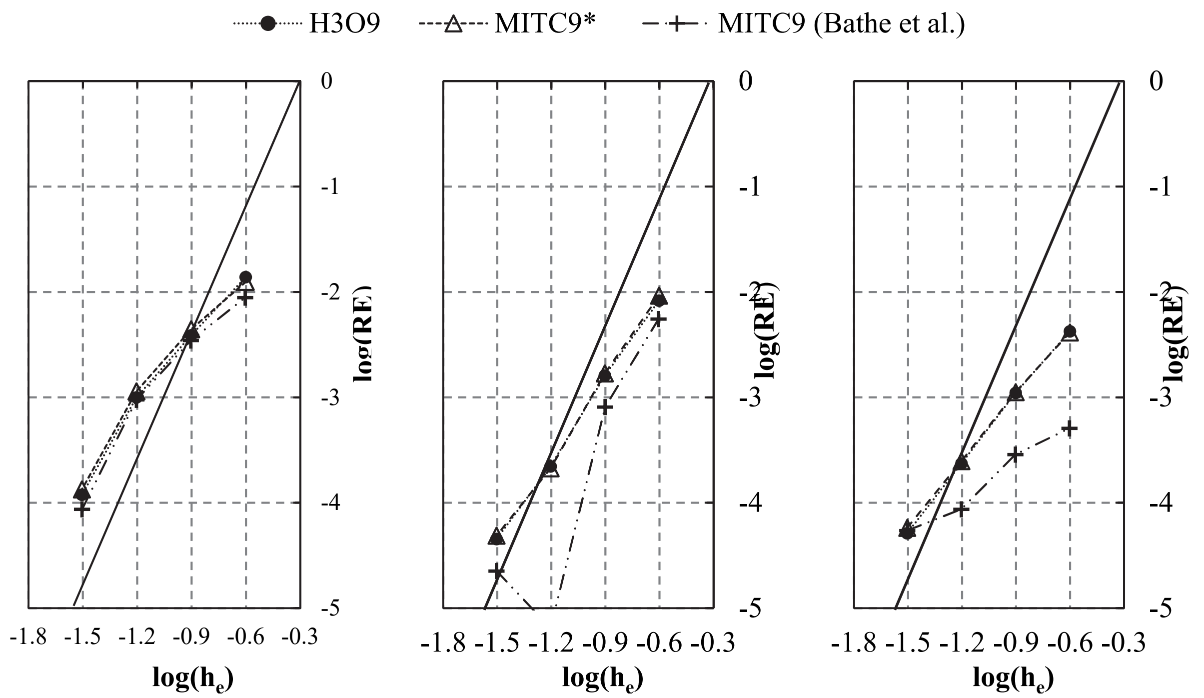

a. h/L = 0.0001 b. h/L = 0.001 c. h/L = 0.01

Figure 4.10: Convergence curves of H3O9, MITC9* and MITC9 elements for the cylindrical shell problem (clamped boundary).

4.2.4 Linear problems

4.2.4.1 Plane-stress cantilever

The problem is depicted in Figure 4.11, where a cantilever is fully clamped at one end and loaded at the other end. This is a plane-stress problem and was presented by Cook et al. (1989) to establish the influence of distortion locking on the conforming 9-noded planar element, where meshes (A)–(C) were considered. A further mesh (D) is also considered here, in which the interior element nodes are kept in their original location, leading to increased sensitivity to distortion locking. Geometric and material parameters are given as: L = 100, h = 1, E = 10^7, and ν = 0.3. An end load P = 2500 is uniformly applied on the free edge. The predicted displacements with various meshes and 9-noded element types, normalised by the theoretical value of the transverse tip displacement, are provided in Table 4.5.

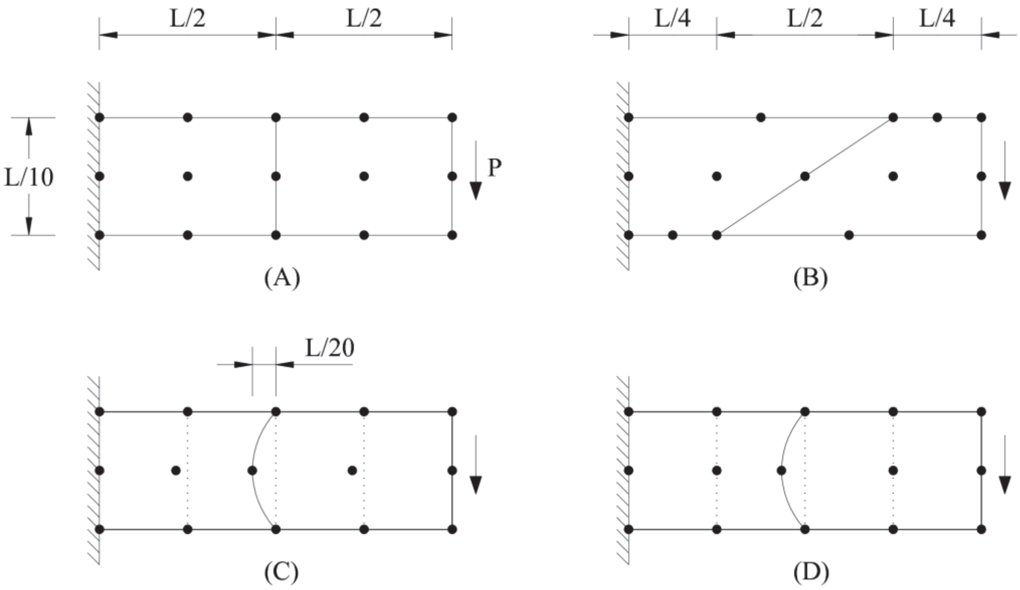

Figure 4.11: Cantilever modelled with different meshes using two 9-noded elements.

It is clear that among the optimised element variants the ones using third or fourth order hierarchic modes provide an effective relief from the distortion locking observed with the conforming element, where the objective alternative approach offers marginally better predictions than the corrective approach. The H3O9 element provides virtually identical accuracy to the H4O9 element with fewer Gauss points required. On the other hand, the MITC9* element in mesh (B)-(D) exhibits significant distortion locking owing to highly irregular element shapes. The accuracy of the MITC9is* element is less sensitive to distorted meshes (B) and (D), but is significantly degraded in mesh (D) where the internal node is highly eccentric from the element centre, in which case the Jacobian extracted at the element centre no more represents an average over the element.

Table 4.5: Normalised cantilever displacement predictions using various 9-noded elements.

Element code	Mesh (A)	Mesh (B)	Mesh (C)	Mesh (D)
CNF9	0.954	0.791	0.737	0.476
H2O9	0.954	0.812	0.904	0.464
H3O9	0.954	0.830	0.971	0.972
H4O9	0.954	0.827	0.972	0.972
H3C9	0.954	0.824	0.913	0.954
H4C9	0.954	0.827	0.972	0.972
MITC9*	0.990	0.255	0.712	0.535
MITC9is*	0.990	0.805	0.958	0.604

4.2.4.2 Square plate under transverse point load

The linear bending response of a clamped square plate subject to a central transverse point load (P) is investigated, where a quarter-model is considered using regular and distorted meshes, as shown in Figure 4.12. The geometric and material parameters are given as: L = 20, h = 0.2, $E = 2.1\times10^6$, and $\nu = 0.3$ .The non-dimensional central deflection ($\bar{u}_z$) is given as:

$$\bar{u}_z = \frac{u_{z0}Eh^3}{12PL^2(1-\nu^2)}$$

The predictions of $\bar{u}_z$ with various 9-noded quadrilateral elements, normalised by the reference value of 0.00560 (Timoshenko, 1940), are presented in Table 4.6. Clearly, the conforming element CNF9 exhibits shear locking, which is compounded in the distorted meshes. Again, the proposed optimisation approach shows good accuracy even with the coarse meshes, whether regular or distorted. In this respect, the objective alternative approach, using third or fourth order hierarchic optimisation, is typically better than the corrective alternative, particularly for the coarser meshes. In this example, the coarse meshes of the MITC9* element provide sufficient accuracy despite distorted element shapes. On the other hand, the results of the MITC9is* element are less accurate than the MITC9* elements for mesh (B) and (D), still resulting from the inability of the constant Jacobian $\mathbf{J}_C$ to represent an element average.

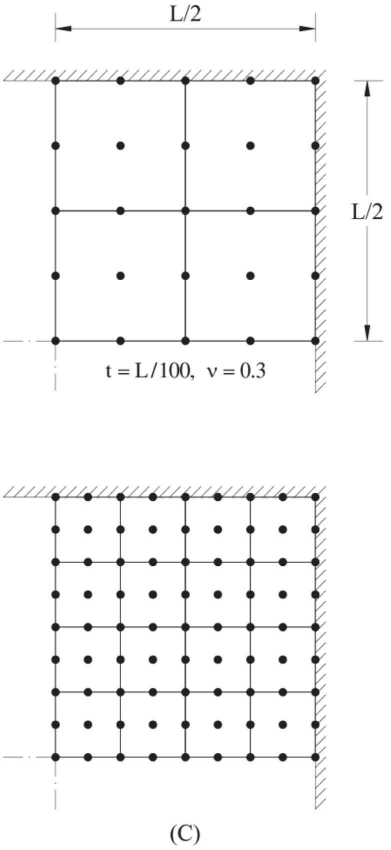

Figure 4.12: A quarter-model of a square plate using different mesh patterns of 9-noded elements.

Table 4.6: Normalised plate central deflections using various 9-noded elements.

Element code	Mesh (A)	Mesh (B)	Mesh (C)	Mesh (D)
CNF9	0.718	0.269	0.925	0.638
H2O9	1.006	0.955	1.006	0.959
H3O9	0.974	0.965	1.001	0.996
H4O9	0.973	0.958	1.001	0.996
H3C9	0.916	0.856	0.997	0.981
H4C9	0.917	0.899	0.997	0.990
MITC9*	1.005	1.000	1.005	1.003
MITC9is*	1.005	0.882	1.005	0.960

4.2.4.3 Pinched cylinder with rigid diaphragms

A cylindrical shell, supported by two rigid diaphragms at both ends, is loaded with two unit forces P, as shown in Figure 4.13. Due to symmetry, an octant of the shell is modelled with uniform meshes. Geometric and material parameters are given as: R = 300, L/R = 2 , R/h = 100 , $E = 3\times10^6$, and $\nu = 0.3$. The predicted deflection at the point of loading is normalised by the analytical solution 0.18248×10^{-4} (Heppler & Hansen, 1986). This problem was also analysed by Kulikov and Plotnikova (2006) with four-noded degenerated solid-shell elements and by Kim et al. (2005) with 8-noded solid-shell elements. In Table 4.7, results of the 9-noded shell elements H3O9, MITC9* and MITC9is* are compared against the results by others with the same number of DOFs, which indicates good performance of the H3O9 element.

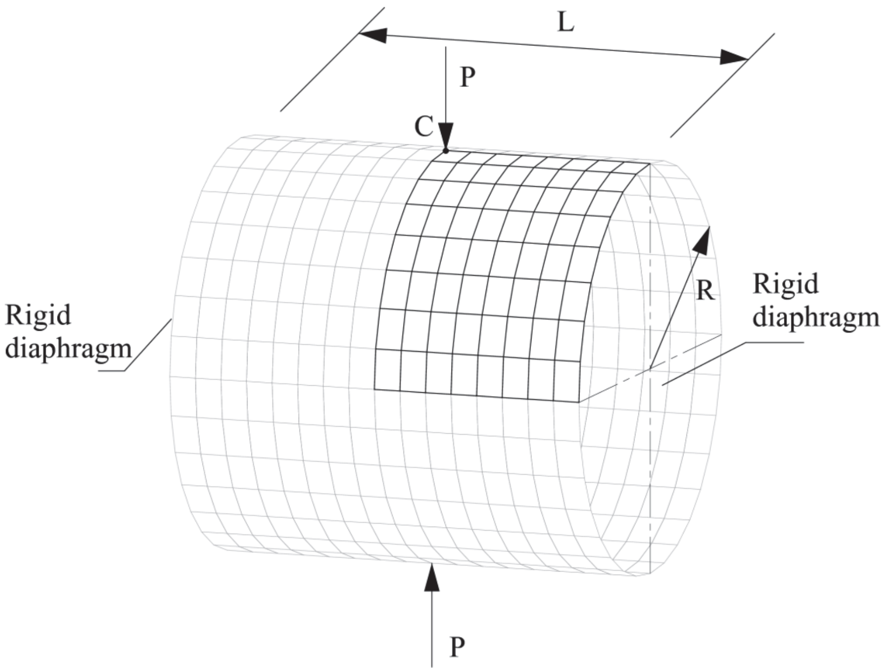

Figure 4.13: Pinched cylindrical shell supported by rigid diaphragms (quadrilateral elements).

Table 4.7: Normalised deflections at the point of loading for the pinched cylinder problem (quadrilateral elements).

Element code	2×2 (4×4×1)	4×4 (8×8×1)	8×8 (16×16×1)
H3O9	0.816	0.938	0.988
MITC9*	0.711	0.962	1.000
MITC9is*	0.711	0.962	1.000
TMS4SA (Kulikov & Plotnikova)	0.890	0.941	0.986
XSOLID85 (Kim et al.)	0.382	0.751	0.932

4.2.5 Large displacement problems

4.2.5.1 Annular plate subject to end loading

An annular plate is fully clamped at one end and subjected to a uniform transverse loading P at the other end, as is shown in Figures 4.14-4.15. The geometric and material properties are specified as: $R_1 = 6$, $R_2 = 10$, $h = 0.03$, $E = 2.1 \times 10^7$ and $\nu = 0.0$. The plate is modelled with a 15×3 mesh of various optimised 9-noded elements, and the load-displacement curves at points A and B are plotted in Figure 4.16. The results with a fine mesh (60×9) of H3O9 is used as a reference solution. It is observed that the H3O9 and H4O9 results are more accurate than other optimized elements. The H3O9 results are also compared with the MITC9* and MITC9is* results in Figure 4.17. Also presented are results with a 15×3 mesh of 9-noded hybrid stress elements by Sansour and Kollmann (2000) and a 30×6×1 mesh of 8-noded solid-shell elements by Norachan et al. (2012), where all models have comparable number of DOFs. Clearly, the meshes of the H3O9 and the MITC9* elements yield more accurate results than others.

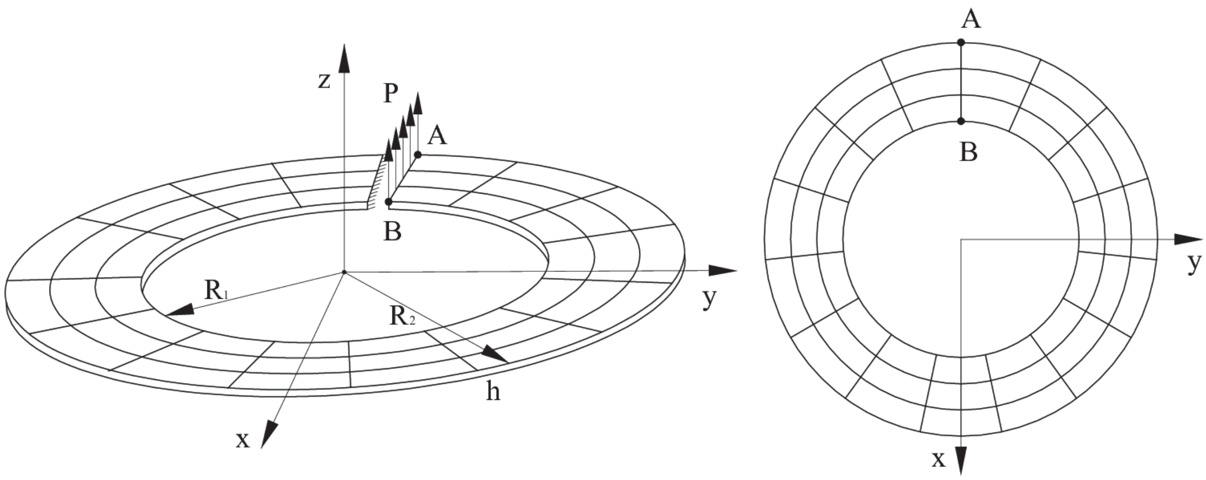

Figure 4.14: Annular plate subject to end loading.

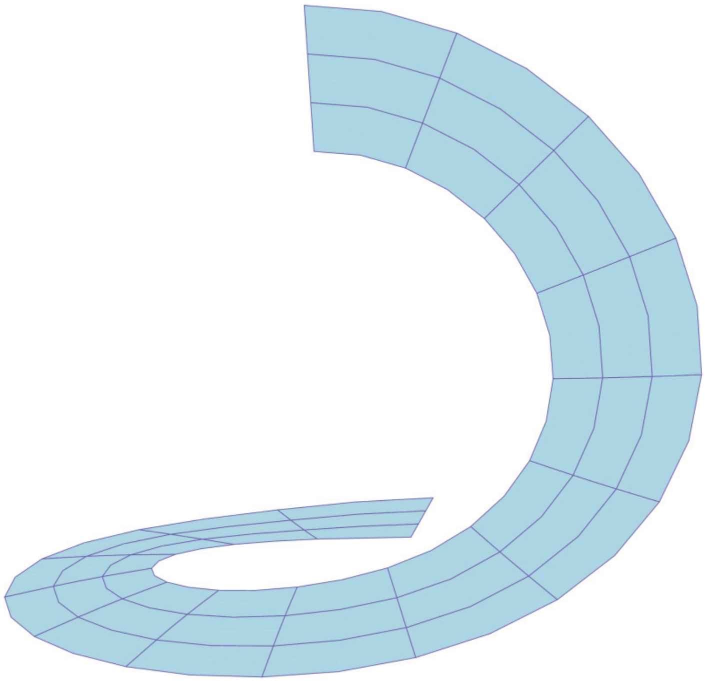

Figure 4.15: Deformed configuration of the annular plate problem.

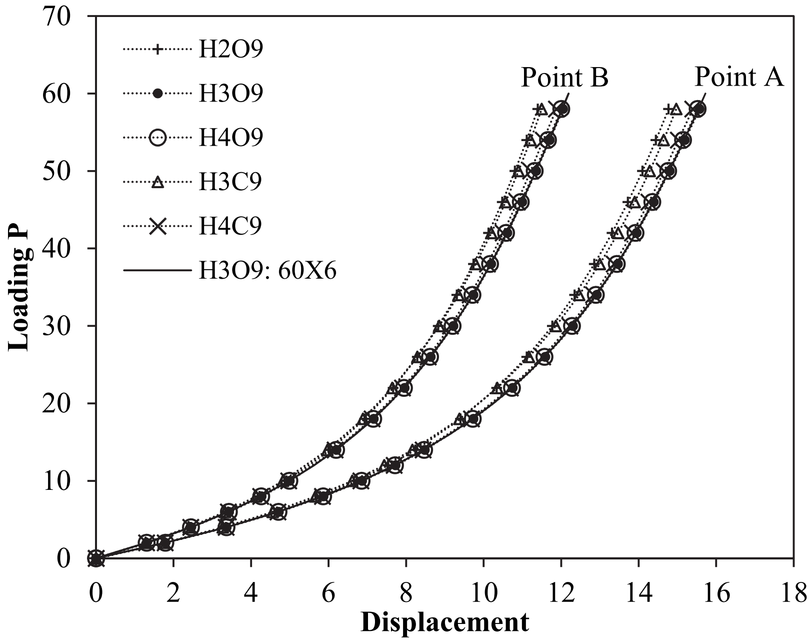

Figure 4.16: Load-displacement curves for a 15×3 mesh of various optimised 9-noded elements.

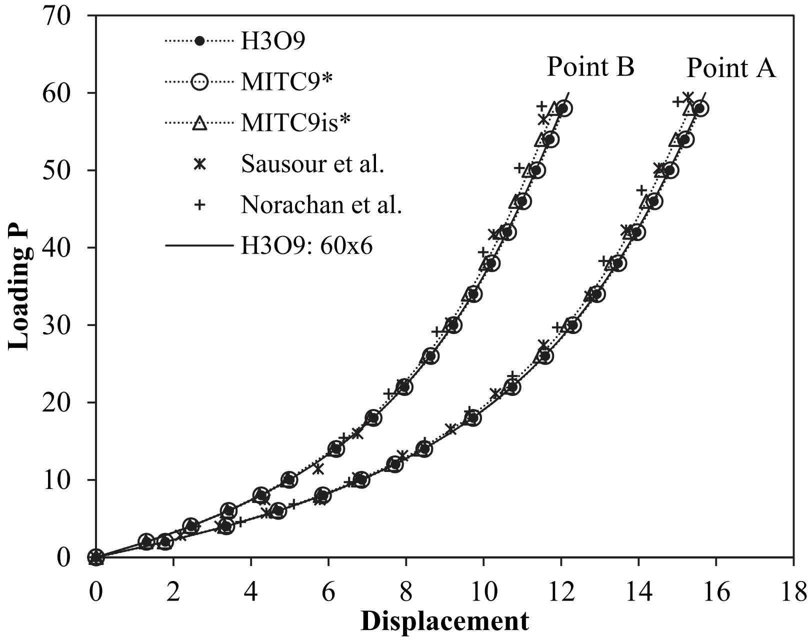

Figure 4.17: Load-displacement curves for meshes of various quadrilateral elements having the same number of DOFs.

4.2.5.2 Pinched hemispherical shell with 18° cut-off

Consideration is given here to a large displacement problem where a hemispherical shell with an 18°circular cut-off at its top is subjected to symmetric concentrated forces at its base, as shown in Figures 4.18-4.19. The geometric and material parameters are: R = 10, h = 0.04, $E = 6.825 \times 10^7$ and $\nu = 0.3$. Due to symmetry, a quarter of the shell is modelled with three uniform meshes (4×4, 8×8 and 16×16) of various 9-noded element types, with the load-displacement curves of the radial displacement at Point A and B compared in Figures 4.20-4.21. The predictions of Celigoj using a 16×16 mesh (Celigoj, 1996) are also presented for comparison purposes.

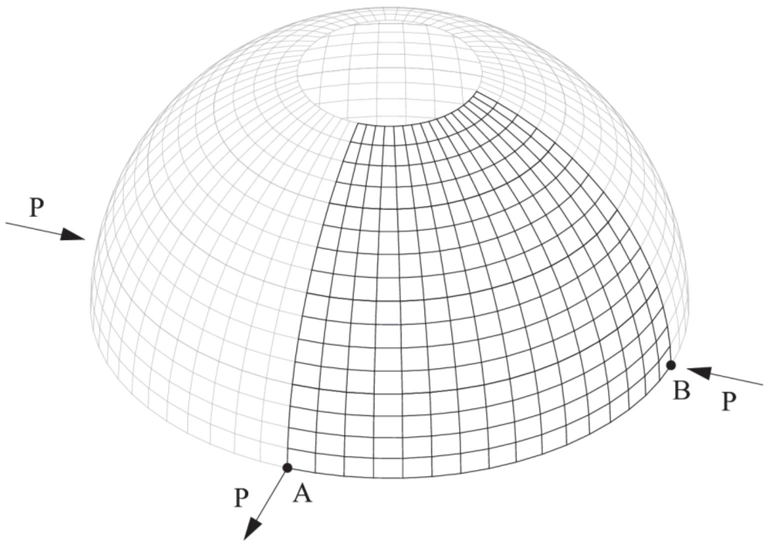

Figure 4.18: Pinched hemispherical shell with a 18° cut-off.

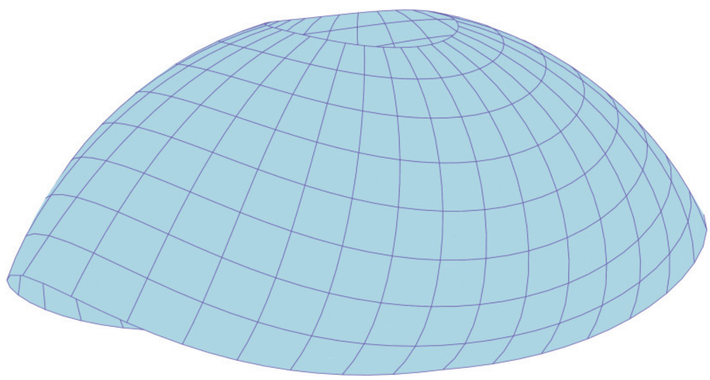

Figure 4.19: Deformed configuration of pinched hemispherical shell with a 18° cut-off.

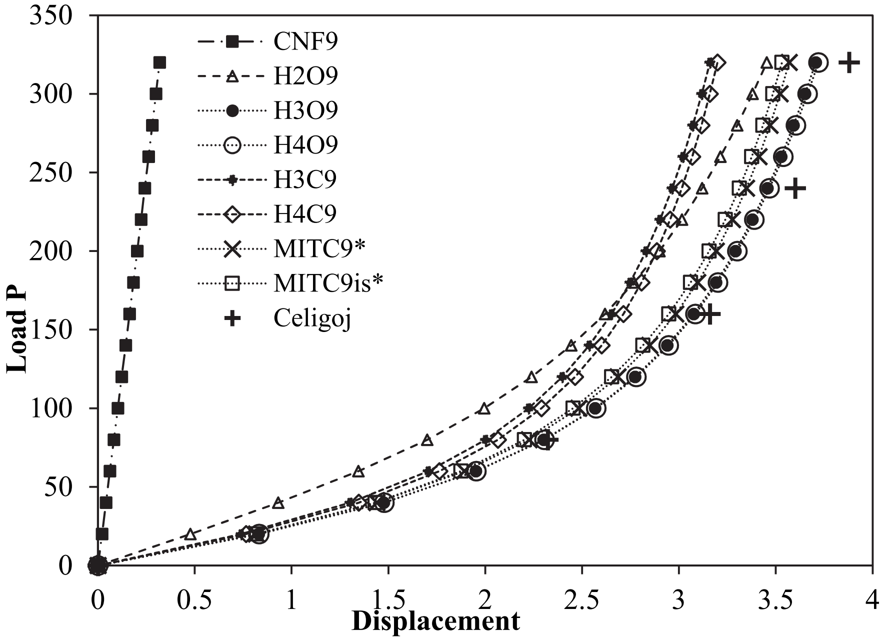

a. 4×4 mesh

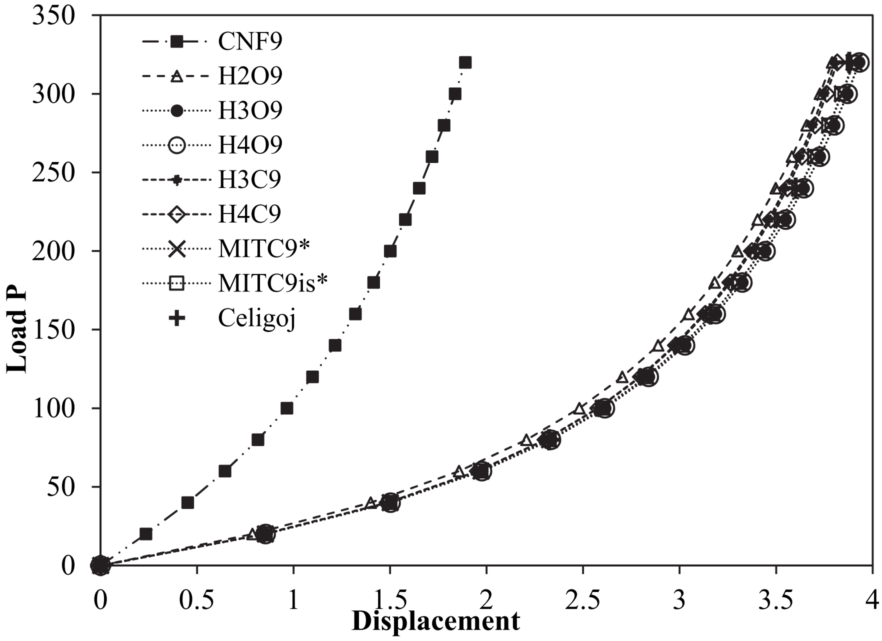

b. 8×8 mesh

Figure 4.20: Load-displacement curves of the radial displacement at Point A with different meshes of 9-noded elements (Cont'd…).

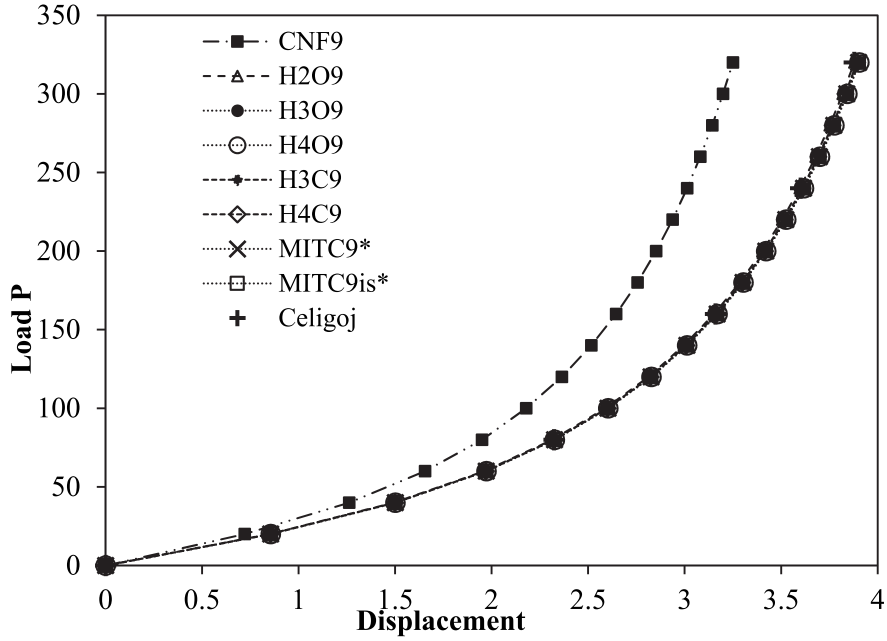

c. 16×16 mesh

Figure 4.20: Load-displacement curves of the radial displacement at Point A with different meshes of 9-noded elements.

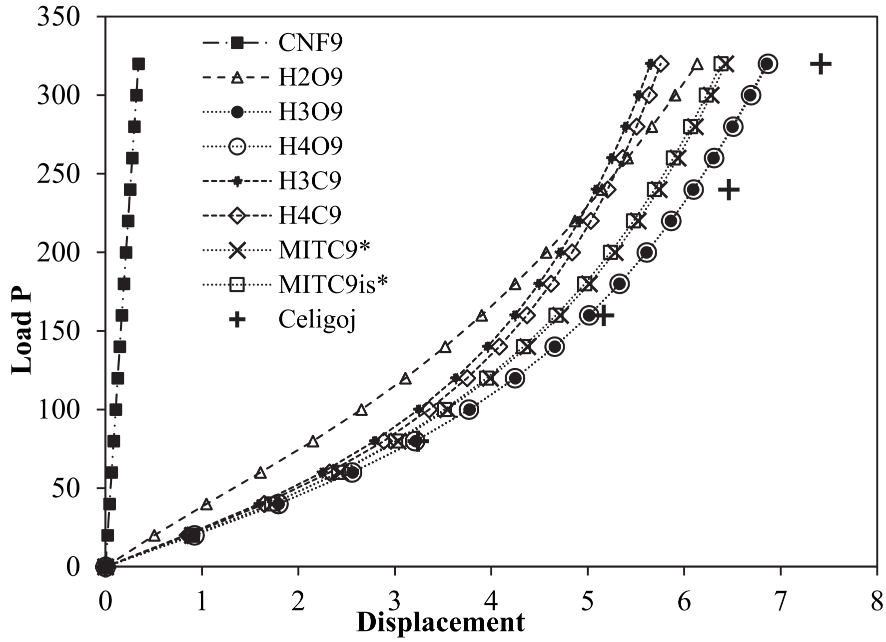

a. 4×4 mesh

Figure 4.21: Load-displacement curves of the radial displacement at Point B with different meshes of 9-noded elements (Cont'd…).

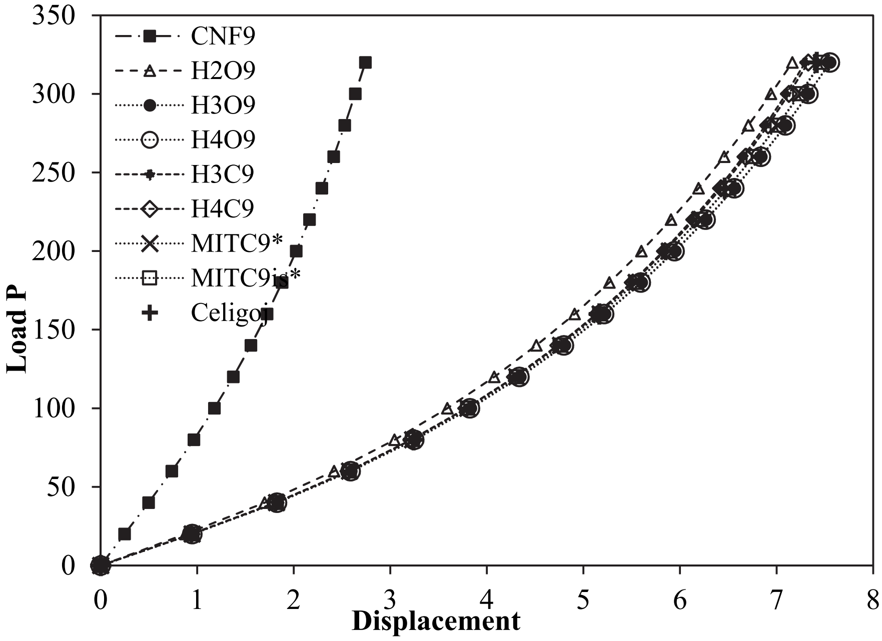

b. 8×8 mesh

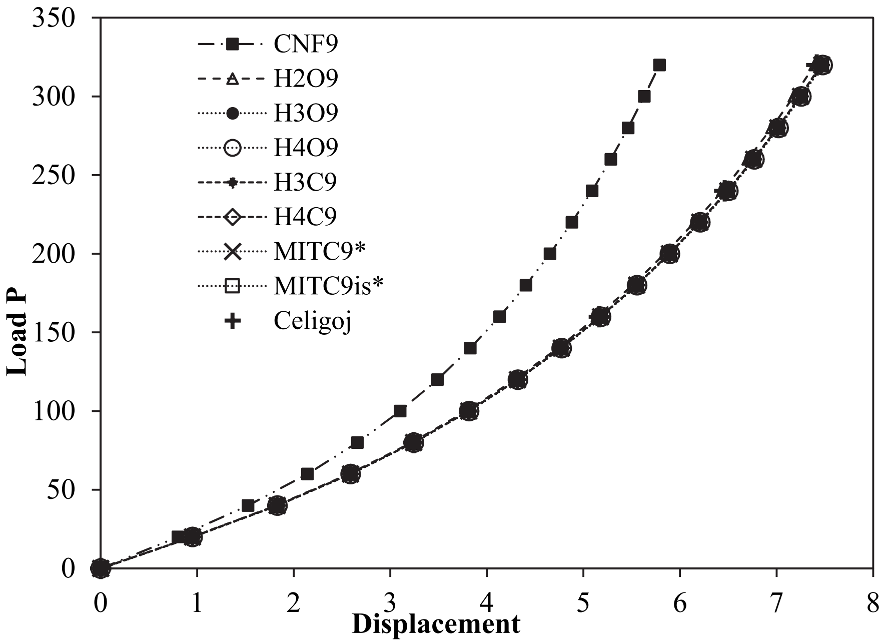

c. 16×16 mesh

Figure 4.21: Load-displacement curves of the radial displacement at Point B with different meshes of 9-noded elements.

Clearly, noticeable locking phenomenon is exhibited in the conforming element model, which persists even in the refined 16×16 mesh mainly attributed to membrane locking. The optimised elements H3O9 and H4O9 provide better approximations of the shell response for a coarse mesh (4×4), followed by the mixed elements MITC9* and MITC9is*. Variants based on the corrective alternative approach, on the other hand, are less accurate than those based on the objective alternative approach particularly for coarse meshes, though this difference diminishes with mesh refinement. It is also observed that the equilibrium paths of the coarse mesh with H2O9 deviate from the other curves in terms of the curve shapes, which indicates the importance of the inclusion of correction hierarchic strain modes in the optimisation. All the elements converge with mesh refinement to Celigoj's solution.

The sensitivity of the element performance to distortion is also investigated with 4×4 and 8×8 irregular meshes, which are obtained by moving the three nodes (C, D, E) in a regular mesh to positions (C', D', E'), as shown in Figure 4.22. By changing the positions of the inward and outward forces, two sets of results are readily obtained with the distorted meshes. Figures 4.23-4.24 depict the two sets of load-displacement curves with the H3O9, MITC9* and MITC9is* elements. It appears that in the coarser mesh the H3O9 element provides better predictions than the mixed elements for both distortion cases. On the other hand, the MITC9is* element performs better than MITC9* element in one distortion case but is not as accurate in the other one. Nevertheless, all the solutions converge in the finer mesh.

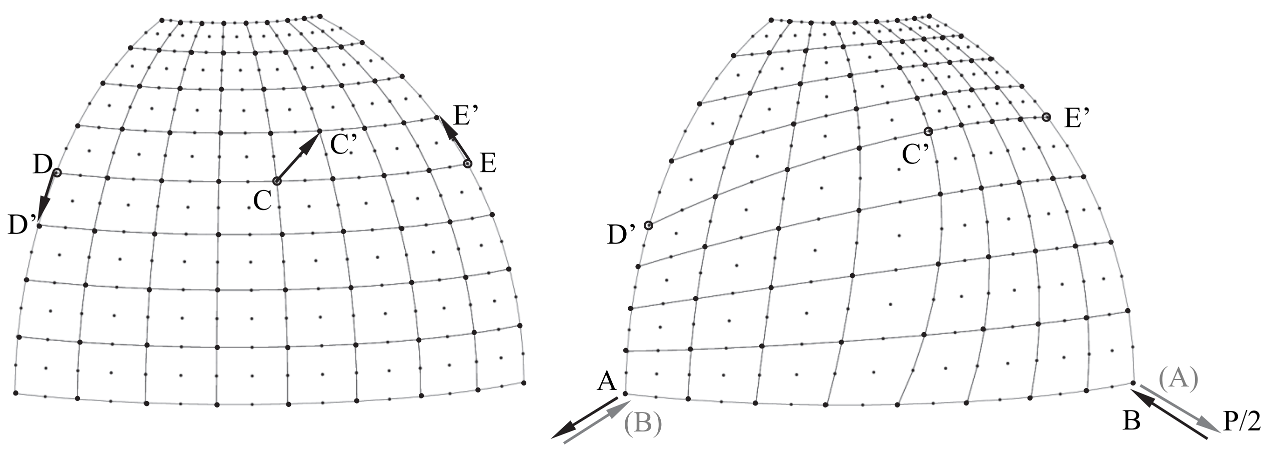

Figure 4.22: Irregular meshes of a quarter model. (The larger points in the figure represent the nodes in a 4×4 mesh. Distorted mesh 1 corresponds to the inward and outward forces denoted in black, while Distorted mesh 2 corresponds to the forces denoted in grey.)

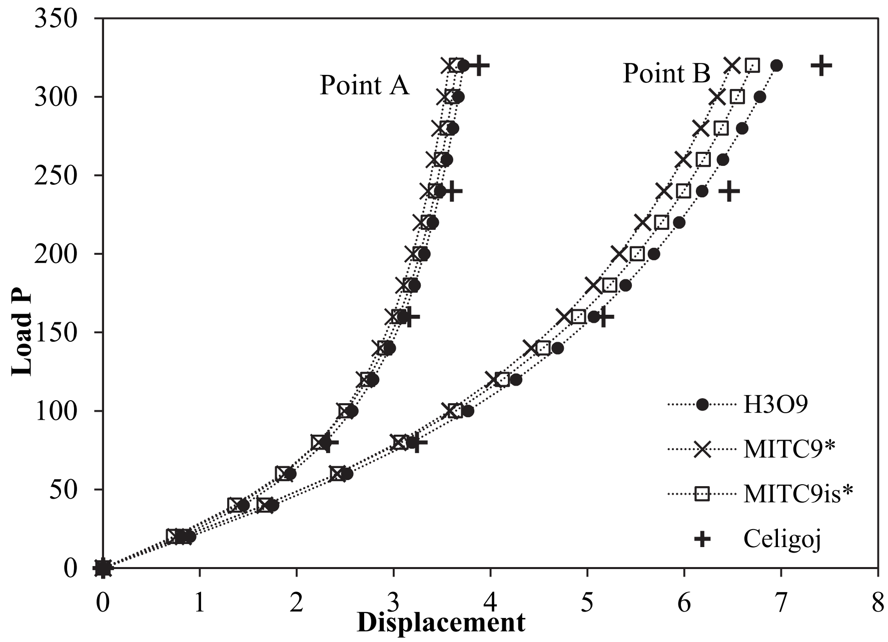

a. 4×4 mesh

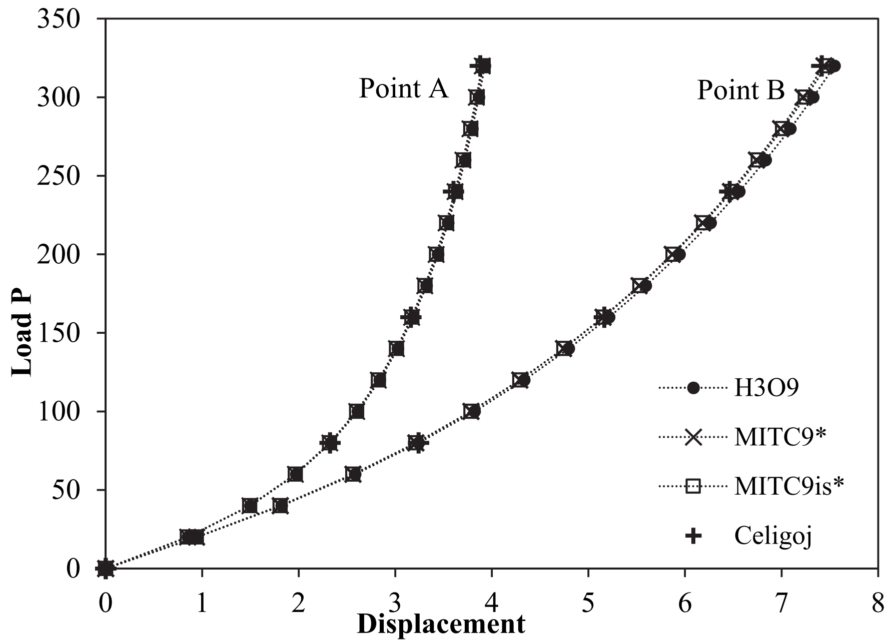

b. 8×8 mesh

Figure 4.23: Load-displacement curves for meshes of different 9-noded elements (Distorted mesh 1).

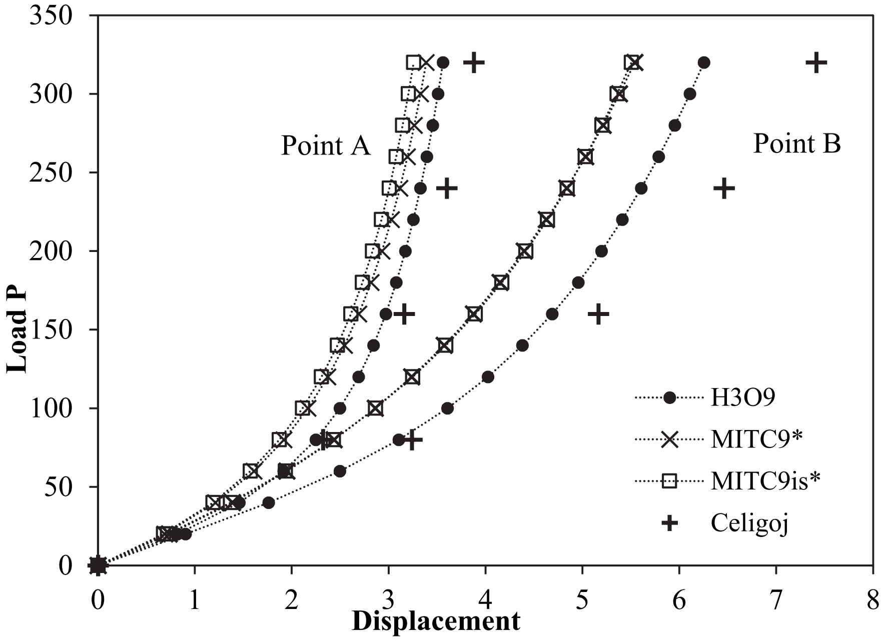

a. 4×4 mesh

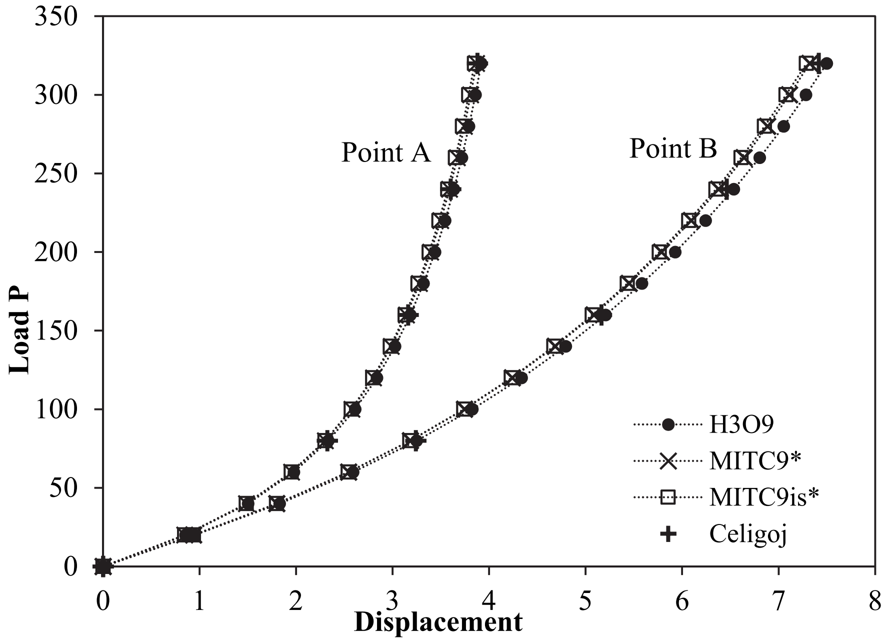

b. 8×8 mesh

Figure 4.24: Load-displacement curves for meshes of different 9-noded elements (Distorted mesh 2).

4.3 Triangular shell element

4.3.1 Zero energy mode test

In this test, the number of zero eigenvalues of the stiffness matrix for an unsupported shell element is counted for each of the 6-noded element types. Both regular and irregular element shapes are considered in this test (Figure 4.25) to allow for more possibilities. All the considered elements have exactly six zero eigenvalues of their element stiffness matrix, hence indicating absence of spurious mechanism.

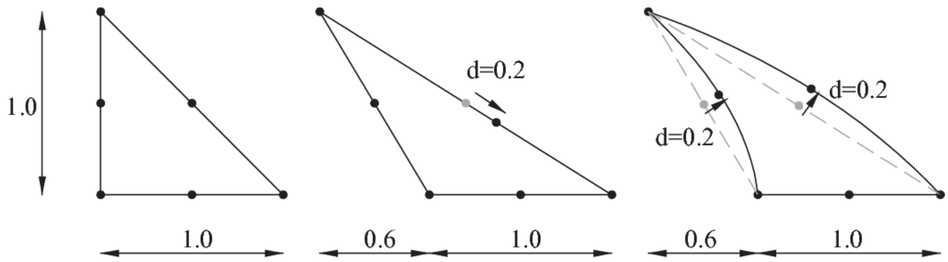

Figure 4.25: Various element shapes for the zero energy mode test of 6-noded shell element.

4.3.2 Isotropic element test

Herein, an arbitrarily shaped triangular element (see Figure 4.26) is employed for the isotropic element test. Geometric and material parameters are given as: thickness t = 0.001, Young's modulus E = 10^6 and Poisson's ratio ν = 0.2. In this test, 24 sets of strain-inducing displacement modes are respectively imposed to the considered 6-noded elements. For each prescribed displacement set, three nodal numbering sequences are used, and the maximum relative error in the predicted total strain energy by using three nodal orderings is presented in Table 4.8. Results show that all the considered elements pass the isotropic element tests.

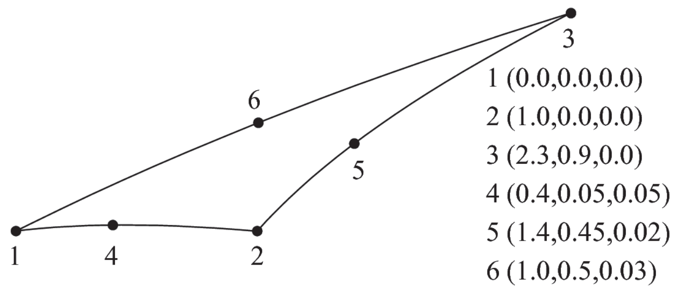

Figure 4.26: Geometry of an arbitrary 6-noded triangular element for isotropic element tests.

Table 4.8: Results of isotropic element tests for various 6-noded elements.

Mode	Displacement fields	Relative error in the predicted total strain energy by using three nodal orderings (%)					
		H2O6	H3O6	H4O6	H3C6	H4C6	MITC6*
1	u=*a*x	0.000	0.000	0.000	0.000	0.000	0.000
2	v=*a*y	0.000	0.000	0.000	0.000	0.000	0.000
3	u=*a*y or v=*a*x	0.000	0.000	0.000	0.000	0.000	0.000
4	$u=ax^2$	0.000	0.000	0.000	0.000	0.000	0.000
5	$v=ay^2$	0.000	0.000	0.000	0.000	0.000	0.000
6	u=*a*xy	0.000	0.000	0.000	0.000	0.000	0.000
7	v=*a*xy	0.000	0.000	0.000	0.000	0.000	0.000
8	$u=ay^2$	0.000	0.000	0.000	0.000	0.000	0.000
9	$v=ax^2$	0.000	0.000	0.000	0.000	0.000	0.000
10	$\theta_x=ax$	0.000	0.000	0.000	0.000	0.000	0.000
11	$\theta_y=ay$	0.000	0.000	0.000	0.000	0.000	0.000
12	$\theta_x=ay$	0.000	0.000	0.000	0.000	0.000	0.000
13	$\theta_y=ax$	0.000	0.000	0.000	0.000	0.000	0.000
14	$\theta_x=ax^2$	0.000	0.000	0.000	0.000	0.000	0.000
15	$\theta_y=ay^2$	0.000	0.000	0.000	0.000	0.000	0.000
16	$\theta_x=axy$	0.000	0.000	0.000	0.000	0.000	0.000
17	$\theta_y=axy$	0.000	0.000	0.000	0.000	0.000	0.000
18	$\theta_x=ay^2$	0.000	0.000	0.000	0.000	0.000	0.000
19	$\theta_y=ax^2$	0.000	0.000	0.000	0.000	0.000	0.000
20	w=*a*x	0.000	0.000	0.000	0.000	0.000	0.000
21	w=*a*y	0.000	0.000	0.000	0.000	0.000	0.000
22	$w=ax^2$	0.000	0.000	0.000	0.000	0.000	0.000
23	$w=ay^2$	0.000	0.000	0.000	0.000	0.000	0.000
24	w=*a*xy	0.000	0.000	0.000	0.000	0.000	0.000

4.3.3 Patch tests

The five-element patch by MacNeal and Harder (1985), described in Section 4.1.2, is adapted to test the 6-noded triangular element, as shown in Figure 4.27. The boundary conditions used for the constant membrane strain and constant bending strain mode tests are the same as those defined in Section 4.1.2.

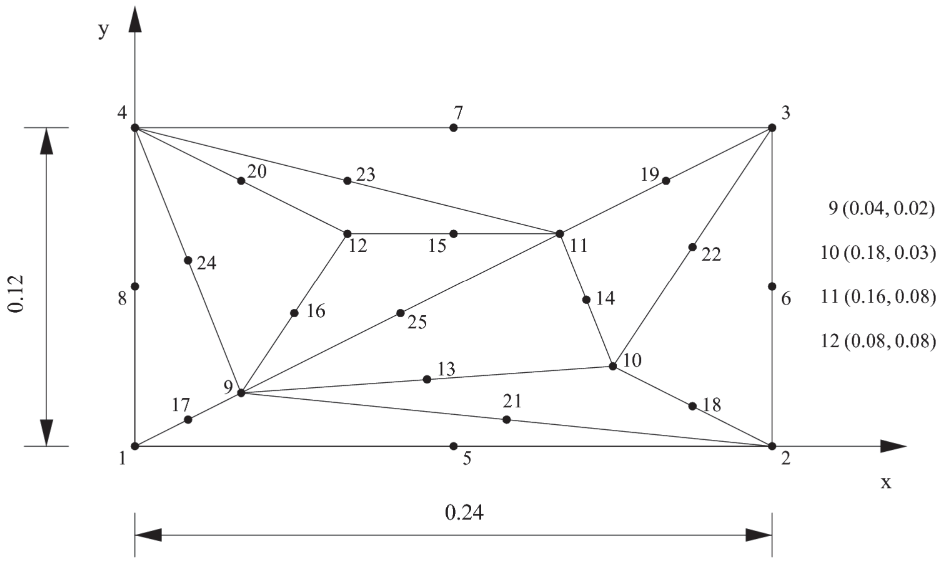

Figure 4.27: Patch test for 6-noded shell elements.

The patch test results of various 6-noded element types corresponding to a constant membrane strain state ($\varepsilon_x = \varepsilon_y = \gamma_{xy} = 0.001$) are listed in Table 4.9, where the planar displacements at all internal nodes, along with planar strains of the two internal elements evaluated at node 25, are compared against the theoretical values. The patch test results of the considered 6-noded elements associated with a constant bending strain state ($\kappa_x = \kappa_y = \kappa_{xy} = 0.001$) are given in Table 4.10, where the transverse displacement and rotations at all internal nodes and curvatures of two internal elements evaluated at node 25 are compared against corresponding theoretical values. It is observed from both tables that the considered 6-noded elements all pass the patch tests.

Table 4.9: Relative error in planar displacements and strain components in membrane patch test.

Approach	Maximum error in u_{x0}	Maximum error in u_{y0}	Maximum error in ε_x	Maximum error in ε_y	Maximum error in γ_{xy}
H2O6	0.000	0.000	0.000	0.000	0.000
H3O6	0.000	0.000	0.000	0.000	0.000
H4O6	0.000	0.000	0.000	0.000	0.000
H3C6	0.000	0.000	0.000	0.000	0.000
H4C6	0.000	0.000	0.000	0.000	0.000
MITC6*	0.000	0.000	0.000	0.000	0.000

Table 4.10: Relative error in transverse and rotational displacements and curvatures in out-of-plane bending patch test.

Approach	Maximum error in u_{z0}	Maximum error in θ_x	Maximum error in θ_y	Maximum error in κ_x	Maximum error in κ_y	Maximum error in κ_{xy}
H2O6	0.000	0.000	0.000	0.000	0.000	0.000
H3O6	0.000	0.000	0.000	0.000	0.000	0.000
H4O6	0.000	0.000	0.000	0.000	0.000	0.000
H3C6	0.000	0.000	0.000	0.000	0.000	0.000
H4C6	0.000	0.000	0.000	0.000	0.000	0.000
MITC6*	0.000	0.000	0.000	0.000	0.000	0.000

The behaviour of the considered 6-noded elements for an irregular mesh, where the original patch is distorted by shifting four edge nodes 13, 14, 15 and 16, either parallel or perpendicular to the edges, and moving the internal node 25 along the x-direction, as illustrated in Figure 4.28. All the shifts of nodal positions are of a magnitude d = 0.01. Results of the membrane patch test with this distorted mesh are given in Table 4.11, which indicate that all the optimised 6-noded elements pass the test owing to the enforcement of zero mean on each hierarchic strain mode. The MITC6*, however fails in the constant strain patch test for the distorted mesh.

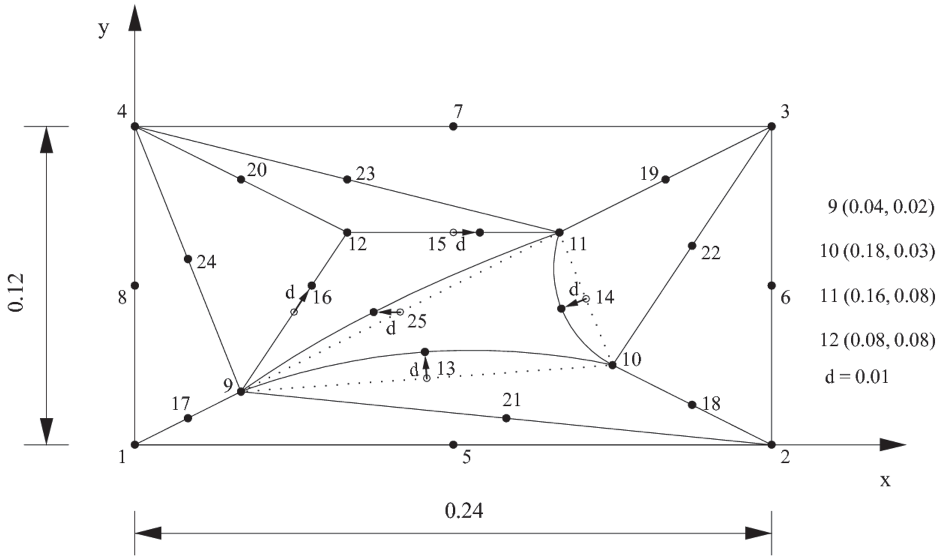

Figure 4.28: Patch test for 6-noded shell elements (distorted mesh).

Table 4.11: Relative error in transverse and rotational displacements and curvatures in membrane patch test (distorted mesh).

Approach	Maximum error in u_{x0}	Maximum error in u_{y0}	Maximum error in ε_x	Maximum error in ε_y	Maximum error in γ_{xy}
H2O6	0.000	0.000	0.000	0.000	0.000
H3O6	0.000	0.000	0.000	0.000	0.000
H4O6	0.000	0.000	0.000	0.000	0.000
H3C6	0.000	0.000	0.000	0.000	0.000
H4C6	0.000	0.000	0.000	0.000	0.000
MITC6*	0.089	0.056	0.185	0.113	0.561

4.3.4 Convergence rate tests

4.3.4.1 Clamped square plate problem

The same numerical example as given in Section 4.1.3.1 is employed herein to assess the convergence rates of various 6-noded elements. Due to symmetry, a quarter of the plate is modelled with uniform meshes of the triangular element, as is shown in Figure 4.29. In this example, the solution with a fine mesh (128×128) of H3O6 elements is regarded as a reference solution. For all the optimised 6-noded elements and the MITC6* element, the accuracy measure (4.1) is employed. Figure 4.30 shows the convergence results of various optimised triangular elements, which show an effective relief from shear locking and have nearly optimal convergence rate in this example. In terms of accuracy, the H2O6 solution, which uses optimisation without hierarchic terms, is not as accurate as those with hierarchic correction. On the other hand, the objective alternative approach, using third or fourth order hierarchic optimisation, is more accurate than the corrective alternative. Note that in the case where h/L = 0.01, the H4O6 and the H4C6 solutions show a lifted tail after reaching a relatively high accuracy level, which may be due to rounding errors and the relative error measure employed.

The H3O6 element is also compared to the MITC6* and the MITC6 (Kim & Bathe, 2009) elements. Note that the MITC6 results employs the s-norm as a measure of accuracy, as given by (4.2). Although (4.1) and (4.2) do not yield equivalence for non-conforming formulations, it is still reasonable to compare the results of the MITC6 element using the measure of (4.2) against the results of the other elements using the measure of (4.1). Figure 4.31 shows that the H3O6 results have better accuracy and the convergence rate than the MITC6 results, although there is a noticeable shift of curves upward as h/L decreases. It is also shown that the convergence rate of the MITC6* solution is much slower for this problem.

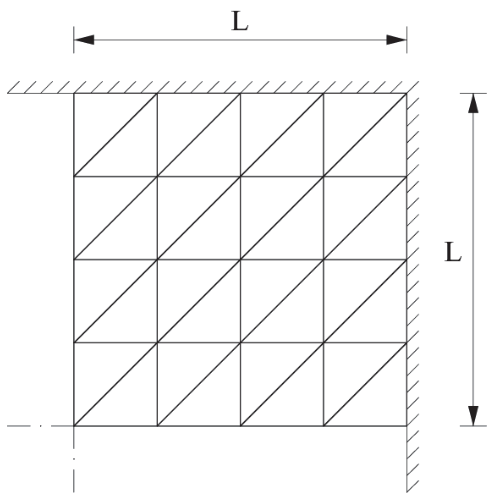

Figure 4.29: A quarter-model of a clamped square plate subjected to uniform pressure (6-noded shell element).

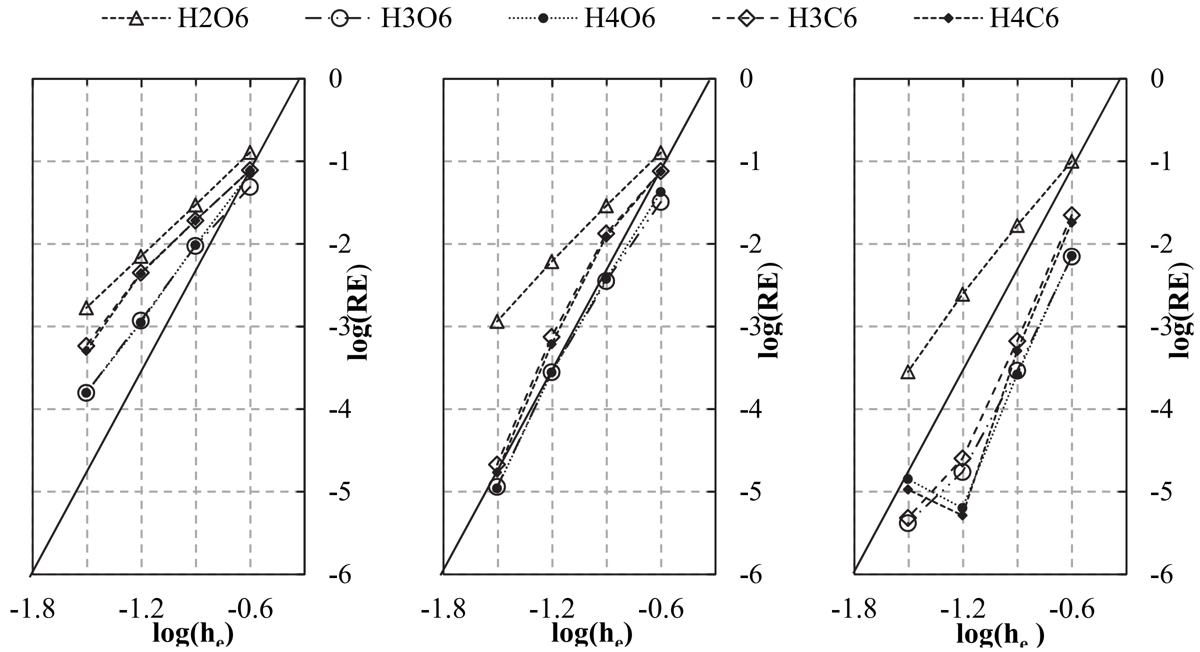

a. h/L= 0.0001 b. h/L = 0.001 c. h/L = 0.01

Figure 4.30: Convergence curves of variants of optimised 6-noded elements for the clamped square plate problem.

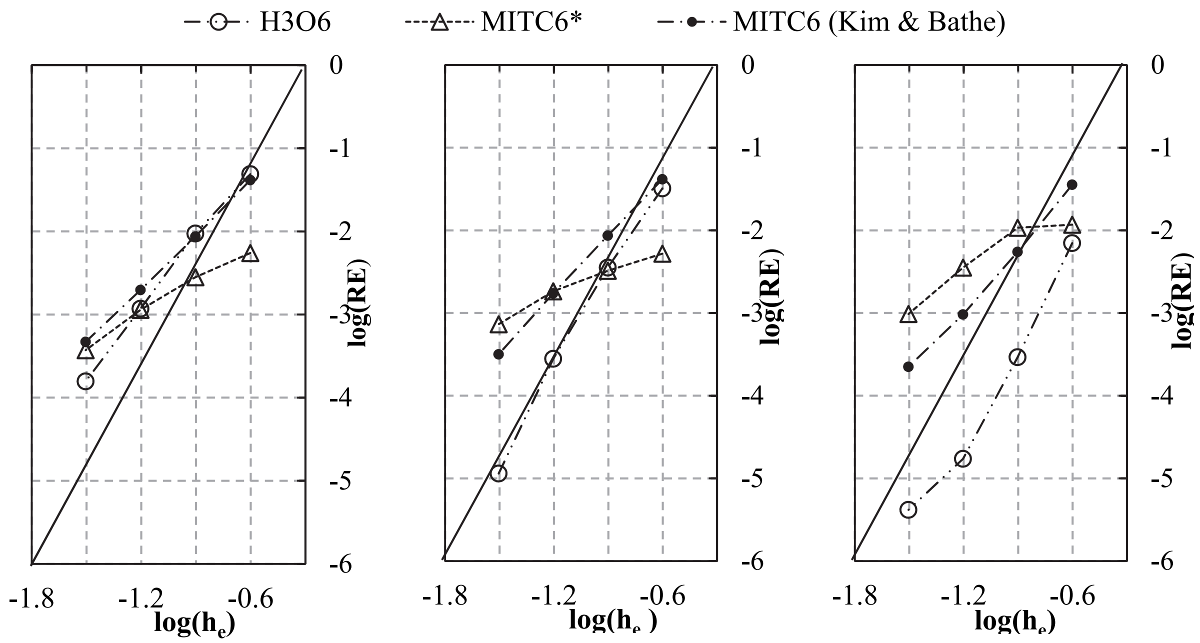

a. h/L= 0.0001 b. h/L = 0.001 c. h/L = 0.01

Figure 4.31: Convergence curves of H3O6 and MITC6* in comparison with MITC6 for the clamped square plate problem.

4.3.4.2 Cylindrical shell problem

The same cylindrical shell problem, as described in Section 4.1.3.2, is employed to assess the convergence rates of various triangular shell elements. Similarly, two boundary conditions at both curved ends are considered: a free boundary condition and a fully clamped boundary condition. Due to symmetry, an octant of the model is analysed with a uniform mesh pattern, as shown in Figure 4.32. Figures 4.33-4.34 present the behaviour of various optimised elements with respectively free edge boundary and clamped edge boundary. The relative error measure (4.1) is employed. Significant locking is observed in the H2O6 solution, in particular for the free edge boundary condition, while the other optimised elements exhibit good accuracy and convergence rate, with the H3O6 solution providing slightly better accuracy. In Figures 4.35-4.36, the H3O6 results are compared against the MITC6* results, and the MITC6 solution (Kim & Bathe, 2009) in accordance with the relative error measure (4.2) is also presented for comparison. It is observed that the H3O6 and MITC6* elements have maginally comparable accuracy and convergence rates for the considered boundary conditions and (h/L) ratios. The figures also show that the MITC6 element has slower convergence rates and less accuracy for thin shells (h/L =0.0001).

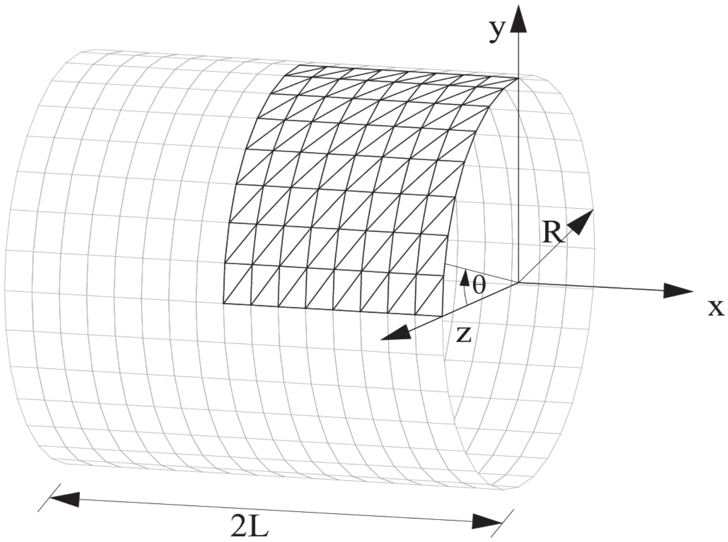

Figure 4.32: An octant model of the cylindrical shell problem with 6-noded shell elements.

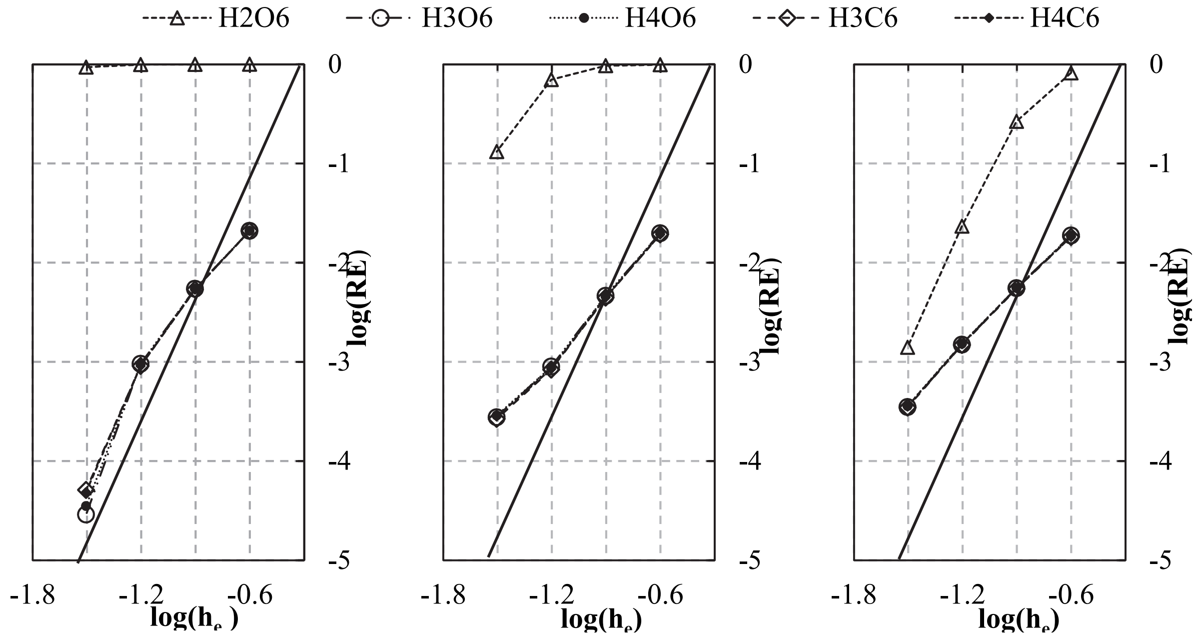

a. h/L= 0.0001 b. h/L= 0.001 c. h/L= 0.01

Figure 4.33: Convergence curves of variants of optimised 6-noded elements for the cylindrical shell problem where both ends are free.

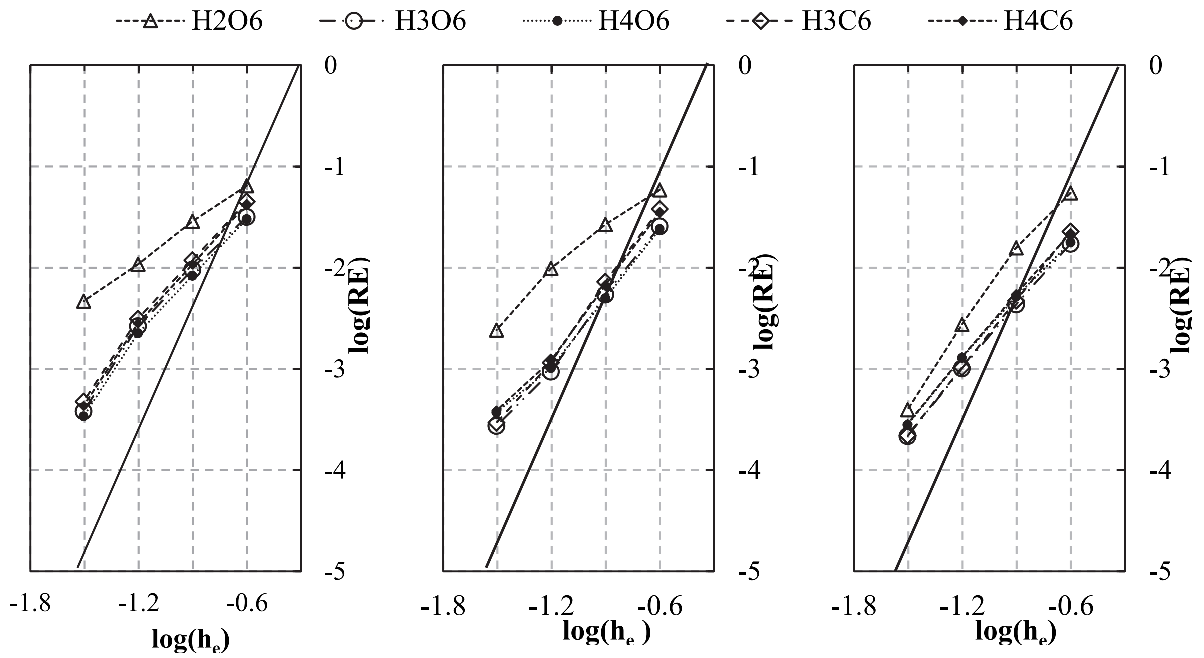

a. h/L= 0.0001 b. h/L= 0.001 c. h/L= 0.01

Figure 4.34: Convergence curves of variants of optimised 6-noded elements for the cylindrical shell problem where both ends are clamped.

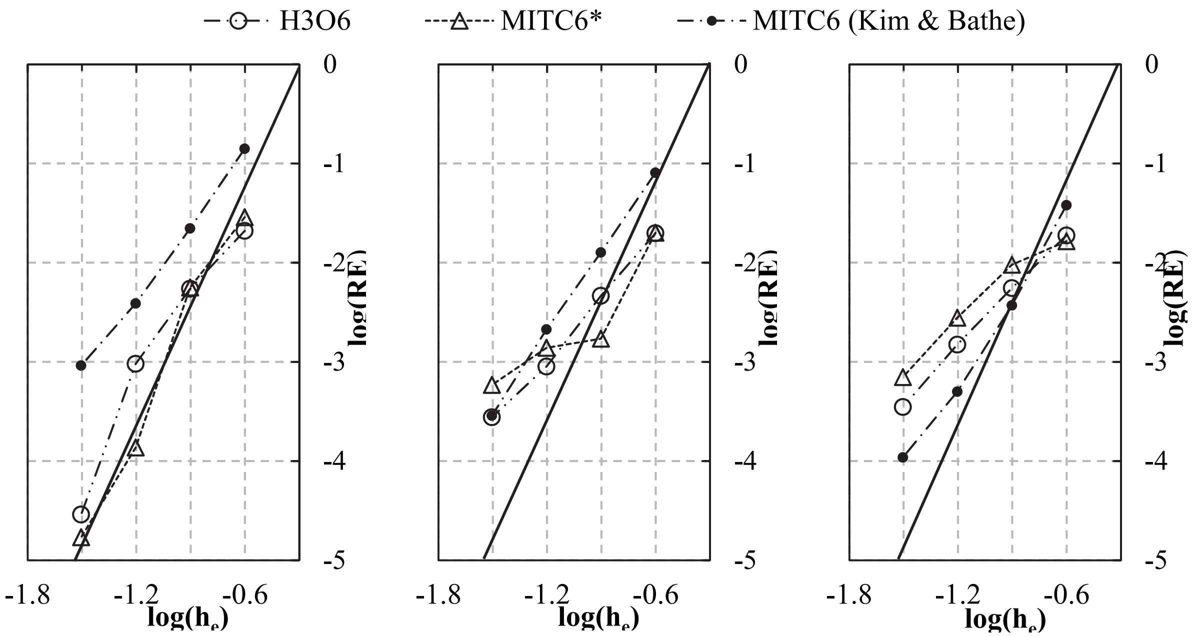

a. h/L= 0.0001 b. h/L= 0.001 c. h/L= 0.01

Figure 4.35: Convergence curves of H3O6 and MITC6* in comparison with MITC6 for the cylindrical shell problem where both ends are free.

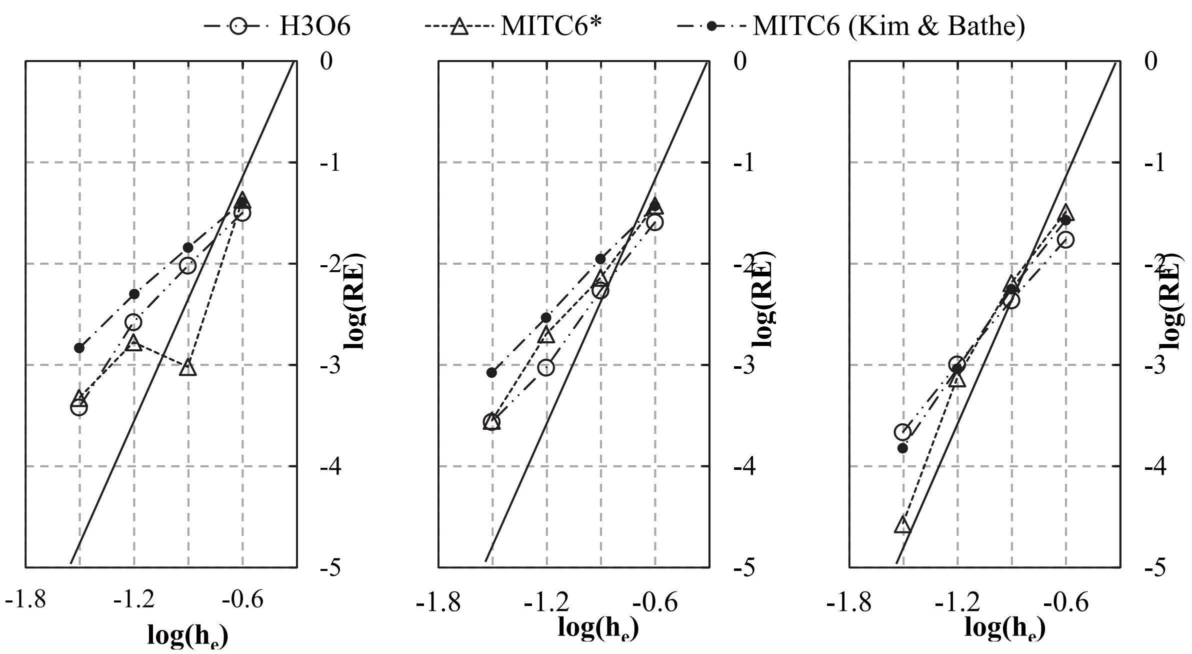

a. h/L= 0.0001 b. h/L= 0.001 c. h/L= 0.01

Figure 4.36: Convergence curves of H3O6 and MITC6* in comparison with MITC6 for the cylindrical shell problem where both ends are clamped.

4.3.5 Linear problems

4.3.5.1 Pinched cylinder problem

This is a linear problem, where a cylindrical shell, supported with rigid diaphragms at both end, is loaded with a pair of pinching loads, as shown in Figure 4.37. The geometric and material properties are given as: $L/R = 2$, $R/h = 100$ and $\nu = 0.3$. Due to symmetry, an octant of the cylindrical shell is modelled with three uniform meshes (4×4, 8×8, and 12×12) of various 6-noded elements, with an 8×8 mesh depicted in Figure 4.37. The non-dimensional deflection the point of loading, $\overline{w}_C = w_C Et/P$, is used for comparison purposes, and the reference result is given by a series solution by Lindberg et al. (1969) ($\overline{w}_C = -164.24$). All the predicted normalised results are listed in Table 4.12. Also provided are the results by Bucalem et al. (2000), where M6-3 and M7-3 correspond to respectively a 6-noded and a 7-noded triangular element employing an assumed strain method. The poor predictions given by the conforming meshes indicate significant locking. The accuracy of the H3O6 and H4O6 is manifested in a very coarse mesh, followed by the H3C6, H4C6, and M6-3 elements. Although M7-3 provides a prediction more close to 1.0 in the coarse 4×4 mesh, its prediction improves slower than the others, evident from persistence of the over-estimation even in a fine mesh of 12×12 elements.

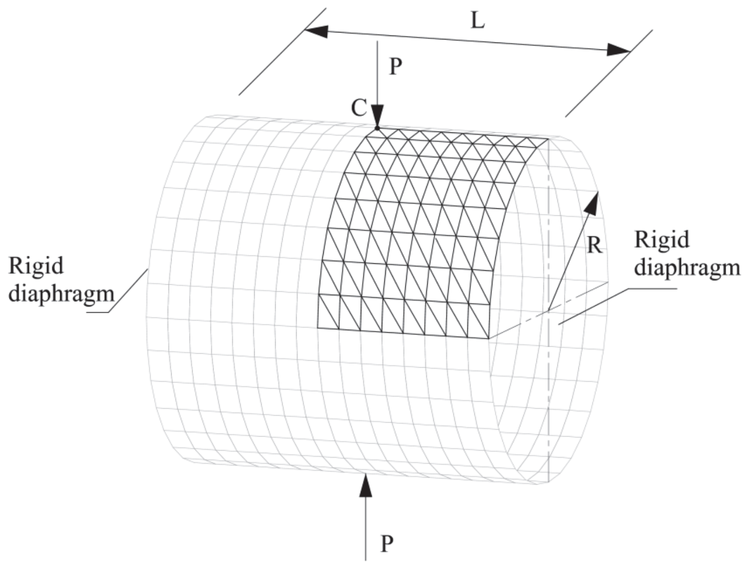

Figure 4.37: Pinched cylindrical shell supported by rigid diaphragms (triangular elements).

Table 4.12: Normalised deflections at the point of loading for the pinched cylinder problem (triangular elements).

Element	4×4	8×8	12×12
CNF6	0.143	0.486	0.743
H2O6	0.389	0.713	0.878
H3O6	0.726	0.922	0.975
H4O6	0.755	0.924	0.976
H3C6	0.599	0.890	0.964
H4C6	0.652	0.907	0.970
MITC6*	0.436	0.834	0.958
M6-3 (Bucalem et al.)	0.640	0.900	0.980
M7-3 (Bucalem et al.)	1.190	1.130	1.100

4.3.5.2 Hemispherical shell with an 18° cut-out

Another benchmark linear problem is used to assess the performance of the proposed quadratic triangular elements. A hemispherical shell with a 18° cut-out on its top, is loaded with an orthogonal set of two inward and two outward forces, 2P, as depicted in Figure 4.38. The loading, geometric and material parameters are: P = 1.0, R = 1.0, h = 0.004, E = 6.825×10^8 and ν = 0.3.

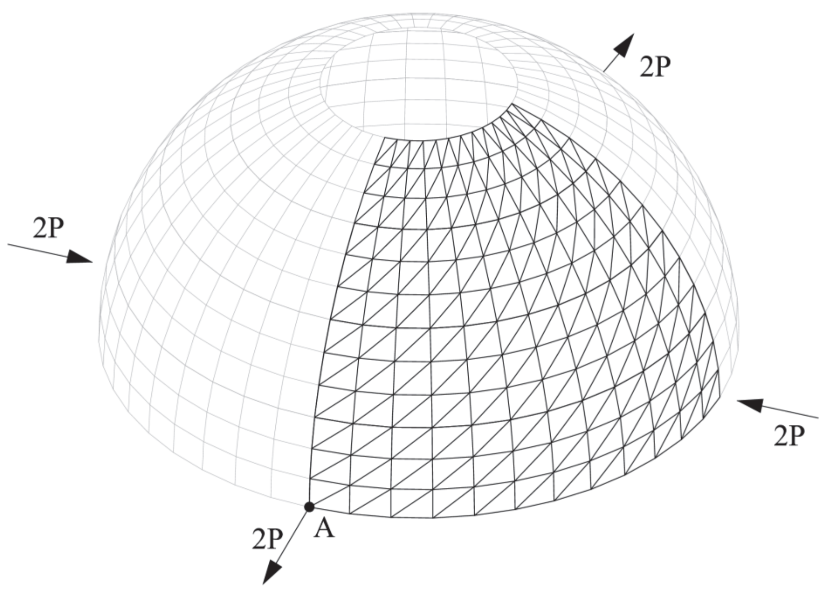

Figure 4.38: Pinched hemispherical shell with a 18° cut-off (triangular element mesh).

Due to symmetry, a quarter of the hemispherical shell is modelled with three uniform meshes (4×4, 8×8, and 12×12), and the predictions by various elements on the radial deflection at the point of loading are compared. A converged solution using MITC6, 0.09355, is used as a reference value. The displacement predictions by different elements, normalised by the reference value, are listed in Table 4.13. The results with M6-3 and M7-3 by Bucalem et al. (2000) are also presented for comparison. Again, the H4O6 and H3O6 elements provide better accuracy with coarser meshes, followed by their corrective counterparts. More distorted meshes (Figure 4.39) are also used to investigate the performance of various elements. The accuracy of all element types degrade significantly for a 4×4 mesh owing to the highly distorted element shapes. It is also noticed that an 8×8 mesh of the optimised elements, in particular H3O6 and H4O6, becomes capable of providing good accuracy.

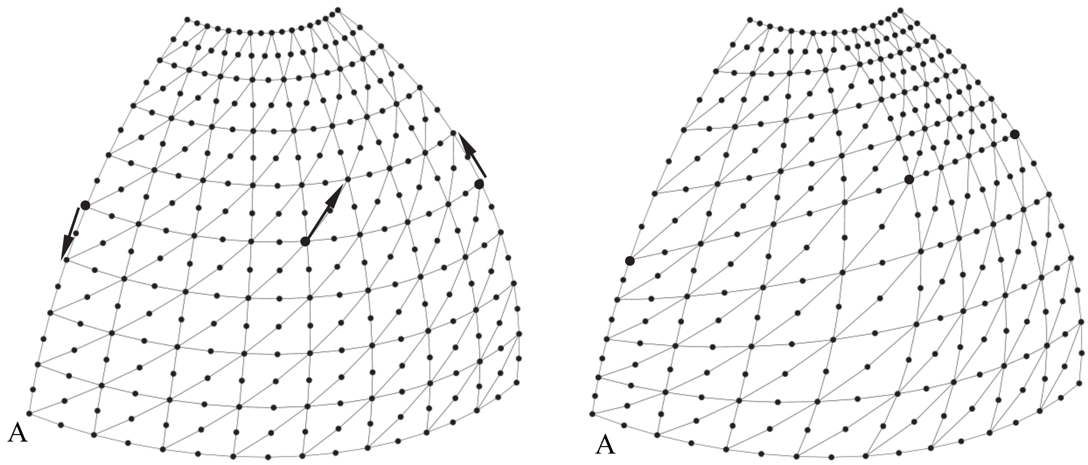

Figure 4.39: Pinched hemispherical shell with a 18° cut-off (distorted 6-noded element mesh).

Table 4.13: Normalised deflections at point A for the pinched hemispherical shell problem (triangular element meshes).

Element	Regular mesh			Distorted mesh		
	4×4	8×8	16×16	4×4	8×8	16×16
CNF6	0.011	0.131	0.419	0.006	0.070	0.256
H2O6	0.049	0.343	0.701	0.051	0.190	0.489
H3O6	0.878	0.986	0.994	0.452	0.952	0.990
H4O6	0.905	0.987	0.995	0.585	0.967	0.991
H3C6	0.692	0.977	0.993	0.209	0.912	0.985
H4C6	0.782	0.982	0.993	0.372	0.944	0.988
MITC6*	0.634	0.949	0.986	0.232	0.835	0.958
M6-3 (Bucalem et al.)	0.160	0.660	0.870	-	-	-
M7-3 (Bucalem et al.)	0.650	0.910	0.960	-	-	-

4.3.6 Large displacement problems

4.3.6.1 Annular plate problem

The same annular plate problem as presented in Section 4.1.5.1 is used here to investigate the performance of various 6-noded shell elements. The plate is modelled with two meshes of the triangular elements (16×1 and 32×2), with the 32×2 mesh depicted in Figure 4.40. Load-vertical displacement curves at Point A, B, and C with different meshes and different element types are investigated.

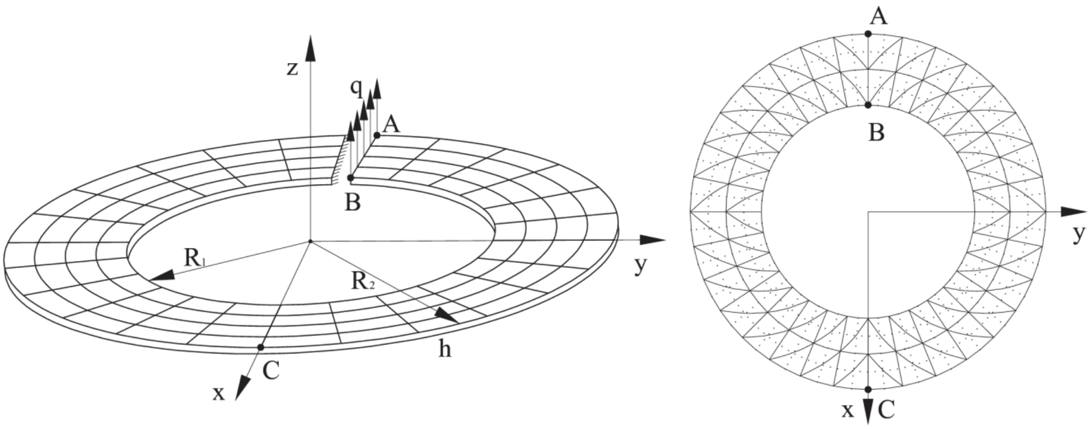

Figure 4.40: Annular plate subject to end loading (triangular element mesh).

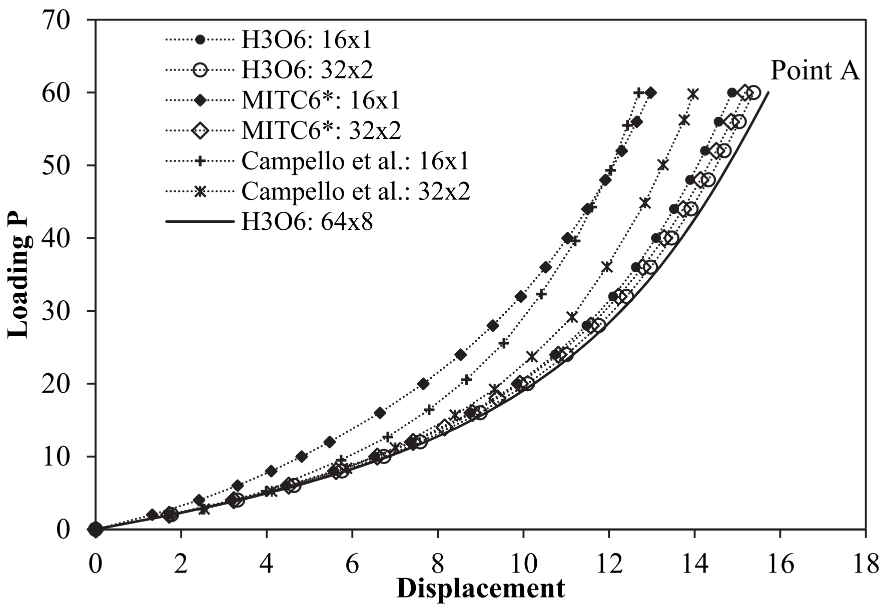

Figure 4.41: Equilibrium paths of vertical displacement at Point A for the annular plate problem (6-noded elements).

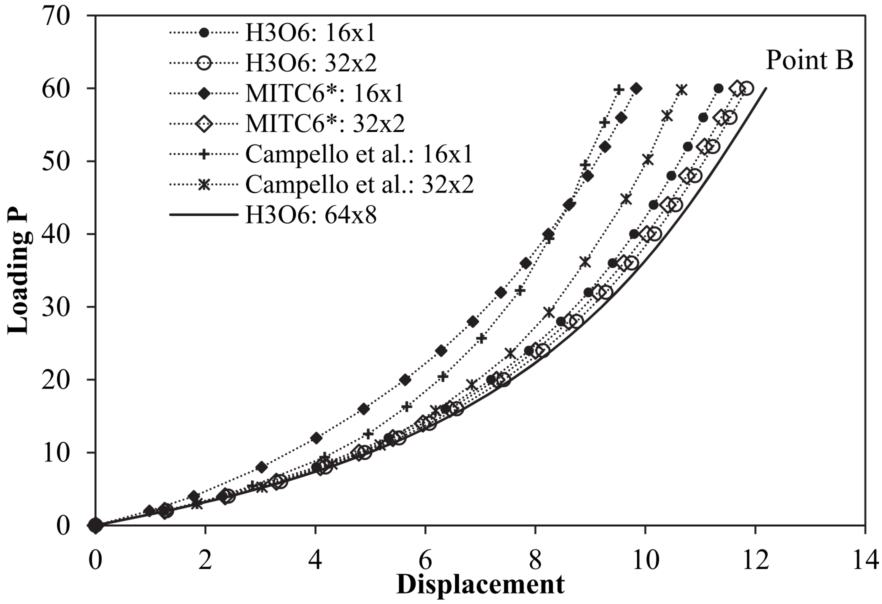

Figure 4.42: Equilibrium paths of vertical displacement at Point B for the annular plate problem (6-noded elements).

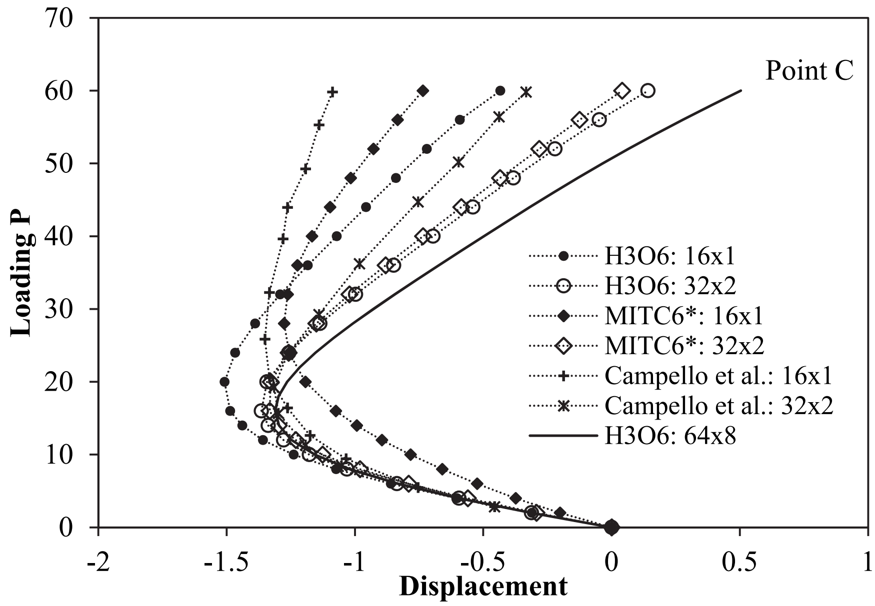

Figure 4.43: Equilibrium paths of vertical displacement at Point C for the annular plate problem (6-noded elements).

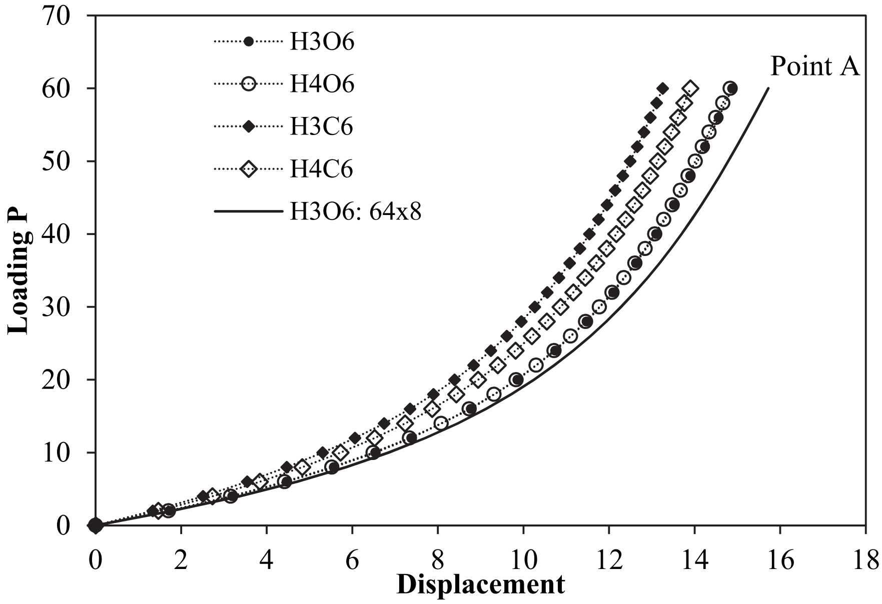

Figure 4.44: Equilibrium paths of vertical displacement at Point A with various optimised 6-noded elements for a 16×1 mesh.

Figures 4.41-4.43 depict the load-displacement curves at point A, B, and C with the H3O6 and the MITC6* elements, and a convergent solution of the H3O6 using a 64×8 mesh is taken as a reference solution. Also plotted are the results by Campello et al. (2003), who employed the same meshes with 6-noded triangular elements that are based on the enhanced displacement method. The results with the H3O6 element are much closer to the reference solution in particular in the coarser mesh. As the mesh is refined, the performance of the MITC6* element becomes almost comparable with the H3O6 element due to the decreased degree of element irregularity. Figure 4.44 also compares the load-deflection curves at point A with various optimised 6-noded elements for a 16×1 mesh. Again, the optimisation approach with an objective alternative is more accurate than the corrective alternative, while the H4O6 element yields slightly better results than the H3O6 element. Still, H3O6 is preferred due to the fewer integration points required than H4O6.

4.3.6.2 Pinched hemispherical shell problem

Figure 4.45 depicts a hemispherical shell subjected to two inward and two outward forces 90° apart at its base. The shell is made of an isotropic material with material properties of $E = 6.825\times10^{7}$ and $\nu = 0.3$. The geometric parameters of the hemispherical shell are radius $R = 10.0$ and thickness $h = 0.04$. Radial displacements at Point A and B against the concentrated force P are investigated, and the solution by Arciniega and Reddy (2007) is used as a reference solution. A quarter-model is employed due to symmetry, and two alternative meshes of 6-noded elements are employed in the model (each of the three subdomains in the quarter model are discretised into respectively a 3×3 and a 6×6 mesh pattern). The deflected configuration of the pinched hemisphere is depicted in Figure 4.46.

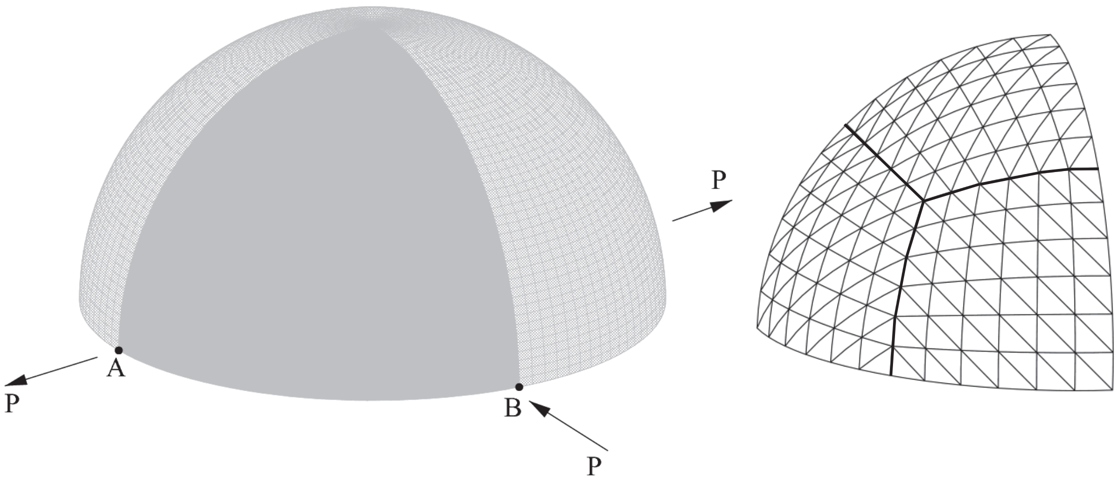

Figure 4.45: Hemispherical shell subject to symmetric concentrated forces at its base and a 6×6 mesh pattern.

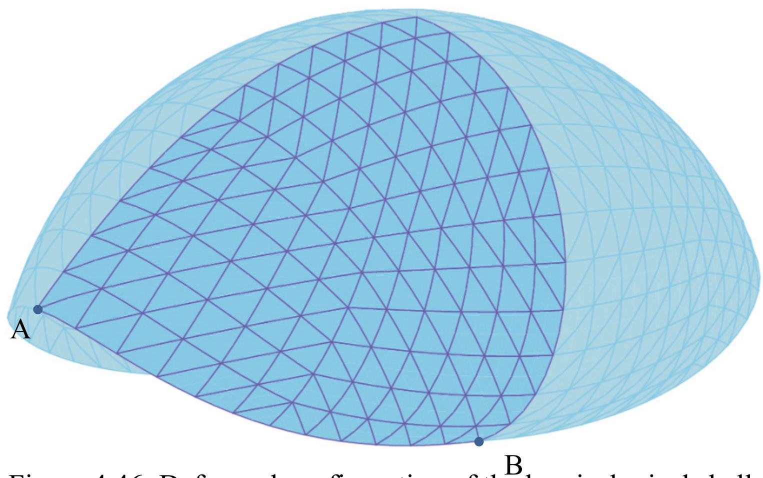

Figure 4.46: Deformed configuration of the hemispherical shell.

Results using optimised 6-noded elements are shown in Figure 4.47 for two meshes. The conforming element CNF6 exhibits considerable inaccuracy, persisting even in the finer mesh, which is mainly attributed to membrane locking. As stated before, the H3O6 and H4O6 elements exhibit superior performance to their corrective counterparts in the coarser mesh, and the discrepancy reduces with mesh refinement. In Figure 4.48, the H3O6 results are compared against the MITC6* solution, which again indicates the effectiveness of the H3O6 element in addressing locking in particular for a coarse mesh.

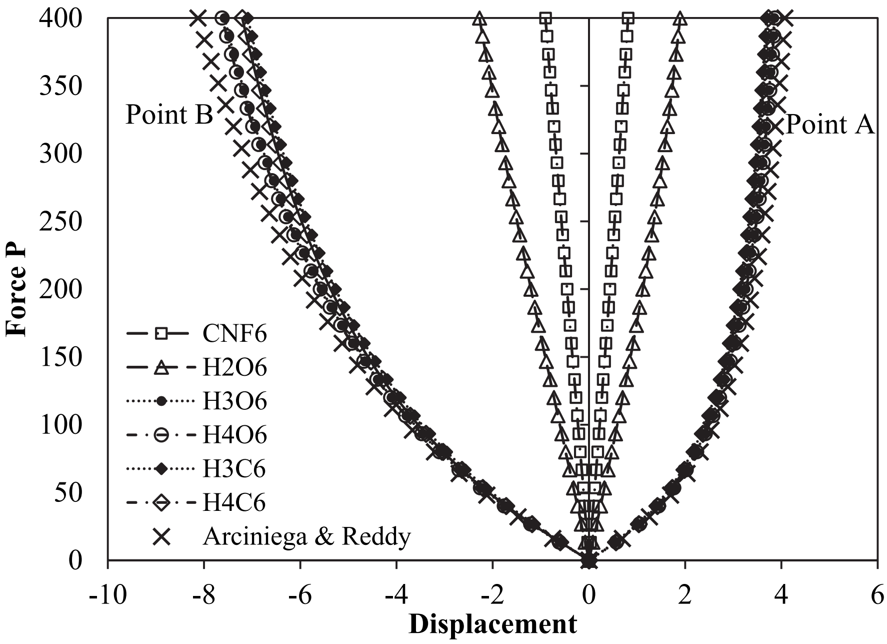

a. 3×3 mesh

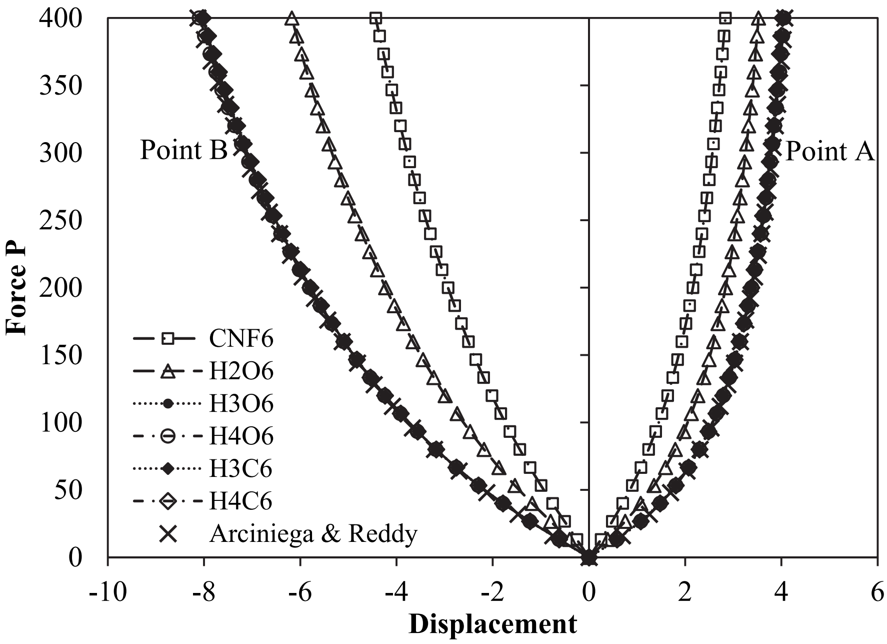

b. 6×6 mesh

Figure 4.47: Load-displacement curves of the radial displacements with different meshes of various optimised 6-noded elements.

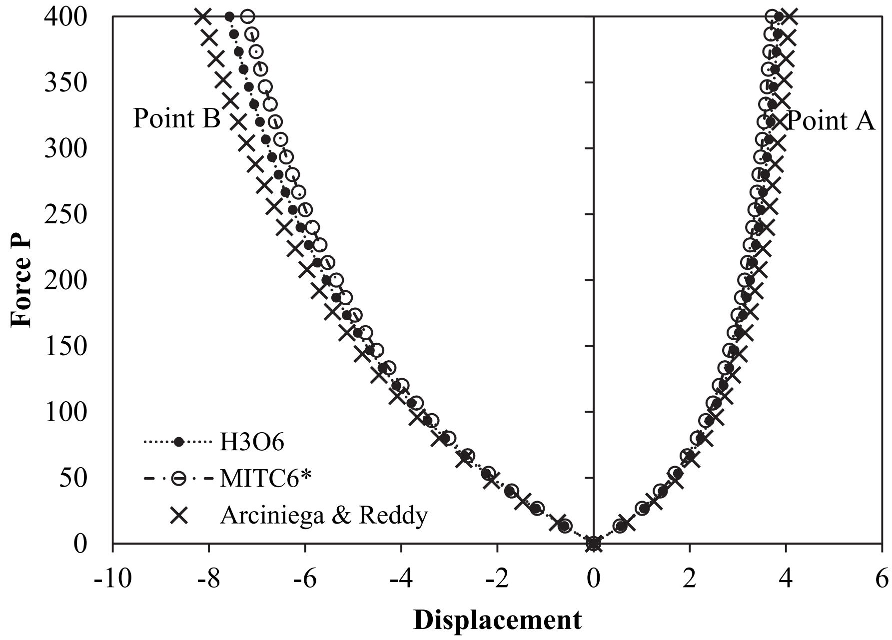

a. 3×3 mesh

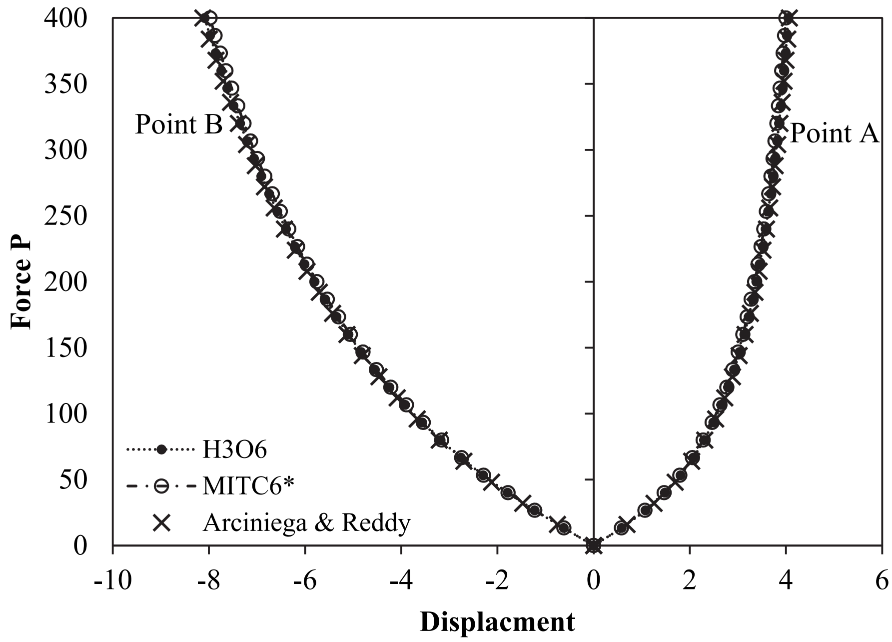

b. 6×6 mesh

Figure 4.48: Load-displacement curves of the radial displacements with different meshes of H3O6 and MITC6* elements.

4.4 Summary

In this chapter, the co-rotational formulations of curved quadrilateral and triangular shell elements presented in Chapter 3 have been applied using ADAPTIC. For comparison purposes, shell elements based on the MITC formulation are also considered, where the strain sampling and mapping are undertaken following respectively the original MITC elements but with distinct strain-displacement relationship and other assumptions, as detailed in Appendix B.

A series of fundamental element tests, including zero strain energy tests, constant strain patch tests and isotropic element tests, are conducted to examine the performance of the newly developed formulation based on hierarchic optimisation. Tests are performed to investigate the convergence rates of the proposed quadrilateral and triangular elements. Several linear and geometrically nonlinear benchmark problems are also presented to assess the accuracy and efficiency of the elements.

Results show that the optimised elements all pass the fundamental element tests, whereas the MITC elements may not pass constant strain tests, in particular for irregular element meshes. Nevertheless, both the optimised elements and the MITC* elements exhibit a significant relief of shear locking and membrane locking. Among the optimised elements, the H2O9 and H2O6 elements, which do not employ corrective hierarchic strain modes in the optimisation, result in degraded performance for curved shell problems compared to elements with hierarchic corrections, which highlights the importance of the inclusion of higher-order strain modes in the optimisation. Furthermore, for the same hierarchic correction order, the objective alternative yields superior results than the corrective alternative in terms of both accuracy and convergence rate, with the objective alternative based on third order hierarchic optimisation (H3O9 and H3O6 elements) exhibiting both accuracy and efficiency. The H3O9 and H3O6 elements also have comparable or even better accuracy than the mixed elements based on the MITC formulations, mainly due to effective relief of distortion locking.

CHAPTER 5

Proposed Laminated Shell Model

5.1 Introduction

This chapter starts with a presentation of a kinematic model for sandwich shells, with specific reference to the through-thickness variation of displacement fields and the transverse shear strains. The efficiency and accuracy of the sandwich model is verified using a one-dimensional (1D) beam problem by comparing the results with other sandwich models. It is important to note that although the proposed kinematic description for sandwich shells is utilised in this research for analysing LG structures, it can also be applied to many other sandwich structures with symmetric and asymmetric lay-ups. Upon verification of the sandwich shell model, a generalisation to multi-layer shells with an alternating stiff/soft lay-up is presented, and this is again verified using 1D beam problems associated with laminated structures. Similar to the special case of sandwich shells, the proposed general kinematic model is applicable to not only multi-layer LG structures but also other laminations with an alternating stiff/soft lay-up.

It is worth noting that although the kinematic descriptions of sandwich and laminated shells in this chapter are initially presented for plate problems, they are equally applicable to local formulations of shallow shells, as will be elaborated in Chapter 6 for application to shallow shell elements. Furthermore, through incorporation within a co-rotational framework, they are also applicable to the nonlinear analysis of general curved shells, which will also be elaborated in Chapter 6.

5.2 Kinematic description for sandwich shells

Figure 5.1 depicts the sandwich model for a plate along with the local coordinates, where the x- and y-axes are located at the middle surface while the z-axis is normal to the plate, and where each layer is identified by a unique index.

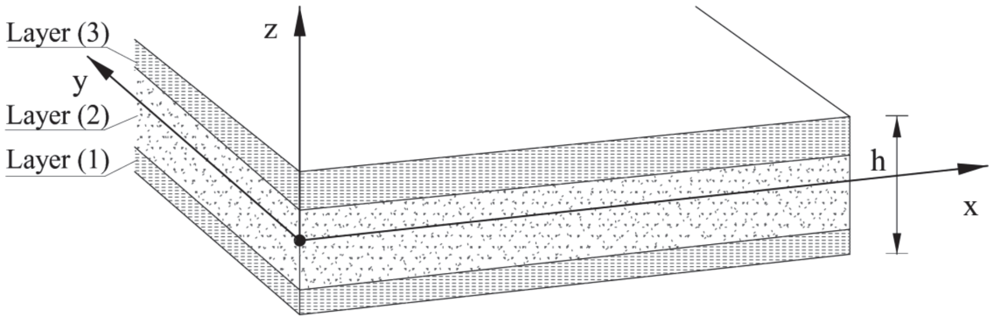

Figure 5.1: Three-layered sandwich plate and local coordinate system.

5.2.1 Zigzag displacement fields

In this sandwich plate model, a piecewise linear variation of planar displacements in the z direction is assumed, thus readily satisfying C^0-continuity at laminar interfaces. Accordingly, the through-thickness distribution of the planar displacements can be decomposed into four independent displacement modes $\Lambda_i(z)\,(i=1\rightarrow 4)$ (Figure 5.2), including a constant and a linear mode, Λ_1 and Λ_2, in accordance with the Reissner-Mindlin kinematic hypothesis, as well as two zigzag modes, Λ_3 and Λ_4, accounting for the zigzag effect. Λ_3 and Λ_4 are both orthogonal to the constant and linear modes while associated with respectively different and identical rotations of the normal in the two face sheets; these are expressed as:

$$\Lambda_3(z)=\begin{cases}\hat{a}_3^{(1)}z+\hat{b}_3^{(1)}, & z\in\left[h_{1-},h_{1+}\right]\\ \hat{a}_3^{(2)}z+\hat{b}_3^{(2)}, & z\in\left[h_{2-},h_{2+}\right]\\ \hat{a}_3^{(3)}z+\hat{b}_3^{(3)}, & z\in\left[h_{3-},h_{3+}\right]\end{cases} \tag{5.1}$$

$$\Lambda_4(z)=\begin{cases}\hat{a}_4^{(1)}z+\hat{b}_4^{(1)}, & z\in\left[h_{1-},h_{1+}\right]\\ \hat{a}_4^{(2)}z+\hat{b}_4^{(2)}, & z\in\left[h_{2-},h_{2+}\right]\\ \hat{a}_4^{(3)}z+\hat{b}_4^{(3)}, & z\in\left[h_{3-},h_{3+}\right]\end{cases} \tag{5.2}$$

in which h_- and h_+ denote the values of z at the bottom and top of the cross-section, respectively; h_{k-} and h_{k+} refer to the values of z at the bottom and top of layer (k), respectively; and expressions of $\hat{a}_i^{(k)}$ and $\hat{b}_i^{(k)}$ (i =3,4) are provided in Appendix C.

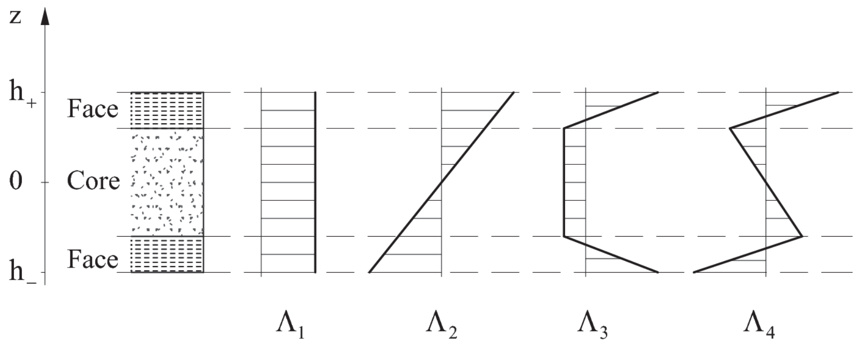

Figure 5.2: Four through-thickness displacement modes for sandwich plate.

The variation of planar displacements under bending is investigated by performing a 2D plane-stress analysis of a sandwich beam with a soft core, which indicates that the two stiff layers have almost identical rotations of their respective normals, whereas the core can have a different rotation. Therefore, following on from the observed cross-sectional behaviour, the contribution from Λ_3 is neglected, and $\Lambda_4(z)$ is proposed as a zigzag function specific to sandwich structures, applicable regardless of cross-sectional symmetry, which is re-denoted as $\Lambda(z) \equiv \Lambda_4(z)$.

It is important to note that for symmetrically laminated sandwich structures, the zigzag function $\Lambda(z)$ is equivalent to Murakami's zigzag function (MZZF) (Murakami, 1986), which is defined as:

$$f(z) = (-1)^k \zeta^{(k)}, \quad \zeta^{(k)} = \frac{2(z - z^{(k)})}{h_k}, \quad z \in [h_{k-}, h_{k+}] \tag{5.3}$$

where h_k is the thickness of layer (k), and $z^{(k)}$ is the extracted value of z on the middle surface of layer (k).

However, if the sandwich plate is asymmetrically laminated, $\Lambda(z)$ is more effective than the MZZF, as will be illustrated in Section 5.3.2.

The addition of the zigzag function to the Reissner-Mindlin planar displacements yields the following planar displacements:

$$u_\alpha(x,y,z) = u_{\alpha 0}(x,y) + z\theta_\alpha(x,y) + \Lambda(z)\vartheta_\alpha(x,y) \quad (\alpha = x,y) \tag{5.4}$$

where $u_{\alpha 0}$ are the planar displacement fields along the x- or y-axis evaluated on the middle surface; θ_α are the components of the normal vector along the x- or y-axis in the absence of zigzag displacements; ϑ_α are the additional fields associated with the proposed zigzag function along the x- or y-axis. The transverse displacement is assumed to be constant through the plate thickness, and is thus denoted by $u_{z0}(x,y)$.

5.2.2 Kinematics of individual layers

Each constitutive layer of the sandwich model is regarded as a pseudo plate. At layer (k) ($k = 1 \to 3$), the translational displacements on its middle surface are obtained as:

$$u_\alpha^{(k)} = u_{\alpha 0} + z^{(k)}\theta_\alpha + \Lambda^{(k)}\vartheta_\alpha \quad (\alpha = x,y) \tag{5.5}$$

$$u_z^{(k)} = u_{z0} \tag{5.6}$$

where $\Lambda^{(k)} \equiv \Lambda(z^{(k)})$ represents the extracted value of the zigzag function $\Lambda(z)$ on the middle surface of layer (k); $z^{(k)}$ is the extracted value of z on the middle surface of layer (k).

The rotational displacements of layer (k) are derived by taking the first derivatives of the planar displacements with respect to z:

$$\theta_\alpha^{(k)} = \left.\frac{\partial u_\alpha}{\partial z}\right|_{z^{(k)}} = \theta_\alpha + \lambda^{(k)}\vartheta_\alpha, \quad \lambda^{(k)} = \left.\frac{\partial \Lambda}{\partial z}\right|_{z^{(k)}} \quad (\alpha = x,y) \tag{5.7}$$

Accordingly, the following relationship holds at each layer:

$$\mathbf{u}^{(k)} = \mathbf{T}_c^{(k)}\mathbf{u}_c + \mathbf{T}_a^{(k)}\mathbf{u}_a \tag{5.8}$$

$$\mathbf{T}_c^{(k)} = \begin{bmatrix} 1 & 0 & 0 & z^{(k)} & 0 \\ 0 & 1 & 0 & 0 & z^{(k)} \\ 0 & 0 & 1 & 0 & 0 \\ 0 & 0 & 0 & 1 & 0 \\ 0 & 0 & 0 & 0 & 1 \end{bmatrix} \tag{5.9}$$

$$\mathbf{T}_a^{(k)} = \begin{bmatrix} \Lambda^{(k)} & 0 \\ 0 & \Lambda^{(k)} \\ 0 & 0 \\ \lambda^{(k)} & 0 \\ 0 & \lambda^{(k)} \end{bmatrix} \tag{5.10}$$

where $\mathbf{u}_c = \left\langle u_{x0}, u_{y0}, u_{z0}, \theta_x, \theta_y \right\rangle^T$ are the basic local displacement fields consistent with the Reissner-Mindlin formulation; $\mathbf{u}_a = \left\langle \vartheta_x, \vartheta_y \right\rangle^T$ are the additional displacement fields associated with the zigzag function $\Lambda(z)$; and $\mathbf{u}^{(k)} = \left\langle u_x^{(k)}, u_y^{(k)}, u_z^{(k)}, \theta_x^{(k)}, \theta_y^{(k)} \right\rangle^T$ are the displacement fields for layer (k) treated as a pseudo plate.

The strain state within each layer (k) is fully determined by the membrane strains $\boldsymbol{\varepsilon}_m^{(k)}$, bending generalised strains $\boldsymbol{\varepsilon}_b^{(k)}$, and transverse shear strains $\boldsymbol{\varepsilon}_s^{(k)}$, which are expressed at the layer level as follows:

$$\boldsymbol{\varepsilon}_m^{(k)} = \begin{Bmatrix} \varepsilon_x^{(k)} \\ \varepsilon_y^{(k)} \\ \gamma_{xy}^{(k)} \end{Bmatrix} = \begin{Bmatrix} \dfrac{\partial u_x^{(k)}}{\partial x} \\ \dfrac{\partial u_y^{(k)}}{\partial y} \\ \dfrac{\partial u_x^{(k)}}{\partial y} + \dfrac{\partial u_y^{(k)}}{\partial x} \end{Bmatrix} + \begin{Bmatrix} \dfrac{1}{2}\left(\dfrac{\partial z_0}{\partial x} + \dfrac{\partial u_z^{(k)}}{\partial x}\right)^2 - \dfrac{1}{2}\left(\dfrac{\partial z_0}{\partial x}\right)^2 \\ \dfrac{1}{2}\left(\dfrac{\partial z_0}{\partial y} + \dfrac{\partial u_z^{(k)}}{\partial y}\right)^2 - \dfrac{1}{2}\left(\dfrac{\partial z_0}{\partial y}\right)^2 \\ \left(\dfrac{\partial z_0}{\partial x} + \dfrac{\partial u_z^{(k)}}{\partial x}\right)\left(\dfrac{\partial z_0}{\partial y} + \dfrac{\partial u_z^{(k)}}{\partial y}\right) - \left(\dfrac{\partial z_0}{\partial x}\right)\left(\dfrac{\partial z_0}{\partial y}\right) \end{Bmatrix} \tag{5.11}$$

$$\boldsymbol{\varepsilon}_b^{(k)} = \begin{Bmatrix} \kappa_x^{(k)} \\ \kappa_y^{(k)} \\ \kappa_{xy}^{(k)} \end{Bmatrix} = \begin{Bmatrix} \dfrac{\partial \theta_x^{(k)}}{\partial x} \\ \dfrac{\partial \theta_y^{(k)}}{\partial y} \\ \dfrac{\partial \theta_x^{(k)}}{\partial y} + \dfrac{\partial \theta_y^{(k)}}{\partial x} \end{Bmatrix} \tag{5.12}$$

$$\boldsymbol{\varepsilon}_s^{(k)} = \begin{Bmatrix} \gamma_{xz}^{(k)} \\ \gamma_{yz}^{(k)} \end{Bmatrix} = \begin{Bmatrix} \theta_x^{(k)} + \dfrac{\partial u_z^{(k)}}{\partial x} \\ \theta_y^{(k)} + \dfrac{\partial u_z^{(k)}}{\partial y} \end{Bmatrix} \tag{5.13}$$

in which z_0 represents the offset of the shell mid-surface along the z-axis, thus generalising the kinematics of flat plates to shallow shells; in this respect, the kinematic expressions presented previously remain unaffected for a shallow shell with z taken as zero along the shell mid-surface. It is worth noting that quadratic terms of the membrane strains in (5.11) take into account the effect of shell curvature, which are not necessary within a co-rotational approach but enable better accuracy with coarser meshes.

5.2.3 Through-thickness distribution of transverse shear strains

The face-to-core stiffness ratio (FCSR) plays an important role in the through-thickness distribution of the transverse shear stresses and strains. To illustrate this point, sandwich beams with various FCSRs have been modelled under bending with 2D plane-stress analysis, where schematic distributions of the transverse shear stress and strain with different FCSRs are depicted in Figure 5.3. Clearly, the distribution of the transverse shear stress changes significantly with different FCSR values. However, the transverse shear strain distribution shows that for the considered FCSR range, the core sustains much larger strains than the face sheets and exhibits a near constant distribution through the constitutive layer. In addition, for a relatively small FCSR where the face sheets and the core have comparable material properties, the associated transverse shear strains then have comparable magnitude with the distribution in the face sheets exhibiting a quasi-linear pattern. Based on the observed pattern of transverse shear strains, it is assumed that in the face sheets the shear strain varies linearly from zero at the outer surface, whereas for the core the shear strain remains constant, as shown in Figure 5.4. The through-thickness distribution of the assumed transverse shear strain can thus be expressed as follows:

$$\boldsymbol{\varepsilon}_{s,AS}^{(k)} = \omega^{(k)} F_k(z) \boldsymbol{\varepsilon}_s^{(k)}, \quad z \in \left[h_{k-}, h_{k+}\right] \tag{5.14}$$

where $\omega^{(k)}$ is the shear correction factor of layer (k), and $F_k(z)$ is the assumed distribution of transverse shear strains at layer (k):

$$F_1(z) = 1 + \frac{2\left(z - z^{(1)}\right)}{h_1}, \quad F_2(z) = 1, \quad F_3(z) = 1 - \frac{2\left(z - z^{(3)}\right)}{h_3} \tag{5.15}$$

The shear correction factors $\omega^{(k)}$ (k=1→3) can be determined from energy equivalence at the generalised stress/strain and material stress/strain levels, considering the equivalence of the generalised shear stresses and the resultant shear forces from equilibrium considerations. The employment of equivalence in transverse shear strain energy at each layer gives:

$$\boldsymbol{\varepsilon}_s^{(k)T} \mathbf{Q}_{AS}^{(k)} = \int_{h_{k-}}^{h_{k+}} \boldsymbol{\varepsilon}_{s,AS}^{(k)T} \boldsymbol{\sigma}_{s,AS}^{(k)} dz \tag{5.16}$$

where $\boldsymbol{\sigma}_{s,AS}^{(k)}$ are material transverse shear stresses associated with $\boldsymbol{\varepsilon}_{s,AS}^{(k)}$, and $\mathbf{Q}_{AS}^{(k)}$ are the corresponding resultant transverse shear forces, expressed as:

$$\mathbf{Q}_{AS}^{(k)} = \int_{h_{k-}}^{h_{k+}} \boldsymbol{\sigma}_{s,AS}^{(k)} dz \tag{5.17}$$

Substituting (5.14)-(5.15) into (5.16) and employing a linear constitutive relationship yield $\omega^{(1)} = \omega^{(3)} = \frac{3}{4}$ and $\omega^{(2)} = 1$.

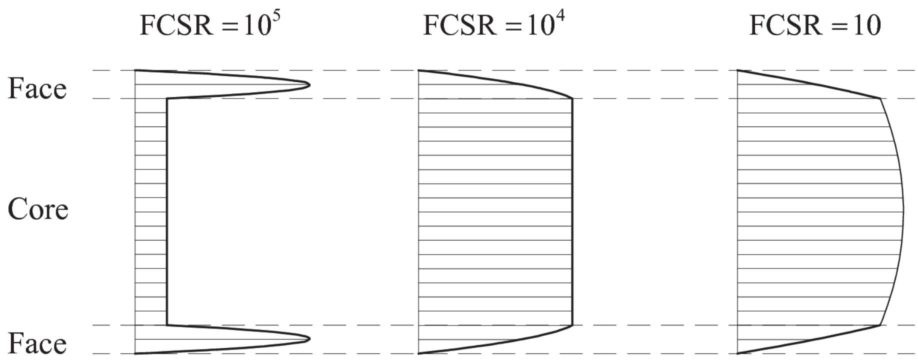

a. transverse shear stress

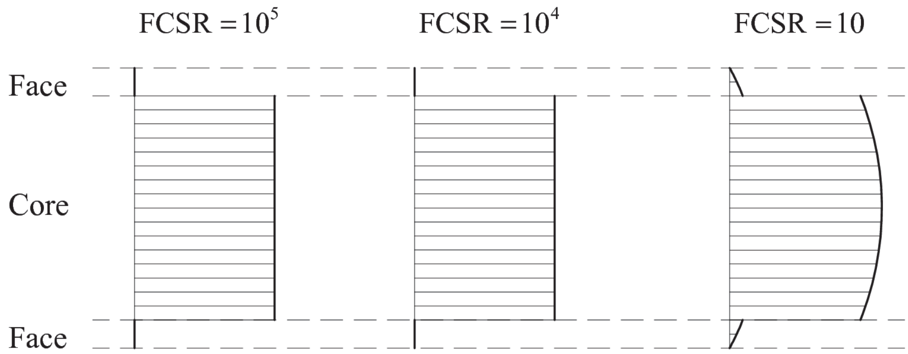

b. transverse shear strain

Figure 5.3: Through thickness distribution of transverse shear stress/strain with various FCSRs (3 layers).

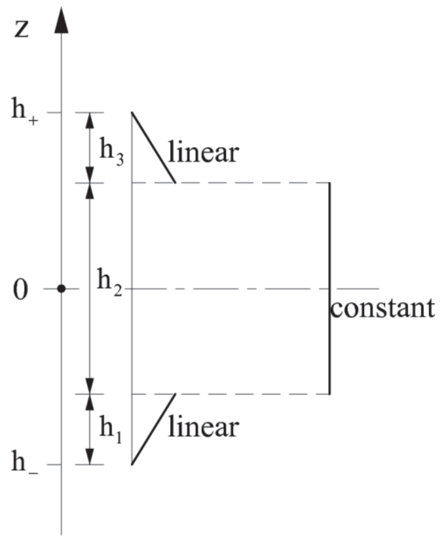

Figure 5.4: Assumed through-thickness distribution of transverse shear strain for sandwich model.

It is important to note that the proposed approach is based on an assumed through-thickness distribution for the transverse shear strains rather than transverse shear stresses, thus no interlayer continuity constraints are imposed on the shear stress. In addition to offering a realistic representation of the exact solution, albeit with discontinuous transvers shear stresses, this assumed strain distribution is much more practical than an assumed stress distribution when considering material nonlinearity, where the continuity requirement on transverse shear stresses necessitates an iterative solution procedure which imposes additional computational demands. Combined with the use of only two additional displacement fields associated with the proposed zigzag function, an effective sandwich shell model is obtained, which is applicable to both symmetric and asymmetric cross-sections, and which achieves good levels of accuracy with high computational efficiency, as demonstrated in the following section.

5.3 Verification of through-thickness kinematics

A three-point bending problem of a sandwich beam is used here to illustrate the effectiveness and efficiency of the proposed sandwich model. As depicted in Figure 5.5, a simply-supported sandwich beam, with length L= 0.5 and depth h = 0.01, is loaded with a concentrated transverse force P=–100 at midspan. The isotropic material properties of the face sheets are identical, with Young's modulus $E^{(1)} = E^{(3)} = 7\times10^{10}$ and Poisson's ratio $\nu^{(1)} = \nu^{(3)} = 0.3$. The Young's modulus and shear modulus for the core are obtained by dividing those of face sheets by the FCSR which is assumed to be respectively 1, 10, 10^2, 10^3, and 10^4. This problem is modelled with 1D 3-noded sandwich beam elements employing the proposed zigzag displacement field and transverse shear strain distribution, where shear locking is eliminated by using two-point strain mapping of the transverse shear strain. The central deflection and stress components at ¼ span are investigated:

$$\bar{u}_z = u_{z0}\left(L/2, 0\right), \quad \bar{\sigma}_x = \sigma_x\left(L/4, h/2\right), \quad \bar{\sigma}_{xz} = \sigma_{xz}\left(L/4, 0\right)$$

where the convergent solution obtained from 2D plane-stress analysis is used as a reference. Note that this is a linear elastic problem of a straight sandwich beam, thus a linear strain-displacement relationship is considered without the inclusion of the second-order terms given in (5.11).

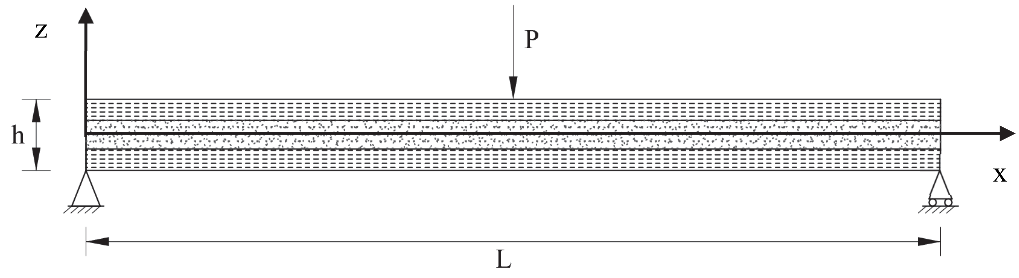

Figure 5.5: A simply-supported sandwich beam loaded with a transverse force at the midspan.

5.3.1 Sandwich beam with symmetric lay-up

Here the performance of the proposed sandwich model is investigated for a symmetric lay-up, where the thicknesses of the three layers are assumed to be identical: $h_1 = h_2 = h_3 = h/3$. A uniform mesh of 32 sandwich beam elements which employ the proposed zigzag displacements and transverse shear strain distribution provides a convergent solution, denoted as 'Present'. By restraining all additional displacement variables in the sandwich beam model, a FSDT solution is also obtained, although the assumed through-thickness distribution of the transverse shear strain proposed in this work is employed. This problem has been analysed by Hu et al. (2008) in the evaluation of various lamination theories, where the results of Model-2, Model-5 and Model-6 are provided in Table 5.1 for comparison. It is worth noting that the 'HSDT' model, which corresponds to Model-2, is based on Reddy's kinematic assumptions. The 'IC-ZZT' and the 'ID-ZZT' model, corresponding to Model-5 and Model-6, are respectively a zigzag formulation with an assumed continuous transverse shear stress based on Touratier kinematic assumptions, and a LW theory without imposing the continuity constraints on transverse shear stress, where the face sheets employ the Kirchhoff assumption and the core employs the Reissner-Mindlin hypothesis.

Table 5.1: Evaluation of different models for a symmetrically laminated sandwich beam with various FCSRs.

Results		Reference value	FSDT	HSDT (Hu et al.)	IC-ZZT (Hu et al.)	ID-ZZT (Hu et al.)	Present
FCSR=10^4	$\bar{u}_z$	-2.24E-04	-4.71E-05	-4.72E-05	-2.23E-04	-2.23E-04	-2.23E-04
	$\bar{\sigma}_x$	-6.90E+05	-3.89E+05	-3.89E+05	-6.90E+05	-6.90E+05	-6.90E+05
	$\bar{\sigma}_{xz}$	-4.64E+03	-7.50E-01	-1.77E+00	-4.63E+03	-4.63E+03	-4.63E+03
FCSR=10^3	$\bar{u}_z$	-7.32E-05	-4.71E-05	-4.72E-05	-7.31E-05	-7.31E-05	-7.32E-05
	$\bar{\sigma}_x$	-3.98E+05	-3.89E+05	-3.89E+05	-3.98E+05	-3.98E+05	-3.98E+05
	$\bar{\sigma}_{xz}$	-6.79E+03	-7.50E+00	-1.77E+01	-6.76E+03	-6.76E+03	-6.76E+03
FCSR=10^2	$\bar{u}_z$	-4.99E-05	-4.71E-05	-4.71E-05	-4.99E-05	-4.99E-05	-4.99E-05
	$\bar{\sigma}_x$	-3.89E+05	-3.89E+05	-3.89E+05	-3.89E+05	-3.89E+05	-3.89E+05
	$\bar{\sigma}_{xz}$	-6.93E+03	-7.46E+01	-1.75E+02	-6.93E+03	-6.93E+03	-6.93E+03
FCSR=10^1	$\bar{u}_z$	-4.72E-05	-4.69E-05	-4.70E-05	-4.72E-05	-4.72E-05	-4.72E-05
	$\bar{\sigma}_x$	-3.88E+05	-3.88E+05	-3.88E+05	-3.88E+05	-3.88E+05	-3.88E+05
	$\bar{\sigma}_{xz}$	-7.00E+03	-7.14E+02	-1.56E+03	-7.01E+03	-6.95E+03	-6.95E+03
FCSR=10^0	$\bar{u}_z$	-4.53E-05	-4.53E-05	-4.53E-05	-4.53E-05	-4.53E-05	-4.53E-05
	$\bar{\sigma}_x$	-3.75E+05	-3.75E+05	-3.75E+05	-3.75E+05	-3.75E+05	-3.75E+05
	$\bar{\sigma}_{xz}$	-7.64E+03	-5.00E+03	-7.50E+03	-7.73E+03	-7.22E+03	-7.22E+03

It is clear from Table 5.1 that the FSDT results show significant inaccuracy except for a unit FCSR value. The HSDT results also lack accuracy in the cases of very soft cores with relatively large FCSR. The proposed model, along with the IC-ZZT and ID-ZZT models are equally accurate for all the considered scenarios, which verifies the ability of the proposed zigzag function in capturing the cross-sectional warping of sandwich structures and confirms the feasibility of neglecting the continuity of transverse shear stresses in such problems.

Figure 5.6 compares the through-thickness distributions of the transverse shear stress at L/4 for the three models with different FCSR values. Clearly, all models provide almost the same predictions on the shear stress distribution in the core. However, the distributions in the face sheets show significant discrepancy. The IC-ZZT model provides a continuous curvilinear distribution, whereas the ID-ZZT gives zero shear stress in the face sheets due to the employment of Kirchhoff assumption in the face sheets. The proposed model yields a piecewise linear distribution of the transverse shear stress, which provides an adequate fit of the real distribution for an FCSR of 10 but indicates a big discrepancy for an FCSR of 10^4. Nevertheless, as noted in the previous section, for sandwich structures that consist of a soft core, the core offers the dominant contribution to the transverse shear strain energy whereas the contribution from the face sheets is not of significance. On the other hand, for sandwich structures where the core is of a comparable stiffness with the face sheets, the contribution from the faces to the overall transverse shear stress becomes important. In this case, the proposed piecewise linear distribution of the transverse shear strain still provides a good approximation of the real shear stress distribution, as is illustrated in Figure 5.6.a. Therefore, the proposed transverse shear strain distribution is applicable to sandwich structures with a wide range of FCSRs. Furthermore, the omission of constraints on inter-laminar continuity of the transverse shear stresses leads to a less coupled multi-layer system, which enhances computational efficiency.

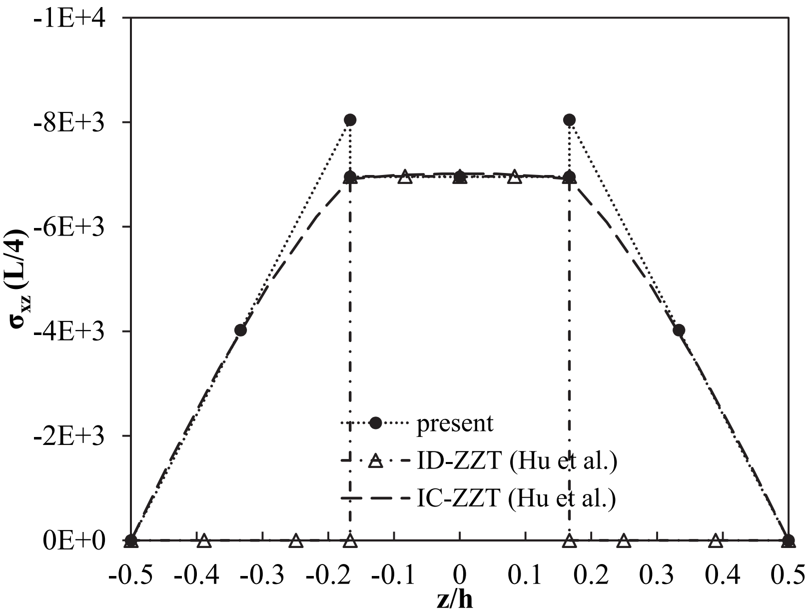

a. FCSR=10

Figure 5.6: Through-thickness distribution of transverse shear stress $\bar{\sigma}_{xz}$ (Cont'd…).

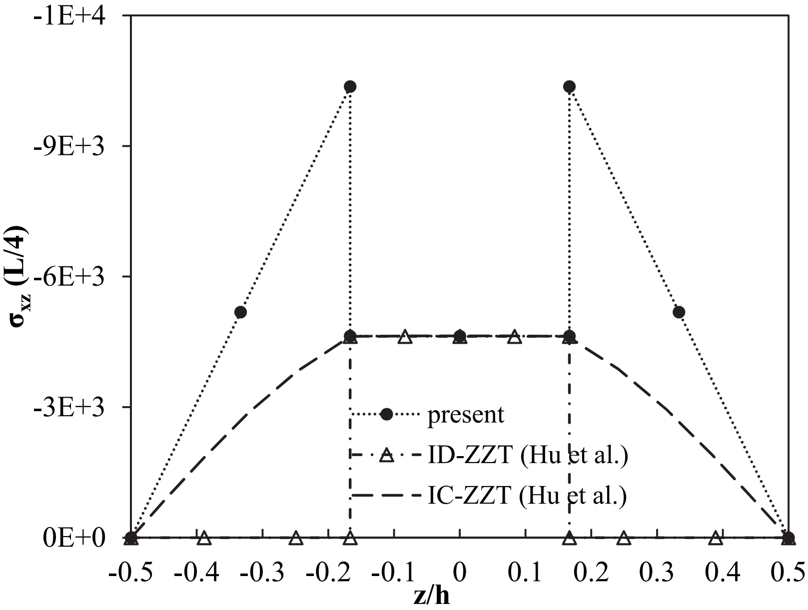

b. FCSR=10^4

Figure 5.6: Through-thickness distribution of transverse shear stress $\overline{\sigma}_{xz}$.

5.3.2 Sandwich beam with asymmetric lay-up

In order to demonstrate the effectiveness of the proposed zigzag function $\Lambda(t)$ in the analysis of asymmetric cross-sections, the proposed formulation is compared against two formulations, denoted as 'MZZF1' and 'MZZF2', which add the MZZF to planar displacements which are respectively first- and second-order polynomials in z. The through-thickness variation of the transverse displacement is neglected in both models. The proposed discrete transverse shear strain distribution is employed for all formulations. Two asymmetric lay-ups are considered: (1) $h_3/h_1 = 2$ and $h_2/h_1 = 7$, and (2) $h_3/h_1 = 2$ and $h_2/h_1 = 2$.

The relative errors of the displacement and stress predictions with the considered models are shown in Table 5.2, from which it is clear that the proposed zigzag function provides high accuracy with various lay-ups and FCSR values. In contrast, the MZZF1 formulation, which has the same number of displacement variables as the proposed formulation, is accurate for relatively small FCSR values only. By adding a quadratic polynomial to the through-thickness distribution, the MZZF2 formulation improves on the MZZF1 results for larger FCSR values, but still lacks accuracy for a larger FCSR, which implies the need for even higher-order z expansions and hence more zigzag displacement variables. Taking into account the number of additional zigzag displacement variables for each of the formulations (one for 'present' and 'MZZF1', and two for 'MZZF2'), it is evident that the proposed zigzag function $\Lambda(t)$ exhibits better efficiency than the MZZF for asymmetrically laminated sandwich structures.

Table 5.2: Evaluation of different models for an asymmetrically laminated sandwich beam with various FCSRs.

Results		Case 1 ($h_3/h_1 = 2$, $h_2/h_1 = 7$)				Case 2 ($h_3/h_1 = 2$, $h_2/h_1 = 2$)			
		Reference value	Relative Error			Reference value	Relative Error		
			Present	MZZF1	MZZF 2		Present	MZZF 1	MZZF 2
FCSR=10^4	$\bar{u}_z$	-4.43E-04	0.00%	82.23%	1.13%	-2.39E-04	0.00%	77.54%	1.57%
	$\bar{\sigma}_x$	-6.38E+05	0.00%	23.26%	0.04%	-7.92E+05	0.00%	52.08%	3.98%
	$\bar{\sigma}_{xz}$	-5.47E+03	0.00%	99.61%	4.95%	-4.31E+03	0.00%	99.66%	3.09%
FCSR=10^3	$\bar{u}_z$	-1.19E-04	0.00%	33.85%	0.53%	-8.08E-05	0.00%	33.62%	0.05%
	$\bar{\sigma}_x$	-4.90E+05	0.00%	0.02%	0.00%	-3.92E+05	0.01%	3.05%	0.24%
	$\bar{\sigma}_{xz}$	-5.79E+03	0.01%	96.47%	5.07%	-6.37E+03	0.00%	97.76%	3.06%
FCSR=10^2	$\bar{u}_z$	-8.08E-05	0.00%	3.90%	0.09%	-5.59E-05	0.00%	4.47%	0.01%
	$\bar{\sigma}_x$	-4.90E+05	0.00%	0.00%	0.00%	-3.80E+05	0.00%	0.00%	0.00%
	$\bar{\sigma}_{xz}$	-5.80E+03	0.07%	73.13%	5.08%	-6.55E+03	0.02%	81.54%	3.02%
FCSR=10^1	$\bar{u}_z$	-7.12E-05	0.00%	0.12%	0.01%	-5.21E-05	0.00%	0.16%	0.00%
	$\bar{\sigma}_x$	-4.86E+05	0.00%	0.00%	0.00%	-3.80E+05	0.00%	0.00%	0.00%
	$\bar{\sigma}_{xz}$	-5.89E+03	0.75%	20.40%	4.87%	-6.58E+03	0.28%	27.69%	2.64%
FCSR=10^0	$\bar{u}_z$	-4.53E-05	0.00%	0.00%	0.00%	-4.53E-05	0.00%	0.00%	0.00%
	$\bar{\sigma}_x$	-3.75E+05	0.00%	0.00%	0.00%	-3.75E+05	0.00%	0.00%	0.00%
	$\bar{\sigma}_{xz}$	-6.65E+03	6.83%	0.88%	0.83%	-7.04E+03	3.34%	0.75%	0.56%

5.4 Kinematic description for laminated shells

Upon verification of the effectiveness and efficiency of the sandwich shell model, a generalised multi-layer shell model specific to an alternating stiff/soft lay-up is proposed.

5.4.1 Characteristics of alternating stiff/soft laminations

Laminations with an alternating stiff/soft lay-up have two main characteristics which distinguish them from other laminations. Firstly, the large stiffness ratio between the stiff layer and the soft layer (still denoted as ‘FCSR’ hereafter) plays an important role in the through-thickness distribution of the transverse shear stresses and strains. To illustrate this point, multi-layer beams with an alternating stiff/soft lay-up have been modelled under bending with 2D plane-stress analysis, where Figures 5.7-5.8 respectively depict the schematic distributions of the transverse shear stress and strain with 5 and 7 constitutive layers and various FCSRs. From Figures 5.3, 5.7-5.8, it is observed that the distribution of the transverse shear stress changes significantly with different FCSR values. However, the transverse shear strain distribution for this type of laminations shows that for the considered FCSR range the softer layers sustain much larger strains than the stiffer layers and exhibit a near constant distribution through the constitutive layer.

Secondly, a large FCSR induces significant zigzag effect in such laminations. The variation of planar displacements under bending is investigated by performing a 2D plane-stress analysis of a multi-layer beam with an alternating stiff/soft lay-up, which indicates that all stiff layers have almost identical rotations of their respective normals, whereas the soft layers can have different rotations.

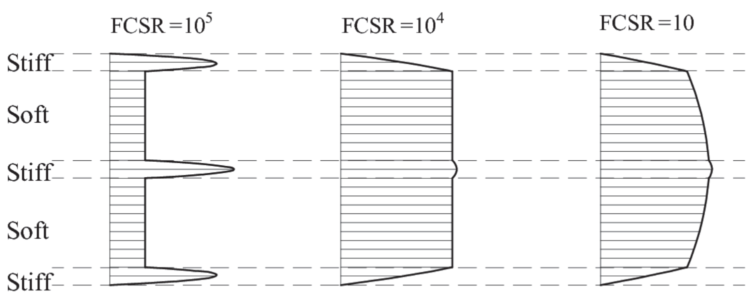

a. transverse shear stress

Figure 5.7: Through thickness distribution of transverse shear stress/strain with various FCSRs (5 layers) (Cont’d…)

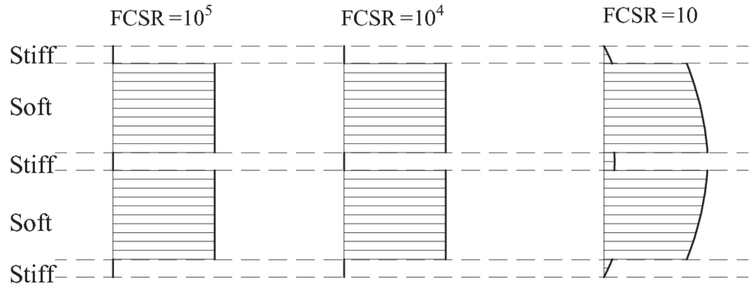

b transverse shear strain

Figure 5.7: Through thickness distribution of transverse shear stress/strain with various FCSRs (5 layers).

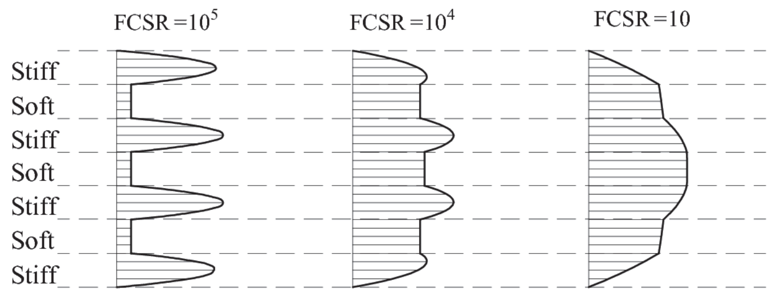

a. transverse shear stress

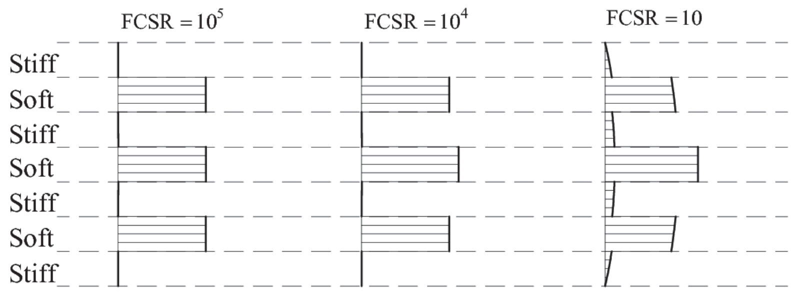

b. transverse shear strain

Figure 5.8: Through thickness distribution of transverse shear stress/strain with various FCSRs (7 layers).

Following on from the above noted characteristics, a laminated shell model with an alternating stiff/soft lay-up is proposed. Figure 5.9 depicts the lamination model for a plate along with the local coordinates, where the x- and y-axes are located at the middle surface, while the z-axis is normal to the plate, and where each layer is identified by a unique index. It is important to note that while the kinematic descriptions is presented for a plate problem, it is equally applicable to local formulations of shallow shells and, through incorporation within a co-rotational framework, to the nonlinear analysis of general curved shells.

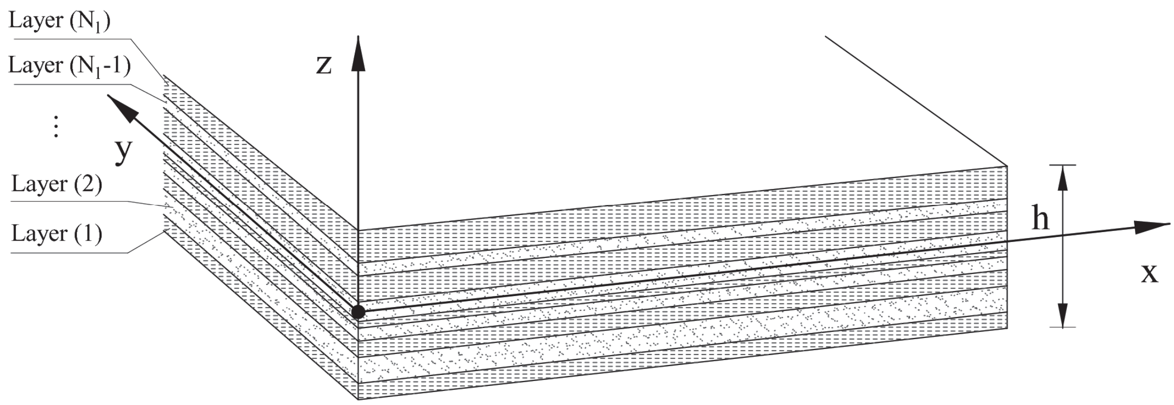

Figure 5.9: Laminated plate and local coordinate system.

5.4.2 Zigzag displacement fields

Similar to the sandwich model, this lamination model assumes a piecewise linear variation of planar displacements in the z direction. Based on the summarised pattern of the zigzag displacements, it is assumed that all stiff sheets have identical rotations of the normal, whereas the soft sheets allow different rotations. Accordingly, for a lamination consisting of $(N_c + 1)$ stiff layers bonded by N_c soft cores (N_c denotes the number of soft core layers), the through-thickness distribution of the planar displacements can be decomposed into a constant and a linear mode, in accordance with the Reissner-Mindlin kinematic hypothesis, as well as N_c zigzag modes, denoted by $\Lambda_j^o(z)$ ($j = 1 \rightarrow N_c$), accounting for the zigzag effect. Each zigzag mode can be initially expressed as (Figure 5.10.b):

$$\Lambda_j^o(z) = \begin{cases} 0, & z \in \left[h_-, h_{2j_-} \right] \\ \dfrac{1}{h_{2j}} \left(z - h_{2j_-} \right), & z \in \left[h_{2j_-}, h_{2j_+} \right] \quad (j = 1 \rightarrow N_c) \\ 1, & z \in \left[h_{2j_+}, h_+ \right] \end{cases} \tag{5.18}$$

By orthogonalising each zigzag mode $\Lambda_j^o(z)$ with respect to the constant and linear modes, with the addition of constant and linear terms, the zigzag mode becomes (Figure 5.10.c):

$$\Lambda_j(z) = \Lambda_j^o(z) + \alpha_{0,j} + \alpha_{1,j} z \tag{5.19}$$

$$\alpha_{0,j} = \frac{h_{2j_-} + h_{2j_+}}{2h} - \frac{1}{2}, \quad \alpha_{1,j} = \frac{4h_{2j_-}^2 + 4h_{2j_-}h_{2j_+} + 4h_{2j_+}^2 - 3h^2}{2h^3} \tag{5.20}$$

The resulting planar displacement fields are expressed as:

$$u_\alpha(x,y,z) = u_{\alpha 0}(x,y) + z\theta_\alpha(x,y) + \sum_{j=1}^{N_c} \Lambda_j(z)\vartheta_\alpha^j(x,y) \qquad (\alpha = x,y) \tag{5.21}$$

where ϑ_α^j are the additional fields associated with the proposed zigzag functions along the x- or y-axis. The transverse displacement is assumed to be constant through the plate thickness, and is thus denoted by $u_{z0}(x,y)$.

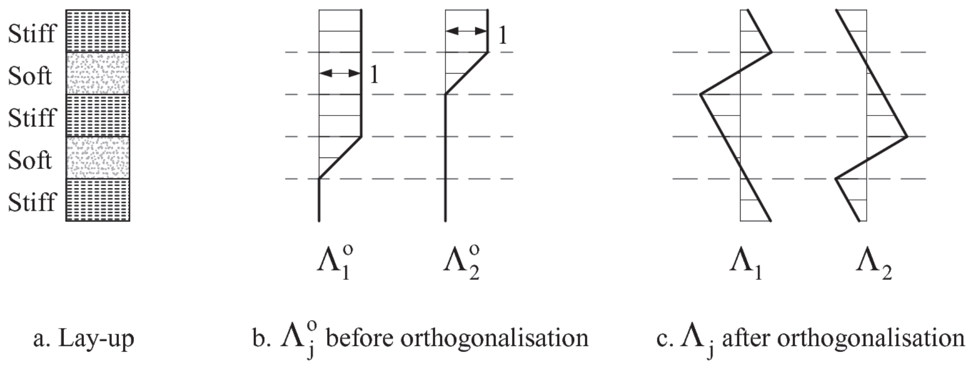

Figure 5.10: Zigzag modes for a 5-layer lamination with alternating stiff/soft lay-up.

5.4.3 Kinematics of individual layer

Each constitutive layer of the lamination model is regarded as a pseudo plate. At layer (k) ($k = 1 \rightarrow N_l$, where N_l denotes the number of constitutive layers), the planar displacements on the layer mid-surface are obtained as:

$$u_\alpha^{(k)} = u_{\alpha 0} + z^{(k)}\theta_\alpha + \sum_{j=1}^{N_c} \Lambda_j^{(k)}\vartheta_\alpha^j \qquad (\alpha = x,y) \tag{5.22}$$

where $\Lambda_j^{(k)} \equiv \Lambda_j(z^{(k)})$ represents the extracted value of the zigzag function $\Lambda_j(z)$ on the middle surface of layer (k). The transverse displacement on the layer mid-surface is obtained from (5.6).

The rotational displacements of layer (k) are derived by taking the first derivatives of the planar displacements with respect to z:

$$\theta_\alpha^{(k)} = \left.\frac{\partial u_\alpha^{(k)}}{\partial z}\right|_{z^{(k)}} = \theta_\alpha + \sum_{j=1}^{N_c} \lambda_j^{(k)} \vartheta_\alpha^j, \quad \lambda_j^{(k)} = \left.\frac{\partial \Lambda_j}{\partial z}\right|_{z^{(k)}} \qquad (\alpha = x, y) \tag{5.23}$$

Denote $\mathbf{u}_c = \left\langle u_{x0}, u_{y0}, u_{z0}, \theta_x, \theta_y \right\rangle^T$ as the basic local displacement fields consistent with the Reissner-Mindlin formulation, $\mathbf{u}_a = \left\langle \vartheta_x^1, \vartheta_y^1 \cdots \vartheta_x^{N_c}, \vartheta_y^{N_c} \right\rangle^T$ as the additional displacement fields associated with $\Lambda_j^o(z)$ $(j = 1 \to N_c)$, and $\mathbf{u}^{(k)} = \left\langle u_x^{(k)}, u_y^{(k)}, u_z^{(k)}, \theta_x^{(k)}, \theta_y^{(k)} \right\rangle^T$ as the displacement fields at layer (k) treated as a pseudo plate. The relationship between the layer displacements, $\mathbf{u}^{(k)}$, and multi-layer displacements, $\mathbf{u}_c$ and $\mathbf{u}_a$, is then identical to (5.8) with $\mathbf{T}_c^{(k)}$ and $\mathbf{T}_a^{(k)}$ obtained from respectively (5.9) and the following equation:

$$\mathbf{T}_a^{(k)} = \left[\begin{array}{cc:c:cc:c:cc} \Lambda_1^{(k)} & 0 & \cdots & \Lambda_j^{(k)} & 0 & \cdots & \Lambda_{N_c}^{(k)} & 0 \\ 0 & \Lambda_1^{(k)} & \cdots & 0 & \Lambda_j^{(k)} & \cdots & 0 & \Lambda_{N_c}^{(k)} \\ \hdashline 0 & 0 & \cdots & 0 & 0 & \cdots & 0 & 0 \\ \hdashline \lambda_1^{(k)} & 0 & \cdots & \lambda_j^{(k)} & 0 & \cdots & \lambda_{N_c}^{(k)} & 0 \\ 0 & \lambda_1^{(k)} & \cdots & 0 & \lambda_j^{(k)} & \cdots & 0 & \lambda_{N_c}^{(k)} \end{array}\right]_{(5\times 2N_c)} \tag{5.24}$$

The membrane strains $\boldsymbol{\varepsilon}_m^{(k)}$, bending generalised strains $\boldsymbol{\varepsilon}_b^{(k)}$, and transverse shear strains $\boldsymbol{\varepsilon}_s^{(k)}$ within each layer (k) are obtained from (5.11)-(5.13) with z_0 representing the offset of the shell mid-surface along the z-axis, thus generalising the kinematics of flat plates to shallow shells.

5.4.4 Through-thickness distribution of transverse shear strains

Based on the aforementioned pattern of transverse shear strains, as depicted in Figures 5.3 and 5.7-5.8, it is assumed that in the external stiff sheets the shear strain varies linearly from zero at the outer surface, whereas for each internal layer the shear strain remains constant.

The through-thickness distribution of the assumed transverse shear strain at each layer (k) is expressed the same as (5.14) with $F_k(z)$ given as follows:

$$F_1(z) = 1 + \frac{2\left(z - z^{(1)}\right)}{h_1}, \quad F_{N_l}(z) = 1 - \frac{2\left(z - z^{(N_l)}\right)}{h_{N_l}}, \quad F_k(z) = 1 \ \ (k = 2 \to N_l - 1) \tag{5.25}$$

The shear correction factor $\omega^{(k)}$ can be derived from energy equivalence at the generalised stress/strain and material stress/strain levels via (5.16), which results in $\omega^{(1)} = \omega^{(N_l)} = \frac{3}{4}$ and $\omega^{(k)} = 1 \ (k = 2 \to N_l - 1)$.

In the range of FCSRs, this assumed distribution for the transverse shear strain offers a realistic representation of the exact solution without imposing continuity constraints on transverse shear stresses, which is also more practical than an assumed stress distribution when considering material nonlinearity. The exclusion of stress coupling between layers leads to a lamination formulation that achieves good levels of accuracy with high computational efficiency, which becomes even more pronounced for laminated shell structures with more layers.

5.5 Verification of through-thickness kinematics of lamination model

A 1D cantilever beam example is used here to illustrate the effectiveness and efficiency of the lamination model. As depicted in Figure 5.11, the laminated cantilever, which has a length of L = 1.0 and a depth of h = 0.1, is clamped at one end and loaded with a transverse force P = –100 at the free end. The lay-up scheme consists of an alternating stiff/soft/… configuration. Material properties for the stiff face sheets are: Young's modulus $E_{(F)} = 7 \times 10^{10}$, and Poisson's ratio $\nu_{(F)} = 0.3$. The Young's modulus and shear modulus for the soft core layers are obtained by dividing those of face sheets by a FCSR which is assumed to be respectively 10, 100, 1000, and 10000. The lamination model is assessed for different numbers of layers and layer thicknesses, with the considered lay-ups listed in Table 5.3 Note that in all considered cases the core layers are of equal thicknesses $h_{(C)}$, and the total thickness of the beam is fixed to h = 0.1.

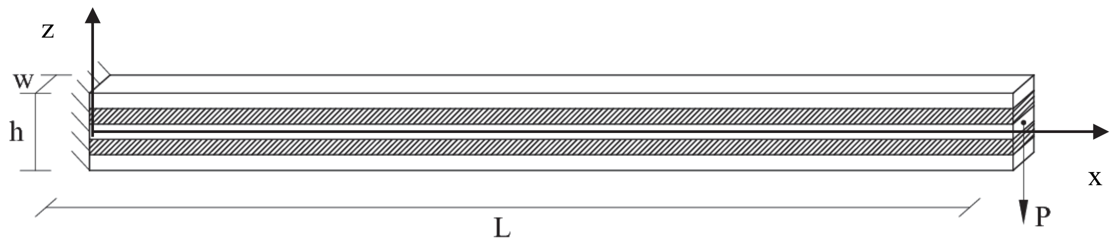

Figure 5.11: A multi-layered cantilever beam loaded with a transverse force at the free end.

Table 5.3: Lay-ups of laminated cantilever beam.

Lay-up	Symmetry	Layer thicknesses
(1)	Symmetric	All stiff layers: $h_{(F)} = 5h_{(C)}$
(2)	Symmetric	All stiff layers: $h_{(F)} = (1/5)\,h_{(C)}$
(3)	Asymmetric	Top stiff layer: $h_{(F)}^{(N_l)} = 10h_{(C)}$; other stiff layers: $h_{(F)} = 5h_{(C)}$
(4)	Asymmetric	Top stiff layer: $h_{(F)}^{(N_l)} = (2/5)h_{(C)}$; other stiff layers: $h_{(F)} = (1/5)h_{(C)}$

The problem is modelled with 1D 3-noded laminated beam elements employing the proposed zigzag displacement fields and transverse shear strain distributions, and shear locking is eliminated by using two-point strain mapping of the transverse shear strain. The free end deflection and the normal stress component at the clamped end are investigated:

$$\overline{u}_z = u_{z0}\left(L,0\right), \quad \overline{\sigma}_x = \sigma_x\left(0,h/2\right)$$

where the convergent solution obtained from 2D plane-stress analysis is used as a reference. Note that this is a linear elastic problem of a straight laminated beam, so a linear strain-displacement relationship is considered without the inclusion of the second-order terms.

The performance of the lamination model for different lay-ups and number of layers is assessed here. For each considered lay-up and number of layers, a uniform mesh of 32 laminated beam elements employing the proposed zigzag displacements and transverse shear strain distribution provides a convergent solution, denoted as ‘Present’. In addition, the so-called ‘MZZFi’ formulations, which include MZZF into the displacements that are of i^{th}-order in z, are also established, with a 32 element mesh providing a convergent solution. For comparison purposes, the z expansion order of the 'MZZFi' formulation is selected such that the same number of nodal displacement parameters are used for both formulation types. Table 5.4 lists the z expansion order of ‘MZZFi’ used for the five-, seven-, nine-, and elevenlayered cases. The proposed discrete transverse shear strain distribution is employed for all formulations.

Table 5.4: Order of z expansion used for 'MZZFi' formulation.

Number of layers	Order of z expansion
5	2
7	3
9	4
11	5

The convergent solutions of 'Present' and 'MZZFi' models for the two symmetric lay-ups (1) and (2) are provided in Tables 5.5-5.6, whereas the results for the two asymmetric lay-ups (3) and (4) are given in Tables 5.7-5.8. It is clear that for lay-ups (1) and (2) both models provide accurate results with the proposed model yielding slightly better accuracy. For lay-ups (3) and (4), the 'MZZFi' models become less accurate, with the relative error increasing with the FCSR. On the contrary, the proposed lamination model still provides a close estimation to the reference solution.

Table 5.5: Evaluation of different laminated beams models with various FCSRs and number of layers for symmetric lay-up (1).

Number of layers	FCSR	$\bar{u}_z$			$\bar{\sigma}_x$		
		Reference	Present	MZZFi	Reference	Present	MZZFi
5	10^1	-6.06E-06	-6.06E-06	-6.06E-06	6.53E+04	6.51E+04	6.51E+04
	10^3	-1.20E-05	-1.20E-05	-1.20E-05	9.46E+04	9.46E+04	9.46E+04
	10^5	-6.80E-05	-6.80E-05	-6.80E-05	2.17E+05	2.17E+05	2.17E+05
7	10^1	-6.22E-06	-6.21E-06	-6.21E-06	6.73E+04	6.68E+04	6.65E+04
	10^3	-1.25E-05	-1.25E-05	-1.24E-05	9.97E+04	9.97E+04	9.69E+04
	10^5	-1.15E-04	-1.15E-04	-1.15E-04	2.80E+05	2.80E+05	2.77E+05
9	10^1	-6.32E-06	-6.32E-06	-6.32E-06	6.86E+04	6.79E+04	6.81E+04
	10^3	-1.28E-05	-1.28E-05	-1.26E-05	1.04E+05	1.04E+05	9.98E+04
	10^5	-1.65E-04	-1.65E-04	-1.65E-04	3.31E+05	3.31E+05	3.27E+05
11	10^1	-6.39E-06	-6.39E-06	-6.39E-06	6.96E+04	6.88E+04	6.80E+04
	10^3	-1.30E-05	-1.30E-05	-1.27E-05	1.07E+05	1.07E+05	9.94E+04
	10^5	-2.13E-04	-2.13E-04	-2.13E-04	3.70E+05	3.71E+05	3.60E+05

Table 5.6: Evaluation of different laminated beams models with various FCSRs and number of layers for symmetric lay-up (2).

Number of layers	FCSR	$\bar{u}_z$			$\bar{\sigma}_x$		
		Reference	Present	MZZFi	Reference	Present	MZZFi
5	10^1	-1.29E-05	-1.29E-05	-1.29E-05	1.39E+05	1.40E+05	1.40E+05
	10^3	-4.61E-05	-4.60E-05	-4.61E-05	3.13E+05	3.14E+05	3.14E+05
	10^5	-1.70E-03	-1.68E-03	-1.70E-03	1.75E+06	1.73E+06	1.75E+06
7	10^1	-1.52E-05	-1.52E-05	-1.52E-05	1.64E+05	1.64E+05	1.64E+05
	10^3	-5.00E-05	-5.00E-05	-4.96E-05	3.60E+05	3.61E+05	3.54E+05
	10^5	-2.20E-03	-2.20E-03	-2.19E-03	1.94E+06	1.93E+06	1.92E+06
9	10^1	-1.67E-05	-1.67E-05	-1.67E-05	1.80E+05	1.79E+05	1.79E+05
	10^3	-5.29E-05	-5.29E-05	-5.20E-05	3.95E+05	3.95E+05	3.80E+05
	10^5	-2.45E-03	-2.45E-03	-2.45E-03	2.03E+06	2.04E+06	2.00E+06
11	10^1	-1.77E-05	-1.77E-05	-1.77E-05	1.91E+05	1.90E+05	1.89E+05
	10^3	-5.51E-05	-5.51E-05	-5.38E-05	4.20E+05	4.20E+05	3.97E+05
	10^5	-2.60E-03	-2.60E-03	-2.60E-03	2.12E+06	2.12E+06	2.05E+06

Table 5.7: Evaluation of different laminated beams models with various FCSRs and number of layers for asymmetric lay-up (3).

Number of layers	FCSR	$\bar{u}_z$			$\bar{\sigma}_x$		
		Reference	Present	MZZFi	Reference	Present	MZZFi
5	10^1	-6.00E-06	-6.00E-06	-6.00E-06	6.33E+04	6.37E+04	6.22E+04
	10^3	-1.06E-05	-1.06E-05	-6.95E-06	9.64E+04	9.74E+04	7.64E+04
	10^5	-4.53E-05	-4.53E-05	-7.19E-06	2.20E+05	2.21E+05	7.87E+04
7	10^1	-6.09E-06	-6.09E-06	-6.08E-06	6.48E+04	6.52E+04	6.29E+04
	10^3	-1.15E-05	-1.15E-05	-7.57E-06	1.05E+05	1.07E+05	8.40E+04
	10^5	-7.94E-05	-7.94E-05	-8.13E-06	3.08E+05	3.10E+05	8.90E+04
9	10^1	-6.17E-06	-6.16E-06	-6.16E-06	6.60E+04	6.63E+04	6.34E+04
	10^3	-1.20E-05	-1.20E-05	-8.09E-06	1.12E+05	1.13E+05	8.90E+04
	10^5	-1.20E-04	-1.20E-04	-9.01E-06	3.95E+05	3.94E+05	9.66E+04
11	10^1	-6.23E-06	-6.23E-06	-6.23E-06	6.69E+04	6.72E+04	6.28E+04
	10^3	-1.24E-05	-1.24E-05	-8.76E-06	1.17E+05	1.19E+05	9.11E+04
	10^5	-1.63E-04	-1.63E-04	-1.05E-05	4.65E+05	4.68E+05	1.03E+05

Table 5.8: Evaluation of different laminated beams models with various FCSRs and number of layers for asymmetric lay-up (4).

Number of layers	FCSR	$\bar{u}_z$			$\bar{\sigma}_x$		
		Reference	Present	MZZFi	Reference	Present	MZZFi
5	10^1	-1.10E-05	-1.10E-05	-1.10E-05	1.08E+05	1.09E+05	1.06E+05
	10^3	-4.20E-05	-4.20E-05	-1.83E-05	2.86E+05	2.87E+05	1.74E+05
	10^5	-1.01E-03	-1.00E-03	-1.99E-05	1.67E+06	1.67E+06	1.83E+05
7	10^1	-1.29E-05	-1.29E-05	-1.29E-05	1.28E+05	1.28E+05	-1.29E-05
	10^3	-4.57E-05	-4.57E-05	-3.17E-05	3.37E+05	3.40E+05	2.73E+05
	10^5	-1.66E-03	-1.66E-03	-5.37E-05	2.20E+06	2.20E+06	3.52E+05
9	10^1	-1.42E-05	-1.42E-05	-1.42E-05	1.43E+05	1.43E+05	1.43E+05
	10^3	-4.84E-05	-4.83E-05	-4.06E-05	3.75E+05	3.79E+05	3.56E+05
	10^5	-2.07E-03	-2.08E-03	-1.19E-04	2.34E+06	2.50E+06	5.97E+05
11	10^1	-1.53E-05	-1.53E-05	-1.53E-05	1.54E+05	1.55E+05	1.54E+05
	10^3	-5.04E-05	-5.04E-05	-4.43E-05	4.06E+05	4.10E+05	4.06E+05
	10^5	-2.34E-03	-2.34E-03	-1.69E-04	2.71E+06	2.70E+06	7.80E+05

5.6 Summary

In this chapter, a three-layered sandwich shell model is firstly proposed. A zigzag function that assumes identical rotations in face sheets is added to the Reissner-Mindlin plate theory to consider the zigzag effect in displacements. Besides, a piecewise linear-constant-linear through-thickness distribution of the transverse shear strain is assumed, which is specifically suitable for sandwich lay-ups. Each layer of the sandwich shell is regarded as a pseudo monolithic shell and employs the corresponding kinematics and constitutive relationships. The governing equations of the laminated shell are derived with the employment of the virtual work principle. Laminations with isotropic and orthotropic materials are readily applicable so far, and other material models may also be used for the individual layers.

A 1D cantilever example has been used to demonstrate the effectiveness and efficiency of the proposed zigzag function for sandwich shells. The adequacy of the assumed discrete transverse shear strain distribution has also been demonstrated in comparison with the results of models with continuous transverse shear stress distributions. In addition, the proposed zigzag function outperforms the MZZF in asymmetrically laminated cases, which provided the inspiration for employing similar assumptions on layer rotations in the development of generalised multi-layered shell model.

The three-layered shell model is then extended to a generalised multi-layered shell model with an alternate (stiff/soft/…) layer-up scheme. A set of zigzag displacement modes are employed in the planar displacements, the number of which is dependent on the number of soft layers. These zigzag displacement modes are defined such that all stiffer layers are assumed to rotate at the same angle while the soft layers may have different rotations. The through-thickness transverse shear strain is assumed such that all internal layers have constant values through the layer thickness while the external ones utilise a linear distribution with zero values at the top and bottom of the plate.

Similar to the three-layered sandwich case, a 1D cantilever example has been used to stress the accuracy of the zigzag displacement set and the assumed transverse shear strain distribution. Furthermore, the accuracy of the proposed zigzag functions in modelling beams composed of identical and different stiff sheets are investigated, and the results are compared against the MZZFi predictions to emphasise the effectiveness of the proposed zigzag functions. It is concluded that the proposed multi-layered shell model is both accurate and efficient. In the next chapter, the incorporation of this model within finite element shell formulations is presented.

CHAPTER 6

Laminated Quadrilateral and Triangular Shell Elements

6.1 Introduction

In this chapter, the application of the proposed lamination model is illustrated for 6-noded and 9-noded co-rotational shell elements, as described in Chapter 3, noting that it can also be similarly applied to other shell elements of various shapes and orders. Owing to the employment of the co-rotational approach, geometric nonlinearity is considered separately from the local element formulations, thus allowing the adoption of a fixed kinematic relationship between the element and layer local displacement fields as well as the employment of low-order, even linear, relationships between the strain and local displacement fields throughout the large displacement analysis. Furthermore, the additional zigzag displacement variables are associated with local cross-sectional warping only; hence, a 2D ‘shell’ coordinate system is employed in this research for direct definition of these additional variables, which effectively minimises the required co-rotational transformations and enhances computational efficiency, and which also facilitates defining the fibre orientation for composite materials.

In the following sections, the merits of the co-rotational approach in the context of laminated shell modelling are first discussed, which is followed by proposing a 2D curvilinear system, so-called ‘shell’ coordinate system, which enables the effective and efficient consideration of the additional zigzag displacement fields, and which, in the consideration of composite materials, facilitates the establishment of the material fibre orientation in relation to the element local system. Nonlinear transformations between the global coordinate system and the local co-rotational system, as well as the required linear transformations between the shell coordinate system and the local co-rotational system, are subsequently given. With the employment of the co-rotational system and the shell system, the formulations of triangular and quadrilateral laminated shell elements are presented.

In order to perform dynamic analysis, effective consistent mass matrices for the considered elements are also provided, which provide good accuracy for thin-to-moderately thick plate and shell applications.

Verification examples are finally presented to demonstrate the accuracy of the developed formulations for nonlinear analysis of laminated plates and shells with an alternating stiff/soft lay-up.

6.2 Co-rotational approach

In formulating large displacement finite elements for small-strain problems, the relationship between the strain and displacement fields is highly nonlinear and complex if the displacement fields are referred to a fixed coordinate system, where the nonlinear strain terms arise mainly from the element rigid body rotations. As demonstrated in Section 3.3, the co-rotational approach enables the use of a low-order strain displacement relationship at the local level and addresses geometric nonlinearity through transformations between the local and global systems that are applied at the level of discrete element parameters.

The embedment of a monolithic Reissner-Mindlin formulation into the co-rotational framework is usually achieved by relating 5 local nodal displacement parameters, 3 translations and 2 rotations, to their counterparts in the global system; the exception would be where adjacent shell elements meet at an angle, in which case 3 rotational parameters would be used (Izzuddin & Liang, 2015). Since the co-rotational system follows the element configuration throughout the large displacement analysis, the transformations between the global and local element systems are nonlinear and vary from step to step.

6.3 Shell coordinate system

For the laminated shell element formulation, if the continuity of the zigzag displacement fields is enforced via additional parameters defined in the global coordinate system, similar to the basic nodal displacement parameters, then these would be subject to co-rotational transformations to the local system, thus imposing further computational demands. Noting that the zigzag fields describe the local effect of cross-sectional warping, it is proposed that they are defined in a 2D orthogonal curvilinear coordinate system over the shell structure, denoted as the 'shell' coordinate system, which thus follows the local co-rotational system at the element level. With the associated additional zigzag parameters defined in this shell coordinate system, continuity of the zigzag fields is ensured. Importantly, the element response associated with the zigzag parameters can thus be evaluated via a fixed linear kinematic transformation between the shell and local element systems, as elaborated in Section 6.4, rather than a varying nonlinear co-rotational transformation, which enhances the computational efficiency of the geometric nonlinear analysis of laminated shells. Another main benefit of using a shell coordinate system relates to defining fibre orientation for composite materials, which will be discussed in Section 6.3.2.

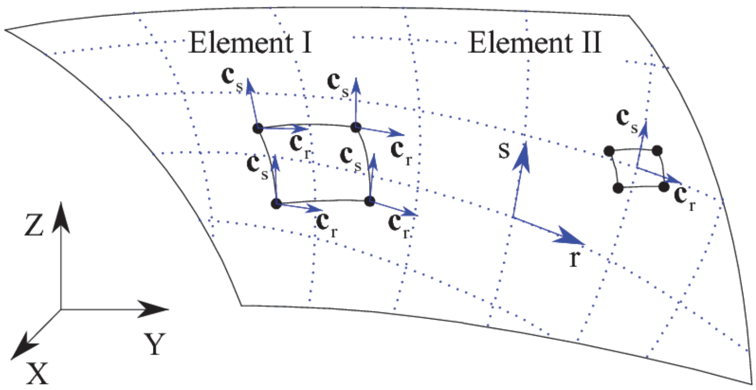

Figure 6.1: 2D curvilinear shell coordinate system.

In order to ensure continuity of the zigzag fields, a key requirement is that the 2D shell coordinate system must be associated with a unique orientation of its orthogonal directional vectors at an arbitrary point on the shell mid-surface. Besides this fundamental requirement of uniqueness, it is desirable for the 2D curvilinear shell system to be defined in a continuous manner, as illustrated by the dotted contour lines in Figure 6.1. For a smooth shell structure, a continuous definition of the shell system can be obtained in different ways, provided the shell surface is open. On the other hand, for a closed shell surface (e.g. a sphere), a discontinuous definition of the 2D shell coordinate system would be necessary, where the discontinuity may be localised to a single point or line. For shell structures with a folded edge, the shell system would not be uniquely defined along the fold line, though there is no requirement for continuity of the zigzag fields in such locations; a typical realistic treatment would be to restrain the additional zigzag parameters at fold lines, though a more relaxed treatment based on a free natural boundary condition for the associated zigzag forces can also be considered with the use of element-specific zigzag parameters along the folds.

With reference to the 2D curvilinear shell system (r,s) shown in Figure 6.1, the additional displacement zigzag parameters of an arbitrary element can be defined along the two curvilinear directions at the node level (refer to Element I). Although the relative orientation of the shell coordinate system and local element system can vary over one element, a constant relative orientation may also be considered at the element level (refer to Element II), where all additional zigzag parameters would be assumed to accord with the surface vectors at the element centre, provided the 2D shell system is continuous. While this assumption is associated with some inaccuracy, especially for a coarse mesh, it simplifies the determination of the additional displacement fields over the element, and importantly it retains the convergence property with mesh refinement. For small-strain problems, the relative orientation of the shell coordinate system and the element local system can be assumed to remain constant throughout the analysis; hence this orientation can be established at the start of nonlinear analysis in terms of a fixed angle β for each element denoting the rotation from $\mathbf{c}_r$ to $\mathbf{c}_x$ (Figure 6.2).

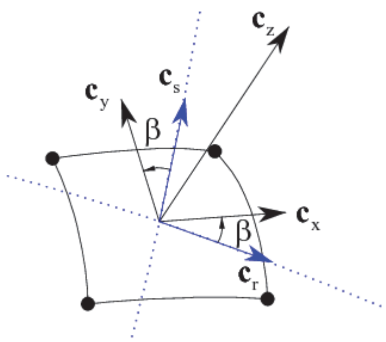

Figure 6.2: Relative orientation between the local element and shell systems.

6.3.1 Alternative definitions of shell system

There are potentially many different methods for defining a unique and continuous 2D curvilinear shell system over a smooth shell structure with a continuous surface. One such definition is proposed here utilising the uniqueness and continuity property of the normal to the surface $\mathbf{c}_z^o$ of such a shell structure. In this definition, the 2D orthogonal shell system is obtained as a rotation of a user-defined reference triad $(\mathbf{c}_{\overline{X}}, \mathbf{c}_{\overline{Y}}, \mathbf{c}_{\overline{Z}})$, where the rotation that transforms $\mathbf{c}_{\overline{Z}}$ to $\mathbf{c}_z^o$ is first obtained, and this then transforms $(\mathbf{c}_{\overline{X}}, \mathbf{c}_{\overline{Y}})$ to $(\mathbf{c}_r^o, \mathbf{c}_s^o)$, respectively, as illustrated in Figure 6.3. The derivation of $\mathbf{c}_r^o$ is given as:

$$\mathbf{c}_r^o = \mathbf{T}_n^T \mathbf{R}_n \mathbf{T}_n \mathbf{c}_{\overline{X}} \tag{6.1}$$

with:

$$\mathbf{T}_n = \begin{bmatrix} \mathbf{c}_1^T \\ \mathbf{c}_2^T \\ \mathbf{c}_3^T \end{bmatrix}, \quad \mathbf{c}_1 = \mathbf{c}_z^o, \quad \mathbf{c}_3 = \frac{\mathbf{c}_{\overline{Z}} \times \mathbf{c}_z^o}{\left\| \mathbf{c}_{\overline{Z}} \times \mathbf{c}_z^o \right\|}, \quad \mathbf{c}_2 = \mathbf{c}_3 \times \mathbf{c}_1 \tag{6.2}$$

and:

$$\mathbf{R}_n = \begin{bmatrix} \cos(\delta) & -\sin(\delta) & 0 \\ \sin(\delta) & \cos(\delta) & 0 \\ 0 & 0 & 1 \end{bmatrix}, \quad \cos(\delta) = \mathbf{c}_{\overline{Z}} \cdot \mathbf{c}_z^o, \quad \sin(\delta) = \left\| \mathbf{c}_{\overline{Z}} \times \mathbf{c}_z^o \right\| \tag{6.3}$$

where δ represents the rotation from $\mathbf{c}_{\overline{Z}}$ to $\mathbf{c}_z^o$.

For a closed shell surface, such as a spherical shell, this definition cannot be applied at the point with the normal $\mathbf{c}_z^o$ pointing just opposite to $\mathbf{c}_{\overline{Z}}$ (i.e. the two vectors are at an angle of 180°).

A second alternative definition is also proposed, as illustrated in Figure 6.4, where $\mathbf{c}_s^o$ in the initial undeformed configuration is considered to be a projection of a user-defined vector **n** on the shell surface, and $\mathbf{c}_r^o$ is obtained from:

$$\mathbf{c}_{\mathrm{r}}^{\mathrm{o}} = \frac{\mathbf{n} \times \mathbf{c}_{\mathrm{z}}^{\mathrm{o}}}{\left\| \mathbf{n} \times \mathbf{c}_{\mathrm{z}}^{\mathrm{o}} \right\|} \tag{6.4}$$

This definition can be used to generate a continuous 2D shell system provided a vector **n** can be specified which is not orthogonal to the shell surface at any point. For some curved shells with open surfaces, such as a hemi-spherical shell, this is not possible, hence a discontinuous definition of the 2D shell system will be required at the point(s) where the shell surface is normal to **n**.

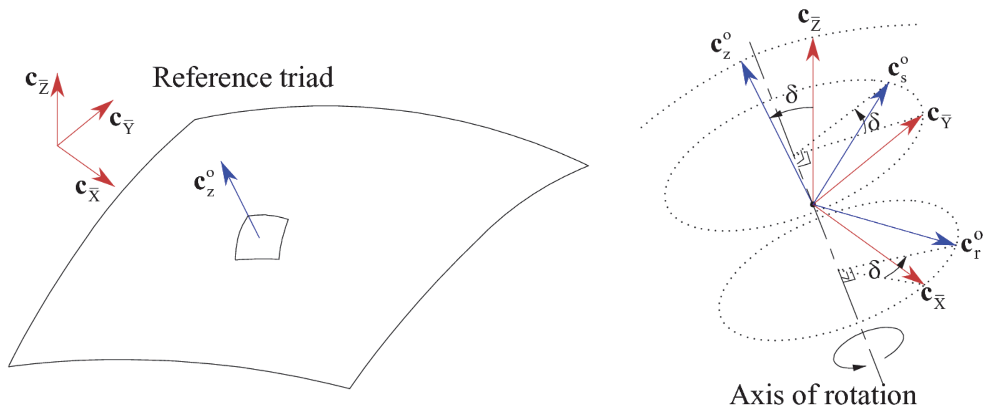

a. Rotation of reference triad

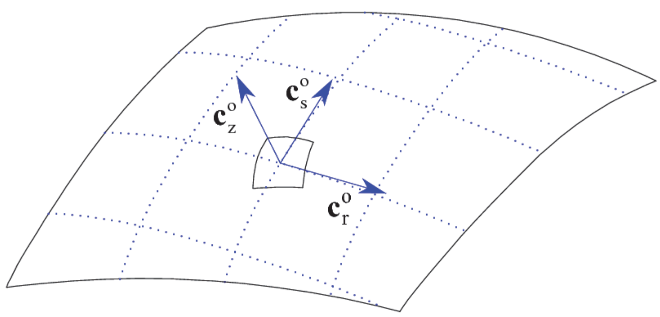

b. Resulting curvilinear axes of shell system

Figure 6.3: An alternative definition of shell coordinate system using a reference triad.

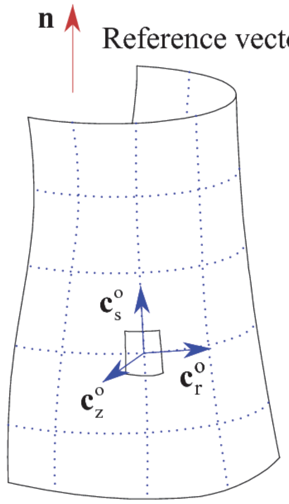

Figure 6.4: An alternative definition of shell coordinate system using a reference vector.

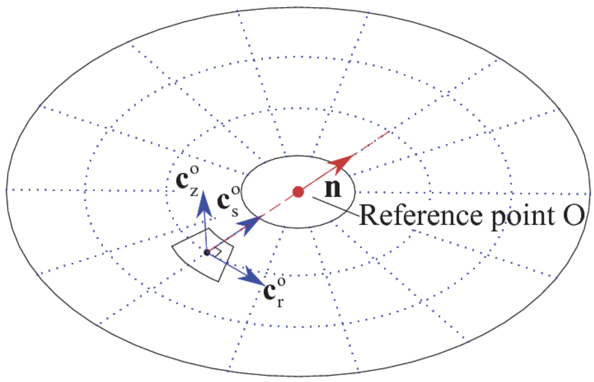

Figure 6.5: An alternative definition of shell coordinate system using a reference point.

Figure 6.5 illustrates a third alternative definition, which is similar to the previous one except that the projection vector **n** points from the shell surface to a reference point O, with similar restrictions to the second alternative in relation to the case where **n** may be orthogonal to the shell surface.

It is worth noting that in cases where a discontinuous definition of the 2D shell coordinate system is inevitable, a unique orientation of $(\mathbf{c}_r^o, \mathbf{c}_s^o)$ can still be prescribed at the point(s) of singularity, and the additional displacement zigzag parameters of the surrounding elements can then be defined at the node level (refer to Element I in Figure 6.1).

6.3.2 Composite materials

Besides the enhancement of the computational efficiency in large displacement analysis, the utilisation of the 2D curvilinear shell system provides the additional benefit of providing the orientation of material fibres in relation to the local element coordinate system when composite materials are considered. In a general arbitrary mesh, the direction of the element local system can vary throughout the mesh, depending on the employed definition of the co-rotational approach, the element configuration and nodal ordering. However, with the use of a continuous 2D shell system, the material fibre orientation can be defined with respect to the shell r-axis, as described by the continuous vector $\mathbf{c}_r^o$ in the initial undeformed configuration. By denoting $\alpha^{(k)}$ to be the angle from the shell directional vector $\mathbf{c}_r^o$ to the material fibre direction at layer (k), $\mathbf{c}_r^{o*(k)}$, the angle from the local element x-axis to the material fibre direction is simply obtained as (Figure 6.6):

$$\varphi^{(k)} = \alpha^{(k)} - \beta \tag{6.5}$$

This then allows the constitutive material response to be established in the local element system through appropriate strain/stress transformations.

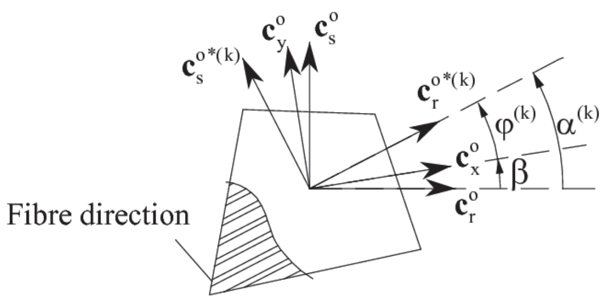

Figure 6.6: Relative orientation between the local element, material, and shell systems.

6.4 Kinematic transformations between global, local and shell systems

As already noted, a co-rotational framework is employed in this research for upgrading the low-order laminated plate/shallow shell model to geometrically nonlinear analysis, where the nonlinear kinematic transformations between the global and local element systems are conveniently restricted to the basic nodal displacement and rotational parameters. On the other hand, the additional zigzag displacement parameters, which describe the local cross-sectional warping behaviour only, are defined in a specific shell system which follows the local element system at a constant orientation, and are therefore excluded from the co-rotational transformations.

The kinematic relationship between local displacement variables and their global counterparts depends on the employed definition of the co-rotational approach and the sequence of nodal numbering. This is illustrated for a 9-noded shell element using a bisector co-rotational system definition in Section 3.4 (Izzuddin, 2005; Izzuddin & Liang, 2015) and for a 6-noded shell element using a zero-macrospin system definition in Section 3.5 (Izzuddin & Liang, 2015). On the other hand, the relationship between the zigzag displacements defined in the shell and local systems is linear for small-strain problems, where the following is employed to transform the additional fields from the shell system to the local element system:

$$\begin{Bmatrix} \vartheta_x^j \\ \vartheta_y^j \end{Bmatrix} = \begin{bmatrix} \hat{c} & \hat{s} \\ -\hat{s} & \hat{c} \end{bmatrix} \begin{Bmatrix} \vartheta_r^j \\ \vartheta_s^j \end{Bmatrix}, \quad \hat{c} = \cos(\beta), \quad \hat{s} = \sin(\beta) \quad (j = 1 \rightarrow N_c) \tag{6.6}$$

where $\left\langle \vartheta_x^j, \vartheta_y^j \right\rangle$ $(j = 1 \rightarrow N_c)$ are additional zigzag displacement fields in the element local system; $\left\langle \vartheta_r^j, \vartheta_s^j \right\rangle$ $(j = 1 \rightarrow N_c)$ are the associated fields defined in the curvilinear shell system; and angle β is the relative orientation of the two systems obtained at the start of analysis.

Note that (6.6) is most effectively accounted for in the kinematic description of (5.8)-(5.9) by re-defining the additional zigzag fields $\mathbf{u}_a$ in the shell coordinate system, i.e. $\mathbf{u}_a = \left\langle \vartheta_r^1, \vartheta_s^1 \cdots \vartheta_r^{N_c}, \vartheta_s^{N_c} \right\rangle^T$, and adjusting the transformation matrix $\mathbf{T}_a^{(k)}$ to:

$$\mathbf{T}_a^{(k)} = \left[\begin{array}{cc|c|cc|c|cc} \hat{c}\,\Lambda_1^{(k)} & \hat{s}\,\Lambda_1^{(k)} & \cdots & \hat{c}\,\Lambda_j^{(k)} & \hat{s}\,\Lambda_j^{(k)} & \cdots & \hat{c}\,\Lambda_{N_c}^{(k)} & \hat{s}\,\Lambda_{N_c}^{(k)} \\ -\hat{s}\,\Lambda_1^{(k)} & \hat{c}\,\Lambda_1^{(k)} & \cdots & -\hat{s}\,\Lambda_j^{(k)} & \hat{c}\,\Lambda_j^{(k)} & \cdots & -\hat{s}\,\Lambda_{N_c}^{(k)} & \hat{c}\,\Lambda_{N_c}^{(k)} \\ \hline 0 & 0 & \cdots & 0 & 0 & \cdots & 0 & 0 \\ \hline \hat{c}\lambda_1^{(k)} & \hat{s}\lambda_1^{(k)} & \cdots & \hat{c}\lambda_j^{(k)} & \hat{s}\lambda_j^{(k)} & \cdots & \hat{c}\lambda_{N_c}^{(k)} & \hat{s}\lambda_{N_c}^{(k)} \\ -\hat{s}\lambda_1^{(k)} & \hat{c}\lambda_1^{(k)} & \cdots & -\hat{s}\lambda_j^{(k)} & \hat{c}\lambda_j^{(k)} & \cdots & -\hat{s}\lambda_{N_c}^{(k)} & \hat{c}\lambda_{N_c}^{(k)} \end{array} \right]_{(5\times 2N_c)} \tag{6.7}$$

This works well provided the shell system is continuous over the element, in which case the response is convergent with mesh refinement even where any variation in the relative orientation of the shell and local element system is ignored for curved shells, with $(\hat{c},\hat{s})$ assumed constant over the element. On the other hand, when the local shell system is discontinuous, as would be the case at specific locations for a closed shell structure, the most effective approach would be to transform the nodal zigzag displacement parameters from the node-specific shell system to the local element system, with the local parameters then used to define the local zigzag fields $\left\langle \vartheta_x^j, \vartheta_y^j \right\rangle$ directly. The latter approach is utilised for generality in the following application to laminated shell elements.

6.5 Application to 6-noded and 9-noded shell elements

The application of the proposed lamination model to the 6-noded and 9-noded co-rotational shell elements is presented hereafter.

6.5.1 Local element kinematics

Local and additional parameters are respectively defined as $\mathbf{U}_C = \left\langle \mathbf{U}_{C1}^T, \cdots, \mathbf{U}_{Ci}^T, \cdots, \mathbf{U}_{CN_e}^T \right\rangle^T$ and $\mathbf{U}_A = \left\langle \mathbf{U}_{A1}^T, \cdots, \mathbf{U}_{Ai}^T, \cdots, \mathbf{U}_{AN_e}^T \right\rangle^T$, where $\mathbf{U}_{Ci}$ and $\mathbf{U}_{Ai}$ contain respectively five local nodal parameters and $2N_c$ additional parameters, which are expressed as $\mathbf{U}_{Ci} = \left\langle u_{x0,i}, u_{y0,i}, u_{z0,i}, \theta_{x,i}, \theta_{y,i} \right\rangle^T$ and $\mathbf{U}_{Ai} = \left\langle \vartheta_{r,i}^1, \vartheta_{s,i}^1, \cdots, \vartheta_{r,i}^{N_c}, \vartheta_{s,i}^{N_c} \right\rangle^T$. The pseudo nodal parameters at layer (k), which are defined as $\mathbf{U}^{(k)} = \left\langle \mathbf{U}_1^{(k)T}, \cdots, \mathbf{U}_i^{(k)T}, \cdots, \mathbf{U}_{N_e}^{(k)T} \right\rangle^T$ with $\mathbf{U}_i^{(k)} = \left\langle u_{x,i}^{(k)}, u_{y,i}^{(k)}, u_{z,i}^{(k)}, \theta_{x,i}^{(k)}, \theta_{y,i}^{(k)} \right\rangle^T$, can be obtained from the following relationship:

$$\mathbf{U}^{(k)} = \mathbf{T}_C^{(k)} \mathbf{U}_C + \mathbf{T}_A^{(k)} \mathbf{U}_A \tag{6.8}$$

$$\mathbf{T}_C^{(k)} = \begin{bmatrix} \mathbf{T}_c^{(k)} & & \mathbf{0} \\ & \ddots & \\ \mathbf{0} & & \mathbf{T}_c^{(k)} \end{bmatrix}_{(5N_e \times 5N_e)} , \quad \mathbf{T}_A^{(k)} = \begin{bmatrix} \mathbf{T}_a^{(k)} & & \mathbf{0} \\ & \ddots & \\ \mathbf{0} & & \mathbf{T}_a^{(k)} \end{bmatrix}_{(5N_e \times 2N_c N_e)} \tag{6.9}$$

where $\mathbf{T}_c^{(k)}$ and $\mathbf{T}_a^{(k)}$ are given in (5.9) and (6.7), respectively. Note that $\mathbf{T}_A^{(k)}$ applies to a continuous shell system definition, ignoring the change of $(\hat{c},\hat{s})$ over the element, but it can be easily modified to account for different shell orientation vectors at individual nodes by adjusting the component diagonal $\mathbf{T}_a^{(k)}$ sub-matrices accordingly.

With the mapped pseudo displacement fields, the generalised strains of each layer (k) are calculated via (5.11)-(5.13) presented in the previous chapter.

6.5.2 Material constitutive response

For linear isotropic and orthotropic materials, the material stresses are obtained from the following equations:

$$\boldsymbol{\sigma}_{p}^{(k)} = \mathbf{C}_{p}^{(k)}\boldsymbol{\varepsilon}_{p}^{(k)}, \quad \boldsymbol{\sigma}_{s,AS}^{(k)} = \mathbf{C}_{s}^{(k)}\boldsymbol{\varepsilon}_{s,AS}^{(k)} \tag{6.10}$$

where $\boldsymbol{\varepsilon}_{p}^{(k)}$ are planar material strains of layer (k), given as:

$$\boldsymbol{\varepsilon}_{p}^{(k)} = \boldsymbol{\varepsilon}_{m}^{(k)} + \frac{h_k}{2}\zeta^{(k)}\boldsymbol{\varepsilon}_{b}^{(k)}, \quad \zeta^{(k)} = \frac{2(z - z^{(k)})}{h_k}, \quad z \in \left[h_{k-}, h_{k+}\right] \tag{6.11}$$

$\boldsymbol{\varepsilon}_{s,AS}^{(k)}$ represents the assumed transverse shear strains as presented in Chapter 5; $\mathbf{C}_{p}^{(k)}$ and $\mathbf{C}_{s}^{(k)}$ are material constitutive matrices for planar and transverse shear stresses/strains of layer (k).

For a linear isotropic material, $\mathbf{C}_{p}^{(k)}$ and $\mathbf{C}_{s}^{(k)}$ are given as:

$$\mathbf{C}_{p}^{(k)} = \frac{E^{(k)}}{1-\nu^{(k)2}}\begin{bmatrix} 1 & \nu^{(k)} & 0 \\ \nu^{(k)} & 1 & 0 \\ 0 & 0 & \dfrac{1-\nu^{(k)}}{2} \end{bmatrix}, \quad \mathbf{C}_{s}^{(k)} = \frac{E^{(k)}}{2(1+\nu^{(k)})}\begin{bmatrix} 1 & 0 \\ 0 & 1 \end{bmatrix} \tag{6.12}$$

with $E^{(k)}$ and $\nu^{(k)}$ representing the Young's modulus and Poisson's ratio of layer (k).

For a linear orthotropic material, $\mathbf{C}_{p}^{(k)}$ and $\mathbf{C}_{s}^{(k)}$ are obtained from:

$$\mathbf{C}_{p}^{(k)} = \mathbf{T}_{p}^{*(k)T}\,\mathbf{C}_{p}^{*(k)}\,\mathbf{T}_{p}^{*(k)}, \quad \mathbf{C}_{s}^{(k)} = \mathbf{T}_{s}^{*(k)T}\,\mathbf{C}_{s}^{*(k)}\,\mathbf{T}_{s}^{*(k)} \tag{6.13}$$

$$\mathbf{C}_p^{*(k)} = \begin{bmatrix} \dfrac{E_1^{(k)}}{1-\nu_{12}^{(k)}\nu_{21}^{(k)}} & \dfrac{\nu_{12}^{(k)}E_2^{(k)}}{1-\nu_{12}^{(k)}\nu_{21}^{(k)}} & 0 \\ \dfrac{\nu_{12}^{(k)}E_2^{(k)}}{1-\nu_{12}^{(k)}\nu_{21}^{(k)}} & \dfrac{E_2^{(k)}}{1-\nu_{12}^{(k)}\nu_{21}^{(k)}} & 0 \\ 0 & 0 & G_{12}^{(k)} \end{bmatrix}, \quad \mathbf{C}_s^{*(k)} = \begin{bmatrix} G_{13}^{(k)} & 0 \\ 0 & G_{23}^{(k)} \end{bmatrix} \tag{6.14}$$

$$\mathbf{T}_p^{*(k)} = \begin{bmatrix} \cos^2(\varphi^{(k)}) & \sin^2(\varphi^{(k)}) & \frac{1}{2}\sin(2\varphi^{(k)}) \\ \sin^2(\varphi^{(k)}) & \cos^2(\varphi^{(k)}) & -\frac{1}{2}\sin(2\varphi^{(k)}) \\ -\sin(2\varphi^{(k)}) & \sin(2\varphi^{(k)}) & \cos(2\varphi^{(k)}) \end{bmatrix}, \quad \mathbf{T}_s^{*(k)} = \begin{bmatrix} \cos(\varphi^{(k)}) & \sin(\varphi^{(k)}) \\ -\sin(\varphi^{(k)}) & \cos(\varphi^{(k)}) \end{bmatrix} \tag{6.15}$$

where $\mathbf{C}_p^{*(k)}$ and $\mathbf{C}_s^{*(k)}$ are the material constitutive matrices in the material coordinate system; $\mathbf{T}_p^{*(k)}$ and $\mathbf{T}_s^{*(k)}$ are constitutive transformation matrices from the material coordinate system to the local element system; $\varphi^{(k)}$ is the angle from the element coordinate system to the material coordinate system at layer (k), as given in (6.5).

Although only linear isotropic and orthotropic material models are considered in this chapter, other linear and nonlinear material models may also be used.

6.5.3 Local resistance forces and stiffness

Local resistance forces of the laminated shell element are obtained from the internal virtual work over the element, which is expressed as:

$$\delta\mathbf{U}_C^T\,\mathbf{f}_C + \delta\mathbf{U}_A^T\,\mathbf{f}_A = \sum_{k=1}^{N_l} \int_{\Omega^e} \left(\int_{h_{k-}}^{h_{k+}} \left(\delta\boldsymbol{\varepsilon}_p^{(k)T}\boldsymbol{\sigma}_p^{(k)} + \delta\boldsymbol{\varepsilon}_{s,AS}^{(k)T}\boldsymbol{\sigma}_{s,AS}^{(k)} \right) dz \right) d\Omega^e, \ \forall\left(\delta\mathbf{U}_C, \delta\mathbf{U}_A\right) \tag{6.16}$$

where integration is performed over the local element domain Ω^e; $\mathbf{f}_C$ and $\mathbf{f}_A$ are resistance forces with respect to basic parameters $\mathbf{U}_C$ and additional parameters $\mathbf{U}_A$, respectively.

By defining the generalised membrane, bending, and transverse shear stresses as follows:

$$\mathbf{F}^{(k)} = \int_{h_{k-}}^{h_{k+}} \boldsymbol{\sigma}_p^{(k)} dz = h_k \mathbf{C}_p^{(k)} \boldsymbol{\varepsilon}_m^{(k)} \tag{6.17}$$

$$\mathbf{M}^{(k)} = \int_{h_{k-}}^{h_{k+}} \boldsymbol{\sigma}_p^{(k)} \left(z - z^{(k)}\right) dz = \frac{1}{12} h_k^3 \mathbf{C}_p^{(k)} \boldsymbol{\varepsilon}_b^{(k)} \tag{6.18}$$

$$\mathbf{Q}_{AS}^{(k)} = \int_{h_{k-}}^{h_{k+}} \boldsymbol{\sigma}_{s,AS}^{(k)} dz = \omega^{(k)} h_k \mathbf{C}_s^{(k)} \boldsymbol{\varepsilon}_s^{(k)} \tag{6.19}$$

Equation (6.16) is expressed in the following form:

$$\delta\mathbf{U}_C^T \mathbf{f}_C + \delta\mathbf{U}_A^T \mathbf{f}_A = \sum_{k=1}^{N_l} \int_{\Omega^e} \left(\delta\boldsymbol{\varepsilon}_m^{(k)T} \mathbf{F}^{(k)} + \delta\boldsymbol{\varepsilon}_b^{(k)T} \mathbf{M}^{(k)} + \delta\boldsymbol{\varepsilon}_s^{(k)T} \mathbf{Q}_{AS}^{(k)} \right) d\Omega^e, \ \forall\left(\delta\mathbf{U}_C, \delta\mathbf{U}_A\right) \tag{6.20}$$

Equation (6.20) can be further manipulated to:

$$\begin{aligned} &\delta\mathbf{U}_C^T \mathbf{f}_C + \delta\mathbf{U}_A^T \mathbf{f}_A = \\ &\sum_{k=1}^{N_l} \left(\delta\mathbf{U}_C^T \mathbf{T}_C^{(k)T} + \delta\mathbf{U}_A^T \mathbf{T}_A^{(k)T} \right) \int_{\Omega^e} \left(\mathbf{B}_m^{(k)T} \mathbf{D}_m^{(k)} \boldsymbol{\varepsilon}_m^{(k)} + \mathbf{B}_b^{(k)T} \mathbf{D}_b^{(k)} \boldsymbol{\varepsilon}_b^{(k)} + \mathbf{B}_s^{(k)T} \mathbf{D}_s^{(k)} \boldsymbol{\varepsilon}_s^{(k)} \right) d\Omega^e, \\ &\qquad \forall\left(\delta\mathbf{U}_C, \delta\mathbf{U}_A\right) \end{aligned} \tag{6.21}$$

where $\mathbf{B}_m^{(k)}$, $\mathbf{B}_b^{(k)}$ and $\mathbf{B}_s^{(k)}$ are the first derivatives of the generalised strains at layer (k) with respect to pseudo parameters $\mathbf{U}^{(k)}$; $\mathbf{D}_m^{(k)}$, $\mathbf{D}_b^{(k)}$, and $\mathbf{D}_s^{(k)}$ are generalised constitutive matrices at layer (k), which are expressed as:

$$\mathbf{D}_m^{(k)} = h_k \mathbf{C}_p^{(k)}, \quad \mathbf{D}_b^{(k)} = \frac{1}{12} h_k^3 \mathbf{C}_p^{(k)}, \quad \mathbf{D}_s^{(k)} = \omega^{(k)} h_k \mathbf{C}_s^{(k)} \tag{6.22}$$

In order to address the locking effects, the hierarchic optimisation approach, which is presented in Section 3.2 and instantiated for 9-noded and 6-noded monolithic shell elements in Section 3.4-3.5, is employed in the local formulation of each constitutive layer. It is worth noting that the optimal transformation between conforming and assumed strains depends only on the element geometry. Therefore, the transformation established for monolithic shell elements is also applicable for a specific set of generalised strains to all layers as well. After the application of the optimisation scheme at each constitutive layer, the conforming strains

$\boldsymbol{\varepsilon}_{\mathrm{m}}^{(\mathrm{k})}$, $\boldsymbol{\varepsilon}_{\mathrm{b}}^{(\mathrm{k})}$ and $\boldsymbol{\varepsilon}_{\mathrm{s}}^{(\mathrm{k})}$, and the matrices $\mathbf{B}_{\mathrm{m}}^{(\mathrm{k})}$, $\mathbf{B}_{\mathrm{b}}^{(\mathrm{k})}$ and $\mathbf{B}_{\mathrm{s}}^{(\mathrm{k})}$ in (6.21) are replaced by $\hat{\boldsymbol{\varepsilon}}_{\mathrm{m}}^{(\mathrm{k})}$, $\hat{\boldsymbol{\varepsilon}}_{\mathrm{b}}^{(\mathrm{k})}$, $\hat{\boldsymbol{\varepsilon}}_{\mathrm{s}}^{(\mathrm{k})}$, $\hat{\mathbf{B}}_{\mathrm{m}}^{(\mathrm{k})}$, $\hat{\mathbf{B}}_{\mathrm{b}}^{(\mathrm{k})}$ and $\hat{\mathbf{B}}_{\mathrm{s}}^{(\mathrm{k})}$ with '$\hat{\ }$' denoting the adoption of the objective assumed strains, or by $\tilde{\boldsymbol{\varepsilon}}_{\mathrm{m}}^{(\mathrm{k})}$, $\tilde{\boldsymbol{\varepsilon}}_{\mathrm{b}}^{(\mathrm{k})}$, $\tilde{\boldsymbol{\varepsilon}}_{\mathrm{s}}^{(\mathrm{k})}$, $\tilde{\mathbf{B}}_{\mathrm{m}}^{(\mathrm{k})}$, $\tilde{\mathbf{B}}_{\mathrm{b}}^{(\mathrm{k})}$ and $\tilde{\mathbf{B}}_{\mathrm{s}}^{(\mathrm{k})}$ with '$\tilde{\ }$' denoting the adoption of the corrective assumed strains.

Considering (6.21), the total resistance forces of the shell element associated with the local nodal parameters $\mathbf{U}_{\mathrm{C}}$ and the additional parameters $\mathbf{U}_{\mathrm{A}}$ are thus obtained as:

$$\mathbf{f}_{\mathrm{C}} = \sum_{\mathrm{k}=1}^{\mathrm{N}_1}\left(\mathbf{T}_{\mathrm{C}}^{(\mathrm{k})\mathrm{T}}\mathbf{f}^{(\mathrm{k})}\right), \quad \mathbf{f}_{\mathrm{A}} = \sum_{\mathrm{k}=1}^{\mathrm{N}_1}\left(\mathbf{T}_{\mathrm{A}}^{(\mathrm{k})\mathrm{T}}\mathbf{f}^{(\mathrm{k})}\right) \tag{6.23}$$

where $\mathbf{f}^{(\mathrm{k})}$ is the vector of pseudo nodal forces at layer (k), with the objective strain form expressed as:

$$\mathbf{f}^{(\mathrm{k})} = \int_{\Omega^{\mathrm{e}}}\left(\hat{\mathbf{B}}_{\mathrm{m}}^{(\mathrm{k})\mathrm{T}}\mathbf{D}_{\mathrm{m}}^{(\mathrm{k})}\hat{\boldsymbol{\varepsilon}}_{\mathrm{m}}^{(\mathrm{k})} + \hat{\mathbf{B}}_{\mathrm{b}}^{(\mathrm{k})\mathrm{T}}\mathbf{D}_{\mathrm{b}}^{(\mathrm{k})}\hat{\boldsymbol{\varepsilon}}_{\mathrm{b}}^{(\mathrm{k})} + \hat{\mathbf{B}}_{\mathrm{s}}^{(\mathrm{k})\mathrm{T}}\mathbf{D}_{\mathrm{s}}^{(\mathrm{k})}\hat{\boldsymbol{\varepsilon}}_{\mathrm{s}}^{(\mathrm{k})}\right)\mathrm{d}\Omega^{\mathrm{e}} \tag{6.24}$$

Furthermore, the local tangent stiffness matrices of the element are obtained as:

$$\mathbf{k}_{\mathrm{C}} = \frac{\partial \mathbf{f}_{\mathrm{C}}}{\partial \mathbf{U}_{\mathrm{C}}^{\mathrm{T}}} = \sum_{\mathrm{k}=1}^{\mathrm{N}_1}\left(\mathbf{T}_{\mathrm{C}}^{(\mathrm{k})\mathrm{T}}\mathbf{k}^{(\mathrm{k})}\mathbf{T}_{\mathrm{C}}^{(\mathrm{k})}\right), \quad \mathbf{k}_{\mathrm{A}} = \frac{\partial \mathbf{f}_{\mathrm{A}}}{\partial \mathbf{U}_{\mathrm{A}}^{\mathrm{T}}} = \sum_{\mathrm{k}=1}^{\mathrm{N}_1}\left(\mathbf{T}_{\mathrm{A}}^{(\mathrm{k})\mathrm{T}}\mathbf{k}^{(\mathrm{k})}\mathbf{T}_{\mathrm{A}}^{(\mathrm{k})}\right) \tag{6.25}$$

$$\mathbf{k}_{\mathrm{CA}} = \mathbf{k}_{\mathrm{AC}}^{\mathrm{T}} = \frac{\partial \mathbf{f}_{\mathrm{C}}}{\partial \mathbf{U}_{\mathrm{A}}^{\mathrm{T}}} = \sum_{\mathrm{k}=1}^{\mathrm{N}_1}\left(\mathbf{T}_{\mathrm{C}}^{(\mathrm{k})\mathrm{T}}\mathbf{k}^{(\mathrm{k})}\mathbf{T}_{\mathrm{A}}^{(\mathrm{k})}\right) \tag{6.26}$$

where $\mathbf{k}^{(\mathrm{k})}$ is the local stiffness of layer (k), with the objective strain form expressed as:

$$\mathbf{k}^{(\mathrm{k})} = \int_{\Omega^{\mathrm{e}}}\left(\hat{\mathbf{B}}_{\mathrm{m}}^{(\mathrm{k})\mathrm{T}}\mathbf{D}_{\mathrm{m}}^{(\mathrm{k})}\hat{\mathbf{B}}_{\mathrm{m}}^{(\mathrm{k})} + \hat{\mathbf{B}}_{\mathrm{b}}^{(\mathrm{k})\mathrm{T}}\mathbf{D}_{\mathrm{b}}^{(\mathrm{k})}\hat{\mathbf{B}}_{\mathrm{b}}^{(\mathrm{k})} + \hat{\mathbf{B}}_{\mathrm{s}}^{(\mathrm{k})\mathrm{T}}\mathbf{D}_{\mathrm{s}}^{(\mathrm{k})}\hat{\mathbf{B}}_{\mathrm{s}}^{(\mathrm{k})} + \frac{\partial^2 \hat{\boldsymbol{\varepsilon}}_{\mathrm{m}}^{(\mathrm{k})\mathrm{T}}}{\partial \mathbf{U}^{(\mathrm{k})}\partial \mathbf{U}^{(\mathrm{k})\mathrm{T}}}\mathbf{D}_{\mathrm{m}}^{(\mathrm{k})}\hat{\boldsymbol{\varepsilon}}_{\mathrm{m}}^{(\mathrm{k})}\right)\mathrm{d}\Omega^{\mathrm{e}} \tag{6.27}$$

It is worth noting that for the considered isotropic and orthotropic material models $\mathbf{k}^{(\mathrm{k})}$ is a symmetric matrix, which leads to $\mathbf{k}_{\mathrm{AC}}$ being the transpose of $\mathbf{k}_{\mathrm{CA}}$. For certain types of nonlinear materials, however, $\mathbf{k}^{(\mathrm{k})}$ may not be symmetric, which requires to determine $\mathbf{k}_{\mathrm{AC}}$ as follows:

$$\mathbf{k}_{AC} = \frac{\partial \mathbf{f}_A}{\partial \mathbf{U}_C^T} = \sum_{k=1}^{N_l} \left(\mathbf{T}_A^{(k)T} \mathbf{k}^{(k)} \mathbf{T}_C^{(k)} \right) \tag{6.28}$$

6.5.4 Co-rotational transformation of resistance forces and stiffness

In accordance with the co-rotational approach, the local resistance forces and stiffness matrices of the sandwich shell element are transformed to the corresponding global system entities before assembly at the overall structural level. It is important to note that the relationship between additional parameters defined in the shell system and their counterparts in the element local system is directly considered by incorporating $(\hat{c}, \hat{s})$ into $\mathbf{T}_a^{(k)}$, as given in (6.7). Furthermore, the resistance forces vector $\mathbf{f}_A$ and the stiffness matrix $\mathbf{k}_A$ are excluded from the co-rotational transformations, since the associated zigzag parameters are defined at the overall structural level in the shell system, which maintains the same relative orientation to the local co-rotational system in the deformed configuration.

The transformation of the resistant forces and stiffness matrices to the global coordinate system are given as:

$$\mathbf{f}_G = \mathbf{T}^T \mathbf{f}_C \tag{6.29}$$

$$\mathbf{k}_G = \frac{\partial \mathbf{f}_G}{\partial \mathbf{U}_G^T} = \mathbf{T}^T \mathbf{k}_C \mathbf{T} + \frac{\partial^2 \mathbf{U}_C^T}{\partial \mathbf{U}_G \partial \mathbf{U}_G^T} \mathbf{f}_C \tag{6.30}$$

$$\mathbf{k}_{GA} = \mathbf{k}_{AG}^T = \frac{\partial \mathbf{f}_G}{\partial \mathbf{U}_A^T} = \mathbf{T}^T \mathbf{k}_{CA} \tag{6.31}$$

in which $\mathbf{T}$ is the nodal displacement transformation matrix from global parameters $\mathbf{U}_G$ to co-rotational parameters $\mathbf{U}_C$ (Izzuddin, 2005; Izzuddin & Liang, 2015), defined as:

$$\mathbf{T} = \frac{\partial \mathbf{U}_C}{\partial \mathbf{U}_G^T} \tag{6.32}$$

Still, for the considered materials, the stiffness matrix $\mathbf{k}_{AG}$ is the transpose of the stiffness matrix $\mathbf{k}_{GA}$, owing to a symmetric local stiffness of each layer (k), $\mathbf{k}^{(k)}$. Otherwise, $\mathbf{k}_{AG}$ can be derived from:

$$\mathbf{k}_{AG} = \frac{\partial \mathbf{f}_A}{\partial \mathbf{U}_G^T} = \mathbf{k}_{AC}\mathbf{T} \tag{6.33}$$

6.6 Consistent mass matrices

The local mass matrix for each layer (k) can be obtained as in Section 3.6.1 except that the layer density ρ_k and layer thickness h_k are used, which results in the layer mass matrix expressed as follows:

$$\mathbf{M}^{(k)} = \begin{bmatrix} \mathbf{M}_{11}^{(k)} & \mathbf{M}_{12}^{(k)} & \cdots & \mathbf{M}_{1N_e}^{(k)} \\ \mathbf{M}_{21}^{(k)} & \mathbf{M}_{22}^{(k)} & \cdots & \mathbf{M}_{2N_e}^{(k)} \\ \vdots & \vdots & \ddots & \vdots \\ \mathbf{M}_{N_e1}^{(k)} & \mathbf{M}_{N_e2}^{(k)} & \cdots & \mathbf{M}_{N_eN_e}^{(k)} \end{bmatrix}, \quad \mathbf{M}_{ij}^{(k)} = \begin{bmatrix} m_t^{(k)} & & & & \\ & m_t^{(k)} & & & \\ & & m_t^{(k)} & & \\ & & & m_r^{(k)} & \\ & & & & m_r^{(k)} \end{bmatrix} \mathbf{\Gamma}_{ij}^{M} \tag{6.34}$$

where $\mathbf{\Gamma}_{ij}^{M}$ can be obtained from (3.65) and $m_t^{(k)}$ and $m_r^{(k)}$ are given as follows:

$$m_t^{(k)} = \rho_k h_k, \quad m_r^{(k)} = \frac{\rho_k h_k^3}{12} \tag{6.35}$$

Since the same through-thickness description is employed for the acceleration fields as those used in displacement fields, the local mass matrices are given as:

$$\mathbf{M}_C = \sum_{k=1}^{N_l} \left(\mathbf{T}_C^{(k)T} \mathbf{M}^{(k)} \mathbf{T}_C^{(k)} \right), \quad \mathbf{M}_A = \sum_{k=1}^{N_l} \left(\mathbf{T}_A^{(k)T} \mathbf{M}^{(k)} \mathbf{T}_A^{(k)} \right) \tag{6.36}$$

$$\mathbf{M}_{CA} = \mathbf{M}_{AC}^T = \sum_{k=1}^{N_l} \left(\mathbf{T}_C^{(k)T} \mathbf{M}^{(k)} \mathbf{T}_A^{(k)} \right) \tag{6.37}$$

It is worth noting that the layer mass matrix $\mathbf{M}^{(k)}$ is symmetric, evident from (6.34) and (3.65). Therefore, $\mathbf{M}_{AC}$ is always the transpose of $\mathbf{M}_{CA}$.

Furthermore, the transformation of $\mathbf{M}_C$, $\mathbf{M}_{CA}$, and $\mathbf{M}_{AC}$ to global system gives:

$$\mathbf{M}_G = \mathbf{T}^{oT} \mathbf{M}_C \mathbf{T}^o \tag{6.38}$$

$$\mathbf{M}_{GA} = \mathbf{M}_{AG}^{T} = \mathbf{T}^{oT}\mathbf{M}_{CA} \tag{6.39}$$

where $\mathbf{T}^{o}$ represents the element transformation matrix from global to local DOFs of the previous time step, as given in (3.67) following the same updated Lagrangian approach discussed in Section 3.6.2. Still, the symmetric layer mass matrix $\mathbf{M}^{(k)}$ leads to $\mathbf{M}_{AG}$ being always the transpose of $\mathbf{M}_{GA}$.

The above formula leads to a mass matrix for laminated shell elements, where the accelerations are assumed to have the same through-thickness distribution as the displacements. Even so, for the considered dynamic analyses in the rest of this thesis, a consistent mass matrix that ignores the mass associated with additional parameters is used for the laminated shell elements, which is owing to the negligible contribution of the mass associated with additional parameters on the overall mass matrix for slender LG applications. Therefore, instead of the above formulation for the mass matrix, the consistent mass matrix for monolithic shell elements provided in Section 3.6 is used for the laminated shell elements in this work. Accordingly, the mass matrix for the laminated shell elements can be obtained by employing (3.64)-(3.68) except that the density ρ in (3.65) requires to be replaced with the average density of the whole LG cross-section.

6.7 Verification of laminated shell elements

The proposed 6-noded and 9-noded multi-layered shell elements have been implemented in ADAPTIC v2.14.2 (Izzuddin, 1991), which is used hereafter in several verification examples to demonstrate their accuracy and effectiveness in modelling linear and nonlinear problems. In the following examples, the locking phenomena is addressed by employing the objective alternative based on third order hierarchic optimisation for each layer. The proposed quadrilateral and triangular laminated shell elements are denoted by acronyms L*n*-H3O9 and L*n*-H3O6, respectively, with 'L' representing 'layer' and *n* the number of layers.

6.7.1 Linear problems

6.7.1.1 Sandwich plate under bidirectional sinusoidal loading

A square sandwich plate, simply-supported along all four edges, is subjected to a bidirectional sinusoidal transverse loading $p = p_0 \sin(\pi x/a)\sin(\pi y/a)$, as depicted in Figure 6.7, where consideration is given here to the linear elastic response. The edge length of the square plate is a, and the thickness is h (with $h_1 = h_3 = 0.1h$ and $h_2 = 0.8h$). The material parameters of the layers are given as:

Core: $E_1^{(2)} = E_2^{(2)} = 0.4\times10^5, G_{12}^{(2)} = 0.16\times10^5, G_{13}^{(2)} = G_{23}^{(2)} = 0.6\times10^5, \nu_{12}^{(2)} = 0.25;$

Face: $E_1^{(1,3)} = 2.5\times10^7, E_2^{(1,3)} = 1.0\times10^6, G_{12}^{(1,3)} = G_{13}^{(1,3)} = 0.5\times10^6, G_{23}^{(1,3)} = 0.2\times10^6, \nu_{12}^{(1,3)} = 0.25;$

where the 1- and 2- material directions for the layers are aligned respectively with the x- and y-axes.

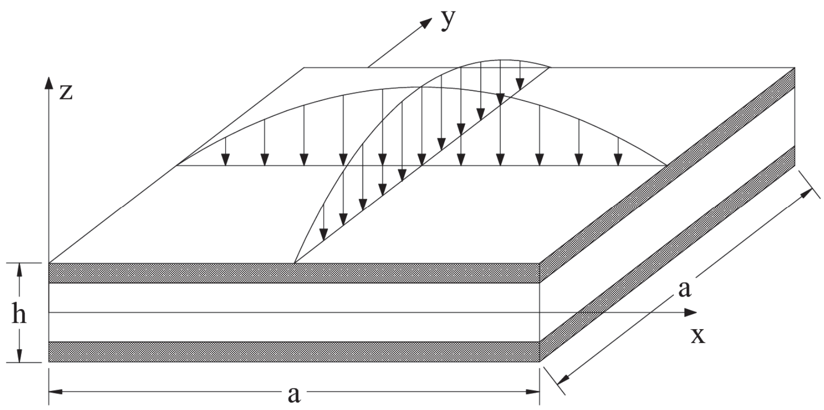

Figure 6.7: Simply-supported sandwich plate under bidirectional sinusoidal loading.

Different length-to-thickness ratios are considered, where due to symmetry only a quarter of the plate is analysed with a uniform 8×8 mesh of the L3-H3O9 element, which provides a convergent solution. The shell system is obtained according to the approach illustrated in Figure 6.3 with the reference triad $(\mathbf{c}_{\bar{X}}, \mathbf{c}_{\bar{Y}}, \mathbf{c}_{\bar{Z}})$ aligned with the global system triad, in which case the curvilinear shell triad maintains the same (x,y) directions for all elements. The elasticity solution by Pagano (1970) is used as a reference solution. Results from other researchers are also considered, including the FSDT solution by Pandya and Kant (1988) using a 2×2 mesh of 9-noded elements, the solution by Balah and Al-Ghamedy (2002) using a 16×16 mesh of 4-noded elements based on a third-order shear deformation theory (TSDT), the layer-wise theory (LWT) solution by Thai et al. (2013) employing an isogeometric approach with quartic B-spline basis, and a higher-order zigzag theory (ZZT) solution by Pandit et al. (2008) with a 12×12 mesh of 9-noded elements for the whole plate. The full results are provided in Table 6.1. Key displacement and stress values are assessed with the corresponding dimensionless results defined as follows:

$$\bar{u}_z = \frac{100E_2^{(1,3)}h^3 u_z\left(\frac{a}{2},\frac{a}{2},0\right)}{p_0 a^4},\ \bar{\sigma}_x = \frac{h^2\sigma_x\left(\frac{a}{2},\frac{a}{2},\frac{h}{2}\right)}{p_0 a^2},\ \bar{\sigma}_y = \frac{h^2\sigma_y\left(\frac{a}{2},\frac{a}{2},\frac{h}{2}\right)}{p_0 a^2}$$

$$\bar{\sigma}_{xz} = \frac{h\sigma_{xz}\left(0,\frac{a}{2},0\right)}{p_0 a},\ \bar{\sigma}_{yz} = \frac{h\sigma_{yz}\left(\frac{a}{2},0,0\right)}{p_0 a},\ \bar{\sigma}_{xy} = \frac{h^2\sigma_{xy}\left(0,0,\frac{h}{2}\right)}{p_0 a^2}$$

It is concluded from Table 6.1 that all the theories agree well for the thin sandwich plate (a/h=100), in particular the deflection and planar stresses. As (a/h) decreases, the zigzag effect on the plate behaviour becomes significant, which leads to a noticeable deviation of the FSDT solution from the reference solution for moderately thick sandwich plates (a/h=10). Although the TSDT solution provides improved accuracy over the FSDT results, its predictions are still not as accurate as those of the other three models owing to the employment of assumed displacement modes at the multi-layer level rather than at the layer level. The L3-H3O9 model, which describes the zigzag effect with only two additional displacement fields, exhibits comparable capability with the LWT, and ZZT models, both of which assume four additional displacement fields, in the approximation of both the deflection and stress components of moderately thick plates, which indicates the validity of the assumed additional displacement modes and distribution of transverse shear strains. Figure 6.8 depicts the through-thickness distributions of the considered stress components for the cases a/h=10 and 20, where the results of the L3-H3O9 model agree well with the LWT results by Thai et al. (2013), with more realistic distributions of transverse shear strains.

Table 6.1: Dimensionless deflection and stresses of a sandwich plate with various (a/h) ratios.

a/h	Model	$\bar{u}_z$	$\bar{\sigma}_x$	$\bar{\sigma}_y$	$\bar{\sigma}_{xz}$	$\bar{\sigma}_{yz}$	$\bar{\sigma}_{xy}$
100	FSDT (Pandya & Kant)	0.883	1.104	0.0546	0.2875	0.0270	-0.0435
	TSDT (Balah & Al-Ghamedy)	0.8903	1.0958	0.0548	0.3741	0.0342	-0.0436
	LWT (Thai et al.)	0.8924	1.0975	0.0549	0.3234	0.0291	-0.0437
	ZZT (Pandit et al.)	0.8917	1.1093	0.0547	0.3412	0.0324	-0.0434
	L3-H3O9	0.8923	1.1010	0.0551	0.3250	0.0288	-0.0438
	Elasticity (Pagano)	0.8923	1.0980	0.0550	0.3240	0.0297	-0.0437
50	LWT (Thai et al.)	0.9348	1.0989	0.0569	0.3225	0.0299	-0.0446
	ZZT (Pandit et al.)	0.9341	1.0948	0.0566	0.3403	0.0333	-0.0445
	L3-H3O9	0.9348	1.1023	0.0570	0.3242	0.0294	-0.0448
	Elasticity (Pagano)	0.9348	1.0990	0.0569	0.3230	0.0306	-0.0446
20	LWT (Thai et al.)	1.2262	1.1090	0.0697	0.3168	0.0352	-0.0511
	ZZT (Pandit et al.)	1.2254	1.1055	0.0694	0.3342	0.0392	-0.0509
	L3-H3O9	1.2264	1.1116	0.0699	0.3185	0.0347	-0.0513
	Elasticity (Pagano)	1.2264	1.1100	0.0700	0.3170	0.0361	-0.0511
10	FSDT (Pandya & Kant)	1.557	1.062	0.0806	0.2779	0.0364	-0.0553
	TSDT (Balah & Al-Ghamedy)	2.0830	1.1470	0.1040	0.3489	0.0578	-0.0687
	LWT (Thai et al.)	2.2011	1.1497	0.1090	0.2993	0.0513	-0.0712
	ZZT (Pandit et al.)	2.2002	1.1483	0.1086	0.3158	0.0570	-0.0709
	L3-H3O9	2.2049	1.1495	0.1093	0.3009	0.0509	-0.0714
	Elasticity (Pagano)	2.2004	1.1530	0.1104	0.3000	0.0527	-0.0707

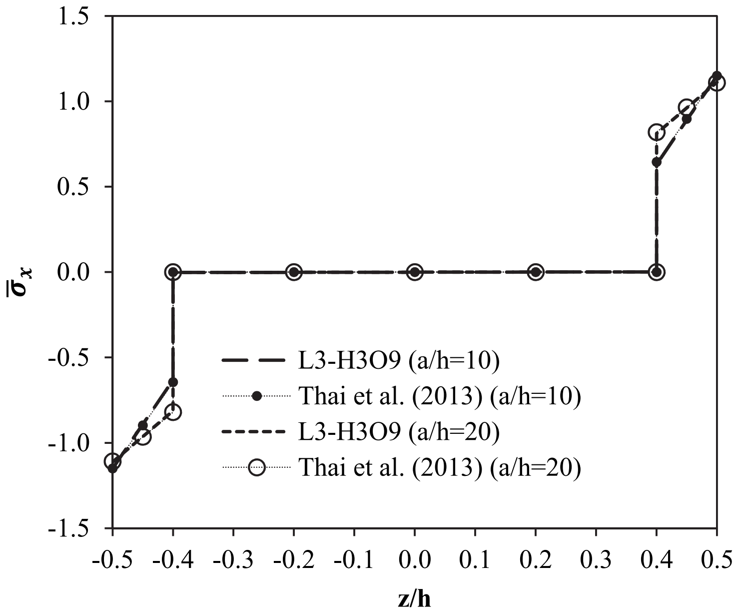

a. Through-thickness distribution of $\bar{\sigma}_x$

Figure 6.8: Through-thickness distribution of non-dimensional stresses for sandwich plate (Cont'd…).

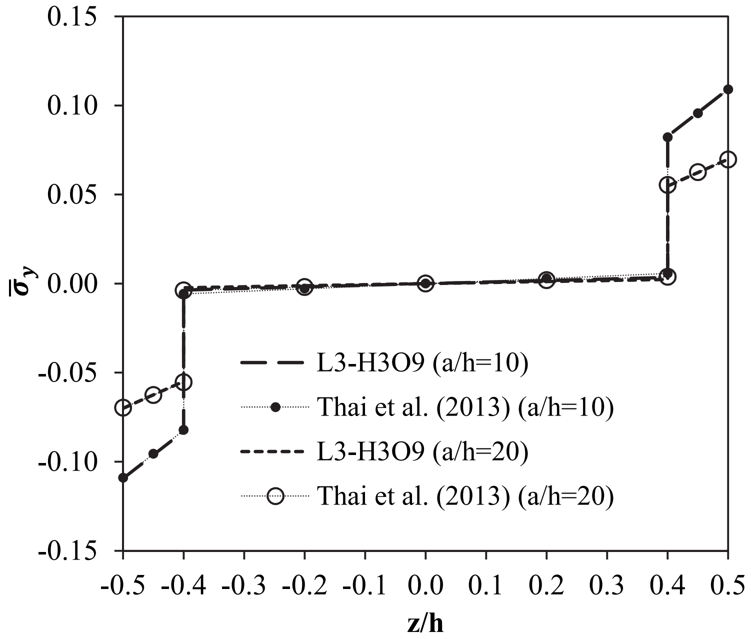

b. Through-thickness distribution of $\bar{\sigma}_y$

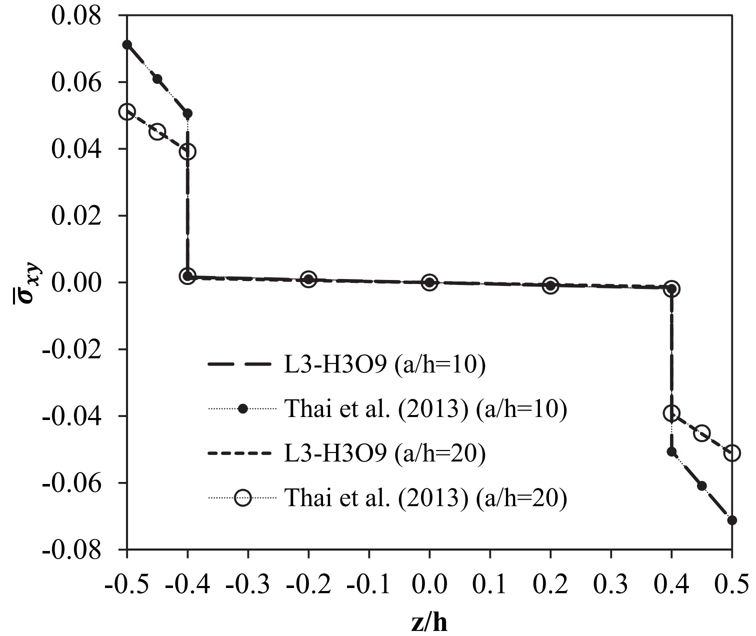

c. Through-thickness distribution of $\bar{\sigma}_{xy}$

Figure 6.8: Through-thickness distribution of non-dimensional stresses for sandwich plate (Cont'd…).

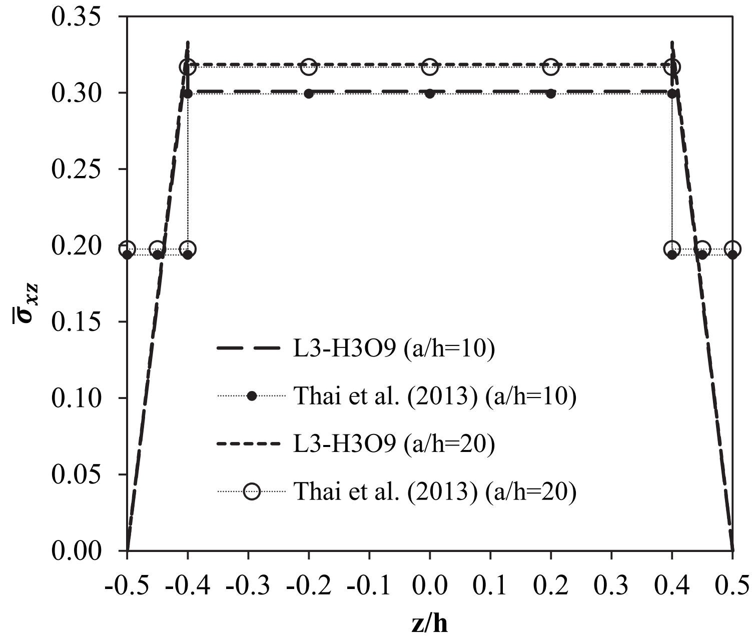

d. Through-thickness distribution of $\bar{\sigma}_{xz}$

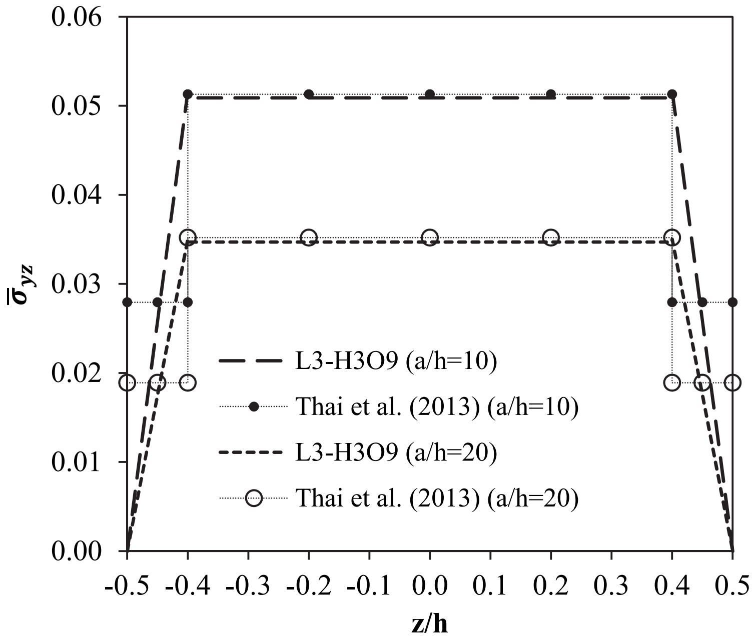

e. Through-thickness distribution of $\bar{\sigma}_{yz}$

Figure 6.8: Through-thickness distribution of non-dimensional stresses for sandwich plate.

6.7.1.2 Sandwich plate under uniformly distributed transverse loading

A simply-supported square sandwich plate is subjected to a uniformly distributed transverse loading p_0, as shown in Figure 6.9, where consideration is again given to the linear elastic response. The length-to-thickness ratio (a/h) of the plate is fixed to 10, and the thickness of each face sheet is 0.1h. The elastic constitutive matrix of the core is:

$$\mathbf{C}^{(2)} = \left[\begin{array}{c|c} \mathbf{C}_p^{(2)} & \mathbf{0} \\ \hline \mathbf{0} & \mathbf{C}_s^{(2)} \end{array}\right] = \left[\begin{array}{ccc|cc} 0.999781 & 0.231192 & 0 & 0 & 0 \\ 0.231192 & 0.524866 & 0 & 0 & 0 \\ 0 & 0 & 0.262931 & 0 & 0 \\ \hline 0 & 0 & 0 & 0.266810 & 0 \\ 0 & 0 & 0 & 0 & 0.159914 \end{array}\right]$$

The constitutive matrix of the faces is given by $\mathbf{C}^{(1)} = \mathbf{C}^{(3)} = \mathrm{FCSR} \cdot \mathbf{C}^{(2)}$, where the value of FCSR is alternatively taken as 5, 10, and 15. A quarter of the plate is modelled due to symmetry, and an 8×8 mesh of the L3-H3O9 elements provides a convergent solution. In this model, the shell system is aligned with the (x,y) planar coordinate system. The dimensionless transverse displacement and stresses at some key positions are assessed, which are defined as follows:

$$\bar{u}_z = \frac{0.999781 u_z\left(\frac{a}{2},\frac{a}{2},0\right)}{p_0 h},\ \bar{\sigma}_x^1 = \frac{\sigma_x^{(3)}\left(\frac{a}{2},\frac{a}{2},\frac{h}{2}\right)}{p_0},\ \bar{\sigma}_x^2 = \frac{\sigma_x^{(3)}\left(\frac{a}{2},\frac{a}{2},\frac{4h}{10}\right)}{p_0}$$

$$\bar{\sigma}_x^3 = \frac{\sigma_x^{(2)}\left(\frac{a}{2},\frac{a}{2},\frac{4h}{10}\right)}{p_0},\ \bar{\sigma}_y^1 = \frac{\sigma_y^{(3)}\left(\frac{a}{2},\frac{a}{2},\frac{h}{2}\right)}{p_0},\ \bar{\sigma}_y^2 = \frac{\sigma_y^{(3)}\left(\frac{a}{2},\frac{a}{2},\frac{4h}{10}\right)}{p_0}$$

$$\bar{\sigma}_y^3 = \frac{\sigma_y^{(2)}\left(\frac{a}{2},\frac{a}{2},\frac{4h}{10}\right)}{p_0},\ \bar{\sigma}_{xz} = \frac{\sigma_{xz}\left(0,\frac{a}{2},0\right)}{p_0}$$

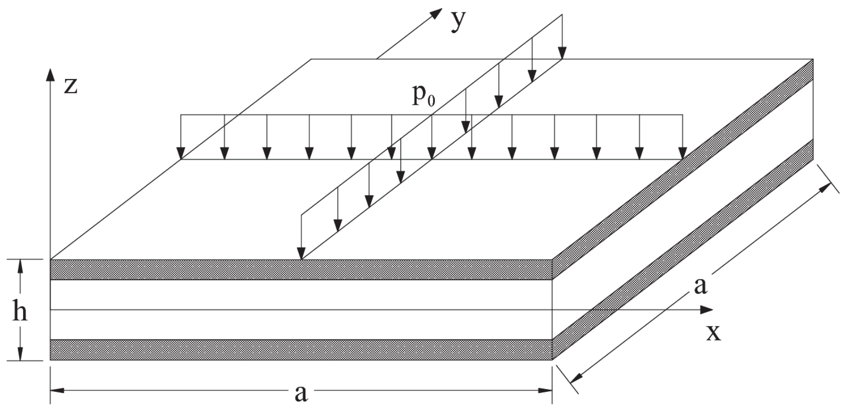

Figure 6.9: Simply-supported sandwich plate under uniformly distributed loading.

The results of the L3-H3O9 model are shown in Table 6.2, which are compared against the exact solution by Srinivas and Rao (1970). The FSDT and HSDT solution by Pandya and Kant (1988) and the LWT solution by Ferreira et al. (2008) are also given for comparison purposes. The results of a L3-H3O6 model with a mesh pattern as depicted in Figure 4.29 are also presented in the table.

It is clear that as the FCSR increases, the difference in the material properties between the faces and the core induces a significant zigzag effect of the sandwich plate, which leads to a deteriorating performance of the FSDT solution. The HSDT solution, despite showing an improvement in accuracy over the FSDT solution, still does not capture well the response of the sandwich shell, particularly when the stiffness ratio FCSR is relatively large. The 8×8 mesh of the L3-H3O9 elements provides better accuracy than the LWT solution in the approximation of both displacement and stresses owing to the employment of the assumed transverse shear strain distribution. It is also observed that the L3-H3O6 element has comparable accuracy with the L3-H3O9 element.

Table 6.2: Dimensionless deflection and stresses of a sandwich plate with various FCSRs.

FCSR	Model	$\bar{u}_z$	$\bar{\sigma}_x^1$	$\bar{\sigma}_x^2$	$\bar{\sigma}_x^3$	$\bar{\sigma}_y^1$	$\bar{\sigma}_y^2$	$\bar{\sigma}_y^3$	$\bar{\sigma}_{xz}$
5	FSDT (Pandya & Kant)	236.10	61.87	49.50	9.899	36.65	29.32	5.864	3.313
	HSDT (Pandya & Kant)	256.13	62.38	46.91	9.382	38.93	30.33	6.065	3.089
	LWT (Ferreira et al.)	258.180	60.063	46.393	9.279	38.364	30.029	6.006	4.095
	L3-H3O9	258.957	60.302	46.604	9.321	38.523	30.155	6.031	4.135
	L3-H3O6	258.957	60.347	46.634	9.327	38.519	30.150	6.030	4.125
	Elasticity (Srinivas & Rao)	258.970	60.353	46.623	9.340	38.491	30.097	6.161	4.364
10	FSDT (Pandya & Kant)	131.095	67.80	54.24	4.424	40.10	32.08	3.208	3.152
	HSDT(Pandya & Kant)	152.330	64.65	51.31	5.131	42.83	33.97	3.397	3.147
	LWT (Ferreira et al.)	158.912	64.993	48.601	4.860	43.491	33.409	3.341	3.980
	L3-H3O9	159.479	65.280	48.836	4.884	43.682	33.554	3.355	4.032
	L3-H3O6	159.479	65.332	48.866	4.887	43.678	33.547	3.355	4.017
	Elasticity (Srinivas & Rao)	159.380	65.332	48.857	4.903	43.566	33.413	3.500	4.096
15	FSDT (Pandya & Kant)	90.85	70.04	56.03	3.753	41.39	33.11	2.208	3.091
	HSDT(Pandya & Kant)	110.43	66.62	51.97	3.465	44.92	35.41	2.361	3.035
	LWT (Ferreira et al.)	121.347	66.436	48.010	3.201	46.385	34.965	2.331	3.902
	L3-H3O9	121.828	66.727	48.272	3.218	46.581	35.138	2.343	3.960
	L3-H3O6	121.828	66.783	48.300	3.220	46.576	35.128	2.342	3.942
	Elasticity (Srinivas & Rao)	121.720	66.787	48.299	3.238	46.424	34.955	2.494	3.964

6.7.1.3 Laminated plate under bidirectional sinusoidal loading

A laminated plate, which has a length-to-width ratio $b/a = 3$ and a plate thickness h, is simply supported on all four edges and transversely loaded with a bidirectional sinusoidal pressure $p = p_0 \sin(\pi x / a) \sin(\pi y / b)$ on its top surface, as shown in Figure 6.10. Four scenarios are considered in this linear elastic problem to assess the accuracy of the proposed multi-layer shell element:

Scenario 1: a 3-layer, asymmetrically laminated plate;

Scenario 2: a 5-layer, asymmetrically laminated plate;

Scenario 3: a 7-layer, symmetrically laminated plate with different thicknesses of stiff sheets;

Scenario 4: 3-, 5-, 7-, 9- and 11-layer, symmetrically laminated plate with the same thicknesses for all stiff sheets.

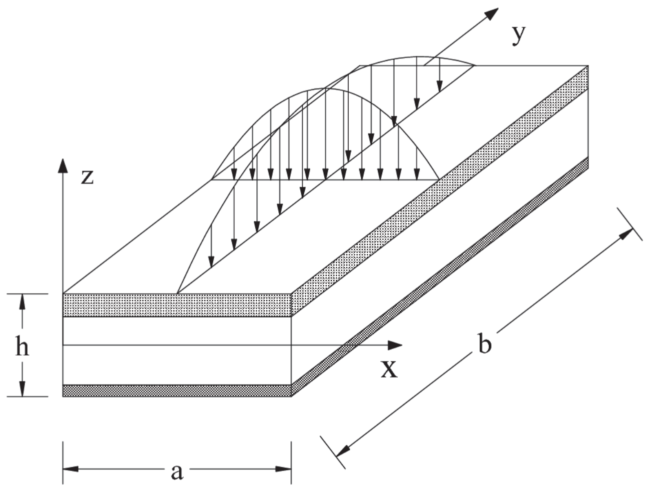

Figure 6.10: Rectangular laminated plate under bidirectional sinusoidal loading.

The elasticity solution for a general laminated plate loaded with a transverse bi-directional sinusoidal loading has been given by Demasi (2008). Brischetto et al. (2009) have presented closed form solutions with EDZ models for Scenario 1, where the zigzag effect of displacements is considered by adding MZZF to Taylor expansions. The results of EDZ models are compared with the results using the L*n*-H3O9 elements. On the other hand, 'EDZ*' formulations, which are based on EDZ models but with further simplifications, are also implemented with the 9-noded co-rotational element for comparison against the L*n*-H3O9 elements in Scenarios 2 to 4. It is important to note that three assumptions have been made which distinguish the implemented EDZ* formulations from the original EDZ models (Brischetto et al., 2009). Firstly the zigzag effect is considered in planar displacements only. Secondly, to facilitate the implementation of the EDZ*-H3O9 element, Taylor expansions are approximated with a piecewise linear curve based on values at the laminar interfaces, as illustrated in Figure 6.11. Thirdly, the proposed transverse shear strain distribution is used for EDZ*. Nevertheless, the aim of providing EDZ* results is to demonstrate the efficiency of the zigzag modes proposed in the present work for laminates with alternating stiff/soft lay-up. In this respect, the only difference between the EDZ*-H3O9 models and the L*n*-H3O9 models is the employed zigzag functions, which facilitates the comparison between both sets of additional displacement variables in modelling the considered laminations. Table 6.3 lists the number of displacement fields for the considered lamination models.

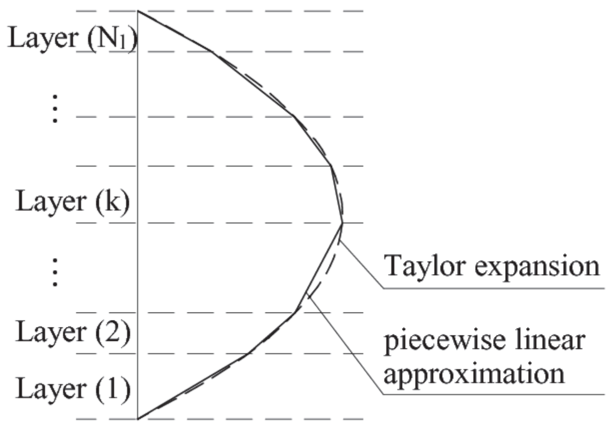

Figure 6.11: Piecewise approximation of Taylor expansion.

Table 6.3: Number of displacement fields for the considered models.

Model	Number of displacement fields
FSDT-H3O9	5
L3-H3O9	7
L5-H3O9	9
L7-H3O9	11
L9-H3O9	13
L11-H3O9	15
EDZ2*-H3O9	9
EDZ3*-H3O9	11
EDZ4*-H3O9	13
EDZ5*-H3O9	15
EDZ1 (Brischetto et al.)	9
EDZ4 (Brischetto et al.)	18
EDZ7 (Brischetto et al.)	27

Due to symmetry, a quarter of the plate is modelled with an 8×8 mesh of the L*n*-H3O9 elements, which provides a convergent solution for all four scenarios. In this model, the shell system is aligned with the (x,y) planar coordinate system The results of the L*n*-H3O9 model are compared against those of the EDZ or EDZ* models as well as the elasticity solution (Demasi, 2008) in terms of non-dimensional displacement, stress and strain values defined as follows:

$$\bar{u}_z = \frac{100 u_z E_{(C)}}{p_0 h (a/h)^4}, \quad \bar{\sigma}_x = \frac{\sigma_x}{p_0 (a/h)^2}, \quad \bar{\sigma}_{xz} = \frac{\sigma_{xz}}{p_0 (a/h)}, \quad \bar{\gamma}_{xz} = \frac{E_{(C)}}{2(1+\nu_{(C)})} \frac{\gamma_{xz}}{p_0 (a/h)}$$

where $E_{(C)}$ and $\nu_{(C)}$ are the Young’s modulus and Poisson’s ratio of soft core layers.

Scenario 1: Three-layer, asymmetrically laminated plate

The thicknesses of three layers are given as: $h_1 = h/10$, $h_2 = 7h/10$, and $h_3 = 2h/10$. All layers are made of isotropic material. The stiffness ratios between the constitutive layers are given as $E^{(1)}/E^{(3)} = 5/4$, and $FCSR \equiv E^{(1)}/E^{(2)} = 10, 10^5$. Poisson's ratios for all layers are 0.34. Two length-to-thickness ratios have been considered by Brischetto et al. with EDZ models (Brischetto et al., 2009): a/h=4, 100. Hereafter, the results of the L3-H3O9 models are compared with the FSDT and EDZ models.

Table 6.4 gives the predictions on central deflection $\bar{u}_z(a/2, b/2)$ at the bottom of the upper sheet with the considered models. Clearly, the L3-H3O9 model provides a much closer estimation of deflection than the EDZ1 model and even better results than the EDZ4 predictions, which utilise more displacement fields as indicated in Table 6.3, except where a/h = 4 and $FCSR = 10^5$, in which case the transverse elastic deformation for such a thick plate with very soft core is too significant to be neglected. Since the proposed model is intended for analysis of thin-to-moderately thick plates and shells, the neglect of the through-thickness variation in the transverse displacement still yields good results within the scope of interest.

Table 6.4: Relative accuracy of various models in the evaluation of central deflection.

a/h	Model	FCSR			
		10		10^5	
		$\bar{u}_z$	Relative error	$\bar{u}_z$	Relative error
4	Elasticity (Demasi)	3.01123	-	0.013159	-
	L3-H3O9	2.98319	0.93%	0.011907	9.51%
	FSDT-H3O9	1.58218	47.46%	0.000180	98.63%
	EDZ1 (Brischetto et al.)	2.34412	22.15%	0.000837	93.64%
	EDZ4 (Brischetto et al.)	2.97886	1.07%	0.012629	4.03%
	EDZ7 (Brischetto et al.)	2.99670	0.48%	0.013136	0.17%
100	Elasticity (Demasi)	1.51021	-	0.002089	-
	L3-H3O9	1.51026	0.00%	0.002089	0.01%
	FSDT-H3O9	1.10845	26.60%	0.000120	94.26%
	EDZ1 (Brischetto et al.)	1.15866	23.28%	0.000163	92.18%
	EDZ4 (Brischetto et al.)	1.51017	0.00%	0.001163	44.34%
	EDZ7 (Brischetto et al.)	1.51019	0.00%	0.002021	3.30%

The through-thickness variations of the planar stress $\overline{\sigma}_x$ (a/2, b/2) for the cases where a/h = 100 (thin plate) and FCSR=10, 10^5 are depicted in Figure 6.12, which highlight the accuracy of the L3-H3O9 model for a wide range of FCSR values. The noticeable deviation of the EDZ1 curve in Figure 6.12.b implies the inaccuracy of Murakami's function in capturing the zigzag effect. This deviation is alleviated with the use of higher-order EDZ models.

Figure 6.13 shows the through-thickness variations of the transverse shear stress $\overline{\sigma}_{xz}$ (0, b/2) for the cases where a/h = 4 (thick plate) and FCSR=10,10^5. Clearly, the continuous transverse shear stress predicted by the EDZ4 model posts a close approximation of the elasticity solution. On the other hand, the L3-H3O9 model, which assumes a piecewise linear-constant-linear transverse shear strain pattern, provides an accurate prediction of transverse shear stresses in the core, though discrepancies arise in the face sheets. With further manipulation, the through-thickness variation of the transverse shear strain $\overline{\gamma}_{xz}$ (0, b/2) for the case a/h = 4 and FCSR = 10 can be obtained for each model, as depicted in Figure 6.14. Clearly, the transverse shear strains in the face sheets are much smaller than the strain in the soft layer, which indicates negligible influence of the stiff layers on the overall transverse shear strain energy.

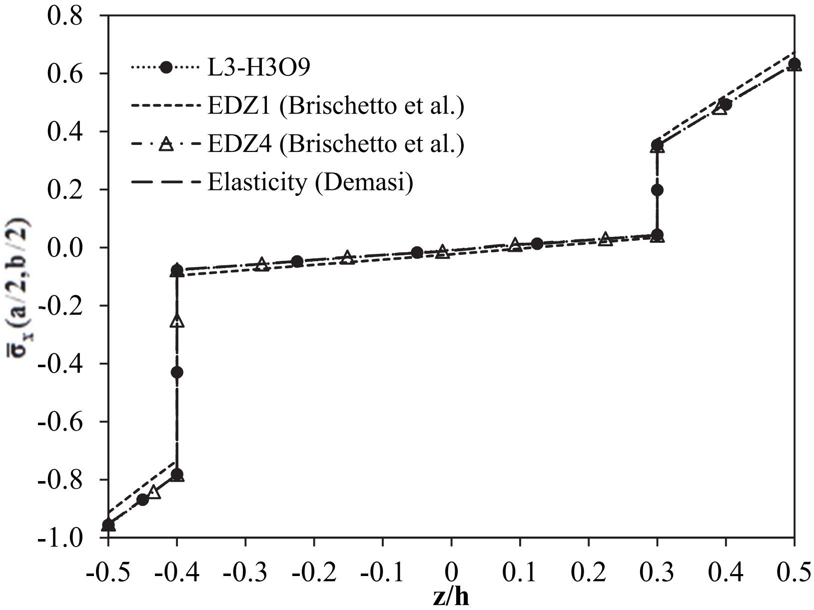

a. FCSR=10, and a/h=100

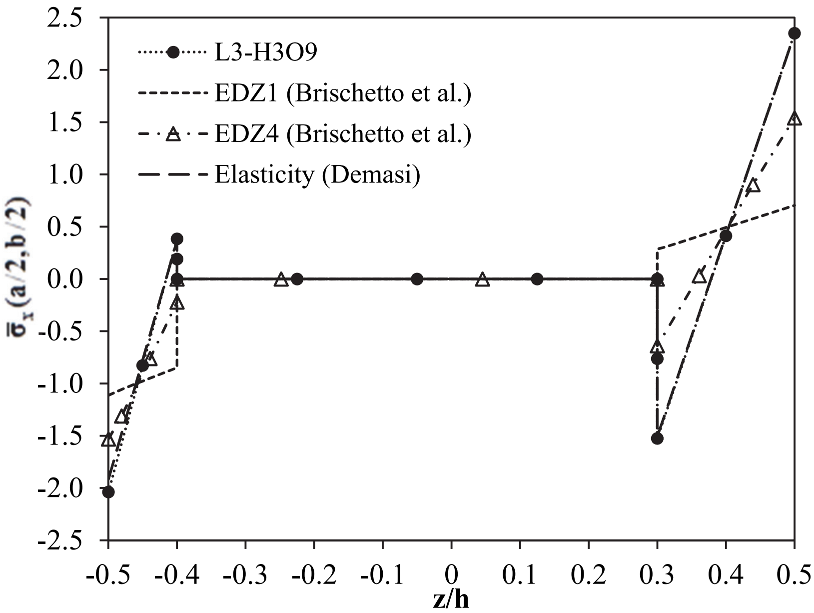

b. FCSR=10^5, and a/h=100

Figure 6.12: Through-thickness distribution of non-dimensional in-plane stress $\overline{\sigma}_x$ for three-layer plate.

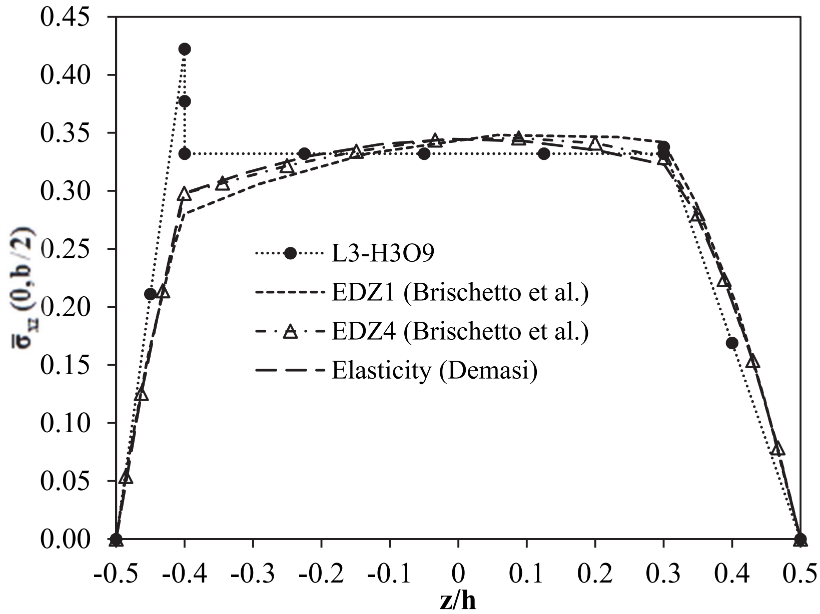

a. FCSR=10, and a/h=4

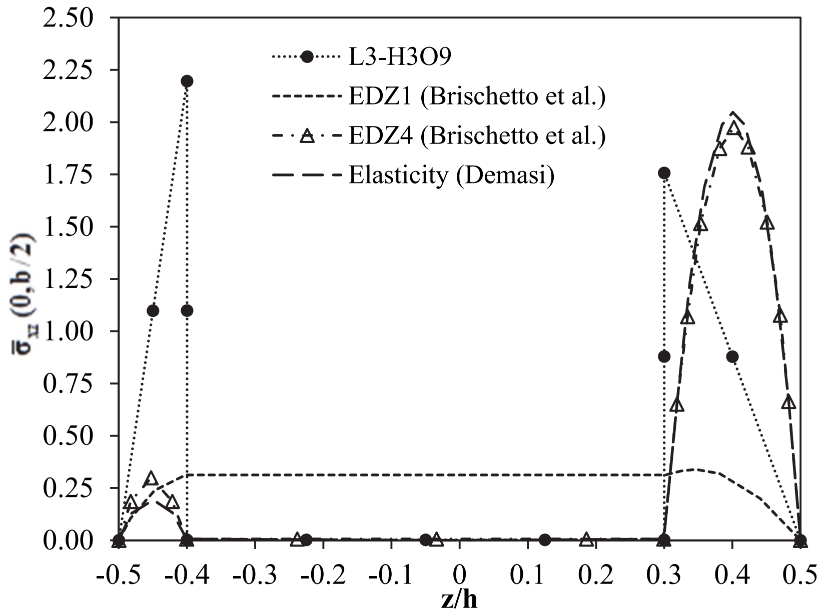

b. FCSR=10^5, and a/h=4

Figure 6.13: Through-thickness distribution of non-dimensional transverse shear stress $\bar{\sigma}_{xz}$ for three-layer plate.

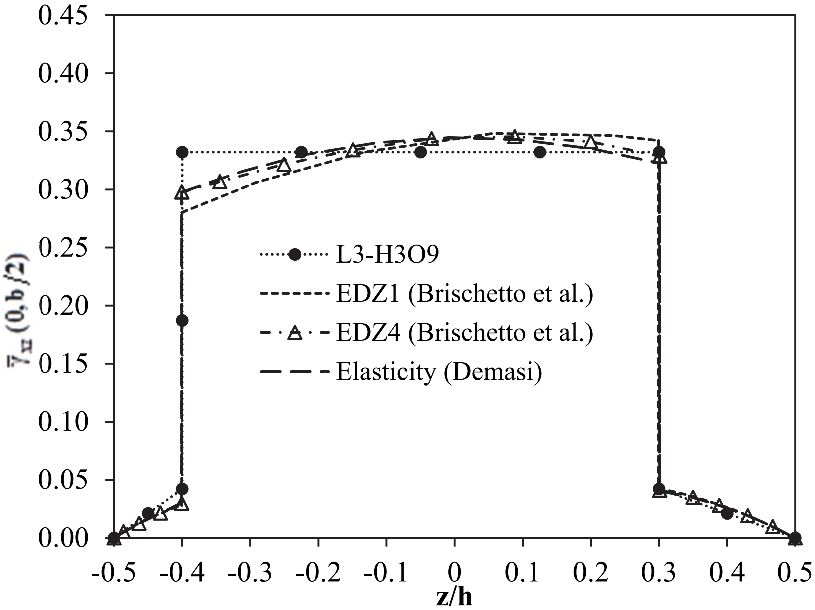

Figure 6.14: Through-thickness distribution of non-dimensional transverse shear strain $\overline{\gamma}_{xz}$ for three-layer plate (FCSR=10, and a/h=4).

<u>Scenario 2: Five-layer, asymmetrically laminated plate</u>

The layer thicknesses and materials of the five-layer laminated panel are given in Table 6.5, with $E_{(B)}/E_{(A)} = 4/5$, and $\nu_{(A)} = \nu_{(B)} = \nu_{(C)} = 0.34$. Different span-to-thickness ratios (a/h=10,100) and stiffness ratios ($FCSR \equiv E_{(A)}/E_{(C)} = 10, 10^3, 10^5$) are considered to investigate the performance of the shell element. Estimations of the non-dimensional central deflection $\overline{u}_z(a/2, b/2)$ at the bottom of the top layer with the L5-H3O9 and EDZ2*-H3O9 models, which have the same number of additional displacement variables, are listed in Table 6.6, compared against the elasticity solution. A FSDT solution is also available by restraining all the additional DOFs of the L5-H3O9 model in the analysis, although the assumed distribution of transverse shear strains is employed. Clearly, both models provide comparable accuracy for a relatively small FCSR = 10. However, the zigzag effect becomes significant as the FCSR increases, evident from the resulting large relative error of FSDT-H3O9 results. Although the EDZ2*-H3O9 model improves the FSDT-H3O9 results somewhat, still significant inaccuracy remains, hence requiring higher-order Taylor expansions for better accuracy. On the other hand, the L5-H3O9 model maintains high accuracy with a wide range of FCSRs owing to the efficiency of the selected zigzag displacement modes for the analysis of such laminations.

Table 6.5: Layer thicknesses and materials for 5-layer plate.

Layer index	Layer thickness	Layer material
1	(2/14)h	(B)
2	(5/14)h	(C)
3	(1/14)h	(A)
4	(5/14)h	(C)
5	(1/14)h	(A)

Table 6.6: Non-dimensional deflection of 5-layer plate with varying FCSR and (a/h).

a/h	Model	FCSR					
		10		10^3		10^5	
		$\bar{u}_z$	Relative error	$\bar{u}_z$	Relative error	$\bar{u}_z$	Relative error
10	Elasticity (Demasi)	2.02302	-	0.22248	-	0.02572	-
	L5-H3O9	2.03898	0.79%	0.22096	0.68%	0.02548	0.94%
	EDZ2*-H3O9	2.02446	0.07%	0.06702	69.88%	0.00080	96.88%
	FSDT-H3O9	1.90176	5.99%	0.02153	90.32%	0.00022	99.16%
100	Elasticity (Demasi)	1.81666	-	0.02252	-	0.00220	-
	L5-H3O9	1.81738	0.04%	0.02253	0.05%	0.00221	0.38%
	EDZ2*-H3O9	1.81724	0.03%	0.02086	7.39%	0.00021	90.45%
	FSDT-H3O9	1.81601	0.04%	0.02039	9.48%	0.00020	90.73%

The through-thickness distribution of the non-dimensional planar stress $\bar{\sigma}_x(a/2, b/2)$ for the cases where a/h = 100 (thin plate) and FCSR=10,10^3 with the L5-H3O9 model is depicted in Figure 6.15, and the elasticity result using Demasi's solution (Demasi, 2008) is also depicted for comparison. The figure highlights the accuracy of the L5-H3O9 model for a wide range of the FCSR values. Figure 6.16 depicts the non-dimensional transverse shear strain $\bar{\gamma}_{xz}$ of the L5-H3O9 model at location (0, b/2), compared against the elasticity results. The results also indicate the adequacy of the proposed transverse shear strain distribution for the problem considered.

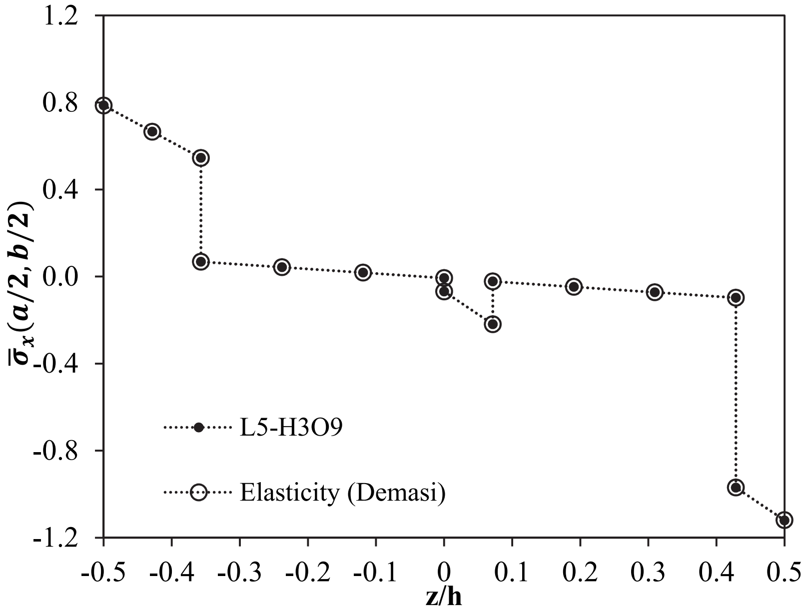

a. FCSR=10, and a/h=100

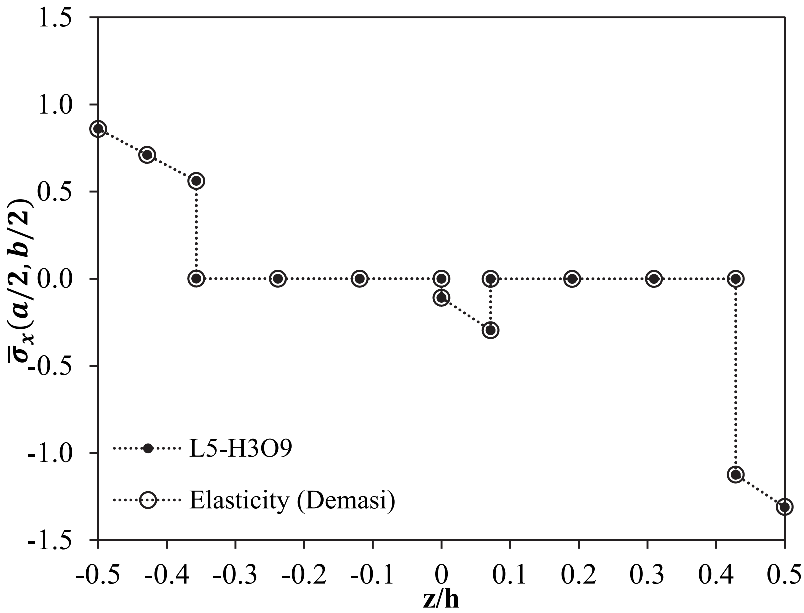

b. FCSR=10^3, and a/h=100

Figure 6.15: Through-thickness distribution of non-dimensional planar stress $\overline{\sigma}_x$ for five-layered plate.

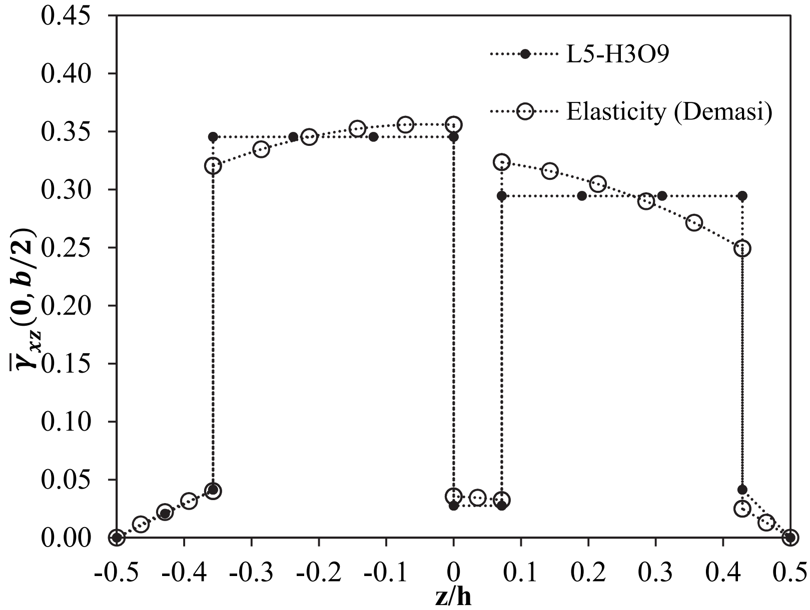

a. FCSR=10, and a/h=10

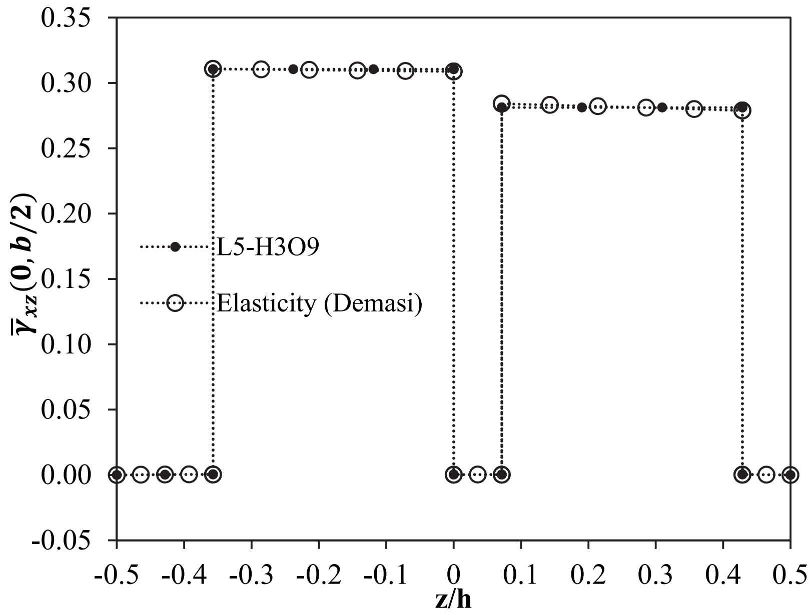

b. FCSR=10^3, and a/h=10

Figure 6.16: Through-thickness distribution of non-dimensional transverse shear strain $\overline{\gamma}_{xz}$ for five-layered plate.

Scenario 3: Seven-layer, symmetrically laminated plate with thicker external layers

In this scenario, the effect of different thicknesses on the accuracy of the zigzag functions is investigated. The layer thicknesses and materials of the seven-layer laminated plate are given in Table 6.7, with $\mathrm{FCSR} \equiv E_{(F)}/E_{(C)}$, and $\nu_{(F)} = \nu_{(C)} = 0.34$. Different span-to-thickness ratios (a/h = 10, 100) and stiffness ratios ($\mathrm{FCSR} = 10, 10^3, 10^5$) are considered to investigate the performance of the shell element.

Table 6.7: Layer thicknesses and materials for 7-layer plate.

Layer index	Layer thickness	Layer material
1	(2/21)h	(F)
2	(5/21)h	(C)
3	(1/21)h	(F)
4	(5/21)h	(C)
5	(1/21)h	(F)
6	(5/21)h	(C)
7	(2/21)h	(F)

Table 6.8: Non-dimensional deflection of 7-layer plate with varying FCSR and (a/h).

a/h	Model	FCSR					
		10		10^3		10^5	
		$\bar{u}_z$	Relative error	$\bar{u}_z$	Relative error	$\bar{u}_z$	Relative error
10	Elasticity (Demasi)	1.8341	-	0.22225	-	0.03861	-
	L7-H3O9	1.8448	0.59%	0.22083	0.64%	0.03744	3.02%
	EDZ3*-H3O9	1.8452	0.61%	0.21799	1.91%	0.02760	28.51%
	FSDT-H3O9	1.7020	7.20%	0.01903	91.44%	0.00019	99.51%
100	Elasticity (Demasi)	1.6245	-	0.02001	-	0.00220	-
	L7-H3O9	1.6253	0.05%	0.02002	0.06%	0.00221	0.58%
	EDZ3*-H3O9	1.6253	0.05%	0.02002	0.05%	0.00218	0.72%
	FSDT-H3O9	1.6238	0.04%	0.01789	10.57%	0.00018	91.84%

Estimations of the non-dimensional central deflection $\bar{u}_z(a/2, b/2)$ at the bottom of the top layer with various models are listed in Table 6.8, compared against the elasticity solution. Similar to Scenario 2, the L7-H3O9 and EDZ3*-H3O9 models provide comparable accuracy for a relatively small FCSR = 10. As the stiffness mismatch becomes very significant, the L7-H3O9 model shows better accuracy than the EDZ3*-H3O9 model, which have the same number of zigzag displacement fields.

The through-thickness distribution of the non-dimensional $\overline{\sigma}_x(a/2, b/2)$ and $\overline{\gamma}_{xz}(0, b/2)$ for the L7-H3O9 model are depicted in Figures 6.17-6.18, compared against the elasticity results using Demasi's solution (Demasi, 2008), where the comparison confirms the accuracy of the L7-H3O9 model for a wide range of FCSR values.

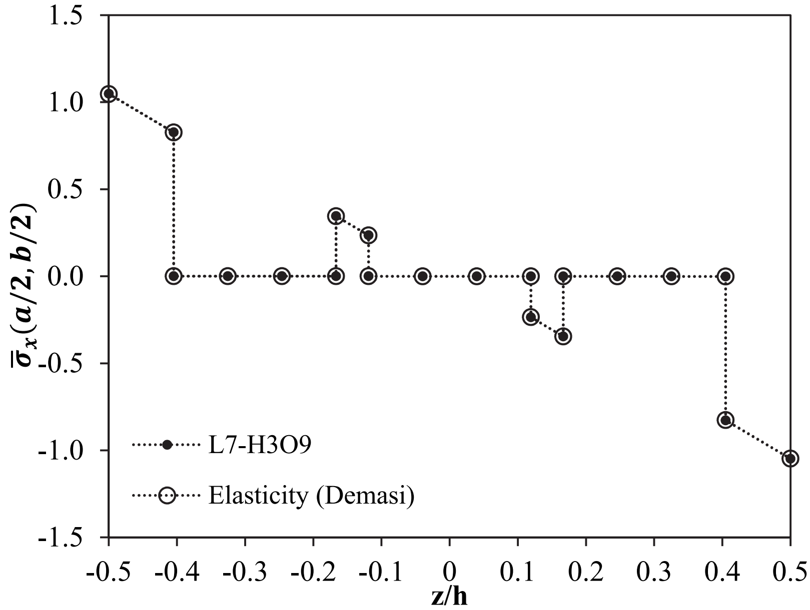

a. FCSR=10, and a/h=100

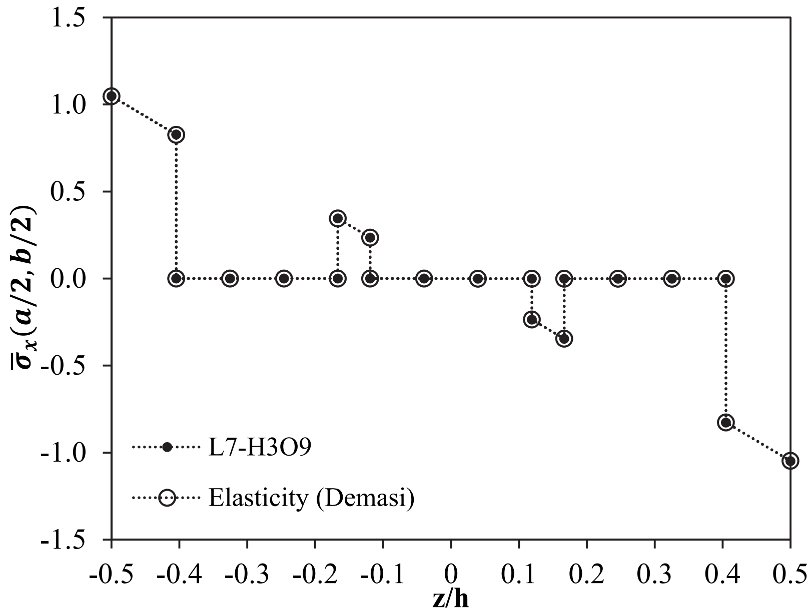

b. FCSR=10^3, and a/h=100

Figure 6.17: Through-thickness distribution of non-dimensional planar stress $\overline{\sigma}_x$ for seven-layered plate.

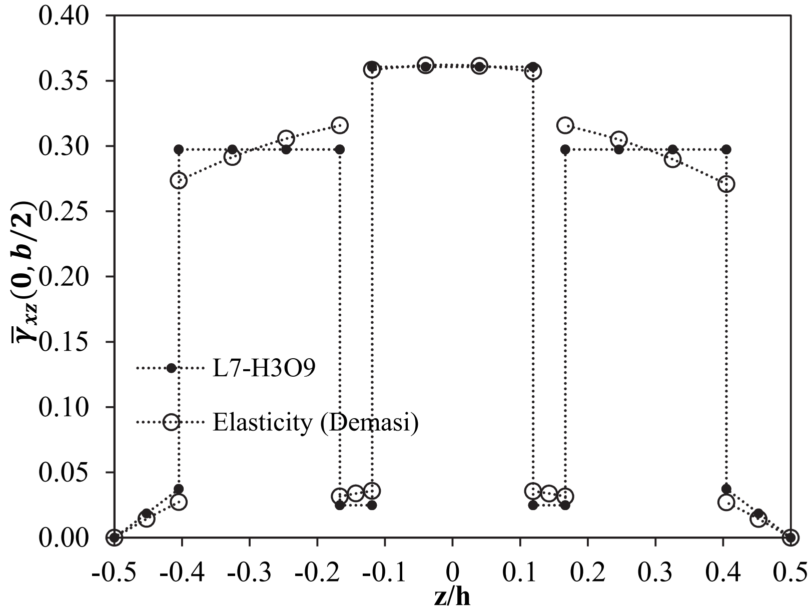

a. FCSR=10, and a/h=10

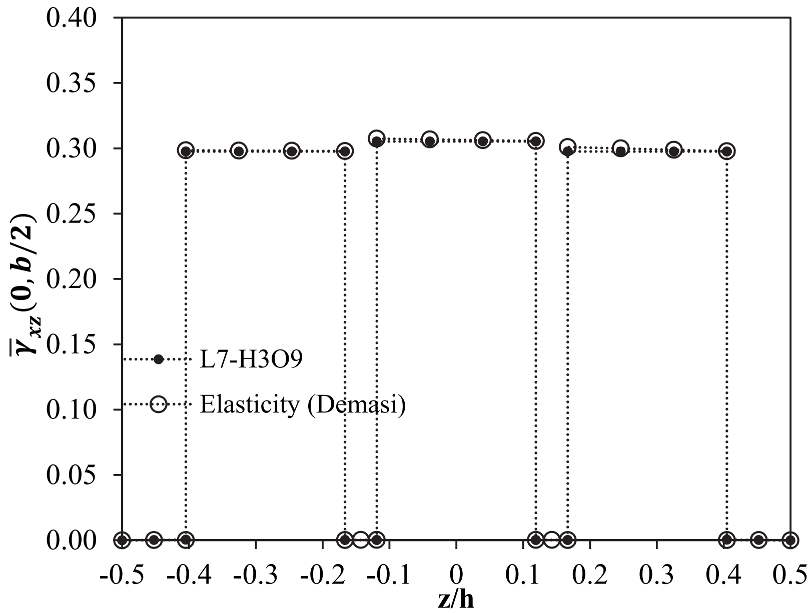

b. FCSR=10^3, and a/h=10

Figure 6.18: Through-thickness distribution of non-dimensional transverse shear strain $\bar{\gamma}_{xz}$ for seven-layered plate.

<u>Scenario 4: Symmetrically laminated plate with same face sheets and core sheets</u>

In this scenario, the laminated plate is composed of the same face sheets and the same cores in an (F/C/F/…/F/C/F) lay-up. The material properties of the face sheet and the core are given as $E_{(F)}/E_{(C)} = 1000$, and $\nu_{(F)} = \nu_{(C)} = 0.34$, while the span-to-thickness ratio is (a/h = 10). This problem is analysed for the cases of 5, 7, 9 and 11 layers, in all of which the plate thickness remains h. Two stiff-to-soft layer thickness ratios $(h_{(F)}/h_{(C)} = 1/5, 5)$ are considered to investigate the performance of the shell models. The estimated non-dimensional central deflection $\bar{u}_z(a/2, b/2)$ at the bottom of the top layer with L*n*-H3O9 and EDZ*-H3O9 models for different lay-ups are given in Table 6.9, compared with the elasticity solution. It is clear that as the number of layers increases, the L*n*-H3O9 model provides better accuracy than the EDZ*-H3O9 model, which verifies the efficiency of the proposed zigzag modes in the analysis of laminations with an alternating stiff/soft lay-up. Note that the L3-H3O9 and the EDZ1* models for a 3-layer case are identical, and therefore not presented, due to the fact that the proposed zigzag function for a 3-layer model becomes identical to MZZF when the two external layers are of identical thickness.

Table 6.9: Non-dimensional deflection of multi-layer plate with varying number of layers.

Number of layers	Model	$h_{(F)}/h_{(C)} = 1/5$		$h_{(F)}/h_{(C)} = 5$	
		$\bar{u}_z$	Relative error	$\bar{u}_z$	Relative error
5	Elasticity (Demasi)	0.23578	-	0.04313	-
	L5-H3O9	0.23428	0.64%	0.04298	0.35%
	EDZ2*-H3O9	0.23428	0.64%	0.04298	0.35%
7	Elasticity (Demasi)	0.24237	-	0.04884	-
	L7- H3O9	0.24090	0.61%	0.04867	0.35%
	EDZ3*-H3O9	0.23915	1.33%	0.04835	1.00%
9	Elasticity (Demasi)	0.24746	-	0.05177	-
	L9-H3O9	0.24594	0.62%	0.05153	0.46%
	EDZ4*-H3O9	0.24191	2.24%	0.05075	1.98%
11	Elasticity (Demasi)	0.25166	-	0.05341	-
	L11-H3O9	0.25014	0.61%	0.05315	0.48%
	EDZ5*-H3O9	0.24389	3.09%	0.05189	2.85%

6.7.2 Geometrically nonlinear examples

6.7.2.1 Sandwich annular plate under end shear

A sandwich annular plate, fully clamped at one end, is subjected to a uniformly distributed transverse shear force at the other end, as is shown in Figure 6.19. The fibre direction of each layer is at a planar angle $\alpha^{(k)}$ from the circumferential direction of the annular plate. The plate dimensions are given as: $R_1 = 6$, $R_2 = 10$, $h = 0.045$, and $h_1 = h_2 = h_3 = 0.015$. The mechanical properties of the core are: $E_1^{(2)} = 2.0 \times 10^6$, $E_2^{(2)} = 6.0 \times 10^5$, $G_{12}^{(2)} = G_{13}^{(2)} = 3.0 \times 10^5$, $G_{23}^{(2)} = 2.4 \times 10^5$, and $\nu_{12}^{(2)} = 0.3$. The Young's modulus and shear modulus of the face sheets are obtained by multiplying those of the core with a FCSR = 1000.

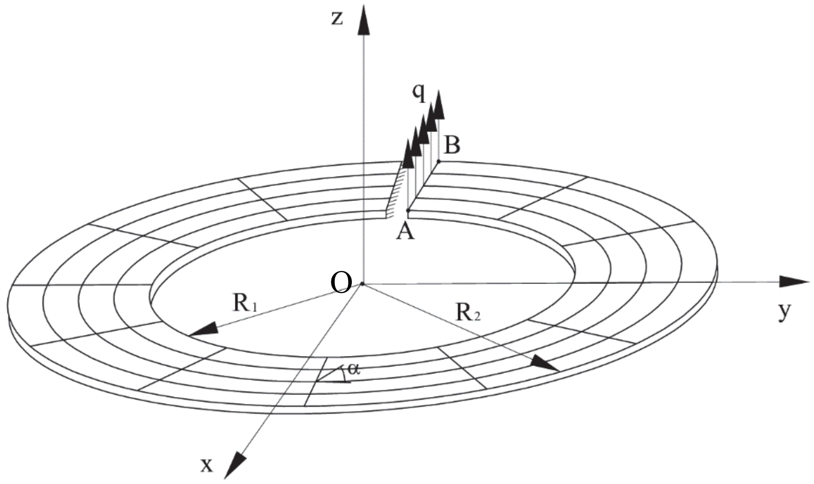

Figure 6.19: Sandwich annular plate subject to end transverse shear.

The shell system is obtained according to the approach illustrated in Figure 6.5 with the reference point O located at the origin of the global system such that the r- and s-axes orient along the circumferential and the radial directions, respectively. Figure 6.20 depicts the load-displacement curves in the z direction at points A and B for two uniform meshes of the whole plate (32×4 and 64×4) using the L3-H3O9 element for a symmetric lay-up ($h_1 = h_2 = h_3 = 0.015$) with a (0°/0°/0°) stacking scheme. Also presented are results from a 96×10×6 mesh of the degenerated shell element SOLSH190 in the finite element software package, ANSYS v14.5 (2012), where each individual sheet is modelled with 2 layers of elements through the thickness to represent the local zigzag effect. Clearly, results from both meshes of the L3-H3O9 element agree well with the SOLSH190 solution, indicating negligible inaccuracy resulting from the element-specific definition of the shell system with the coarser 32×4 mesh. Figures 6.21-6.22 depict the results from a 32×4 mesh of the L3-H3O9, EDZ1*-H3O9, and FSDT-H3O9 element for respectively a symmetric lay-up ($h_1 = h_2 = h_3 = 0.015$) and an asymmetric lay-up ($h_1 = 0.02$, $h_2 = 0.015$, and $h_3 = 0.01$), both of which employ a (0°/0°/0°) stacking scheme. Still, the results of the L3-H3O9 element are identical to the EDZ1*-H3O9 solution for the symmetric lay-up, while it surpasses the accuracy of the EDZ1*-H3O9 element for the asymmetric lay-up. In addition, the results with the L3-H3O6 element are almost identical to the L3-H3O9 solution. Figure 6.23 compares the results of a 32×4 mesh of the quadrilateral element L3-H3O9 and a 32×4 mesh of the triangular element L3-H3O6, which show comparable accuracy.

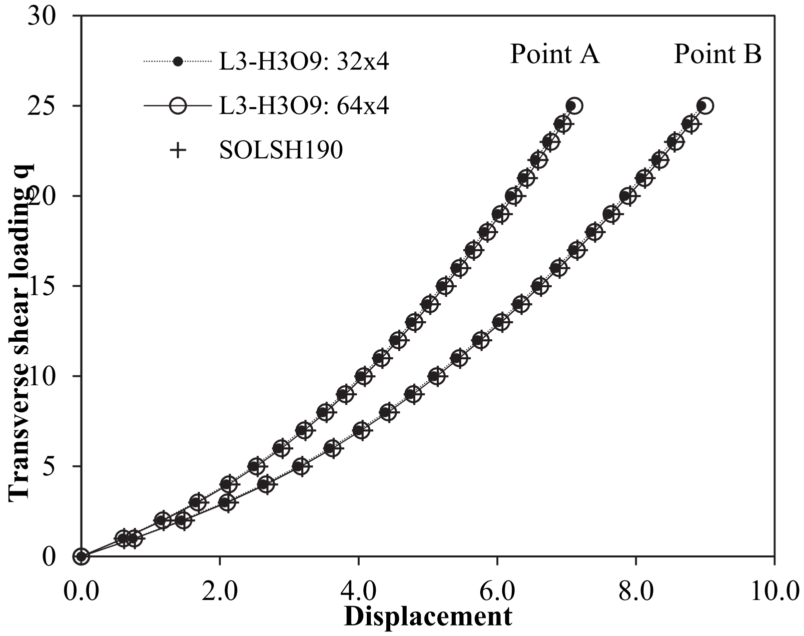

Figure 6.20: Convergence study along the circumferential direction for L3-H3O9 models

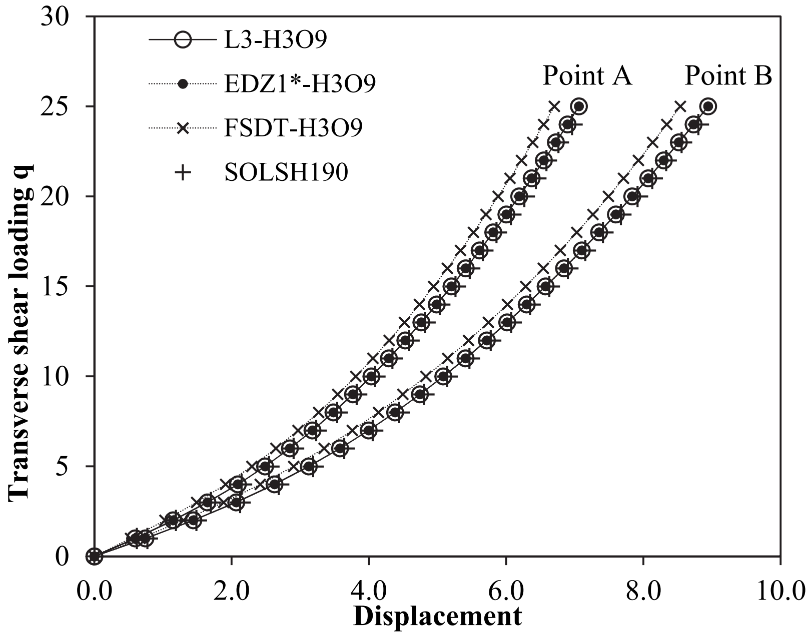

Figure 6.21: Load-displacement curves for a symmetric lay-up with a (0°/0°/0°) stacking scheme.

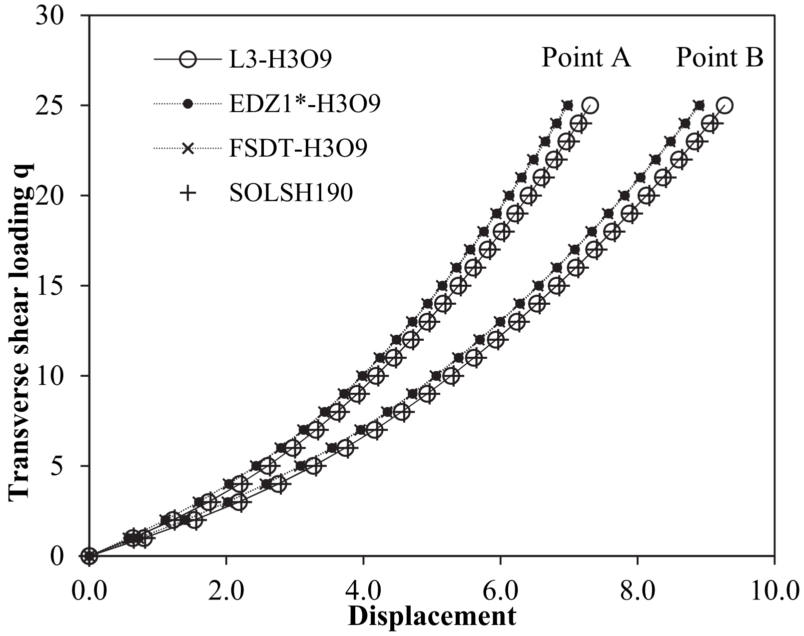

Figure 6.22: Load-displacement curves for an asymmetric lay-up with a (0°/0°/0°) stacking scheme.

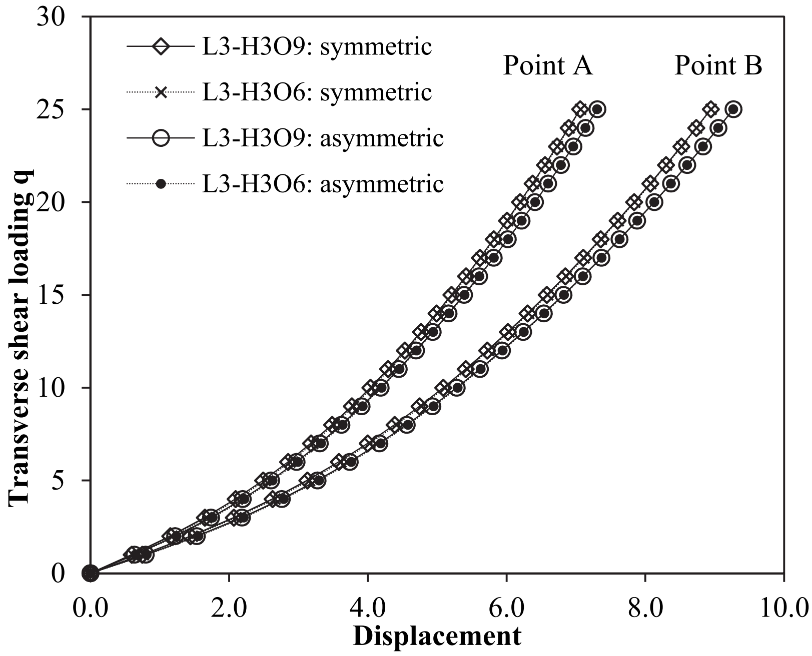

Figure 6.23: Comparison of quadrilateral and triangular elements for symmetric/asymmetric lay-ups.

Figure 6.24 depicts the results from a 32×4 mesh of the L3-H3O9 and L3-H3O6 element for symmetric lay-ups ($h_1 = h_2 = h_3 = 0.015$) with various fibre orientations, where the coincident plots of the sandwich shell models and the SOLSH190 models confirm the accuracy and effectiveness of the proposed laminated elements in solving large displacement problems with arbitrary fibre orientations.

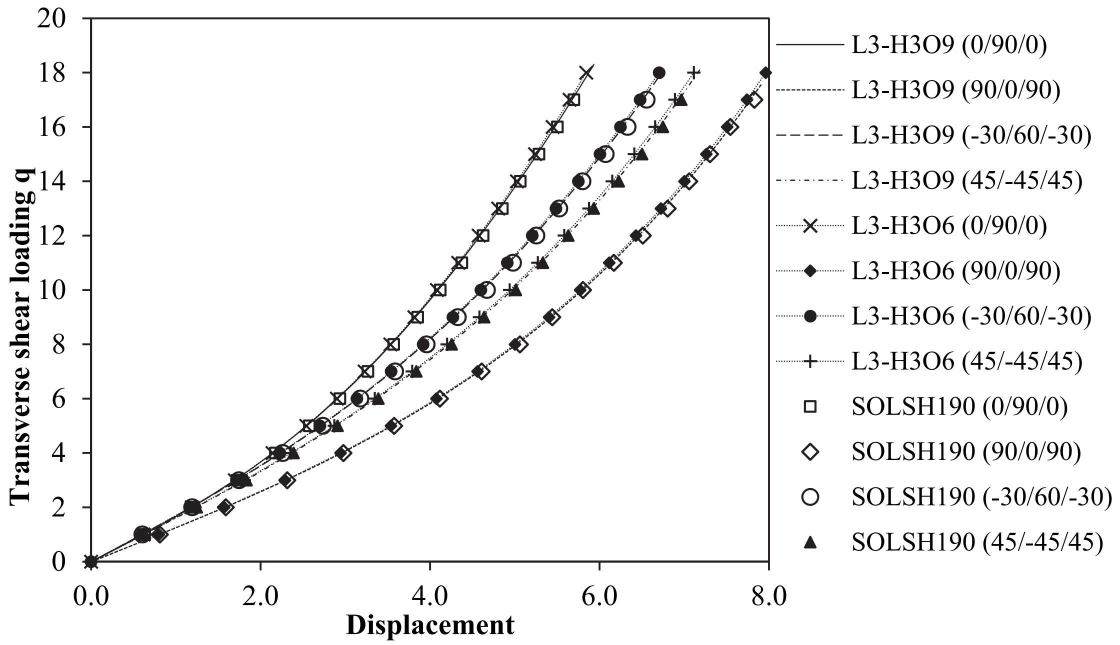

a. Point A

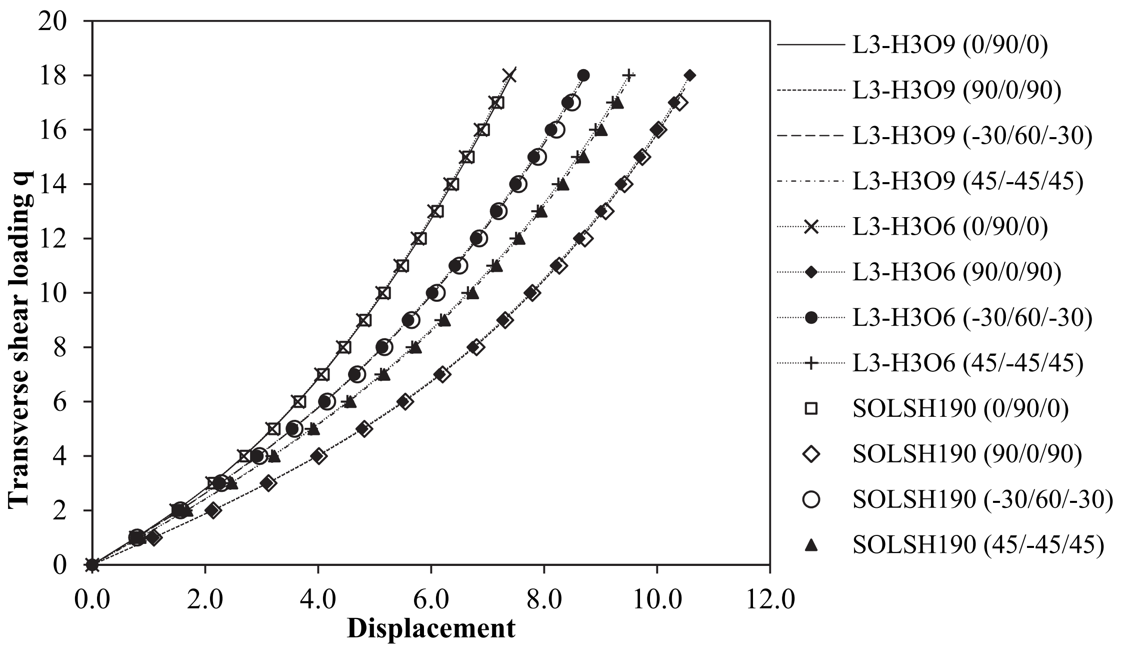

b. Point B

Figure 6.24: Load-displacement curves for a symmetric lay-up with various stacking schemes.

6.7.2.2 Circular plate under uniform pressure

The geometrically nonlinear response of a circular laminated plate is considered here, where the plate is fully clamped along its edge and is subjected to a uniformly distributed transverse loading p, as shown in Figure 6.25. The geometric and material parameters are given by

$R = 20$, $E^{(1)} = E^{(3)} = 1.0 \times 10^7$, $E^{(2)} = 3750$, and $\nu^{(1)} = \nu^{(2)} = \nu^{(3)} = 0.25$. Due to symmetry, a quarter of the circular plate is modelled with a mesh of 9-noded sandwich shell elements, which provides a convergent solution. The mesh is depicted in Figure 6.26, where the quarter model is divided into three sections, with each section discretised into a 6×6 mesh of the 9-noded laminated shell elements. The shell system is aligned with the (x,y) planar coordinate system. By restraining all the additional DOFs, a FSDT solution is also available. On the other hand, an 'EDZ*' formulation is also implemented with the 9-noded co-rotational element for comparison. It is worth noting that the only difference between the EDZ*-H3O9 model and the L*n*-H3O9 model is the employed zigzag function, which facilities the comparison between both additional displacement variables in modelling the considered laminations. In addition, an 8×8 shell model with a mixture of L*n*-H3O9 and L*n*-H3O6 elements is also employed (Figure 6.27), where a ring of 6-noded elements is employed surrounding the plate centre and seven rings of 9-noded shell elements are employed for the remaining part of the model.

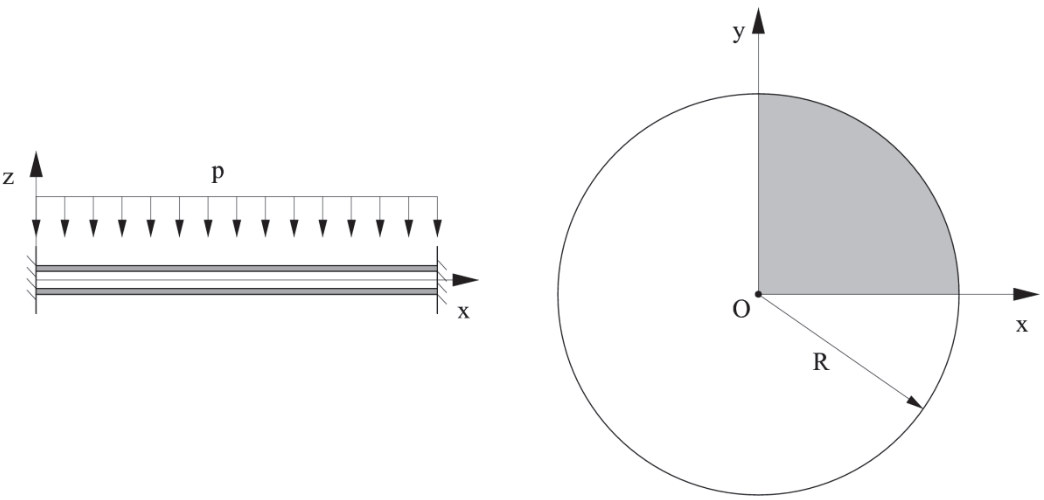

Figure 6.25: Clamped circular laminated panel under uniform loading.

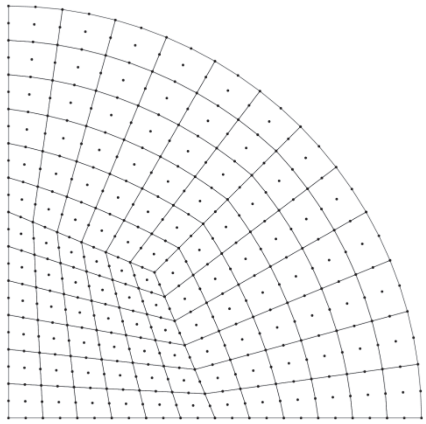

Figure 6.26: Mesh pattern for a 6×6×3 mesh of 9-noded laminated shell elements.

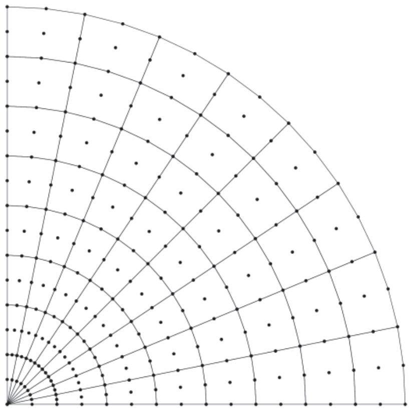

Figure 6.27: Mesh pattern for a 8×8 mixed mesh of 6-noded and 9-noded laminated shell elements.

A symmetric sandwich lay-up is first considered, where the layer thicknesses are given as $h_1 = h_3 = 0.025$ and $h_2 = 0.45$. The load-deflection curves at the plate centre O with the considered models are depicted in Figure 6.28, along with the series solution by Smith (1968) and the solution with axisymmetric sandwich shell elements by Sharifi and Popov (1973). As is expected, the L3-H3O9 and the EDZ1*-H3O9 results are identical for the symmetric lay-up, both of which agree with the series solution. An asymmetric sandwich lay-up is also considered, where the thicknesses of the layers are given as $h_1 = 0.05$, $h_2 = 0.35$, and $h_3 = 0.1$. The reference solution is taken from the results with a fine 3D model using a standard 20-noded quadratic brick element (Zienkiewicz & Taylor, 2000), denoted as 'BK20', where in the planar surface each of the three sections are meshed with 24×24 of the BK20 elements, and in the through-thickness direction an element size of 0.025 is employed leading to a total of 20 element divisions. The L3-H3O9, EDZ1*-H3O9 and FSDT-H3O9 results with the same mesh as Figure 6.26 are given in Figure 6.29, compared with the solution from the

3D elasticity model of the BK20 element. The L3-H3O9 element still shows high accuracy in predicting the large displacement response of the asymmetrically laminated sandwich plate, but the EDZ1*-H3O9 results are as inaccurate as the FSDT-H3O9 solution owing to the inadequacy of MZZF in capturing the real zigzag mode, hence requiring higher-order Taylor expansions with more additional displacement variables for improved estimation. In addition, from Figures 6.28-6.29 it is observed that the mixed model of L3-H3O9 and L3-H3O6 elements yields identical results with the pure L3-H3O9 model, which indicates the potential benefit of using a mixture of the 6-noded and the 9-noded laminated shell elements for problems involving complex geometry.

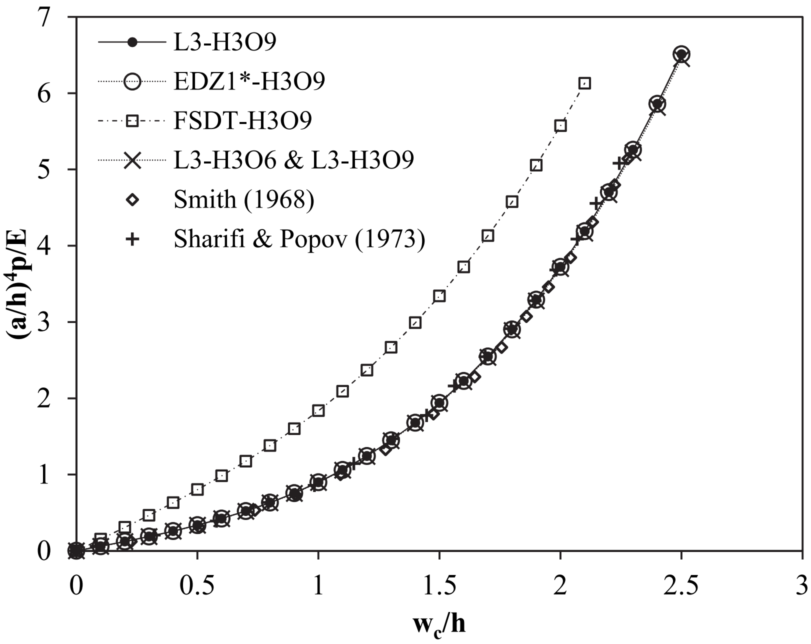

Figure 6.28: Load-deflection curves at point O of various models for a symmetric lay-up.

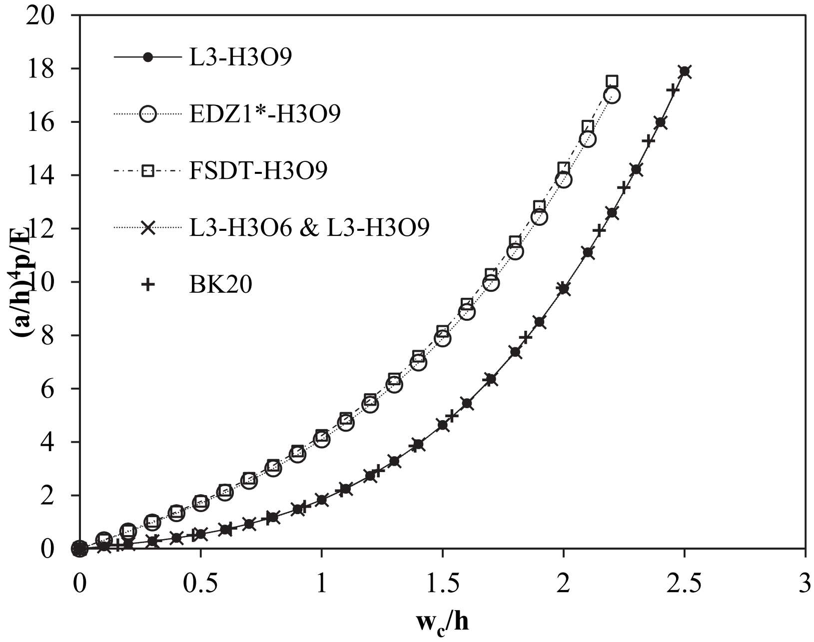

Figure 6.29: Load-deflection curves at point O of various models for an asymmetric lay-up.

Hereafter, the same circular plate problem is analysed for an 11-layer lamination, which is composed of the same stiff sheets, denoted by 'F', and the same soft sheets, denoted by 'C', with an alternating stiff/soft lay-up. Two stiff-to-soft layer thickness ratios $(h_{(F)}/h_{(C)} = 1/5, 5)$, denoted as schemes (1) and (2) respectively, are considered to investigate the performance of the shell models. The material parameters are given as $E_{(F)} = 1.0\times10^7$, $E_{(C)} = 3750$, and $\nu_{(F)} = \nu_{(C)} = 0.25$. The same mesh as shown in Figure 6.26 is used for the L11-H3O9 element. The reference solution is obtained from a 3D continuum model using a fine mesh of BK20, where on the planar surface each of the three sections is meshed with 24×24 BK20 elements, and two elements are employed for each constitutive layer. The load-deflection curves at the plate centre, point O, obtained with various models are depicted in Figure 6.30. Clearly, the disparity of the FSDT-H3O9 results from the others indicates the significance of the zigzag effect. The L11-H3O9 model matches well with the solid model, confirming its high accuracy for both lay-up schemes. Again, the results of a mixed model with a mesh pattern depicted in Figure 6.27 are also presented in Figure 6.30, which show the same accuracy with the results of the L11-H3O9 model.

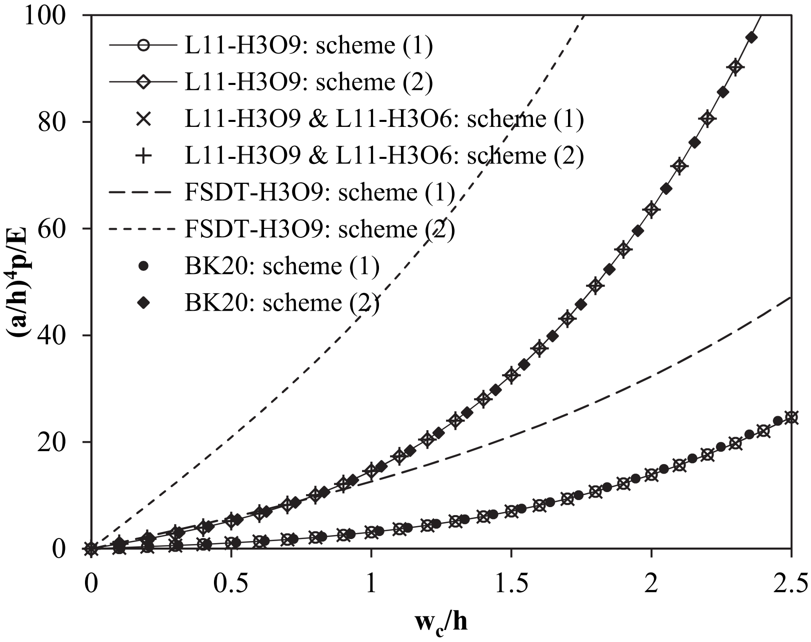

Figure 6.30: Load-deflection curves at point O of 11-layer laminated plate.

6.7.2.3 Multi-layer hemispherical shell with 18° cut-off

Another large displacement problem is considered here, where a five-layer hemispherical shell with a circular cut-off at its top is subjected to symmetric concentrated forces at its base, as shown in Figure 6.31. The hole aperture is 18°, the sphere radius is 10, and the shell thickness is h = 0.075. Three alternative lay-ups are considered to investigate the performance of the multi-layer shell element in problems involving both symmetric and asymmetric cross-sections. The layer material type and thickness for each scenario are listed in Table 6.10, where layer (1) corresponds to the interior layer of the hemispherical shell. The material parameters for the stiff layers (F) and soft layers (C) are given as: $E_{(F)} = 1.0 \times 10^7$, $E_{(C)} = 5.0 \times 10^3$, and $\nu_{(F)} = \nu_{(C)} = 0.2$.

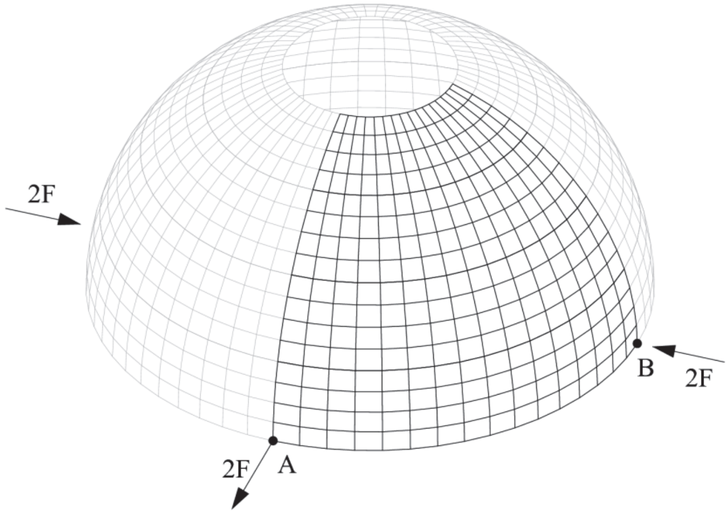

Figure 6.31: Pinched laminated hemispherical shell with a $18°$ hole.

Table 6.10: Lay-ups for 5-layer hemispherical shell.

Layer index	Layer material	Layer thickness		
		Scheme (1)	Scheme (2)	Scheme (3)
1	(F)	(1/5)h	(1/15)h	(3/25)h
2	(C)	(1/5)h	(2/15)h	(5/25)h
3	(F)	(1/5)h	(3/15)h	(9/25)h
4	(C)	(1/5)h	(4/15)h	(5/25)h
5	(F)	(1/5)h	(5/15)h	(3/25)h

Note that in this model, the shell system is defined to follow the longitudinal and latitudinal lines of the sphere, which can be easily realised with the use of the approach illustrated in Figure 6.4 by aligning the reference vector **n** with the axis of symmetry. Due to the curved geometry, the curvilinear shell triads vary in orientation between adjacent elements, though any inaccuracy diminishes with mesh refinement, as confirmed in the presented results. Due to symmetry, only a quarter of the hemispherical shell is modelled with a 16×16 mesh of the L5-H3O9 and EDZ2*-H3O9 elements, both of which provide convergent solutions. By restraining all additional zigzag parameters, the corresponding FSDT-H3O9 results are also available. A 16×16 mesh of the triangular L5-H3O6 element is also employed. The results of a 64×64×10 solid model using the BK20 element are utilised for a reference solution. Figures 6.32-6.34 depict the equilibrium paths of the radial displacements at points A and B for the respective lay-up schemes. The deviation of the FSDT-H3O9 results from the reference solution indicates the significance of the zigzag effect for this problem. It is interesting to note that the EDZ2*-H3O9 results agree with the reference solution for lay-up (1) but is as inaccurate as the FSDT-H3O9 solution for the other two lay-up scenarios. This is attributed to the inadequacy of MZZF in capturing the real zigzag mode for the last two lay-ups, hence requiring higher-order Taylor expansions with more additional displacement variables for improved estimation. On the other hand, the results of the L5-H3O9 and the L5-H3O6 models present an excellent match against the results obtained from the 3D continuum solid model for all of the considered lay-up schemes.

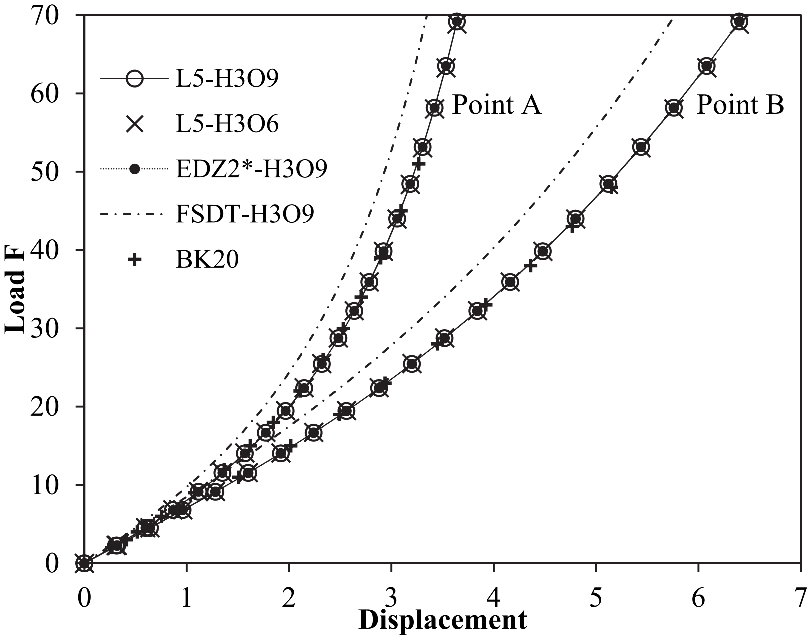

Figure 6.32: Load-deflection curves at point A and B of various models with lay-up scheme (1).

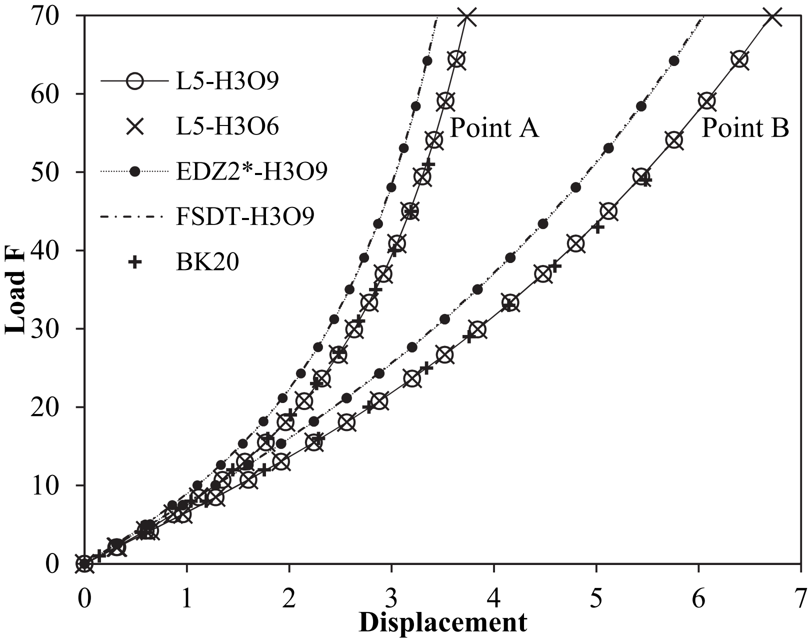

Figure 6.33: Load-deflection curves at point A and B of various models with lay-up scheme (2).

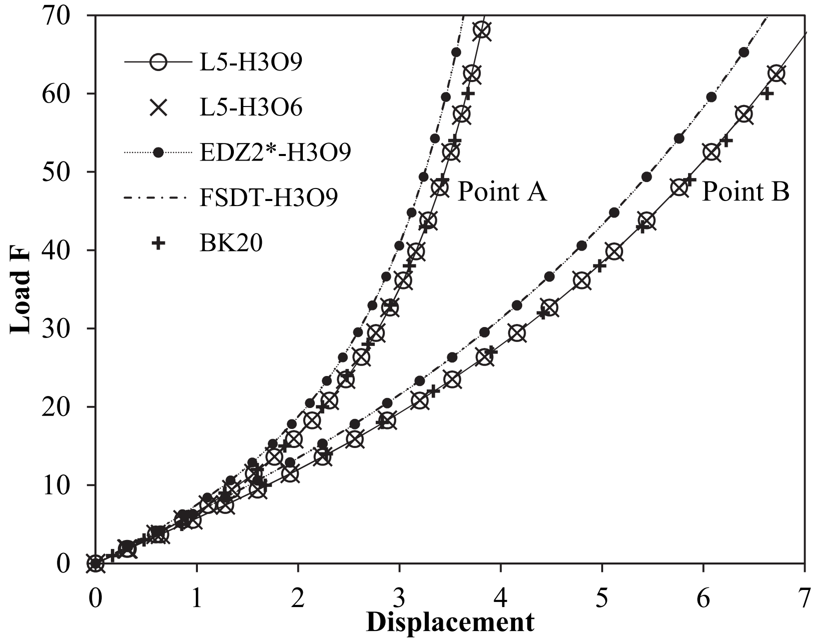

Figure 6.34: Load-deflection curves at point A and B of various models with lay-up scheme (3).

6.8 Summary

In this chapter, the proposed multi-layer shell modelling approach has been implemented for 9-noded and 6-noded co-rotational shell elements, which can be applied in large displacement analysis. Importantly, to eliminate the need for co-rotational transformations for the additional zigzag displacement parameters, a 2D curvilinear shell system is proposed in this research for the direct definition of these parameters, such that a simple and fixed transformation of these additional parameters to their counterparts in the local element system holds throughout the analysis. Moreover, consistent mass matrices for the laminated shell elements are also derived in this chapter, which enables the analysis of dynamic problems.

Linear and geometrically nonlinear numerical examples are finally solved with the proposed multi-layer shell elements, where excellent accuracy is generally achieved in comparison with elasticity solutions, and superior performance is typically demonstrated compared to existing models for laminated shells with alternating stiff/soft lay-ups.

CHAPTER 7

Application to Laminated Glass

7.1 Introduction

The effectiveness of the proposed multi-layered shell elements has been verified in Chapter 6. In this chapter, their application to LG is presented. Although structural glass is a brittle material and will fracture when tensile stress is exceeded, in this research the scope of interest is the structural behaviour prior to the initiation of cracking. Therefore, a linear elastic isotropic material model is employed for glass, while the PVB interlayer is considered as a linear viscoelastic material, which is appropriate for small-strain problems. With the appropriate material models used in the laminated shell elements, geometrically nonlinear analysis of LG structures under static and dynamic loadings can be performed.

Insulated glazing, or double glazing, has been increasingly used owing to its good heat and noise insulating performance. It is composed of two glazing panes separated by an insulating air gap, which helps reduce the thermal and sound transfer. Moreover, the sealed air gap has influence on the structural performance of the insulated glazing system via the generation of air pressure onto both panes once the pane deflection causes a volume change for the sealed air. Ding et al. (2014) investigated the performance of a double-skin steel façade subjected to blast loading and found that during the blast loading there was a significant increase in the cavity pressure due to the changed cavity volume through the panel deflection. Deng and Jin (2010) simulated the response of insulated glass subject to blast loading, where both the air area between explosive and structure and the sealed air were modelled with equations of state employed to describe the pressure-volume-energy relationship. They found that under blast loading the interior glass pane suffered fewer cracks, which indicates that the air space alleviates the blast and helps to protect the interior pane. Wagner and Müller (2010) considered the effect of the enclosed air on the behaviour of insulated glass under blast loading by employing a static relationship between the change in the gas volume and the hydrostatic pressure, which can be included into an existing structural model with ease. Therefore, in order to allow the analysis of insulated glazing systems, a volume-pressure control procedure based on a simple static relationship is established and implemented in ADAPTIC v2.14.2 for recording the volume change of enclosed gas and hence calculation of the generated pressure, which will allow the analysis of double glazing units.

In the following sections of this chapter, a linear viscoelastic material model for the PVB material is reviewed, which is employed in this work with 3D solid elements as well as 2D shell elements. The verification of the linear viscoelastic material model is then provided with two illustrative LG examples. Subsequently, a volume-pressure control algorithm is presented, which allows the consideration of the effect of enclosed air in insulated glazing on the structural behaviour under external loading, followed by two double glazing examples to verify accuracy and efficiency of the proposed approach.

7.2 Linear viscoelastic material model

A linear viscoelastic material model is implemented in this research to simulate PVB, which employs the assumption of a constant bulk modulus as made by Bennison et al. (1999) and is formulated based on the recursive formula presented by Sedef et al. (2006) in the calculation of current stresses of viscoelastic materials.

7.2.1 Recursive formula

In a generalised Maxwell model, the viscoelastic material property is represented by a combination of springs and dashpots, which results in a Prony series expression for the stress relaxation function, as is given in (2.20). The Boltzmann superposition principle yields a stress-strain relationship given in (2.21). The substitution of (2.20) into (2.21) derives the following expression for the stress relaxation:

$$\sigma(t)=\int_0^t E_\infty \frac{\partial\varepsilon(s)}{\partial s}ds+\sum_{j=1}^{N_M}\int_0^t E_j\, e^{-\frac{t-s}{\tau_j}}\frac{\partial\varepsilon(s)}{\partial s}ds=E_\infty\,\varepsilon(t)+\sum_{j=1}^{N_M}h_j(t) \tag{7.1}$$

where N_M is the number of Maxwell elements.

Temporal discretisation leads to the following expression for stress at the previous time t_n and the current time t_{n+1}:

$$\sigma^n=E_\infty\,\varepsilon^n+\sum_{j=1}^{N_M}h_j^n \tag{7.2}$$

$$\sigma^{n+1}=E_\infty\,\varepsilon^{n+1}+\sum_{j=1}^{N_M}h_j^{n+1} \tag{7.3}$$

Defining the current time step size as $\Delta t^{n+1}=t_{n+1}-t_n$, and assuming a linear strain variation in the current time step (i.e. $\frac{\partial\varepsilon(s)}{\partial s}=\frac{\varepsilon^{n+1}-\varepsilon^n}{\Delta t^{n+1}}$), each function h_j^{n+1} is related to h_j^n with the following relationship (Sedef et al., 2006):

$$h_j^{n+1}=e^{-\frac{\Delta t^{n+1}}{\tau_j}}h_j^n+E_j\left(\int_{t_n}^{t_{n+1}}e^{-\frac{t_{n+1}-s}{\tau_j}}ds\right)\left(\frac{\Delta\varepsilon^{n+1}}{\Delta t^{n+1}}\right) \tag{7.4}$$

where $\Delta\varepsilon^{n+1}=\varepsilon^{n+1}-\varepsilon^n$.

Further integration of (7.4) yields:

$$h_j^{n+1}=e^{-\frac{\Delta t^{n+1}}{\tau_j}}h_j^n+E_jA_j\Delta\varepsilon^{n+1} \tag{7.5}$$

with:

$$A_j = \frac{1-e^{-\frac{\Delta t^{n+1}}{\tau_j}}}{\frac{\Delta t^{n+1}}{\tau_j}} \tag{7.6}$$

Substitution of (7.5) into (7.3) results in the recursive formula for stress relaxation.

7.2.2 Application to PVB

Bennison et al. (1999) stated that the bulk modulus of PVB is almost constant, the value of which is around 2.0 GPa. Therefore, a linear viscoelastic material model based on the recursive formula presented by Sedef et al. (2006) is implemented, where a constant bulk modulus K is assumed and a Maxwell series of the shear relaxation function G is employed.

In the linear viscoelastic material model, the stress relaxations can be obtained from the following equations:

$$\sigma_{ii}(t) = \int_0^t G(t-s)\left(\frac{4}{3}\frac{\partial \varepsilon_{ii}}{\partial s} - \frac{2}{3}\frac{\partial \varepsilon_{i_+i_+}}{\partial s} - \frac{2}{3}\frac{\partial \varepsilon_{i_-i_-}}{\partial s}\right)ds + K\left[\varepsilon_{ii}(t) + \varepsilon_{i_+i_+}(t) + \varepsilon_{i_-i_-}(t)\right] \tag{7.7}$$

$$\sigma_{ii_+}(t) = \int_0^t G(t-s)\frac{\partial \gamma_{ii_+}}{\partial s}ds \tag{7.8}$$

with $i = 1 \to 3$, $i_+ = \mathrm{mod}(i,3)+1$, and $i_- = \mathrm{mod}(i+1,3)+1$.

Application of the recursive formula to (7.7)-(7.8) yields the stresses at time t_{n+1} as follows:

$$\sigma_{ii}^{n+1} = \left[\left(\frac{4}{3}G_\infty + K\right)\varepsilon_{ii}^{n+1} + \left(-\frac{2}{3}G_\infty + K\right)\varepsilon_{i_+i_+}^{n+1} + \left(-\frac{2}{3}G_\infty + K\right)\varepsilon_{i_-i_-}^{n+1}\right] + \sum_{j=1}^{N_M} h_{j,ii}^{n+1} \tag{7.9}$$

$$\sigma_{ii_+}^{n+1} = G_\infty \gamma_{ii_+}^{n+1} + \sum_{j=1}^{N_M} h_{j,ii_+}^{n+1} \tag{7.10}$$

where the functions $h_{j,\alpha\beta}^{n+1}$ $(\alpha,\beta = 1 \to 3)$ are expressed in an recursive manner as:

$$h_{j,ii}^{n+1} = e^{-\frac{\Delta t^{n+1}}{\tau_j}} h_{j,ii}^{n} + G_j A_j \left(\frac{4}{3} \Delta\varepsilon_{ii}^{n+1} - \frac{2}{3} \Delta\varepsilon_{i_+ i_+}^{n+1} - \frac{2}{3} \Delta\varepsilon_{i\_i\_}^{n+1} \right) \tag{7.11}$$

$$h_{j,ii_+}^{n+1} = e^{-\frac{\Delta t^{n+1}}{\tau_j}} h_{j,ii_+}^{n} + G_j A_j \Delta\gamma_{ii_+}^{n+1} \tag{7.12}$$

7.2.2.1 Application to shell elements

The triaxial viscoelastic material model described above can be directly applied to 3D solid elements. In order to apply it to 2D shell elements which ignore transverse normal stresses, a further modification is required. By imposing a zero value constraint on the transverse normal stress σ_{33}, the constitutive equations between the stresses and strains are expressed as follows:

$$\boldsymbol{\sigma}_p^{n+1} = \mathbf{C}_{v,p}^{n+1} \boldsymbol{\varepsilon}_p^{n+1} + \boldsymbol{\sigma}_{hist,p}, \quad \boldsymbol{\sigma}_s^{n+1} = \mathbf{C}_{v,s}^{n+1} \boldsymbol{\varepsilon}_s^{n+1} + \boldsymbol{\sigma}_{hist,s} \tag{7.13}$$

where $\boldsymbol{\sigma}_p^{n+1} = \left\langle \sigma_{11}^{n+1}, \sigma_{22}^{n+1}, \sigma_{12}^{n+1} \right\rangle^T$ and $\boldsymbol{\sigma}_s^{n+1} = \left\langle \sigma_{13}^{n+1}, \sigma_{23}^{n+1} \right\rangle^T$ denote respectively the planar and transverse shear stresses at time t_{n+1}; $\boldsymbol{\varepsilon}_p^{n+1} = \left\langle \varepsilon_{11}^{n+1}, \varepsilon_{22}^{n+1}, \gamma_{12}^{n+1} \right\rangle^T$ and $\boldsymbol{\varepsilon}_s^{n+1} = \left\langle \gamma_{13}^{n+1}, \gamma_{23}^{n+1} \right\rangle^T$ denote respectively the planar and transverse shear strains at time t_{n+1}; $\mathbf{C}_{v,p}^{n+1}$ and $\mathbf{C}_{v,s}^{n+1}$ are viscoelastic constitutive matrices for respectively the planar and transverse shear stresses/strains at time t_{n+1}; and $\boldsymbol{\sigma}_{hist,p}$ and $\boldsymbol{\sigma}_{hist,s}$ are stresses related to the loading history. The derivations of $\mathbf{C}_{v,p}^{n+1}$,$\mathbf{C}_{v,s}^{n+1}$, $\boldsymbol{\sigma}_{hist,p}$ and $\boldsymbol{\sigma}_{hist,s}$ are provided in Appendix D.

7.3 Verification of viscoelastic material model

Hereafter, two LG problems presented in the literature are reproduced to verify the linear viscoelastic material model implemented for PVB. In both problems, the laminated shell elements proposed in Chapter 6 are used, and the linear viscoelastic material models are employed for the PVB interlayer.

7.3.1 Laminated glass under biaxial bending

7.3.1.1 Description of problem

The presented example consists of a series of biaxial flexural tests conducted by Bennison et al. (1999), which are used to investigate the response of circular LG panels at a wide range of loading rates. The LG is composed of two circular glass plies with a diameter of 100 mm and bonded with a PVB interlayer. The circular panel is supported at three points located on a radius r_2 = 44.7 mm and is loaded with a circular punch which effectively produces a ring loading with a radius of r_1 = 4.498 mm, as depicted in Figure 7.1. The ring load is applied monotonically at various displacement rates in the range of 10^{-3} to 10^{2} mm/s. From the conducted material tests on the PVB interlayer, Bennison et al. also proposed a generalized Maxwell material model for the description of the shear relaxation modulus, with the material parameters corresponding to a reference temperature of 20°C listed for the 11 Maxwell components in Table 7.1. The parameter values for a different temperature can be obtained by employing the WLF equation, as given in (2.18), with C_1 = 20.7 and C_2 = 91.1 (Bennison et al., 1999).

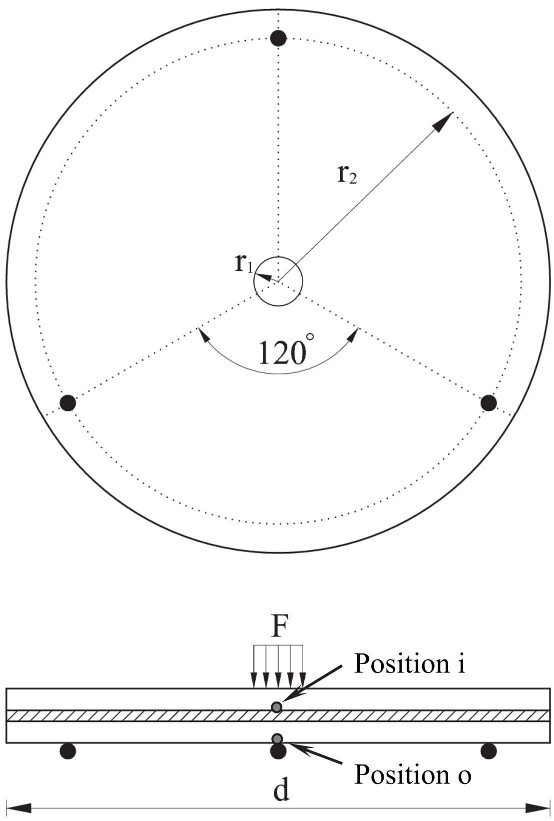

Figure 7.1: Schematic drawing of the biaxial bending tests on LG panels.

Table 7.1: Terms of the generalised Maxwell series description (Bennison et al., 1999).

j	G_j/G_0	τ_j(s)
1	0.1606000	3.2557E-11
2	0.0787770	4.9491E-09
3	0.2912000	7.2427E-08
4	0.0711550	9.8635E-06
5	0.2688000	2.8059E-03
6	0.0895860	1.6441E-01
7	0.0301830	2.2648E+00
8	0.0076056	3.5364E+01
9	0.0009634	9.3675E+03
10	0.0004059	6.4141E+05
11	0.0006143	4.1347E+07

Instantaneous shear modulus G0 = 0.471GPa; WLF parameters C_1 = 20.7 and C_2 = 91.1, at a reference temperature of 20°C.

7.3.1.2 Laminated shell model

Due to symmetry, a 60° segment of the circular plate is modelled with meshes of the proposed sandwich shell elements. With respect to the fan-shaped geometry, an efficient mesh type is used, where a ring of 6-noded triangular elements is employed surrounding the panel center and rings of 9-noded quadrilateral elements are employed for the remaining part. A 10×10 mesh, as shown in Figure 7.2 provides a convergent solution. This mesh is thus used to reproduce some of the tests and compare with both the experimental data and the numerical results given by Bennison et al. (1999) who used 8-noded 3D solid models with ten elements employed through the plate thickness (four for each glass ply and two for the interlayer).

7.3.1.3 Results

<u>Stress-force relationship</u>

In one of the tests, the uniform ring load was applied at a displacement rate of 10^{-3}mm/s, and the temperature was maintained 22.8°C during the test. In this case, the thickness of each glass ply is h_g=2.195mm and the PVB layer is h_p=0.799mm. Bennison et al. (1999) used uniaxial electrical-resistance strain gauges to record the strain of the lower ply on the supported (lower) glass surface along with the applied force. Figure 7.3 shows the stress-force curve of the 10×10 shell model, which is in agreement with the experimental data and the numerical results of Bennison et al.

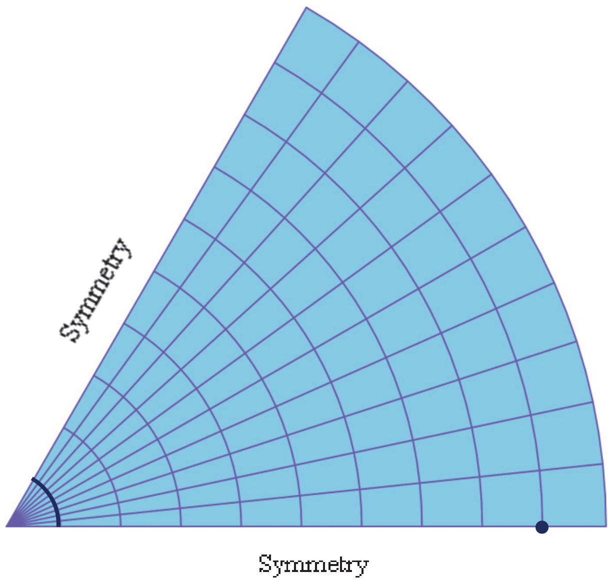

Figure 7.2: A sixth model of the LG problem (bold line denotes ring loading; point denotes support).

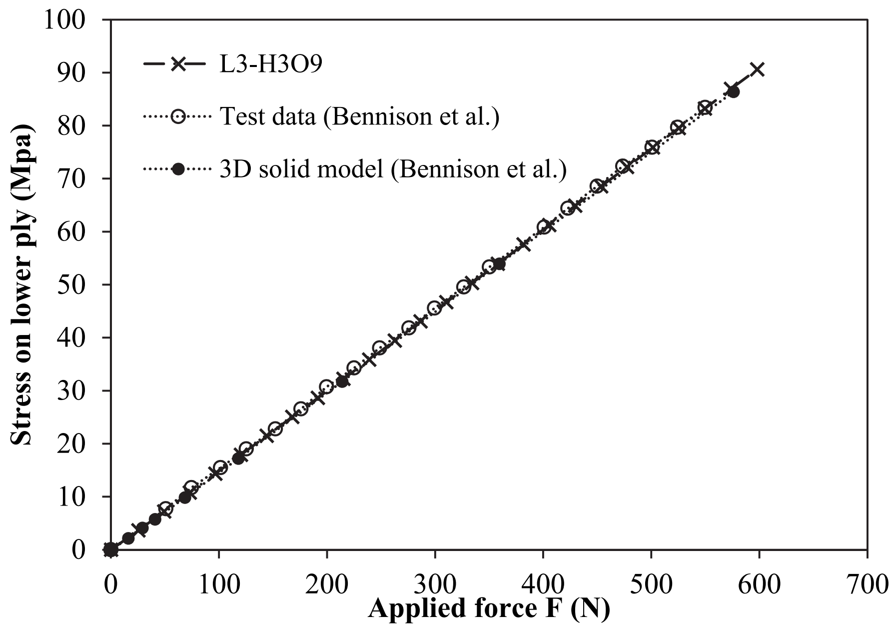

Figure 7.3: The stress-force curves of experimental data and numerical models.

Through-thickness stress distribution

The through-thickness principal stress distribution at the LG centre is obtained with the 10×10 shell model of L3-H3O9 and L3-H3O6 elements, as depicted in Figure 7.4 in comparison with the results of the 3D solid model by Bennison et al. It is noted that for the considered case the glass plies and the PVB have thicknesses of h_g = 2.246mm and h_p = 0.76mm, and the loading history is conducted at a fixed temperature of 22°C. Two normalised loading rates are considered: v^* =0.675 and 6.75×10^8, where $v^* = \frac{va_T\tau^*}{\delta}$, with τ^* =1127s denoting the characteristic time for G(t) to relax to a value of around 1MPa, and δ =0.6mm representing the maximum plate deflection. a_T is a coefficient associated with temperature, as given in Section 2.5.3. From Figure 7.4 it is observed that the predicted stress distribution of the L3-H3O9 shell model matches well with the 3D solid model by Bennison et al. (1999) at both loading rates.

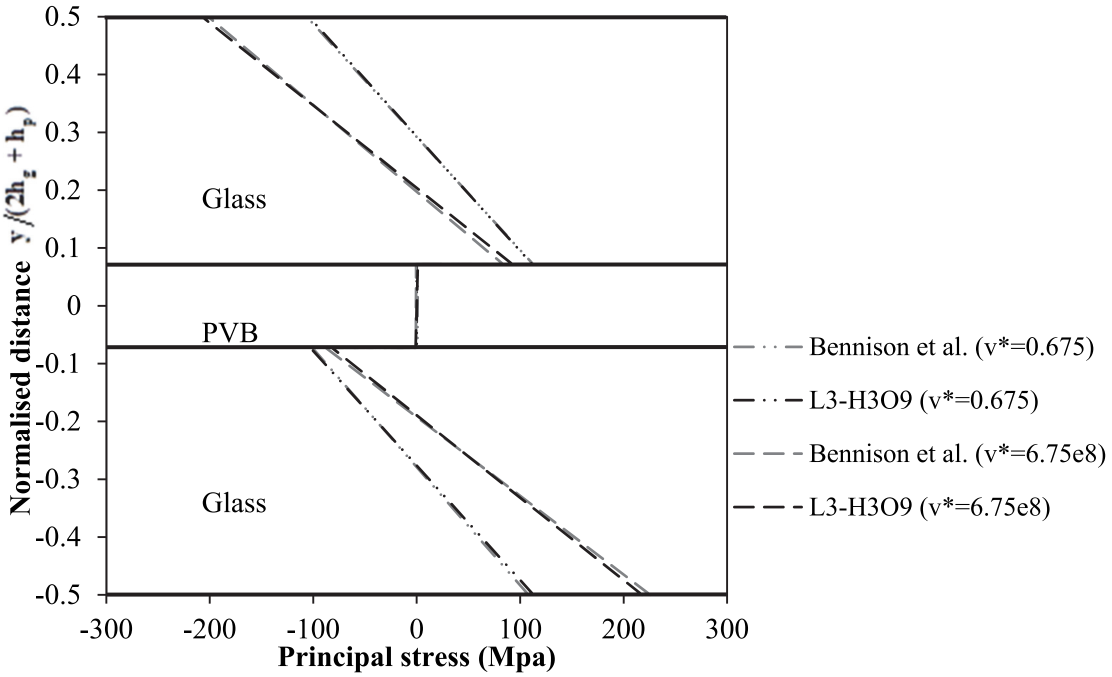

Figure 7.4: Distribution of normal stress for different loading rates.

Influence of loading rate on stress distribution

The influence of the loading rate on the stress distribution is investigated with the glass and PVB thicknesses of h_g = 2.246mm and h_p = 0.7mm. The central principal stresses at the bottom of both glass plies, denoted as position 'i' and 'o', respectively (Figure 7.1), corresponding to a 0.6mm maximum deflection are obtained. Define the stress-to-force coefficients ζ^o (outer) and ζ^i (inner) as:

$$\zeta^{o} = \frac{\sigma_{11}^{o}}{F}, \quad \zeta^{i} = \frac{\sigma_{11}^{i}}{F}$$

where σ_{11}^{o} and σ_{11}^{i} are principal stresses at the bottom of respectively the lower and the upper glass ply; F is the recorded punch force associated with a maximum deflection of 0.6mm. The coefficients ζ^{o} and ζ^{i} are normalised by the corresponding coefficient ζ^{m} for a monolithic glass pane of thickness $2h_g$.

Figure 7.5 depicts the variation of the normalised stress-to-force ratios with loading rates via the use of the 10×10 shell model. At a relatively slow loading rate, the PVB interlayer has a limited shear stiffness to transfer shear forces. Accordingly, the LG can be regarded as layered glass panels, which results in rapid development of stresses in each glass ply. For a rapid loading rate, the PVB interlayer exhibits stiff material properties, which leads to the three layers working as a whole and hence reducing the normalised ratio at position ‘o’ to around 1.0 and ζ^{i}/ζ^{m} at position ‘1’ to an even smaller value. The results of the sandwich shell model are in good agreement with the curves obtained by Bennison et al., which verifies the accuracy of the proposed sandwich shell model and the viscoelastic material model in the simulation of LG. Also shown in Figure 7.5 are the FSDT results with the same 10×10 shell model, which are obtained by restraining all additional DOFs in the sandwich shell elements. The deviation of the FSDT results from the others indicates the significant zigzag effects of the LG panels throughout the considered range of loading rates due to the modulus mismatch between glass and PVB. On the other hand, as indicated in the figure, this deviation of results reduces with much higher loading rates.

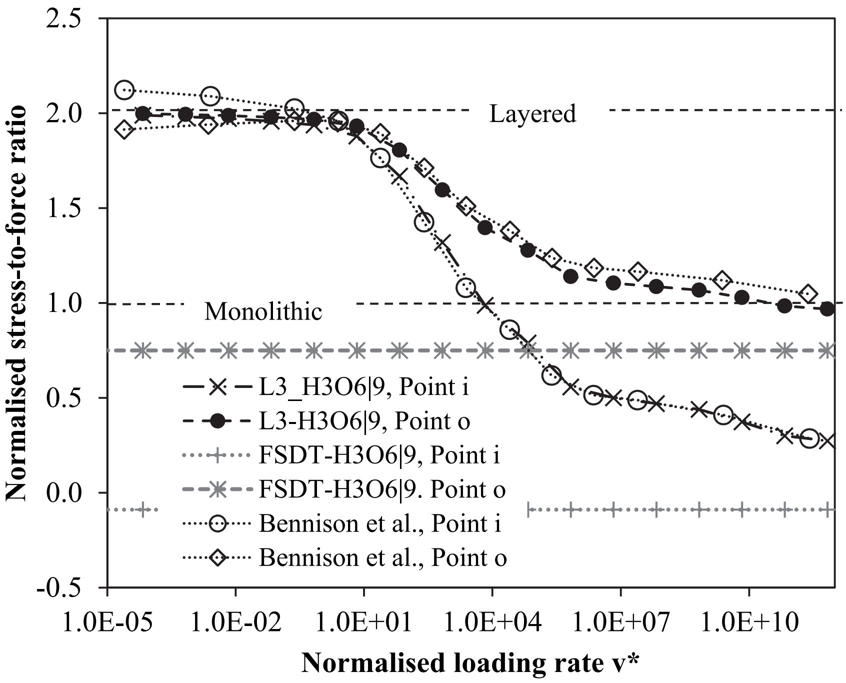

Figure 7.5: Stress-to-force ratios with various loading rates.

7.3.2 Laminated glass panel under blast loading

7.3.2.1 Description of problem

Consideration is given here to the dynamic problem of LG glazing subjected to low-level blast loading, which has been numerically analysed by Wei et al. (2006). The considered LG panel, which has the dimensions of 2.65m × 2.65m, is subjected to a uniform blast loading, as depicted in Figure 7.6. Simply-supported boundary conditions are applied to the LG plate. Each glass ply is of thickness $h_{glass} = 11.04\text{mm}$ and the PVB layer is of thickness $h_{PVB} = 1.52\text{mm}$. The glass plies are modelled as a linear elastic material with $E_{glass} = 72\text{GPa}$ and $\nu_{glass} = 0.25$. The PVB is modelled as a linear viscoelastic material with the shear relaxation modulus of the form $G(t) = G_\infty + (G_0 - G_\infty)e^{-\beta t}$, where $G_0 = 0.33\text{GPa}$, $G_\infty = 0.69\text{MPa}$, and $\beta = 12.6\text{s}^{-1}$, while the bulk modulus is taken as $K = 20\text{GPa}$. The densities of glass and PVB are 2500kg/m^3 and 1100kg/m^3, respectively. As shown in Figure 7.7, the blast loading curve employs the following expression:

$$p(t) = p^0(1 - t/t_d)e^{-\alpha t/t_d} \tag{7.14}$$

where p(t) is the instantaneous overpressure at time t, $p^0 = 6894.8\text{Pa}$ is the peak overpressure observed at t = 0, α = 0.55 is the decay factor, and t_d = 7.7ms is the positive overpressure duration.

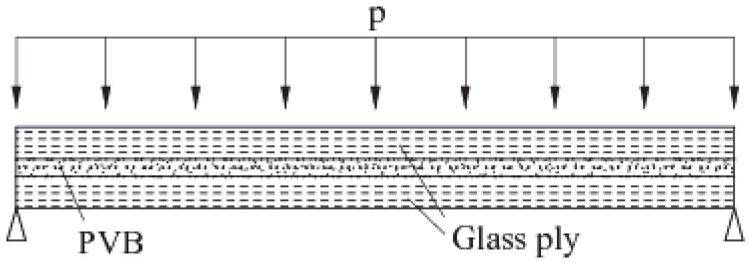

Figure 7.6: A rectangular LG plate under uniform blast load.

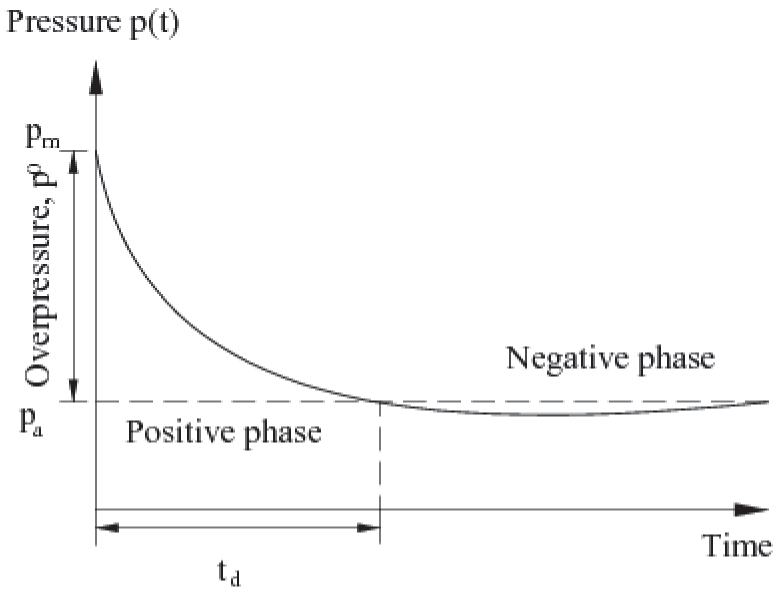

Figure 7.7: A schematic representation of the blast loading curve (Wei et al, 2006).

7.3.2.2 Laminated shell model

Due to symmetry, a quarter of the panel is modelled with an 8×8 mesh of the proposed L3-H3O9 element, which provides a convergent solution. The central deflection time history and mid-span maximum principal stress time histories are respectively plotted in Figures 7.8-7.9, which show good agreements with the results by Wei et al. (2006), who used a 60×60×10 solid model of 8-noded solid elements, hence demonstrating the accuracy and efficiency of the proposed laminated shell element in dynamic problems. Also depicted in Figure 7.8 is the deflection time history for a linear elastic PVB model which employs the instantaneous shear modulus G_0. The result almost coincides with that of the viscoelastic material model. It is concluded that for LG problems associated with short-duration loadings, the interlayer can be simply simulated with an elastic material model without degradation of accuracy.

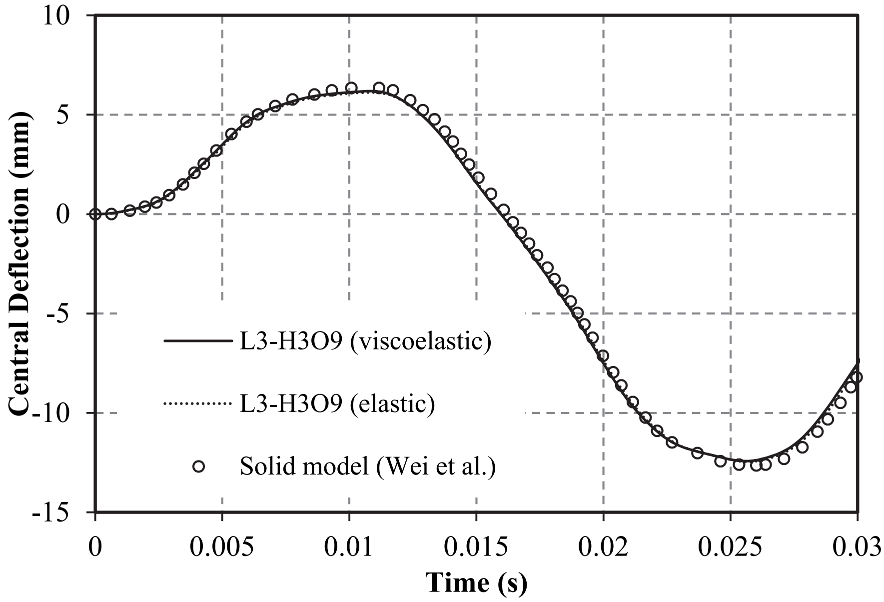

Figure 7.8: Time history of deflection at the LG centre.

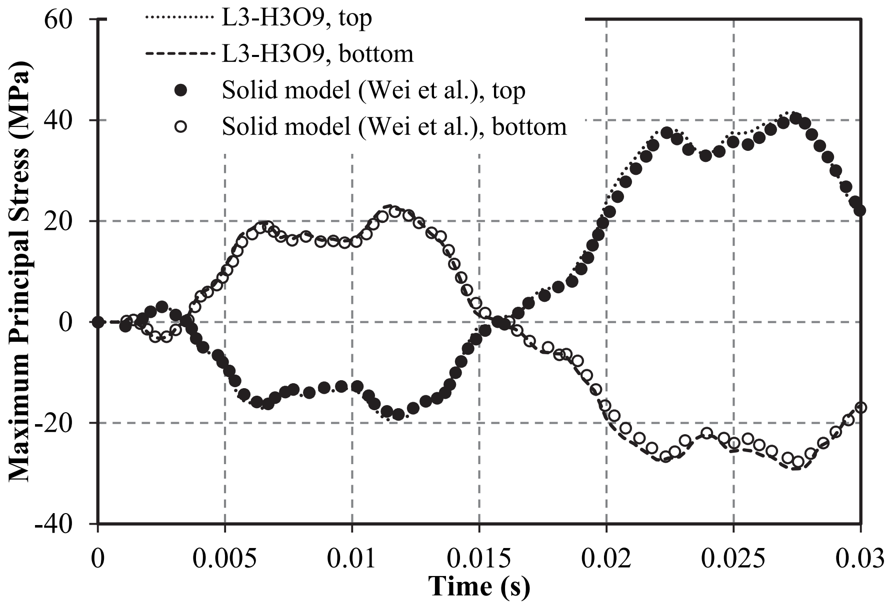

Figure 7.9: Time history of maximum principal stress at the LG centre.

<u>**Influence of G_0 on the response**</u>

The influence of changing the short-term shear modulus G_0 on the LG response is investigated. Figures 7.10-7.12 show the displacement and stress time histories of LG panels with different G_0 values. In Figure 7.12, results of a FSDT-H3O9 shell model are also presented, where the corresponding stress time history remains unchanged with the G_0 value, due to ignoring the zigzag effect and the relatively low contribution of normal stresses by the interlayer.

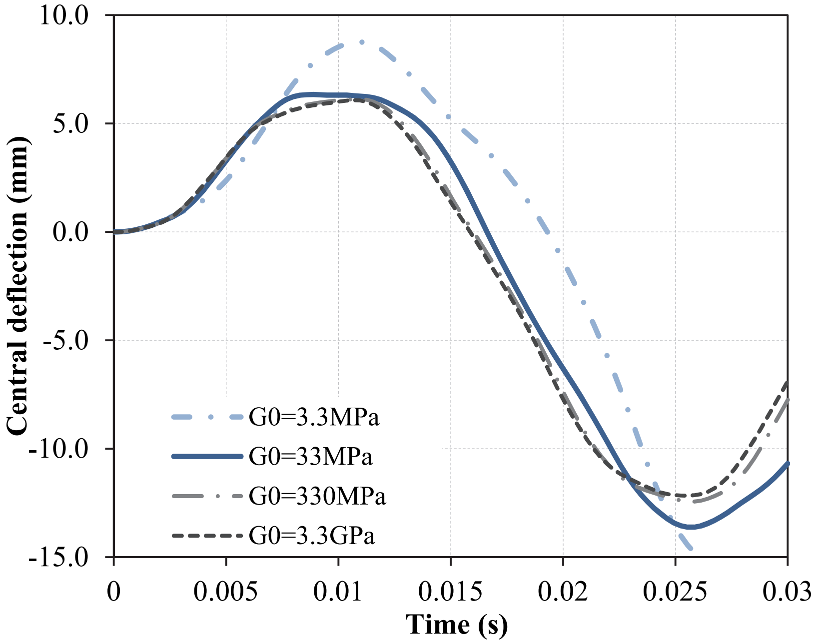

Figure 7.10: Influence of short-term PVB shear modulus on the deflection time history.

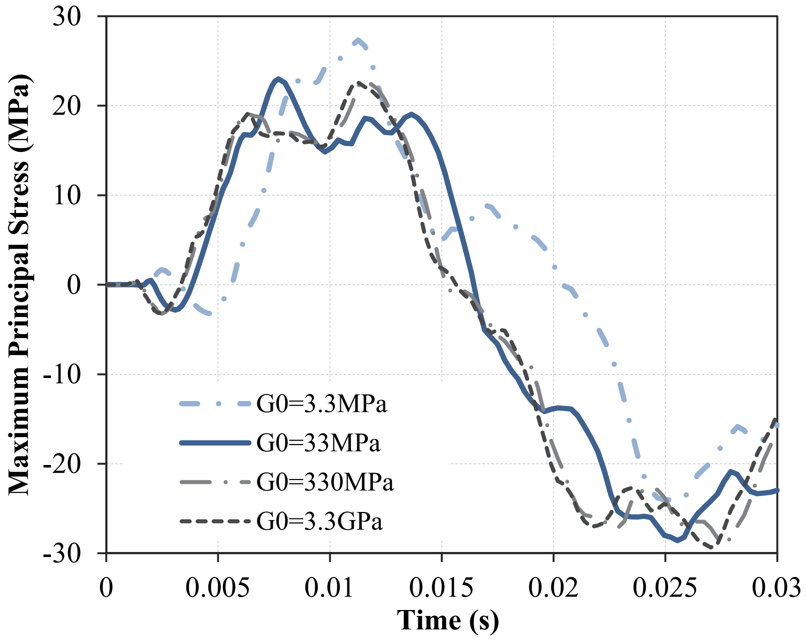

Figure 7.11: Influence of short-term PVB shear modulus on the stress time history (bottom).

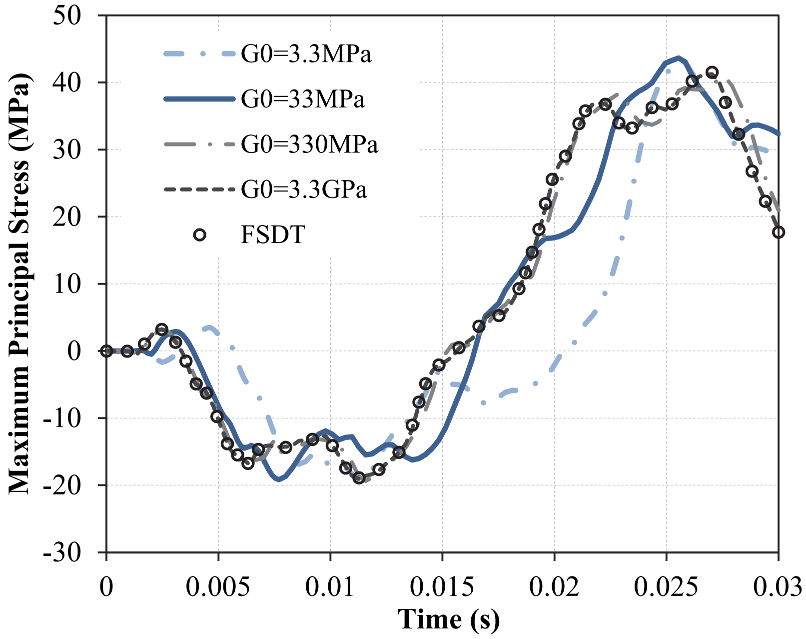

Figure 7.12: Influence of short-term PVB shear modulus on the stress time history (top).

It is observed that for a relatively large G_0 value (330MPa and 3.3GPa), the resulting time-histories have little difference, which indicates that, for both scenarios, the glass-to-PVB stiffness ratio is not large enough to induce significant zigzag effect. For a relatively small G_0 value, however, the glass-to-interlayer stiffness mismatch generates noticeable cross-sectional warping, which affects the shape and magnitude of the time history curve as well as the natural period of the structure. Within this range of G_0, the FSDT model is not suitable to accurately capture the structural behaviour owing to the assumed linear through-thickness variation of displacements.

7.4 Volume-pressure control algorithm

In the analysis of double glazing systems, the influence of the volume change in the enclosed air on the structural behaviour needs to be taken into consideration. In this section, a simple volume-pressure control algorithm is presented with the employment of Boyle's law.

It is assumed that the gas enclosed by a surface can be regarded as an ideal gas and has no viscosity or inertia effects, and that the analysis is at an isothermal state. Therefore, the relationship between the gas volume and the generated pressure follows Boyle's law, which is expressed as:

$$p_1 V_1 = p_2 V_2 \tag{7.15}$$

where p_1 and p_2 are gas pressures at states 1 and 2, respectively, and V_1 and V_2 are gas volume at the respective states.

Denote the enclosed gas volume and pressure at the initial undeformed configuration as respectively V_E^0 and p_E^0 (where 'E' represents the enclosure), the pressure generated by the gas at the current deformed configuration, p_E^{n+1}, is expressed as

$$p_E^{n+1} = \frac{p_E^0 V_E^0}{V_E^{n+1}} \tag{7.16}$$

where V_E^{n+1} is the enclosed gas volume at the current configuration.

There is an interaction between p_E^{n+1} and V_E^{n+1}, evident from the fact that the current gas pressure is dependent on how the volume of the enclosure changes, while the deformation of the enclosure is in turn affected by the applied gas pressure. An intuitive way of solving p_E is to treat it as a pressure DOF. This method derives correct gas pressure for each time step, but the pressure DOF leads to a coupled relationship between the deformation of the enclosing surface and the gas pressure. Owing to the coupling of all structural elements forming the enclosing surface to the pressure DOF, the computational efficiency may be significantly reduced.

An alternative approach is to apply the gas pressure based on the deformed enclosure configuration of the previous time step, which maintains fast convergence rate of the model owing to the employment of a decoupled relationship between the displacement parameters and the pressure parameter, though smaller time steps are required to ensure the accuracy of the generated gas pressure. In the following, a more effective volume-pressure control algorithm is presented, which maintains a decoupled relationship between the gas pressure and structural deformation, and which can also be employed for large displacement analysis.

7.4.1 Volume-pressure control procedure

Figure 7.13 depicts the configurations of the enclosed surface at time t_n and t_{n+1}, where t_n corresponds to the last known configuration, while t_{n+1} corresponds to the current unknown configuration. The current enclosure volume V_E^{n+1} can be calculated by adding an incremental volume change of the enclosure to that of the last known configuration:

$$V_E^{n+1} = V_E^n + \Delta V_E^{n+1} \tag{7.17}$$

where the subscript 'E' stands for the considered enclosure; ΔV_E^{n+1} is the volume change of the enclosure during the current time step $\Delta t^{n+1} = t_{n+1} - t_n$.

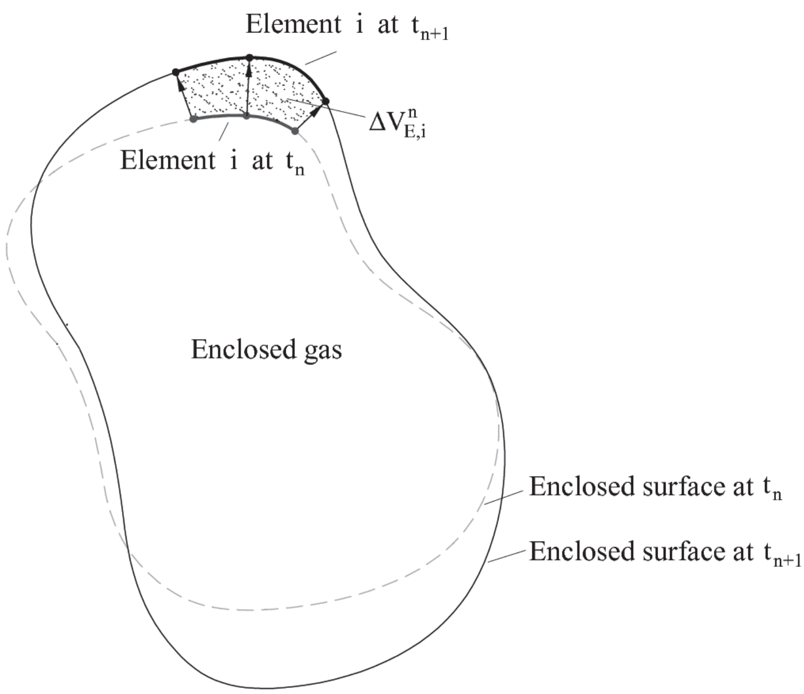

Figure 7.13: The volume change of enclosure from time t_n to time t_{n+1}.

As has been stated, there is a coupled relationship between the enclosure volume and the generated gas pressure. In the proposed volume-pressure control procedure, the incremental volume change ΔV_E^{n+1} is approximated based on the known parameters of the previous time step. It is assumed that the enclosure in the current time step has the same rate of volume change as that in the previous time step, which leads to an adequate prediction of ΔV_E^{n+1} as follows:

$$\Delta \bar{V}_E^{n+1} = \frac{\Delta V_E^n}{\Delta t^n} \Delta t^{n+1} \tag{7.18}$$

where the bar on the variable $\Delta \bar{V}_E^{n+1}$ indicates an approximating value.

At the beginning of each time step, the value $\Delta \bar{V}_E^{n+1}$ is estimated using (7.18), which is then used to obtain an approximated value of the current enclosure volume:

$$\bar{V}_E^{n+1} = V_E^n + \Delta \bar{V}_E^{n+1} \tag{7.19}$$

where $\bar{V}_E^{n+1}$ is an estimation of the current enclosure volume.

Rather than defining a pressure DOF and coupling it with the enclosure displacements, the proposed algorithm calculate the current gas pressure, p_E^{n+1}, only once at the beginning of the time step with the use of the estimated volume $\bar{V}_E^{n+1}$:

$$p_E^{n+1} = \frac{p_E^0 V_E^0}{\bar{V}_E^{n+1}} \tag{7.20}$$

where p_E^0 and V_E^0 represent the gas pressure and the volume of the enclosure in the initial undeformed state.

Subsequently, the analysis for the current time step is performed with the use of p_E^{n+1} in combination with other external loads. Once the displacement parameters of the current time step have been solved for, the real volume change ΔV_E^{n+1} can be calculated by integrating the normal component of incremental displacements $\mathbf{d}^{n+1}$ throughout the enclosed surface Ω_E^n (Figure 7.13):

$$\Delta V_E^{n+1} = \sum_{i=1}^{N} \Delta V_{E,i}^{n+1} \tag{7.21}$$

$$\Delta V_{E,i}^{n+1} = \int_{\Omega_E^{e\,n}} (\mathbf{d}^{n+1} \cdot \mathbf{c}_\zeta^n) \, d\Omega_E^{e\,n} \tag{7.22}$$

where N stands for the number of shell elements that compose the enclosure; $\Omega_E^{e\,n}$ denotes the domain of the shell element composing the enclosure, with the superscript 'n' denoting the previous configuration at time t_n ; $\mathbf{d}^{n+1}$ represents the incremental translational displacements at time t_{n+1} in terms of the global system, which is interpolated as:

$$\mathbf{d}^{n+1} = \sum_{i=1}^{N_e} N_i \mathbf{d}_i^{n+1} \tag{7.23}$$

$\mathbf{c}_\zeta^n$ is the unit outward normal vector of the element in the previous configuration, which varies over the curved shell configuration:

$$\mathbf{c}_\zeta^n = \frac{\mathbf{v}_\xi^n \times \mathbf{v}_\eta^n}{\left\| \mathbf{v}_\xi^n \times \mathbf{v}_\eta^n \right\|}, \quad \mathbf{v}_\xi^n = \frac{\partial \mathbf{X}^n}{\partial \xi}, \quad \mathbf{v}_\eta^n = \frac{\partial \mathbf{X}^n}{\partial \eta} \tag{7.24}$$

with $\mathbf{X}^n = \left\langle X^n, Y^n, Z^n \right\rangle^T$ representing the global nodal coordinates of the element at the previous time step t_n, interpolated as:

$$\mathbf{X}^n = \sum_{i=1}^{N_e} N_i \mathbf{X}_i^n \tag{7.25}$$

It is important to note that although (7.18)-(7.20) give an approximation of the current gas pressure, the accuracy improves with finer temporal discretisation. In addition, the employment of (7.18)-(7.20) leads to a decoupled system of equations for the displacement parameters and the gas pressure, which provides good accuracy without a significant increase computation time.

7.5 Verification of volume-pressure control algorithm

The volume-pressure control algorithm is verified with two simple dynamic examples, where the convergence studies on the mesh size and the time step are included in the first example, and the comparison against the results of others is given in the second example.

7.5.1 Clamped double glazing

7.5.1.1 Description of problem

As depicted in Figure 7.14, a double glazing, which is composed of two 1.2m × 1.2m × 5mm AG panes with a 10mm insulated air gap in between, is subjected to a uniform transverse pressure loaded on one glazing pane, with the loading history presented in Figure 7.15. The material properties of the glass are $E = 7.2 \times 10^{10}$, $\nu = 0.25$, and $\rho = 2500\,\mathrm{kg/m^3}$. The translational DOFs are all restrained at the glazing edges. The central deflections $u_z(L/2, L/2)$ and stress components $\sigma_x(L/2, L/2)$ for each pane are used to assess accuracy, with the evaluation positions in the thickness direction shown in Figure 7.14.

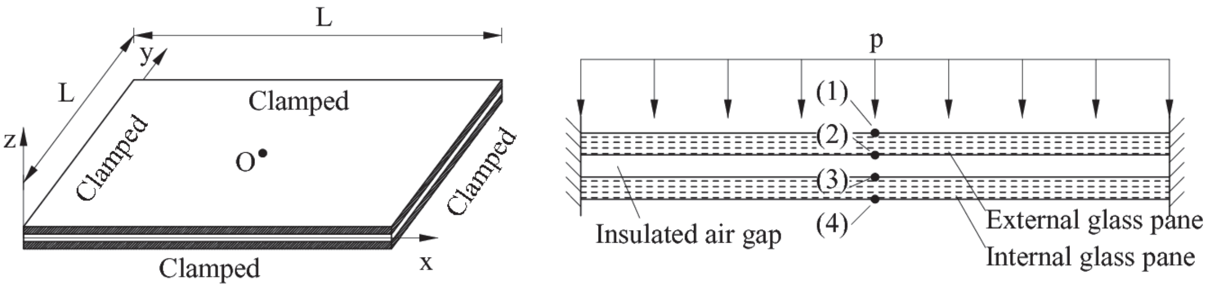

Figure 7.14: Clamped double glazing with insulated air gap subject to uniform pressure.

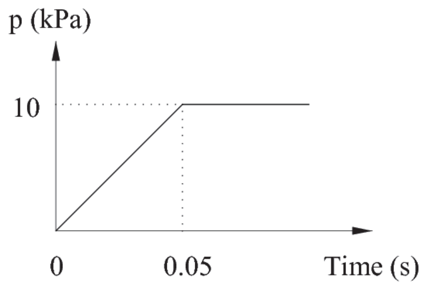

Figure 7.15: Loading history of uniform pressure p.

7.5.1.2 Results of proposed volume-pressure control algorithm

Due to symmetry, a quarter of the glazing is modelled with the monolithic H3O9 elements using ADAPTIC (Izzuddin, 1991). The volume-pressure control algorithm is employed for all the shell elements forming the enclosure, where the element normals of the elements are all oriented outward, which is a requirement for the direct application of (7.21)-(7.22) without sign adjustment. In order to ensure the accuracy of the results, a time step of $\Delta t = 2.5 \times 10^{-4}$ sec is employed. The time histories of the central displacements and stresses are depicted in Figures 7.16-7.17 for three successive meshes (4×4, 6×6 and 8×8 for each of the quarter-pane), which shows that the 6×6 mesh provides a convergent solution, although the results with a 4×4 mesh are already reasonably accurate. From Figure 7.17 it is also observed that that the problem is associated with large displacement, evident from the much larger magnitudes of stress σ_x at positions (2) and (4) , owing to the stretching of the glass panes under loading.

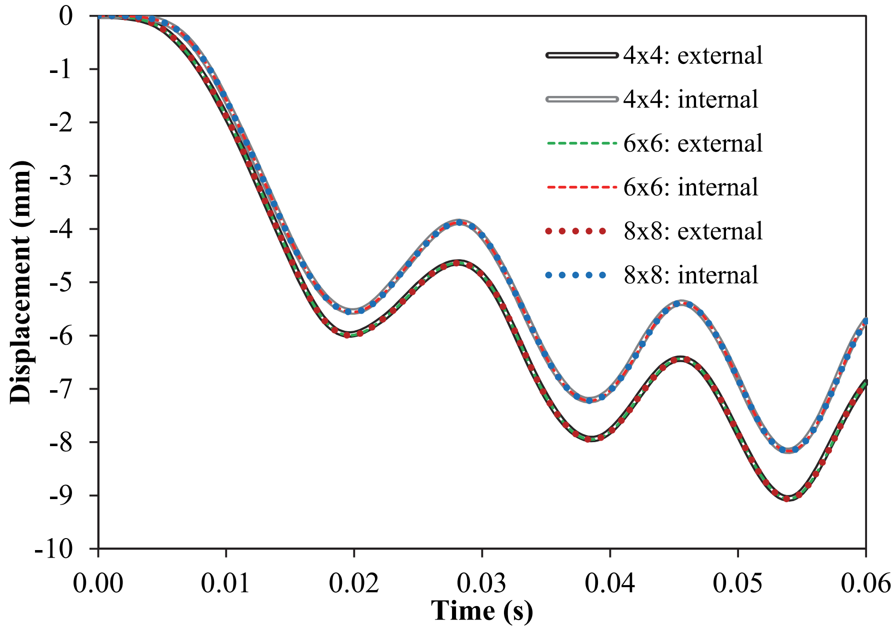

Figure 7.16: Displacement time histories of ADAPTIC models with three successive meshes ($\Delta t = 2.5 \times 10^{-4}$ sec).

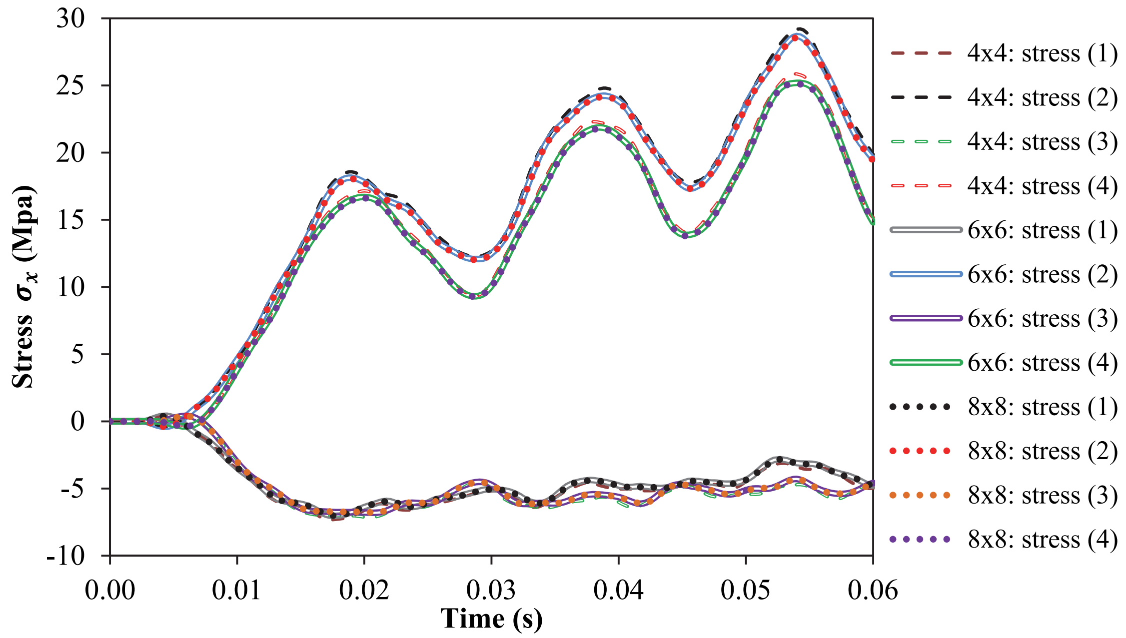

Figure 7.17: Stress time histories of ADAPTIC models with three successive meshes ($\Delta t = 2.5\times10^{-4}$ sec).

7.5.1.3 Comparison with ANSYS model

The same problem is analysed in ANSYS, where 4-noded shell elements, SHELL181, are employed for the modelling of the two glass panes, and the volume-pressure relationship is computed with the use of the hydrostatic fluid element, HSFLD242 element, as shown in Figure 7.18. The HSFLD242 element is a 3D pyramid-shaped element, where the base (I-J-K-L) is overlayed on the faces of shell elements enclosing the volume so as to share the translational displacement DOFs with the overlayed shell elements for the calculation of the gas volume. On the other hand, a pressure node Q is defined for the whole enclosure, as described in Section 7.4, which is shared by all HSFLD242 elements composing the same gas enclosure. Therefore, the HSFLD242 element correctly derives the current gas pressure and deformed configuration, but the pressure node in turn couples the displacement parameters and the pressure parameter.

A quarter of the double glazing is modelled with three successive meshes (8×8, 12×12, and 16×16) of the SHELL181 element for each pane, and a time step of $\Delta t = 2.5\times10^{-4}$ sec is used. Figures 7.19-7.20 depict the displacement and stress results with the three meshes, which shows that the 12×12 mesh provides a convergent solution, which employs the same number of displacement variables as the 6×6 mesh of the ADAPTIC model. Figures 7.21-

7.22 compare the results of the 6×6 ADAPTIC model with the 12×12 ANSYS model, which show a good agreement of both models, hence indicating the accuracy of the proposed volume-pressure control algorithm for a time step of $\Delta t = 2.5\times10^{-4}$ sec.

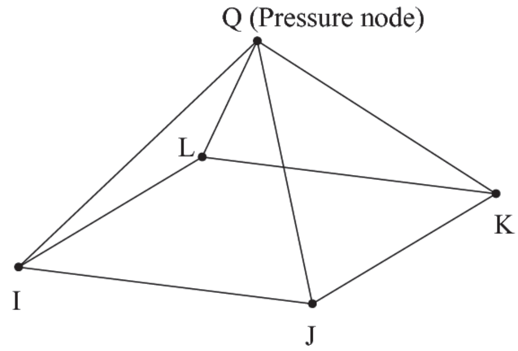

Figure 7.18: Geometry of HSFLD242 element (ANSYS, 2012).

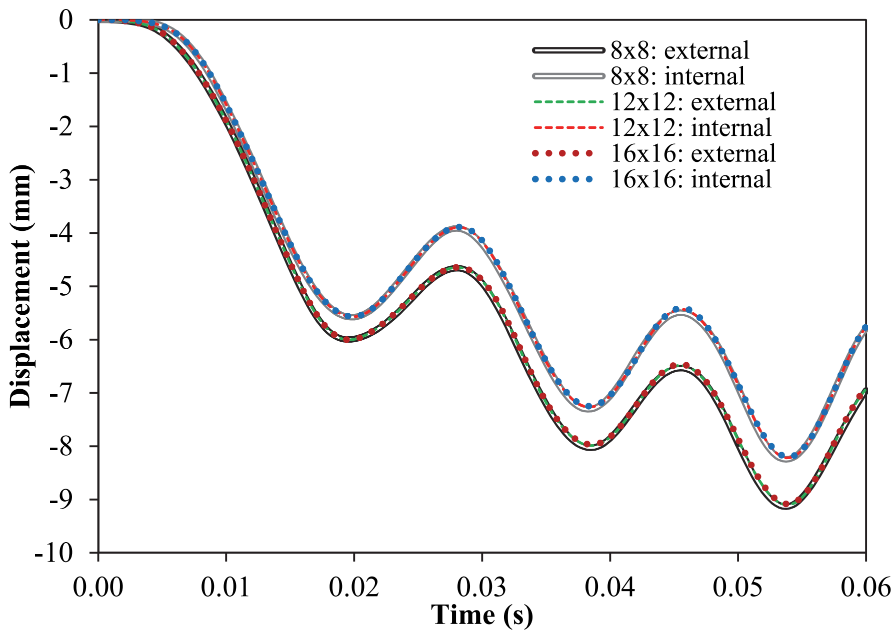

Figure 7.19: Displacement time histories of ANSYS models with three successive meshes ($\Delta t = 2.5\times10^{-4}$ sec).

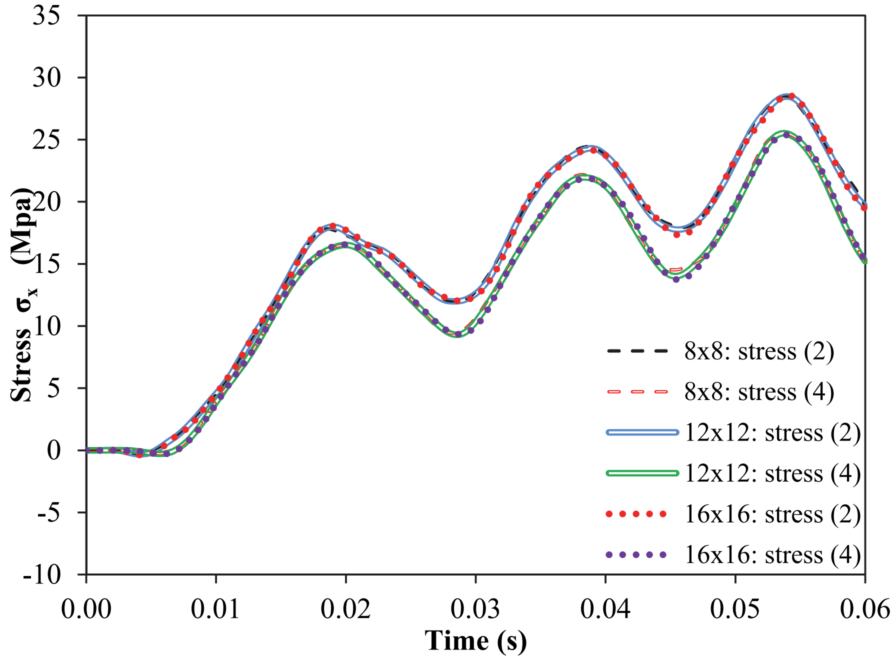

Figure 7.20: Stress time histories of ANSYS models with three successive meshes ($\Delta t = 2.5\times10^{-4}$ sec).

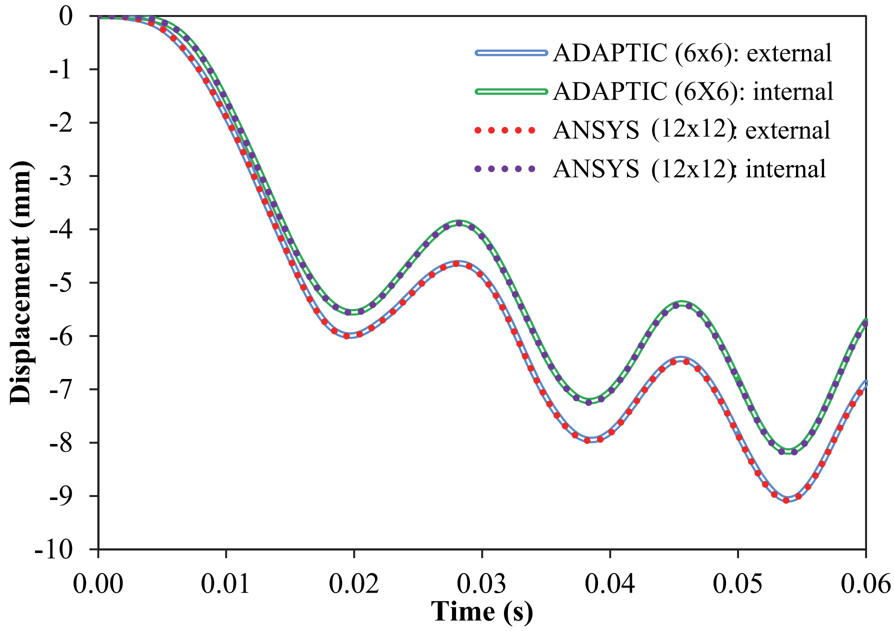

Figure 7.21: Comparison of displacement time histories between the ADAPTIC and the ANSYS models ($\Delta t = 2.5\times10^{-4}$ sec).

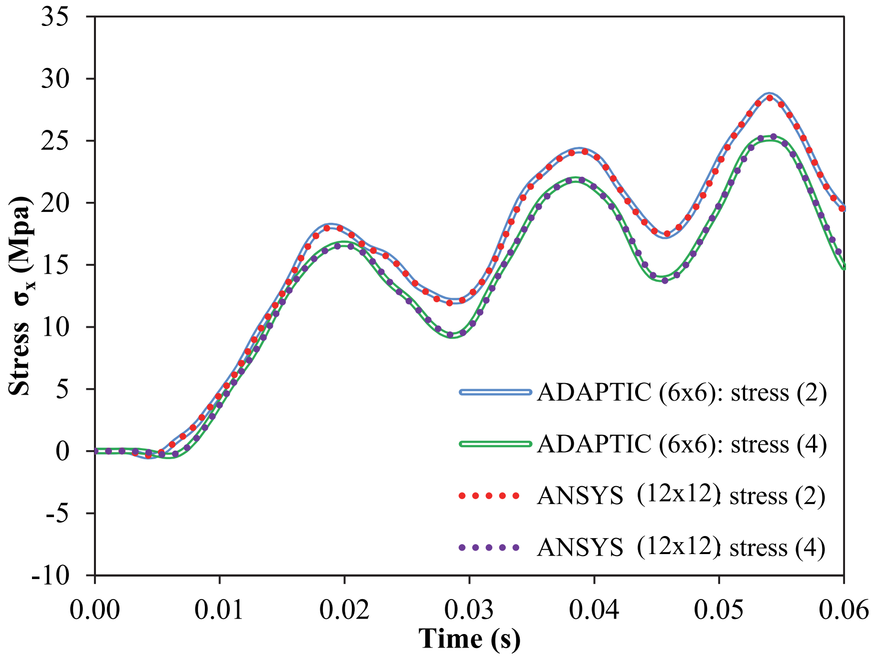

Figure 7.22: Comparison of stress time histories between the ADAPTIC and the ANSYS models ($\Delta t = 2.5 \times 10^{-4}$ sec).

As noted before, the proposed volume-pressure control algorithm excludes the use of a pressure node and avoids the coupling between the nodal displacements and the pressure DOF, though this in turn can require a relatively smaller time step than the algorithm involving a pressure parameter, as illustrated in Figures 7.23-7.24. In the figures, the stress results of each model with two incremental time steps ($\Delta t = 2.5 \times 10^{-4}$ sec and 5.0×10^{-4} sec) are depicted. The results of the ADAPTIC model employing the proposed volume-pressure control algorithm for a larger time step ($\Delta t = 5.0 \times 10^{-4}$ sec) are not as accurate as those of the ANSYS model utilising a pressure node. Nevertheless, the proposed algorithm enables the analysis of double glazing with a relatively simple modification to conventional analysis.

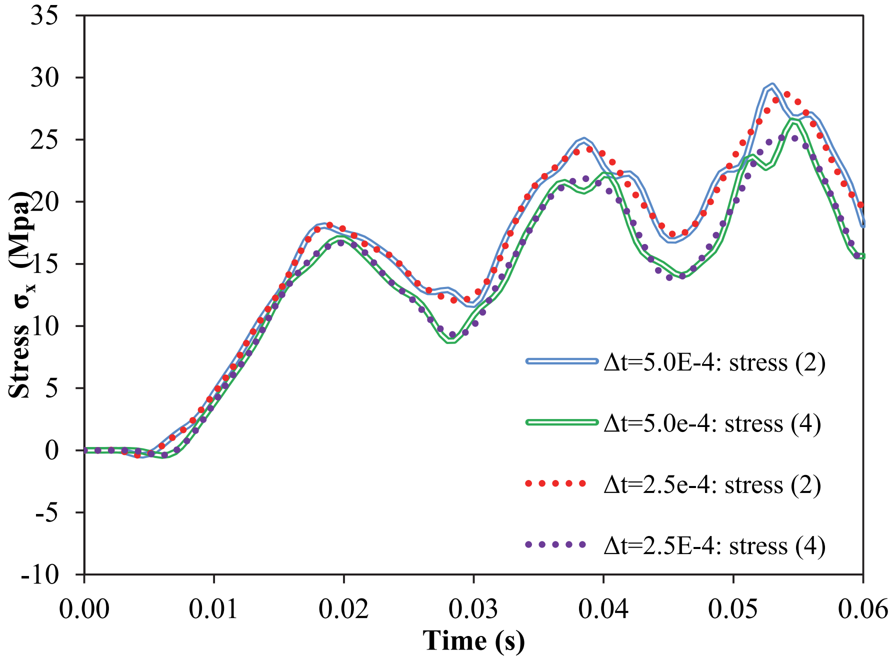

Figure 7.23: Stress time histories of ADAPTIC models with two time increments.

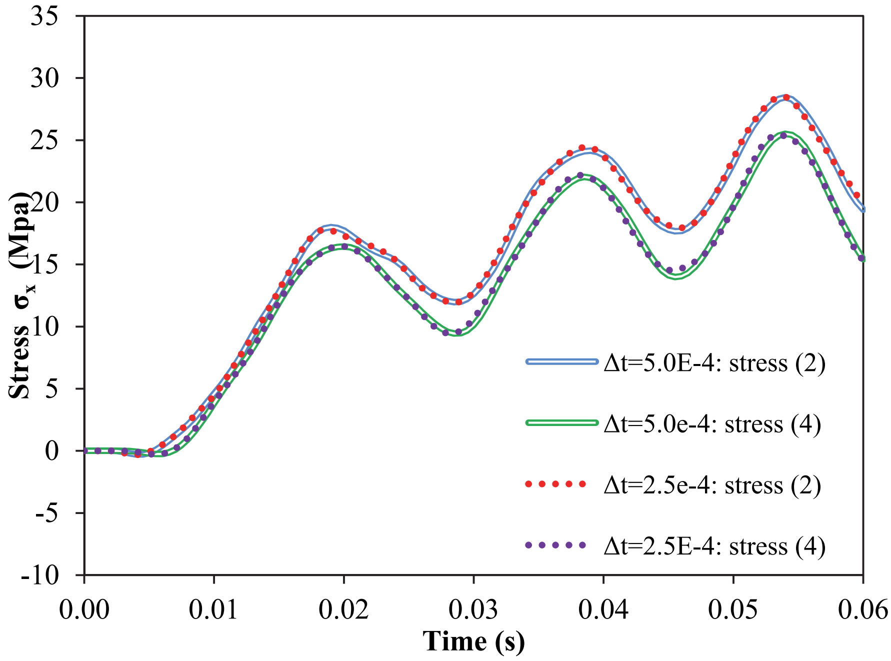

Figure 7.24: Stress time histories of ANSYS models with two time increments.

7.5.2 Pinned double glazing

7.5.2.1 Description of problem

Similar to the previous example, the response of a 1m × 1m square insulated glazing with all edges pinned under a triangular impulse load is investigated, as depicted in Figure 7.25. The insulated glazing is composed of two 10mm thick structural glass panes insulated by an air gap of 12mm. The material properties of glass are given as: $E = 72\text{GPa}$, $\nu = 0.22$, and $\rho = 2500\text{kg}/\text{m}^3$. The triangular impulse is shown in Figure 7.26, which has a magnitude of $22.3\text{kPa}\cdot\text{ms}$ with a peak pressure of 6.9kPa at time t = 0s. The deflection and principal stresses at the pane centre are evaluated, with the evaluation positions in the thickness direction shown in Figure 7.25.

Here, each glazing panel is modelled with a 16×16 mesh of the monolithic H3O9 element, and a time step of 1.5×10^{-4} sec is selected, which provides a convergent solution to the problem. The time histories of the pane central deflections and maximum principal stresses for both panes are depicted in Figures 7.27-7.28. Also presented are the results by Seica et al. (2010), where a 16×16 mesh of 9-noded elements were used for each panel. Clearly, the results of both models match well, which verifies that the proposed volume-pressure control algorithm works well, hence enabling the effective nonlinear analysis of insulated glazing.

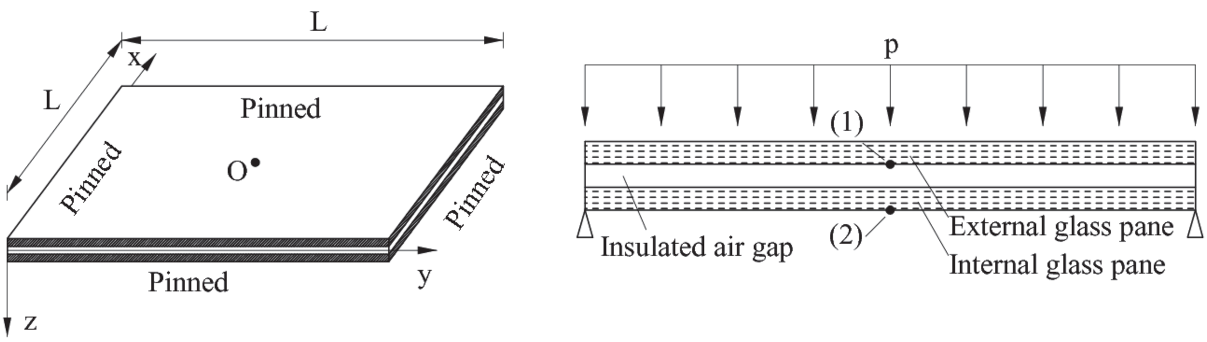

Figure 7.25: Pinned double glazing with insulated air gap subject to triangular impulse.

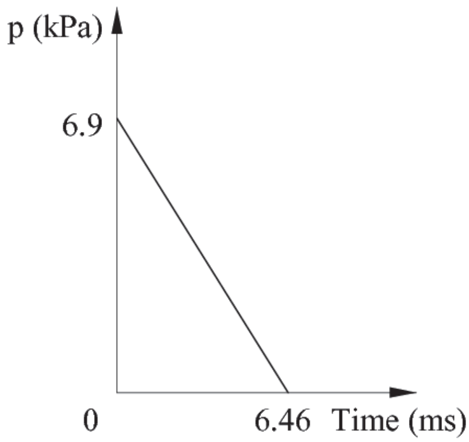

Figure 7.26: Schematic representation of the triangular impulse.

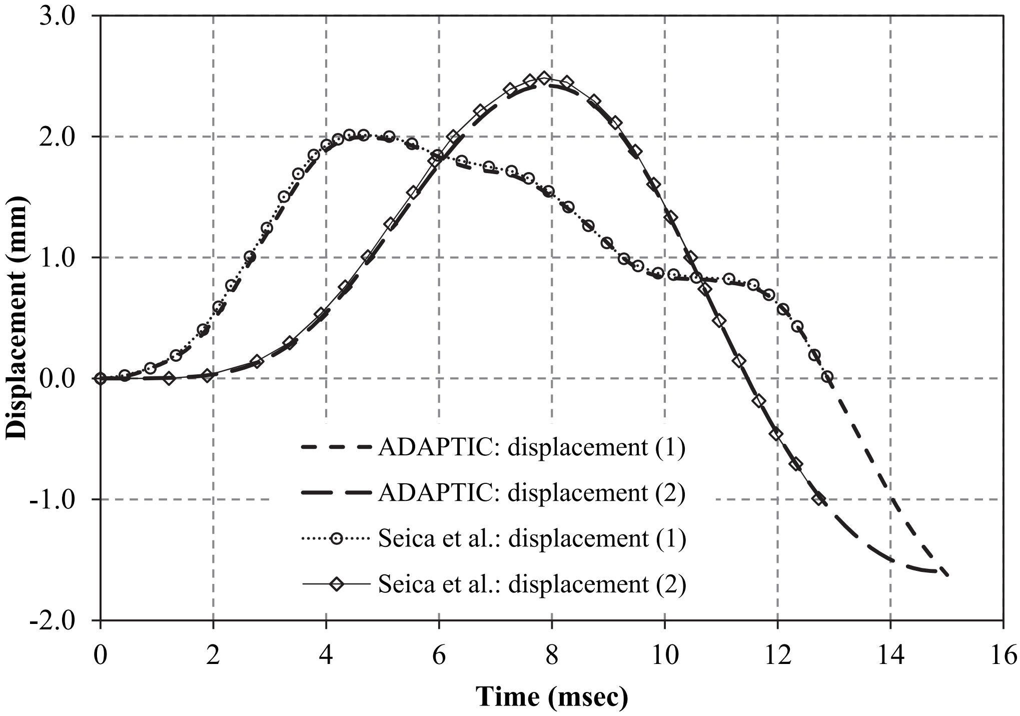

Figure 7.27: Displacement time histories of different double glazing models.

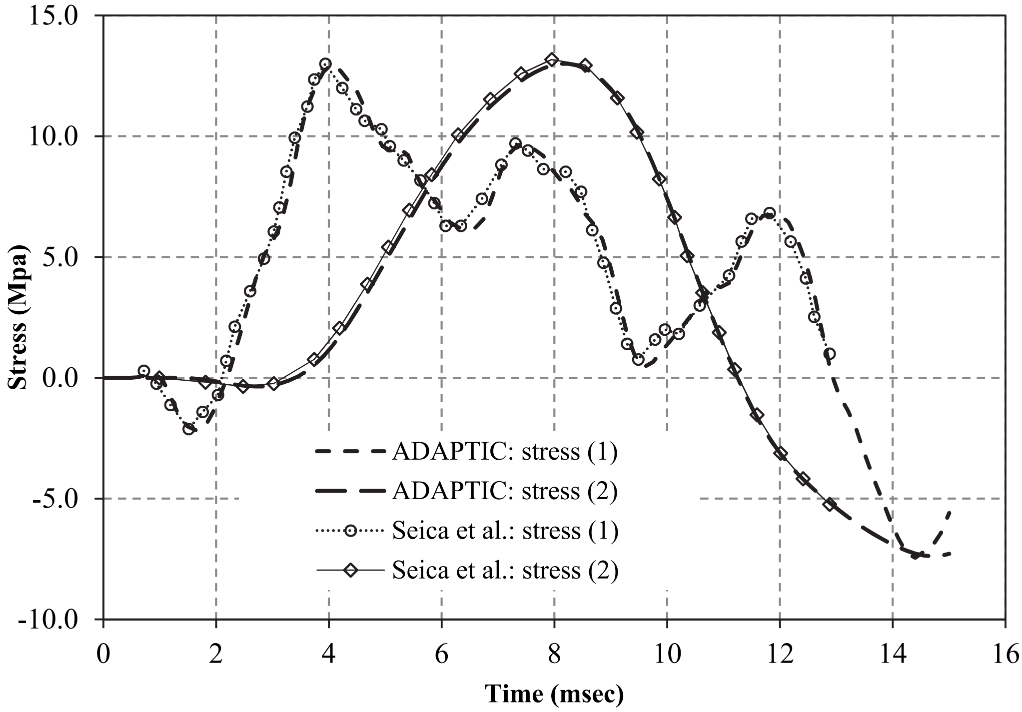

Figure 7.28: Principal stress time histories of different double glazing models.

7.6 Summary

In this chapter, the proposed laminated shell elements are used to model LG problems. Since the scope of interest is the response before the generation of cracks in glass, an elastic material model is used for glass. For the PVB interlayer, the generalised Maxwell series is adopted to describe the viscoelastic material characteristics. A recursive formula for the viscoelastic material model is employed to capture the characteristics of PVB, which is applicable to both 3D solid elements and plate and shell elements.

Subsequently, a LG problem in literature is simulated, where circular LG panels are subject to monotonously applied loading, and the structural response under different displacement loading rates is investigated. The implemented viscoelastic material model is verified with a good match between the results of the laminated shell model and the experimental and numerical data. It is also concluded from the results that: (1) under short-duration loading, the response of the LG can be regarded the same as the response of a monolithic glass pane with the same nominal glass thickness owing to the large shear stiffness generated by PVB; (2) under long-duration loadings, the shear stiffness of PVB becomes quite small, which leads to the response of the LG becoming similar to the response of two glass plies layered with no connection. Then a LG problem associated with short-duration loading is simulated, where both a linear viscoelastic material model and a linear elastic material model are used for PVB, which shows that it is feasible to use a linear elastic material model for PVB in blast analysis without loss of accuracy.

In order to allow the simulation of double glazing, a volume-pressure control algorithm is proposed, which considers the effect of insulated air by assuming a hydrostatic pressure state in the insulated air gap and relating the generated pressure to the relative volume change in the air gap. The algorithm computes the air pressure with the use of the structural configuration and rate of volume change from the previous step, which eliminates the need to introduce a pressure parameter, and hence avoids coupling between the displacement parameters with the pressure loading. The accuracy of this volume-pressure control algorithm has been verified with two numerical examples of double glazing. It is shown that for an adequate time step, the model with the proposed volume-pressure control algorithm agrees well with the solutions by others utilising coupled pressure-displacement models.

CHAPTER 8

Case Studies

8.1 Introduction

This chapter presents several applications of the proposed laminated shell elements in the modelling of LG structures, which are illustrated through a number of numerical examples. Two practical problems related to the design and assessment of LG structures are first given, with one problem associated with the buckling analysis of a partial LG structure and the other the creep analysis of a LG stair. Subsequently, a comprehensive double glazing system under blast loading is analysed, and the results are compared with existing experimental and numerical data. All numerical examples are geometrically nonlinear and modelled with the laminated shell elements proposed in the previous chapters. The first two examples are related to static analysis, and the last example examines the performance of the element in dynamic applications.

8.2 Buckling analysis of laminated glass fin

In recent years, not only has LG been widely used for secondary structural components (such as curtain wall glazing), but it has also become increasingly adopted for structural applications owing to its aesthetic appearance (Figure 8.1.a). LG members that are used in real structures are typically associated with large slenderness, which post an equal importance of stability analysis to cross-sectional strength analysis. This section focuses on the stability analysis of a partial LG structure under transverse loading (say wind load), which is extracted from a pure LG structure (Figure 8.1.a), where a laminated shell model using the proposed elements is built, with its efficiency and accuracy compared with other models.

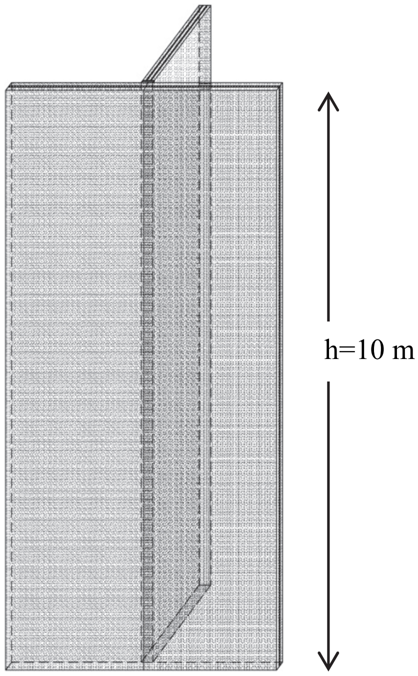

a. Apple Store Fifth Avenue New York. (www.idesignarch.com).

b. A partial model extracted from structure.

Figure 8.1: A LG structure.

8.2.1 Description of the problem

The partial LG structure shown in Figure 8.1.b is composed of two halves of curtain wall glazing panels supported by a LG fin. The glass fin is 10m in height and 400mm in depth, and consists of three 12mm glass plies bonded by two 1.52mm PVB interlayer (Figure 8.2). Each curtain wall glazing is 10m high and 2m wide, and is composed of two 10mm glass plies sandwiched by a 1.52mm PVB interlayer. Adhesive silicone bond is used between the glass fin and the glazing panes, which provides a continuous elastic support along the vertical glazing edge.

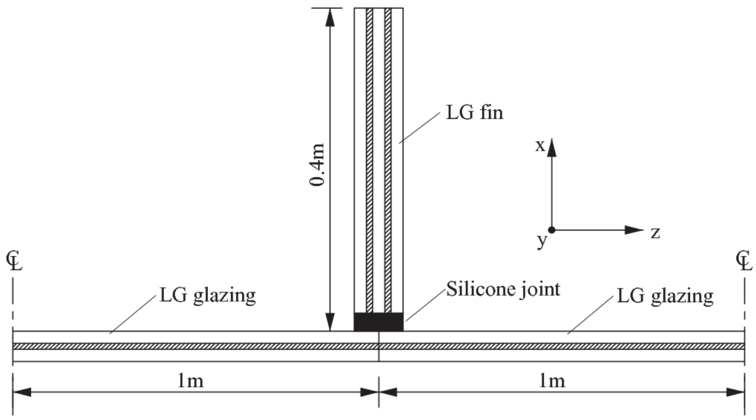

Figure 8.2: Plan view of the partial LG structure.

The material parameters of glass are $E_{glass} = 70GPa$ and $\nu_{glass} = 0.2$. For design purpose, the ASTM (2012) E1300-12 standard suggests using a linear elastic material model for the PVB with the shear relaxation modulus for a 3s load duration at a 50°C operation temperature for the analysis of wind load. Therefore, a linear elastic material model is used, where the bulk modulus is 2.0GPa and the shear modulus is 0.44MPa, which is extracted from the shear relaxation model proposed by Bennison et al. (1999) (Table 7.1) for a load duration of 3s at a 50°C operation temperature. The corresponding Young's modulus and Poisson's ratio are $E_{PVB} = 1.32MPa$ and $\nu_{PVB} = 0.4999$.

A uniform transverse pressure is applied to the two halves of glazing to represent the wind load. In this case study, a static analysis is performed to determine the critical wind load for structural buckling.

8.2.2 Consideration of silicone joint

The continuous elastic support provided by the silicone joint is modelled with matrix elements along the edge. In order to obtain the effective stiffness of the matrix element, the silicone is assumed to be virtually under plane strain conditions with negligible strains in the vertical direction. Figure 8.3 provides a schematic representation of the silicone joint cross-section, where t_g = 36mm is the overall thickness of glass plies of the LG fin and t_s = 20mm is the thickness of the silicone joint. There are three displacement fields of significance (u_x, u_z, θ), each of which is assumed to vary linearly along the x-axis:

$$u_x = \frac{u_{x0}}{t_s}\cdot x, \quad u_z = \frac{u_{z0}}{t_s}\cdot x, \quad \theta = \frac{r_y}{t_s}\cdot x \tag{8.1}$$

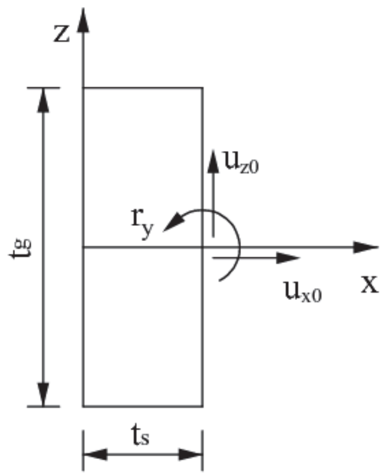

Figure 8.3: Schematic representation of the silicone joint cross-section.

The strains are given as:

$$\varepsilon_x = \frac{\partial(u_x + \theta z)}{\partial x} = \frac{u_{x0}}{t_s} + \frac{r_y z}{t_s}, \; \gamma_{xz} = \frac{\partial(u_x + \theta z)}{\partial z} + \frac{\partial u_z}{\partial x} = \frac{r_y x}{t_s} + \frac{u_{z0}}{t_s} \tag{8.2}$$

which results in the following stresses:

$$\sigma_x = \frac{E(1-\nu)}{(1+\nu)(1-2\nu)}\varepsilon_x, \quad \tau_{xz} = \frac{E}{2(1+\nu)}\gamma_{xz} \tag{8.3}$$

The internal equivalent forces can be obtained from the virtual work statement:

$$\delta u_{x0} f_{x0} + \delta u_{z0} f_{z0} + \delta r_y m_{ry} = \int_{\Omega^e} \left(\delta\varepsilon_x \sigma_x + \delta\gamma_{xz}\tau_{xz}\right) d\Omega^e \tag{8.4}$$

which yields:

$$\begin{cases} f_{x0} = \dfrac{E(1-\nu)}{(1+\nu)(1-2\nu)} \dfrac{t_g}{t_s} u_{x0} \\ f_{z0} = \dfrac{E}{2(1+\nu)} \dfrac{t_g}{t_s} u_{z0} + \dfrac{E}{2(1+\nu)} t_g r_y \\ m_{ry} = \left(\dfrac{E(1-\nu)}{(1+\nu)(1-2\nu)} \dfrac{t_g^3}{12t_s} + \dfrac{E}{2(1+\nu)} t_s t_g \right) r_y + \dfrac{E}{2(1+\nu)} t_g u_{z0} \end{cases} \tag{8.5}$$

By ignoring the coupling terms between u_{z0} and r_y, and taking the material parameters of the structural silicone to be $E = 1.4\text{MPa}$ and $\nu = 0.499$, the equivalent uncoupled stiffness terms are obtained as:

$$\begin{cases} k_x = f_{x0}/u_{x0} = \dfrac{E(1-\nu)}{(1+\nu)(1-2\nu)} \dfrac{t_g}{t_s} = 4.211 \times 10^8 \ \text{N/m}^2 \\ k_z = f_{z0}/u_{z0} = \dfrac{E}{2(1+\nu)} \dfrac{t_g}{t_s} = 8.406 \times 10^5 \ \text{N/m}^2 \\ k_{ry} = m_{ry}/r_y = \dfrac{E(1-\nu)}{(1+\nu)(1-2\nu)} \dfrac{t_g^3}{12t_s} + \dfrac{E}{2(1+\nu)} t_s t_g = 4.582 \times 10^4 \ (\text{N} \cdot \text{m})/\text{m} \end{cases} \tag{8.6}$$

Since silicone is associated with a large Poisson's ratio, the silicone joint undergoes large bulk deformation under loading. Therefore, a solid model with a fine mesh is also used to model the silicone joint, which has a width t_g, a depth t_s, and a height H = 50mm. As shown in Figure 8.4, the top and bottom surfaces are restrained in the y direction, whereas the left surface is fully restrained. Three displacement modes are applied on the right surface, respectively:

(1) Elongation in the x direction, at $x = t_s$: $u_x = 10^{-6}$, $u_y = u_z = 0$;

(2) Shearing in the z direction, at $x = t_s$: $u_z = 10^{-6}$, $u_x = u_y = 0$;

(3) Rotation about the y axis, at $x = t_s$: $u_x = 10^{-6}(z - t_g/2)$, $u_y = 0$.

The three models then correspond to respectively a tensile force F_x, a shear force F_z, and a bending moment M_{ry}, respectively, which result in the effective stiffness terms as follows:

$$\begin{cases} k_x = \dfrac{F_x}{u_x H} = 6.32\times10^6\,\mathrm{N/m^2} \\ k_z = \dfrac{F_z}{u_z H} = 6.28\times10^5\,\mathrm{N/m^2} \\ k_{ry} = \dfrac{M_{ry}}{r_y H} = 405.6(\mathrm{N\cdot m})/\mathrm{m} \end{cases} \tag{8.7}$$

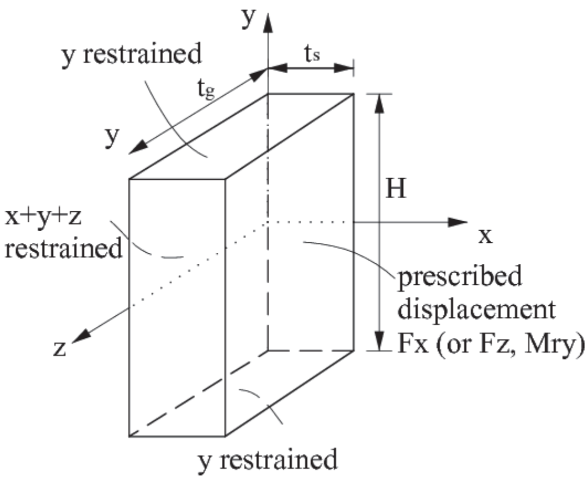

Figure 8.4: Boundary conditions for the silicone joint model.

Clearly, the bulk deformation of silicone (Figure 8.5) has a significant influence on the stiffness terms, in particular k_x and k_{ry}. In the following analyses, the effective stiffness terms of (8.7) are used for the spring matrix elements. Denoting h_e as the element size of the fin along the y axis, then equivalent stiffness parameters at each discrete node along the edge for quadratic shell elements are:

Edge node: $K_x = \frac{2}{3}k_x h_e$, $K_z = \frac{2}{3}k_z h_e$, $K_{ry} = \frac{2}{3}k_{ry} h_e$;

Corner node: $K_x = \frac{1}{3}k_x h_e$, $K_z = \frac{1}{3}k_z h_e$, $K_{ry} = \frac{1}{3}k_{ry} h_e$.

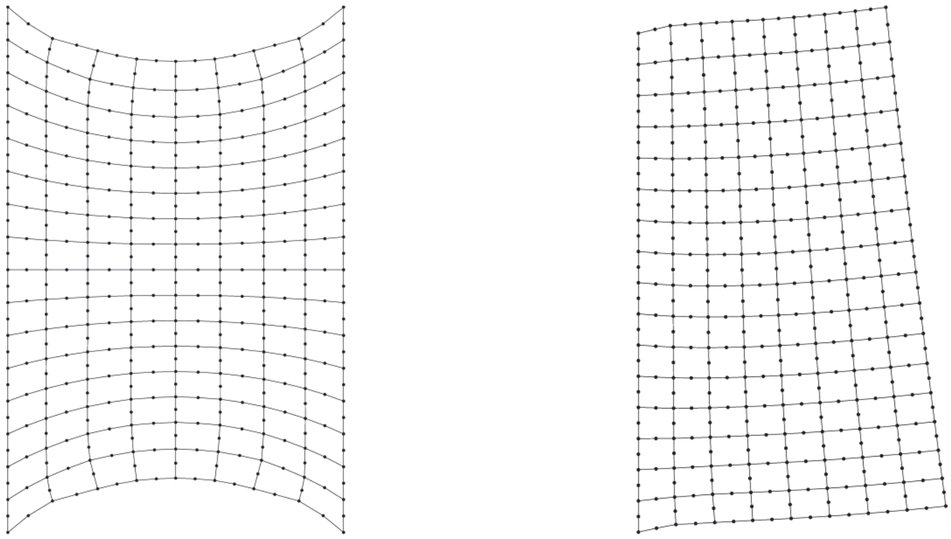

a. Deformation mode for a uniform elongation. b. Deformation mode for a uniform rotation.

Figure 8.5: Representative cross-sectional deformation modes due to bulk deformation.

8.2.3 Finite element modelling with different methods

8.2.3.1 Laminated shell element model

The partial fin-glazing structure is simulated with a laminated shell element model, where the glass fin is modelled with a 16×4 mesh of the L5-H3O9 element, and each half glazing is modelled with a 16×8 mesh of the L3-H3O9 element. The boundary conditions of the partial model are depicted in Figure 8.6.a. The structure is more vulnerable to the suction load, hence uniform loads in the negative x direction are considered in this buckling analysis. Besides the fin-glazing model, a more simplified fin model is also used which consists of the glass fin only with the same element size. Figure 8.6.b shows the boundary conditions of the simplified model, and the suction load is assumed to be a uniform line load applied to the silicone joint. Both considered models provide convergent solutions. Figure 8.7 depicts the load-displacement curves of Point A in the z direction with both the fin-glazing model and the fin model. Note that for the fin-glazing model the effective suction load is obtained by dividing the sum of the uniform loading on the glazing panels, minus the reaction forces associated with the restraints in x at the top and bottom glazing edges (illustrated in Figure 8.6.a), by the glazing width. It is evident that the predicted buckling curve of the fin model matches well that of the fin-glazing model. The fin model with a 16×4 mesh of the proposed

L5-H3O9 is denoted as Model 1, which will be compared with other models. On the other hand, by restraining all the additional DOFs, a FSDT-based laminated shell model is also obtained for comparison, which is denoted as Model 2.

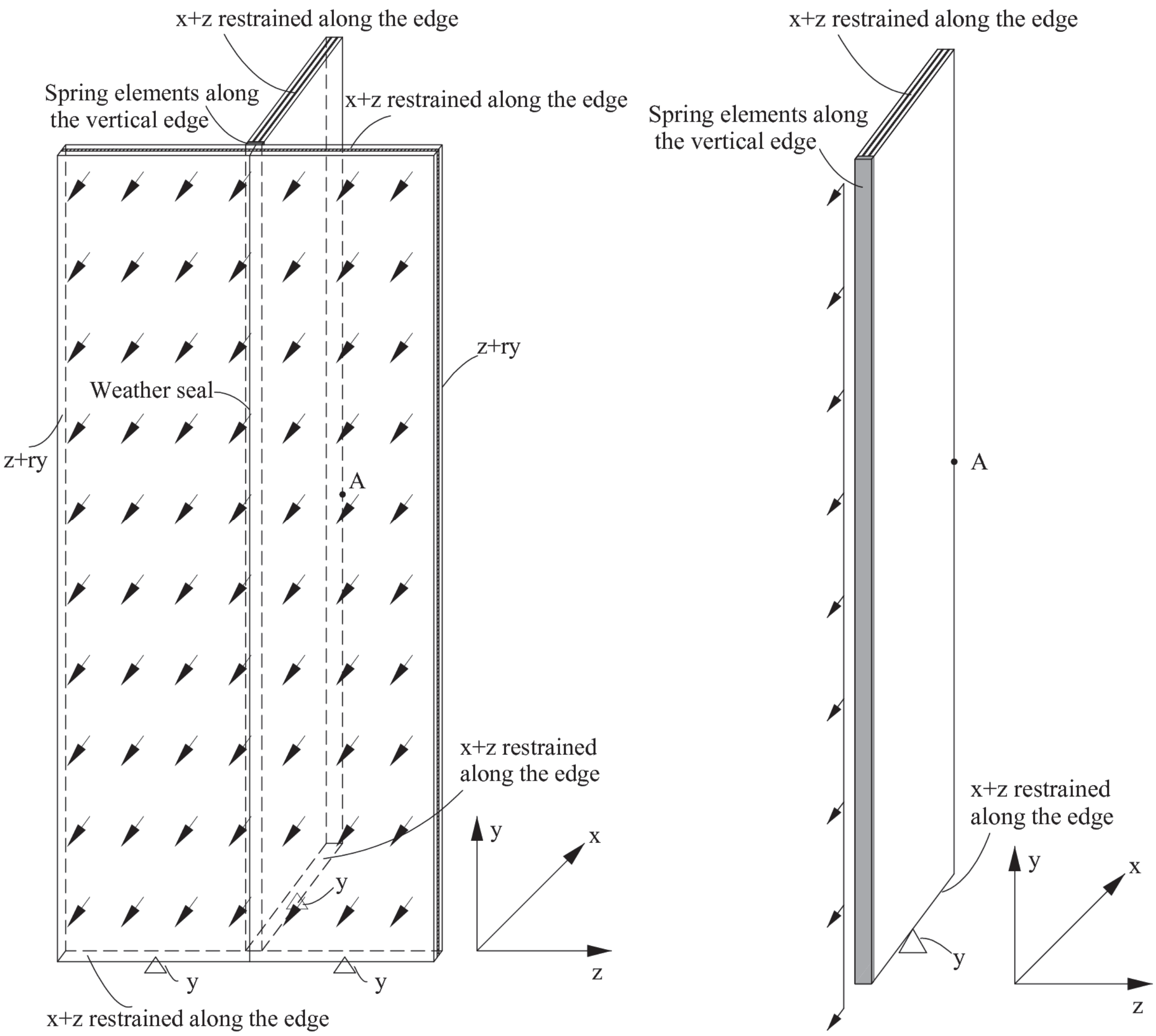

a. fin-glazing model

b. fin model

Figure 8.6: Boundary conditions for the fin-glazing model and the fin model.

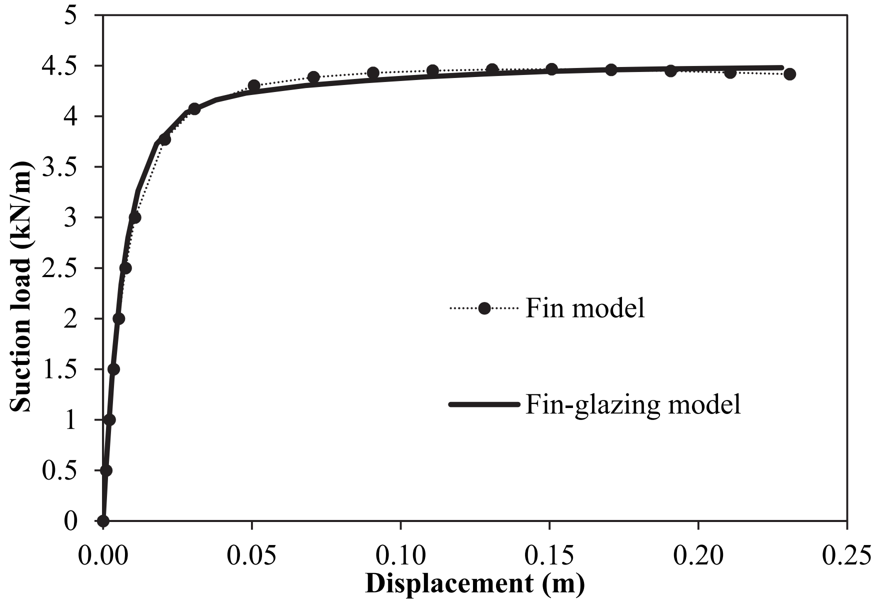

Figure 8.7: Load-displacement curves of the fin-glazing model and the fin model.

8.2.3.2 Monolithic shell element model

In the ASTM (2012) E1300-12 standard, an engineering formula is provided in Appendix X9 for calculating the effective thickness of two-ply LG, which allows the use of a monolithic shell model to predict the displacements or stresses of glass laminates. A shear transfer coefficient is defined to measure the shear stress transfer across the interlayer, which is used in two separate effective thickness equations for the estimation of the maximum deflection and glass bending stress, respectively (Appendix E). The effective thickness expression for two plies is then extended to three-ply LG by substituting the effective thickness of two-ply LG back into the equation, as described by Zenkert and Industrifond (1997). For the prediction of deflection for the three-ply LG fin, Zenkert and Industrifond's model yields an effective thickness of 20.79 mm, which is then used in a 16×4 monolithic shell model employing the H3O9 element, denoted as Model 3.

8.2.3.3 Solid element model

Apart from the laminated and monolithic shell element models, buckling analysis is also performed with a 3D solid model using the 20-noded solid element BK20, where the fin is discretised into 4 elements along the x-axis and 50 elements along the y-axis, and each layer is discretised into 2 elements through the thickness. The solid model, denoted as Model 4, provides a reference solution for comparison.

8.2.3.4 Results and discussions

Figure 8.8 depicts the load-displacement curves of Point A in the z direction using different models, where the predicted buckling load and the number of DOFs used for each of the models are listed in Table 8.1. Clearly, Model 2 employing FSDT corresponds to a much stiffer response than the others owing to the assumption of a linear displacement variation through the thickness, which, in comparison with Model 1, indicates a significant zigzag effect that cannot be ignored. Although Model 3 takes into consideration the layer thicknesses and the material mismatch by employing a reduced effective thickness for the glass laminate, the results are not accurate and overestimate the buckling load significantly, which may lead to an unsafe design. It is also observed that Model 1, which employs slightly more DOFs than Models 2 and 3 but shows comparable accuracy with Model 4, achieves good accuracy with much better efficiency compared to the 3D Model 4, where Model 1 is found to be 71.4 times faster than Model 4. Figure 8.9 also depicts the through-thickness distribution of the stress component at point A for Model 1 and 4, which shows a good agreement between the two models.

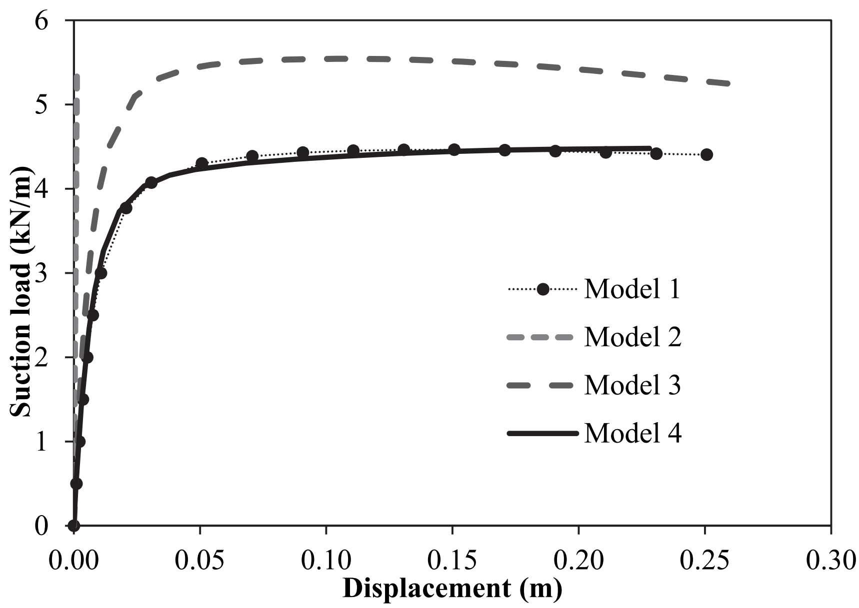

Figure 8.8: Load-displacement curves at point A for different models.

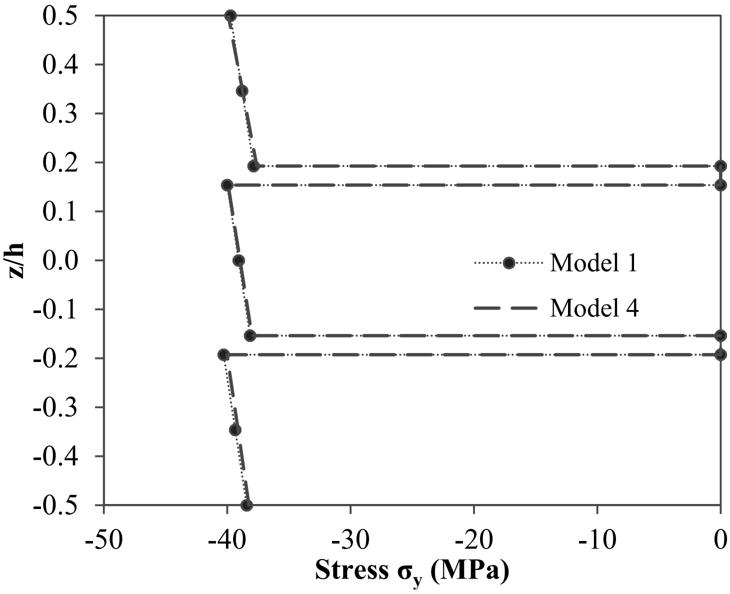

Figure 8.9: Through-thickness distribution of stress σ_y at point A for different models for a suction load of 3 kN/m.

Table 8.1: Accuracy and Efficiency comparisons of results using different models.

Model	Critical suction load (kN/m)	Number of DOFs
1	4.47	2660
2	-	1510
3	5.54	1510
4	4.48	30747

The influence of the PVB material stiffness on the predictions of the effective thickness method is investigated, where four different shear modulus values for PVB are considered (0.44 MPa, 4.4 MPa, 44 MPa, and 440MPa) while the bulk modulus remains constant at 2.0 GPa. Figure 8.10 depicts the buckling curves of Model 1 and 3 with various PVB shear modulus values. It is concluded that the effective thickness proposed by Zenkert and Industrifond (1997) overestimates the buckling load for a relatively small PVB shear modulus whereas it underestimates the buckling load for a moderate PVB shear modulus.

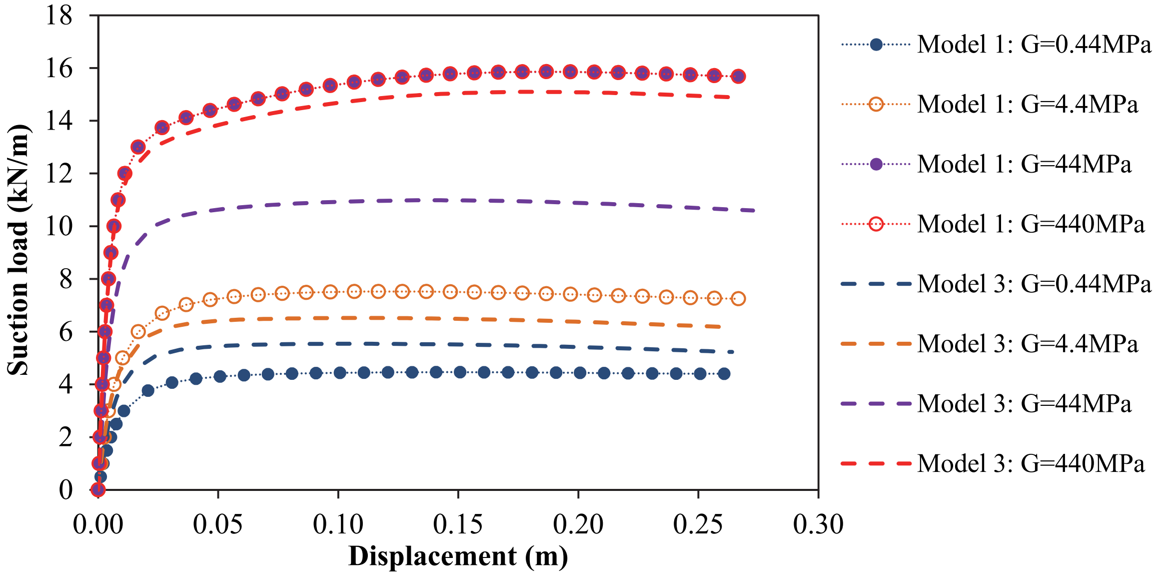

Figure 8.10: Load-displacement curves at point A with different PVB shear modulus (three-ply LG).

The accuracy of the effective thickness method for a LG fin with only two plies of the same planar dimensions is also investigated, which comprises two 3.6mm glass plies and one 1.52mm PVB interlayer. Still, Model 1 represents a 16×4 sandwich shell model using the proposed L3-H3O9 elements, and Model 3 represents a 16×4 monolithic shell model with the effective thickness calculated with reference to the ASTM (2012) E1300-12 X9 recommendation. The resulting equilibrium paths with various interlayer shear stiffness values and models are depicted in Figure 8.11. It is concluded that the effective thickness method in ASTM E1300-12 X9 results in a conservative prediction except for a large PVB shear modulus, owing to the inadequate analogy between the LG and a conventional monolithic plate. The use of two sets of equations for the prediction of displacements and stresses accounts for the inadequacy of using a monolithic plate model for the replacement of a lamination model. Nevertheless, for the considered PVB shear modulus values, the predictions of the buckling loads ensures a safe design of LG panels.

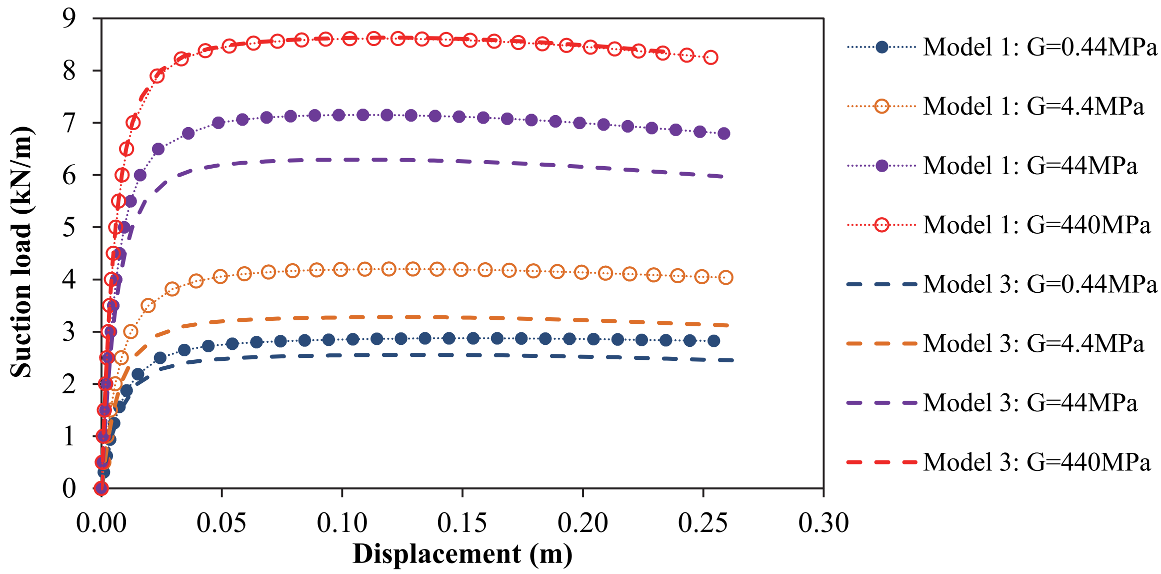

Figure 8.11: Load-displacement curves at point A with different PVB shear modulus (two-ply LG).

8.3 Creep of laminated glass stair

Owing to the fact that the interlayers used in LG typically consist of viscoelastic material, the LG is associated with noticeable creep under long-duration loadings. The linear viscoelastic material model implemented in Chapter 7 considers the influence of loading duration and temperature on the material mechanical properties, thus enabling the investigation of creep development in LG panes with time. As depicted in Figure 8.12, the creep of glass stairs is a typically encountered problem, which is considered in this case study.

8.3.1 Description of the problem

Figure 8.13 shows a 1.8m wide, 0.3m deep LG stair, which is installed horizontally with both edges simply supported and loaded with a self-weight of w = 1219.7 N/m^2. The glass stair is composed of four 12mm glass plies and three 1.52mm PVB interlayers. The material parameters of glass are $E_{glass} = 70\text{GPa}$ and $\nu_{glass} = 0.2$. The linear viscoelastic model proposed by Bennison et al. (1999) is used for the PVB, so that the creep behaviour of the glass stair at different operation temperatures can be investigated.

Considering the constant loads and the long time span of the analysis, this problem can be regarded as a pseudo static problem. A static analysis is performed on a quarter model of the stair, which uses an 8×2 mesh of the L7-H3O9 elements to provide a convergent solution. In the following, the influence of loading duration and operation temperature is investigated and the results are discussed.

Figure 8.12: Glass staircase in Soho Apple Store, New York.

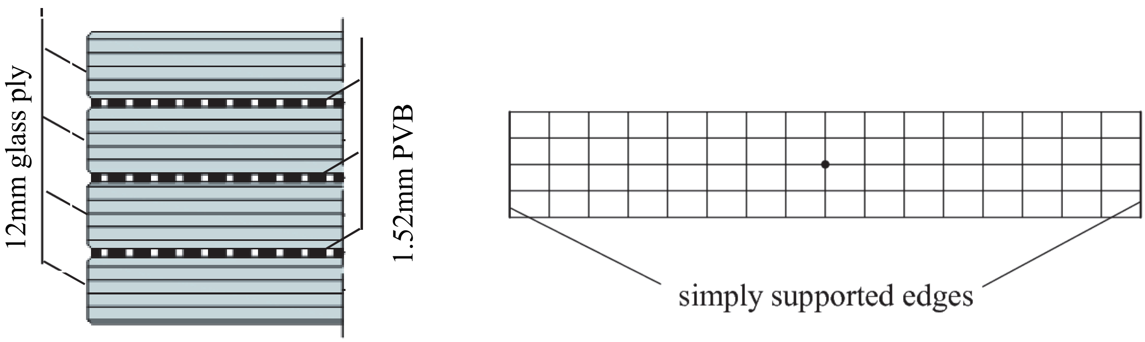

a. through-thickness representation.

b. shell model of the glass stair.

Figure 8.13: Schematic representation of the LG stair.

8.3.2 Influence of temperature on creep behaviour

Figure 8.14 depicts the time-history curves of the central deflection with various operation temperatures for 10 years. The same results in the logarithmic time scale is presented in Figure 8.15, which shows that for an operation temperature of 30°C the stair deflection approaches to the asymptotic value (3.05mm) at around 98 days after installation, whereas for an operation temperature of 10°C the deflection at 10 years is around 1.90mm, which is much lower than the other three curves.

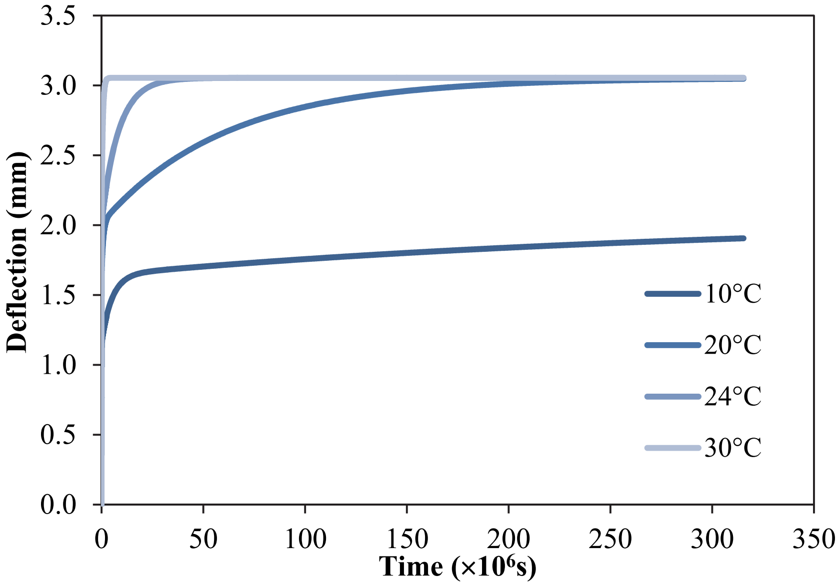

Figure 8.14: Deflection time history of the LG stair with different operation temperatures.

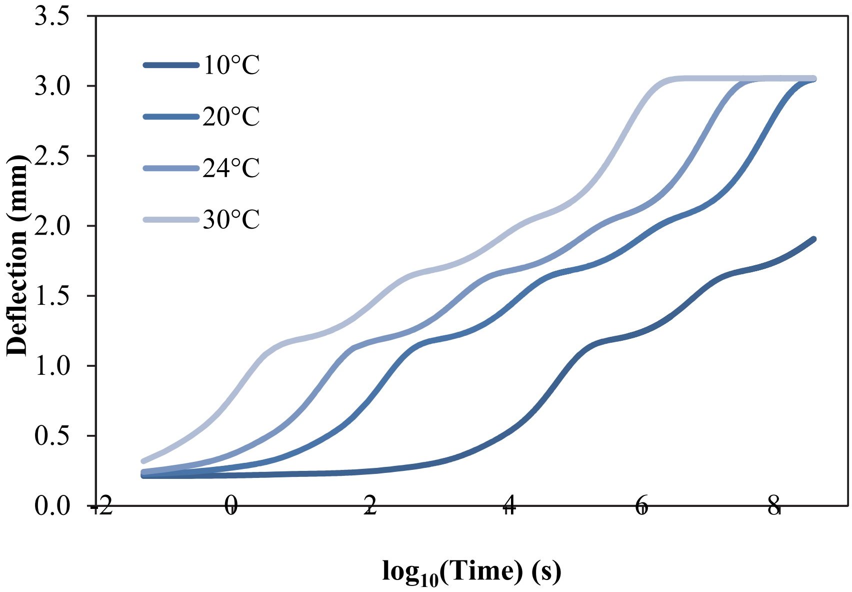

Figure 8.15: Deflection time history of the LG stair with different operation temperatures.

8.3.3 Influence of loading history on creep behaviour

Assume that during operation a uniform load p=1000N/m^2 is exerted at some point in time on the glass stair, which stays permanent afterwards, as shown in Figure 8.16. Three loading histories are considered, as shown in Figure 8.17. The deflection time histories at a 20°C operation temperature with various load histories are depicted in Figure 8.18, where it is evident that the deflections converge after a sufficiently long duration. Results with various operation temperatures for load history 1 are also shown in Figure 8.19. Clearly, temperature has a major influence on the time required for the deflections to reach the maximum steady state value.

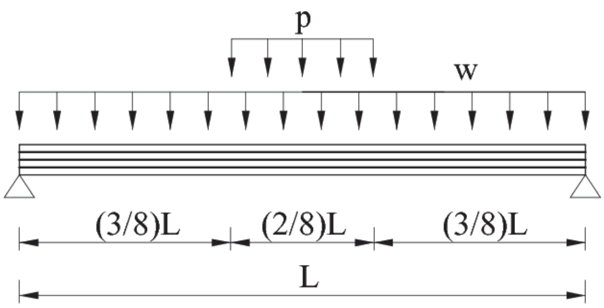

Figure 8.16: Schematic representation of applied external loading.

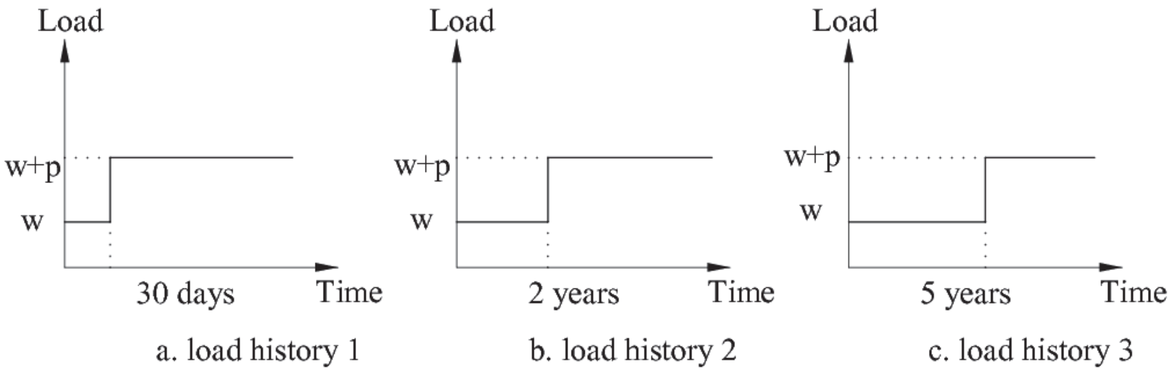

Figure 8.17: Three load histories with different times of load application.

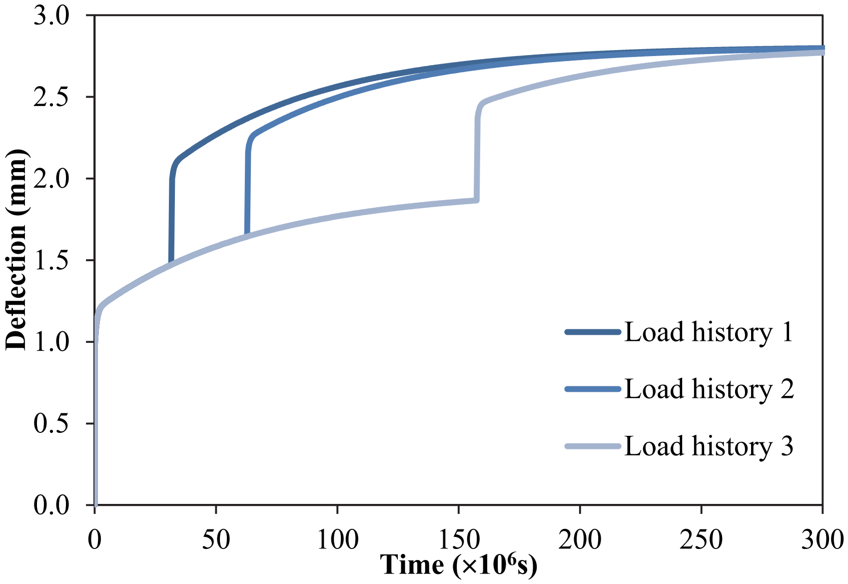

Figure 8.18: Deflection time history of the LG stair with different time of loading.

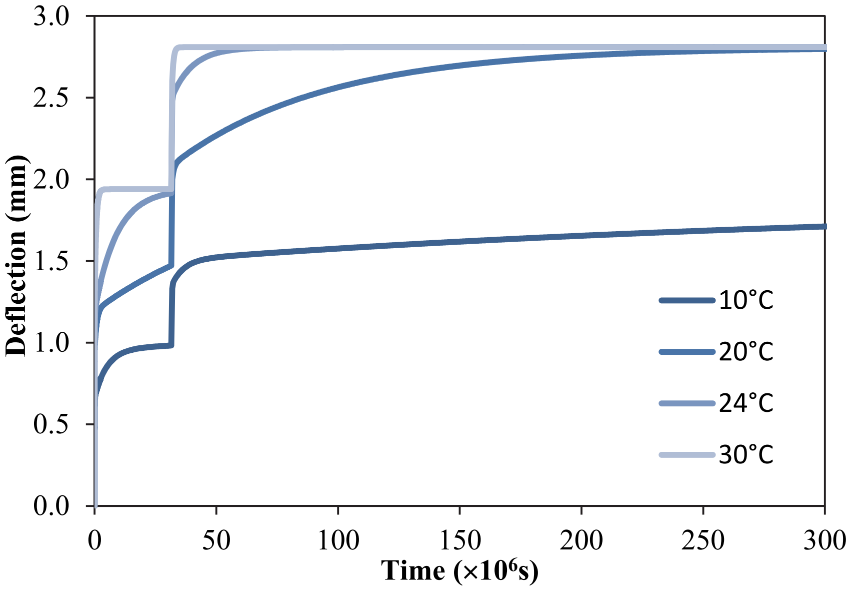

Figure 8.19: Deflection time history of the LG stair with different operation temperatures.

8.4 Insulated glazing curtain wall system subject to blast loading

Insulated laminated architectural glazing systems, which consist of two glass panels separated by a sealed air gap, have been widely used in building construction for thermal and sound insulations. Currently, there are a variety of sources for such systems to experience blast loading, whether due to petro-chemical explosions or terrorism. Since these curtain wall glazing system typically represent the first line of defence for building occupants, their response under blast loading has drawn special attention from structural engineers. The potential benefit of insulated glazing under blast events was pointed out by Nawar et al. (2013), noting that an annealed glass (AG) layer can provide added blast resistance by serving as a sacrificial layer. They have conducted an impressive experimental programme on a double glazing curtain wall system under shock pressure, which is simulated here using the models developed in this work.

8.4.1 Description of problem

The tested curtain wall system consisted of two identical insulated glazing units supported by two aluminium frames and a vertical mullion at the centre line, as depicted in Figure 8.20. Both insulated glazing units were 1.524m wide and 3.05m high, resulting in a curtain wall system that is 3.05m×3.05m. Each insulated glazing unit was composed of a 6.35 mm AG panel and a LG panel (two 4.76mm heat strengthened glass plies bonded with a 1.52mm UVEKOL-S interlayer), separated by a 12.7 mm air gap in between. The cross-sections of the aluminium frame and mullion are shown in Figure 8.21, and the material properties of the glazing system were provided by Nawar et al. (2013), as listed in Table 8.2. A shock pressure was exerted on the AG side of the curtain wall system, with the blast wave history depicted in Figure 8.22. The curtain wall was supported vertically along the mullion only, which was attached to the head and sill using aluminium angles. Besides, the flanges of frames were also attached to the head and sill on the side where the shock pressure was imposed. Figure 8.23 provides a schematic representation of the boundary conditions.

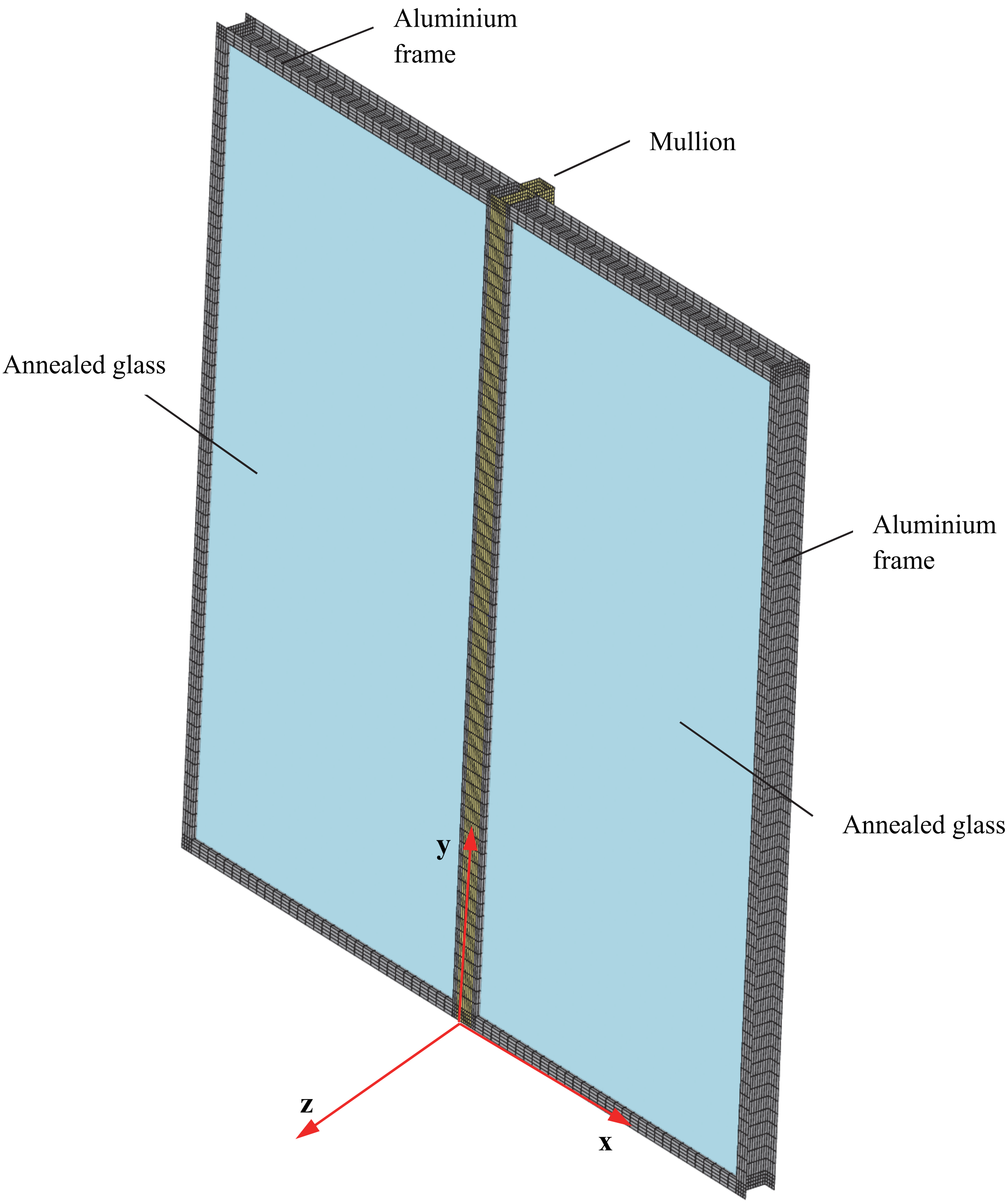

a. front view

Figure 8.20: Schematic representation of the double glazing system (Cont'd…).

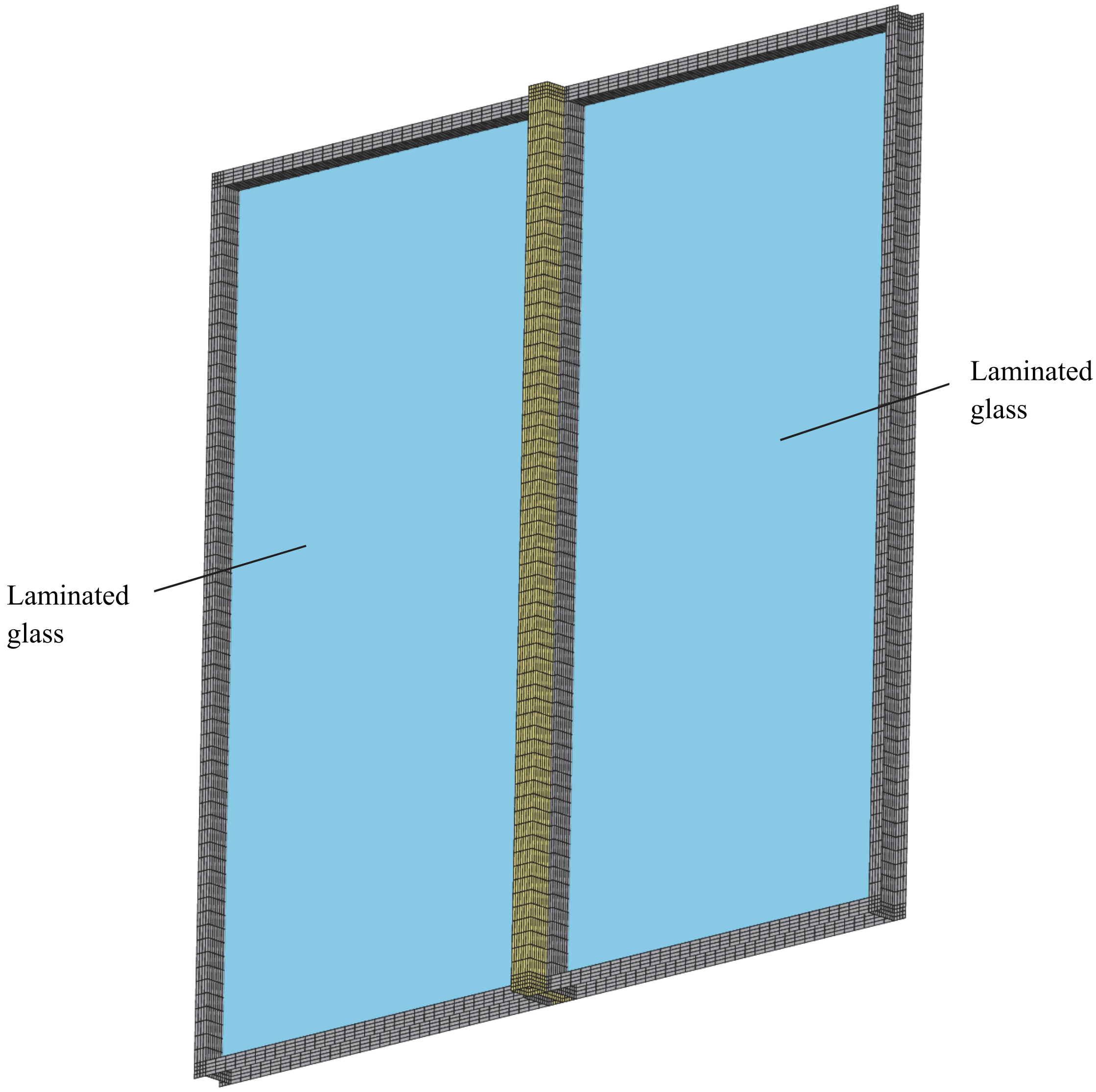

b. back view

Figure 8.20: Schematic representation of the double glazing system.

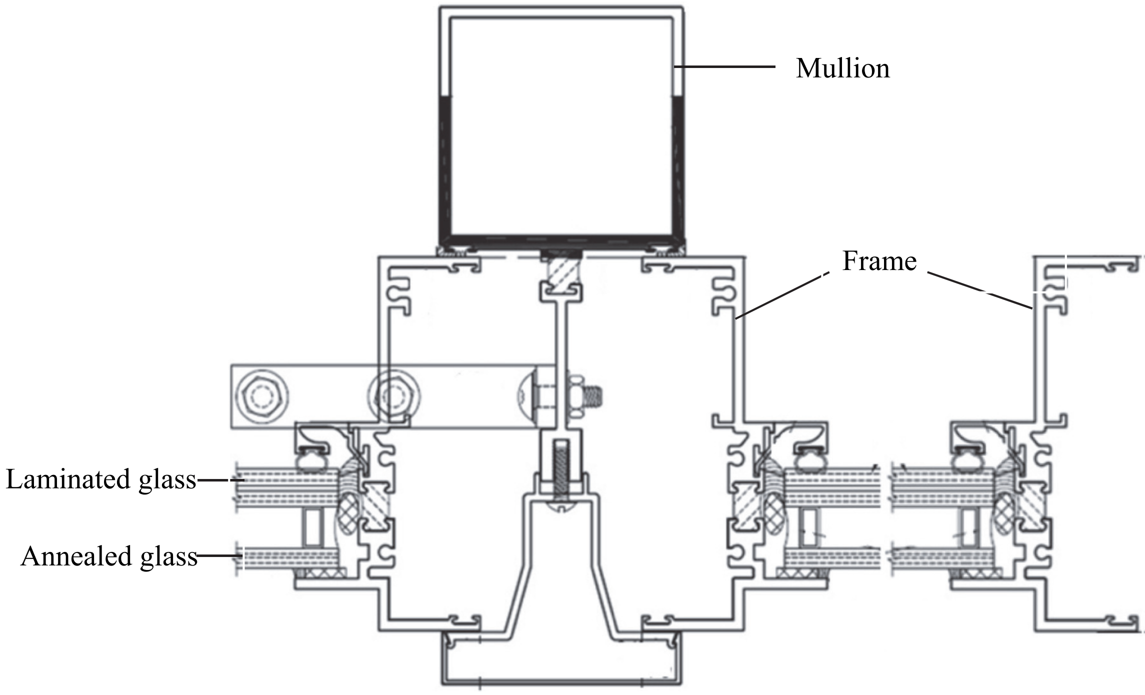

Figure 8.21: Details of the curtain wall and mullion (Nawar et al., 2013).

Table 8.2: Material parameters of the curtain wall system (Nawar et al., 2013).

Material	Material parameters
Glass	E = 69GPa, ν = 0.22, ρ = 2500 kg/m^3
Uvekol-S	E = 0.207 GPa, ν = 0.495, ρ = 1100 kg/m^3 , Elastic limit = 17.6 MPa, Failure strain = 1.94, Failure stress = 21.4 MPa
Aluminium	E = 69 GPa, ν = 0.33, ρ = 2700 kg/m^3 , Elastic limit = 214MPa, Failure strain = 0.12, Failure stress = 241 MPa

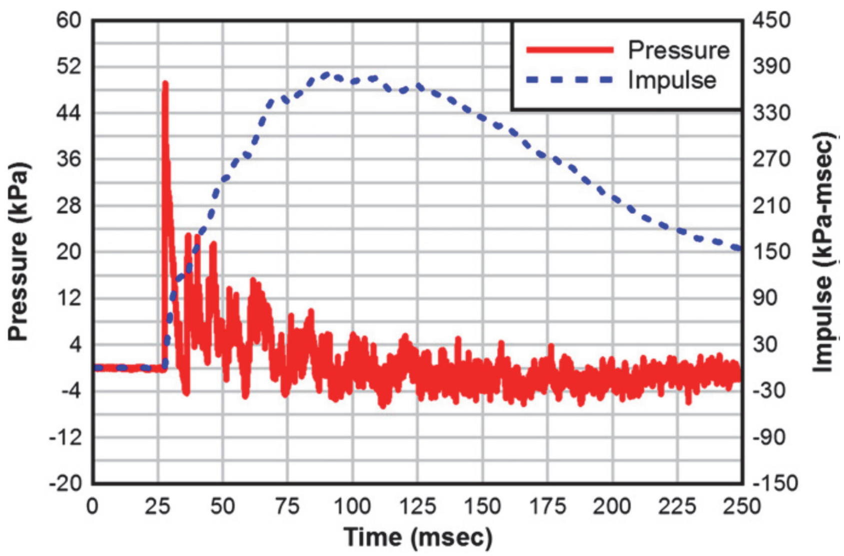

Figure 8.22: Blast wave history (Nawar et al, 2013).

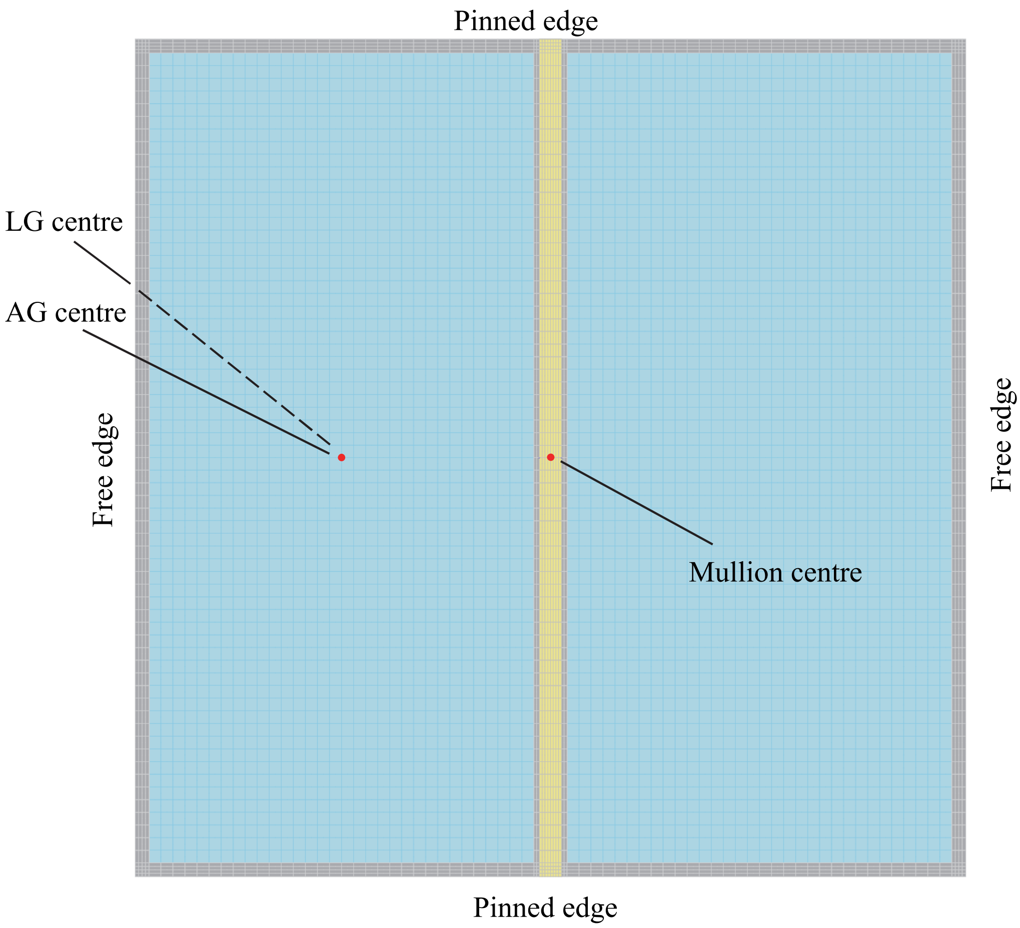

Figure 8.23: Boundary conditions of curtain wall system (Nawar et al, 2013).

This problem is analysed in this section to investigate the effect of enclosed air pressure on the structural behaviour of the double glazing, where a shell element model, along with the volume-pressure control algorithm developed in the previous chapter, is employed.

8.4.2 Low-level blast analysis

Before the simulation of the actual blast test, a low-level blast analysis of the curtain wall system is first considered so as to exclude the contact between the double glazing and reduce modelling complexity. By scaling down the blast pressure in Figure 8.22 to one tenth of the measured blast loading, a low-level blast input is obtained and used in the analysis.

The monolithic shell element H3O9 is used for the modelling of the AG panels, aluminium frames, and mullion, while the sandwich shell element L3-H3O9 is used for the modelling of LG panels. In order to ensure accuracy of the finite element simulations, convergence studies were conducted. Two models are considered: i) a full model of the whole curtain wall system, and ii) a half model comprising one double glazing unit, one frame and half of the mullion. In addition, two mesh sizes are considered: i) a coarse mesh, where each glazing panel is discretised with 64×32 of the shell elements, and ii) a finer mesh, where each glazing panel is discretised with 64×32 of the shell elements. For all of the models considered, the glazing and the aluminium frame are assumed to be pin-connected. In all of the three models, the effect of air gap is considered with the employment of the volume-pressure control algorithm. The time increment of $\Delta t = 2\times10^{-4}$ sec is selected throughout this case study, which ensures the stability of the analysis.

For the purpose of computational enhancement, a parallel computing procedure utilising dual partition super-elements (Jokhio & Izzuddin, 2015; Jokhio & Izzuddin, 2013) is employed to each of the considered models. As illustrated in Figure 8.24 for a full model with the finer mesh, the whole curtain wall system is decomposed into 10 partitions (four glass pane partitions, four half frame partitions, and two half mullion partitions). The collection of the boundary nodes between the different partitions is the parent structure (Jokhio & Izzuddin, 2015). Communication between the partitions is achieved through the parent structure (shown in red in Figure 8.24) which collects all the nodes at the partition boundary. In this way, the parent structure is represented by a dual super-element, with one super-element used in the parent process and another used as a wrapper around the partitioned boundary in the child process (Jokhio & Izzuddin, 2015). This partitioned modelling approach allows a significant increase of computational speed by increasing the number of partitions and processing the partitions on parallel processors. In order to consider the effect of volume change in the enclosed air on the results, the volume-pressure control algorithm has also been incorporated in the partitioned model for each of the double glazing units.

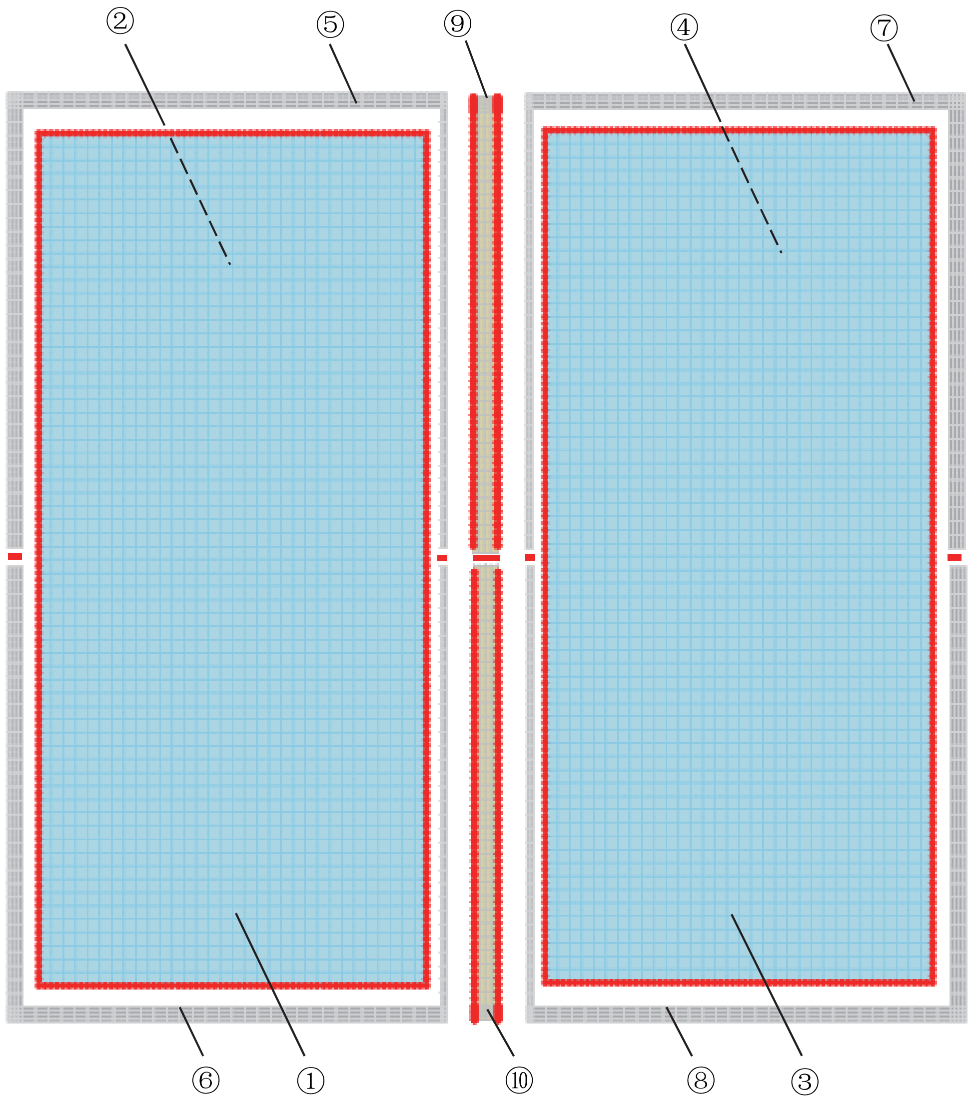

Figure 8.24: Schematic representation of the partitioned modelling approach.

The time histories of the panel central deflections and stresses for both full models and half models using either the coarse mesh or the finer mesh show that the half model with a coarse mesh provides a convergent solution for the low-level blast analysis at a much reduced computational demand. This model is therefore used in the following to investigate the influence of several key parameters on the behaviour of double glazing.

8.4.2.1 Glazing-to-frame connection

In several previous works, the silicone seal was modelled with matrix spring elements, with the normal, shear and rotational stiffness terms obtained from experimental tests. Weggel et al. (2007) performed experiments on the silicone connection and provided a range of typical spring constants, which was summarised by Seica et al. (2010) as listed in Table 8.3. Although there is no clue for applying the structural silicone in the considered curtain wall system (see Figure 8.21), discussions are made on the influence of different glazing-to-frame connections. Here, three glazing-to-frame boundaries are considered:

- Pinned connection, where there is no relative translational displacements at the glazing-to-frame connections;
- Elastic connection with maximum spring stiffness, where the effect of silicone is considered by using the matrix spring elements with the maximum stiffness values;
- Elastic connection with minimum spring stiffness, where the effect of silicone is considered by using the matrix spring elements with the minimum stiffness values.

The central deflection time histories of both glass panels with the three models are depicted in Figure 8.25. The maximum absolute values of deflection in the considered time span are also listed in Table 8.4. The displacement curves show that the spring supports provide a larger response period than a pinned connection for both glass panels. It is also shown that the deflection amplitudes of silicone-supported models are slightly larger than the pin-supported model, where the maximum deflection for the AG panel using a minimum spring stiffness shows an increase of 14.9%.

Table 8.3: Typical spring constants for silicone support (Seica et al., 2010).

Direction	Min	Max
Normal (N/m^2)	1.03E+06	5.17E+06
Shearing (N/m^2)	3.10E+06	1.55E+07
Rotational (N/rad/m)	1.38E+05	6.90E+05

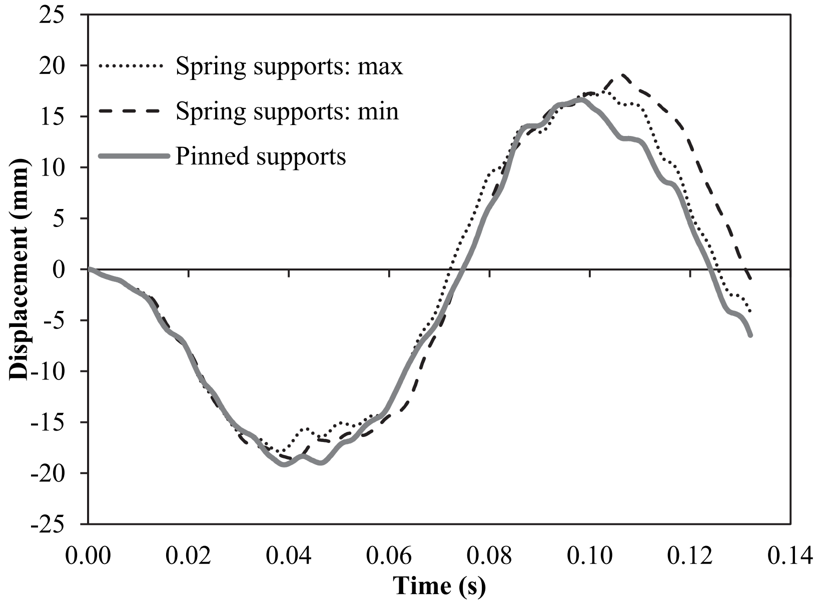

a. deflection (AG)

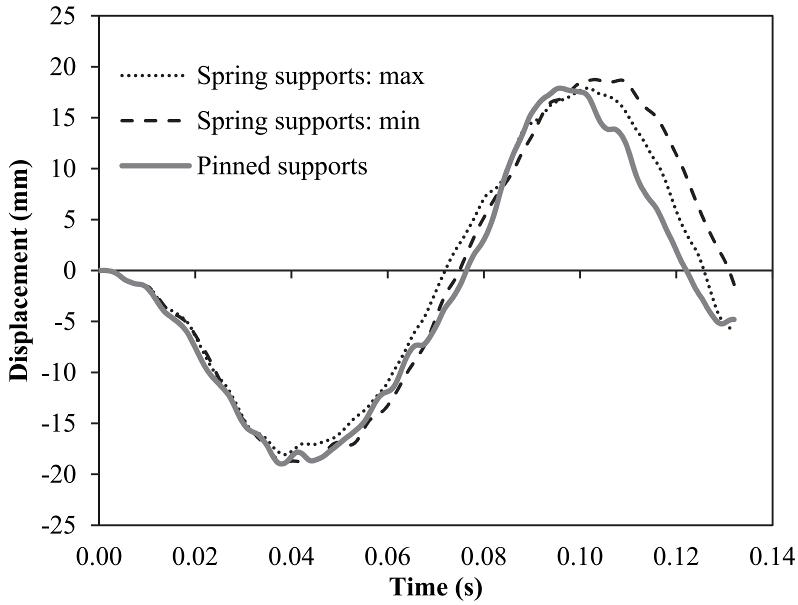

b. deflection (LG)

Figure 8.25: Displacement time histories at the AG and LG centres with different supports.

Table 8.4: Maximum deflection predictions by using different glazing-to-frame supports.

Glass panel	Maximum deflection (mm)					Minimum deflection (mm)				
	Pinned	Spring_max		Spring_min		Pinned	Spring_max		Spring_min	
AG	16.63	17.43	(+4.8%)	19.11	(+14.9%)	-19.18	-17.85	(-6.9%)	-18.60	(-3.0%)
LG	17.89	17.91	(+0.1%)	18.75	(+4.8%)	-18.99	-18.08	(-4.8%)	-18.80	(-1.0%)

The time histories of the stress component σ_x at the external and internal extreme fibres for the AG panel are depicted in Figure 8.26, with the maximum tensile and compressive stress components listed in Table 8.5. It is observed that the time history curves of silicone-supported models correspond to larger response periods and that the magnitude of the peaks is much reduced.

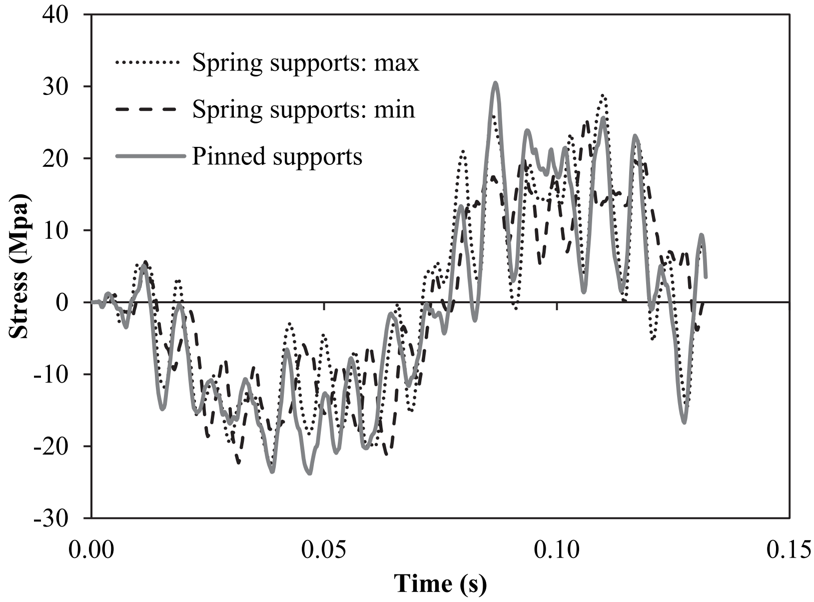

a. external fibre.

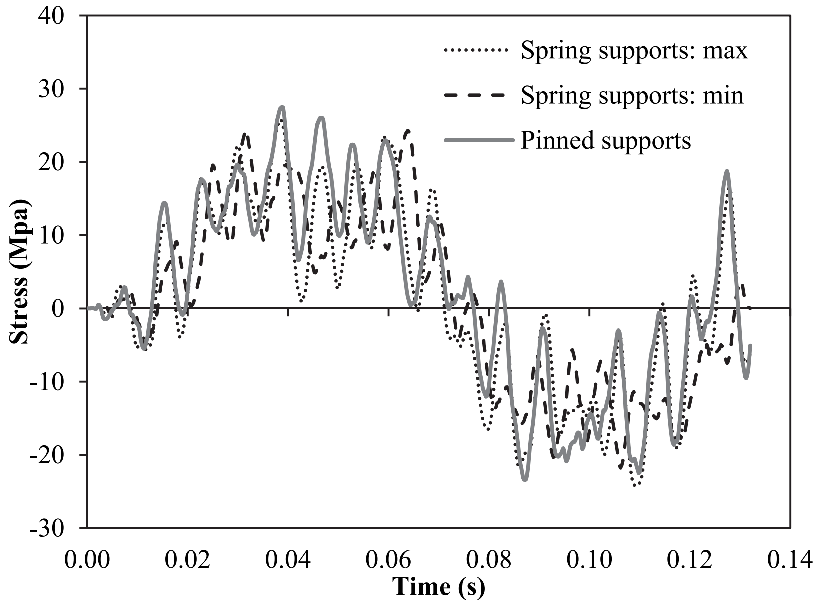

b. internal fibre.

Figure 8.26: Time histories of the stress component σ_x at the AG centre with different supports.

Table 8.5: Maximum tensile and compressive stresses using different glazing-to-frame supports.

Position	Maximum tensile stress (MPa)					Maximum compressive stress (MPa)				
	Pinned	Spring_max		Spring_min		Pinned	Spring_max		Spring_min	
External	30.52	28.89	(-5.3%)	25.70	(-15.8%)	23.80	22.32	(-6.2%)	22.30	(-6.3%)
Internal	27.51	25.77	(-6.3%)	24.47	(-11.1%)	23.41	24.16	(+3.2%)	21.78	(-7.0%)

8.4.2.2 Air gap

The effect of the air gap to the response of double glazing is studied. Four different gap widths are considered in this case study (3 mm, 6 mm, 12.7 mm, and 20 mm) with pinned connections used for all scenarios.

Time histories of central deflections for the AG and LG panels are depicted in Figure 8.27. From the displacement curves it is observed that the displacement curves of the AG and LG panels for a 3mm air gap are much closer than those for a larger air gap of 20mm, and the air gap time histories in Figure 8.27 also show a higher level of fluctuation for large air gaps, which indicates that a small air gap is more sensitive to the pane deflection such that a very small displacement of one pane will have immediate influence on the other one. In addition, the deflections of the model increase with the gap width.

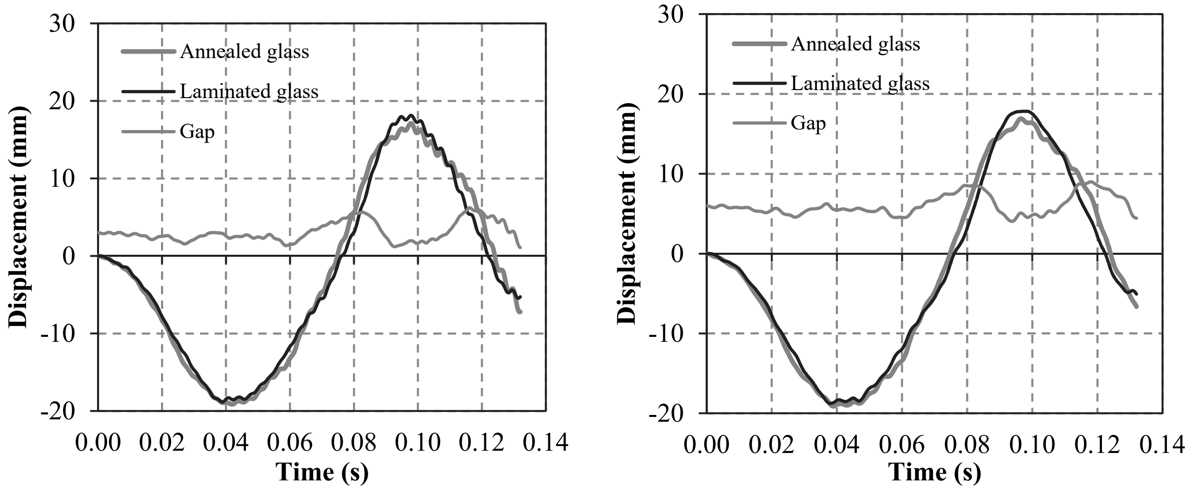

a. 3mm b. 6mm

Figure 8.27: Displacement time histories at the AG and LG centres with different gap widths (Cont'd …).

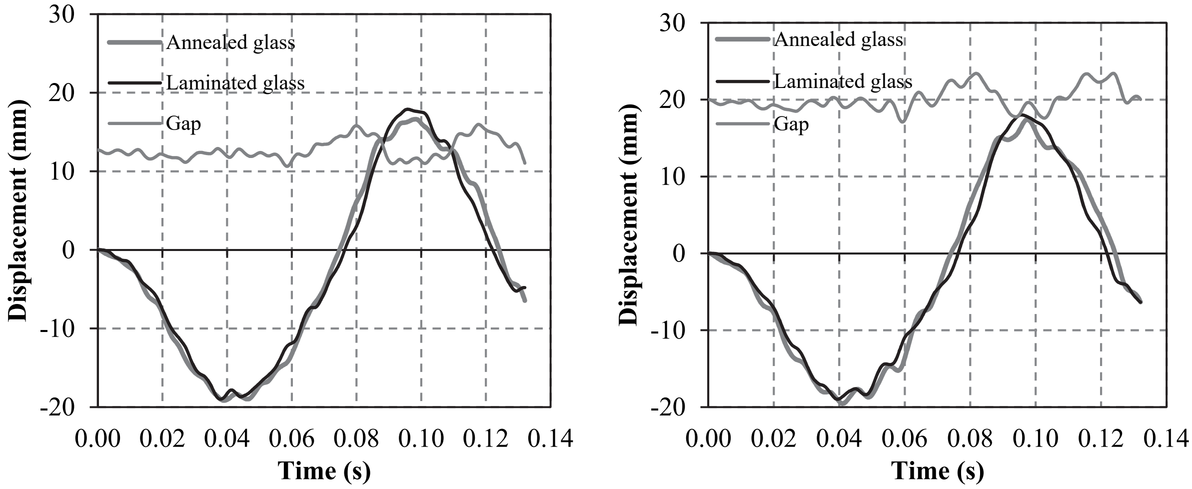

c. 12.7mm d. 20mm

Figure 8.27: Displacement time histories at the AG and LG centres with different gap widths.

The stress time histories of models with different air gap widths are depicted in Figure 8.28. Clearly, the stresses for the 3mm gap have a higher level of fluctuation owing to the sensitivity of the enclosed air to the panel deflection. By contrast, the models with larger air gaps result in a reduced frequency of vibration in the stress components but higher stress magnitudes, as shown in Figure 8.28 and Table 8.6. The stress results indicate that the insulated air provides a protection of the glazing by generating an air pressure on both of the glazing panels.

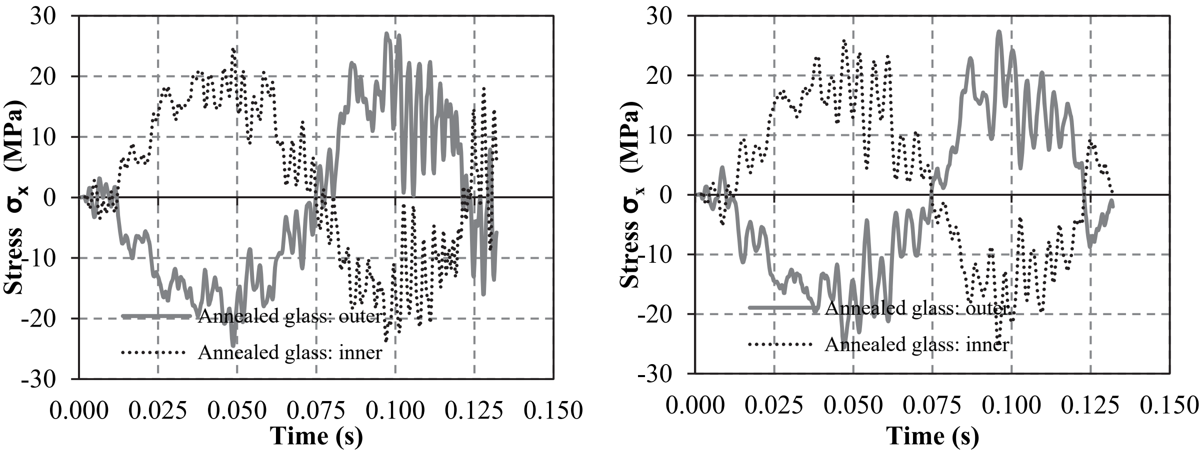

a. 3mm b. 6mm

Figure 8.28: Time histories of the stress component σ_x at the AG centre with different gap widths (Cont'd …).

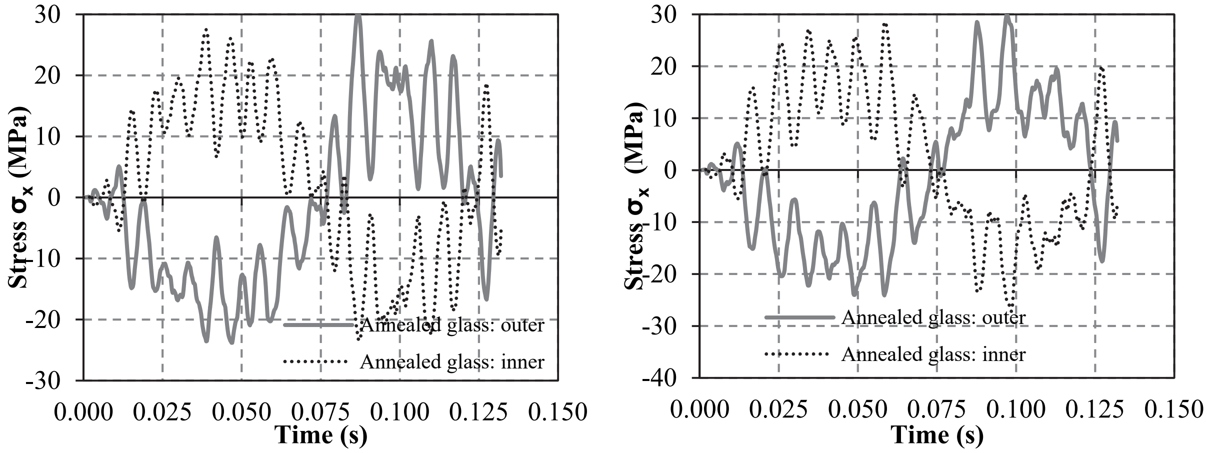

c. 12.7mm d. 20mm

Figure 8.28: Time histories of the stress component σ_x at the AG centre with different gap widths.

Table 8.6: Maximum tensile stress values for different air gap widths.

Position	Maximum tensile stress σ_x (Mpa)			
	3 mm gap	6 mm gap	12.7 mm gap	20 mm gap
External	27.10	27.38	30.52	29.99
Internal	24.82	26.06	27.51	28.52

8.4.3 Real-level blast loading

The analysis of the curtain wall system under the real blast loading is performed here, where a full model with a fine mesh (64×32 mesh for glazing) is employed. The blast loading is large enough to cause the contact between the AG and LG panels. In the consideration of possible contact between the panels under the blast load, a node-to-surface contact element is employed (Zolghadr Jahromi, 2014). The element is a 10-noded contact element, where 9 master nodes are attached to the surface of the LG pane, and a slave node is attached to the surface of the annealed glass pane. A velocity constraint is activated when the distance between the master node and the slave surface is equal to or less than the sum of half thicknesses of both panes. In order to compare the results of the present model to those in the literature, the time history curves of the present study are translated along the time axis for 0.03 sec, owing to the fact that the insulated glazing unit is loaded around 30 ms after the explosion. The deflected shape of the curtain wall system is depicted in Figure 8.29. The time histories of the central deflections of the AG and LG panels as well as the gap variation with time are shown in Figure 8.30.

Nawar et al. (2013) also performed a numerical simulation on the double glazing, where the LG pane and aluminium frames and mullion were modelled with shell elements, whereas the annealed glass pane and aluminium angles were modelled with solid elements. The effect of sealed air was ignored in the model, and surface-to-surface contact elements were employed to consider the contact between the two glass panels during the blast loading input.

In Figure 8.31, the transverse displacements of the LG and the mullion centre, as shown in Figure 8.23, are compared against the test data and the numerical prediction by Nawar et al. (2013) without considering the influence of enclosed air. Compared with the numerical model by Nawar et al., the resulting displacement curves of the present model provide a better prediction, evident from the good agreement between the results of the present model and those of the test data. The maximum deflections for both the present model and that used by Nawar et al. (2013) are all presented in Table 8.7. Comparing Figure 8.31 with Figure 8.27.c also shows an elongated response period for a high-level blast loading, which is attributed to the plastic deformation of the aluminium frame and mullion, and the coupling between the two glass panels in the insulated glazing.

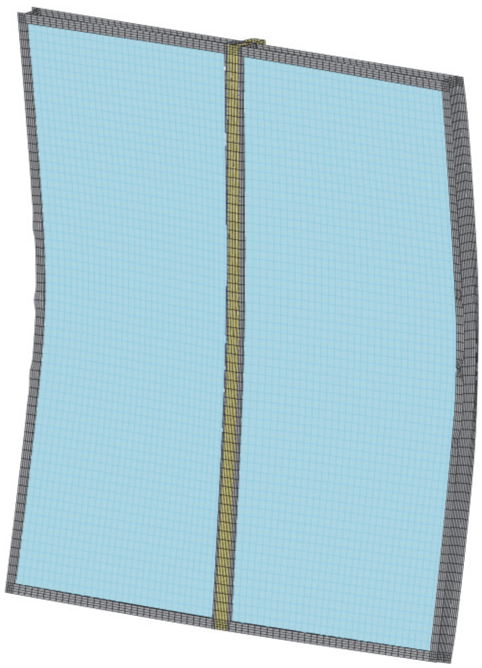

Figure 8.29: Deflected shape of curtain wall under blast loading.

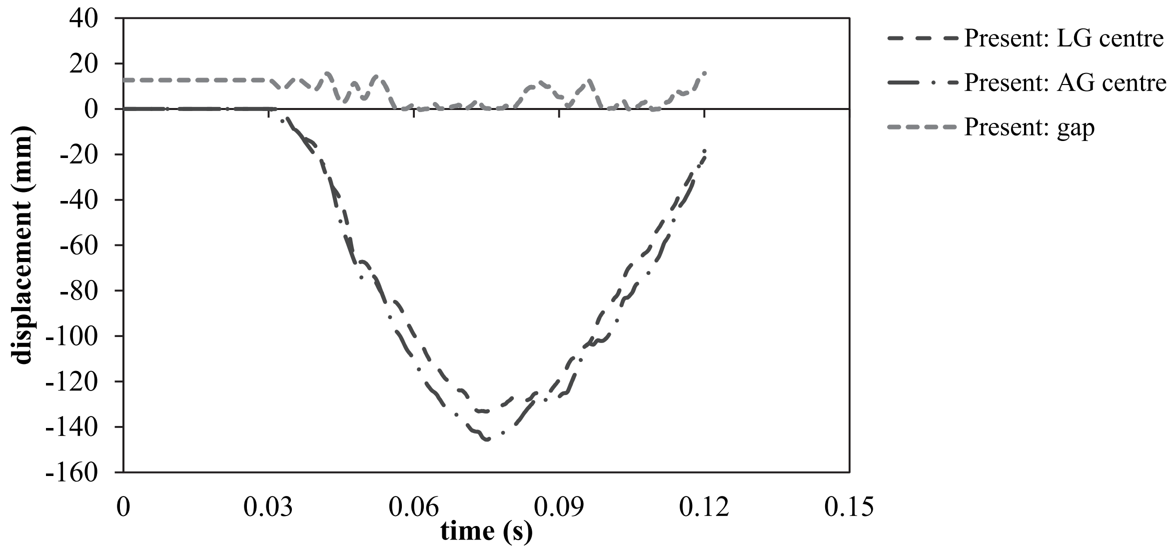

Figure 8.30: Displacement time histories at the AG and LG panel centres using the present shell model.

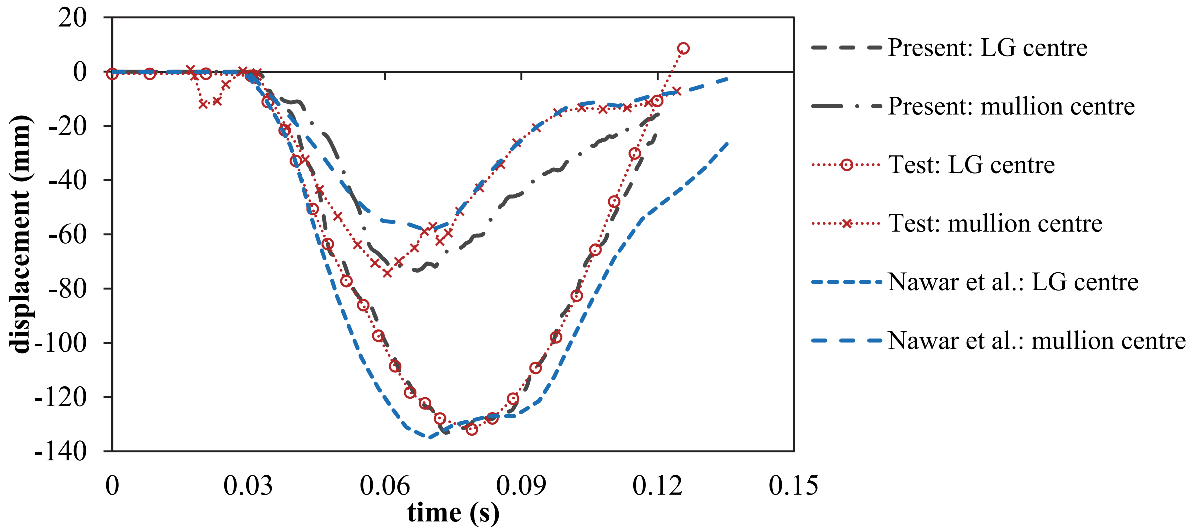

Figure 8.31: Comparison of displacement time histories with results by others.

Table 8.7: Comparisons of maximum deflection predictions.

Results	Maximum dynamic deflection (mm)			
	LG		Mullion	
	Value	Relative error	Value	Relative error
Test (Nawar et al.)	132	-	77	-
Present	133	0.8%	73	5.2%
Numerical (Nawar et al.)	134	1.5%	58	24%

The time histories of stress components σ_x and σ_y at the external and internal extreme fibres of the AG are plotted in Figure 8.32. It is observed that the stress variations show a similar fluctuation frequency to Figure 8.28.c until about 0.05 sec, when the stress curves exhibit high frequency oscillations owing to the contact between two glass panels, as observed in Figure 8.30 for the gap width. According to Nawar et al. (2013), the failure tensile stress of the AG is 84.8 MPa, and in their FE model the tensile stress of the AG exceeded its tensile strength. Figure 8.32 also indicates the exceeding of the maximum tensile strength for the AG at several time points, with the maximum tensile stresses at the external and internal glazing fibres listed in Table 8.8. However, Nawar et al. (2013) observed that the AG panel remained undamaged after the application of shock loading in the experiment. This phenomenon may be explained by the scattered strength of brittle glass due to randomly introduced Griffith flaws of differing severity. It is also important to note that neither the deflection nor the stresses in the real-level blast problem are about 10 times those in the low-level blast analysis, owing to the significant membrane action in constraining the deflection and the high ductility of the aluminium frame and mullion in absorbing blast energy upon yielding.

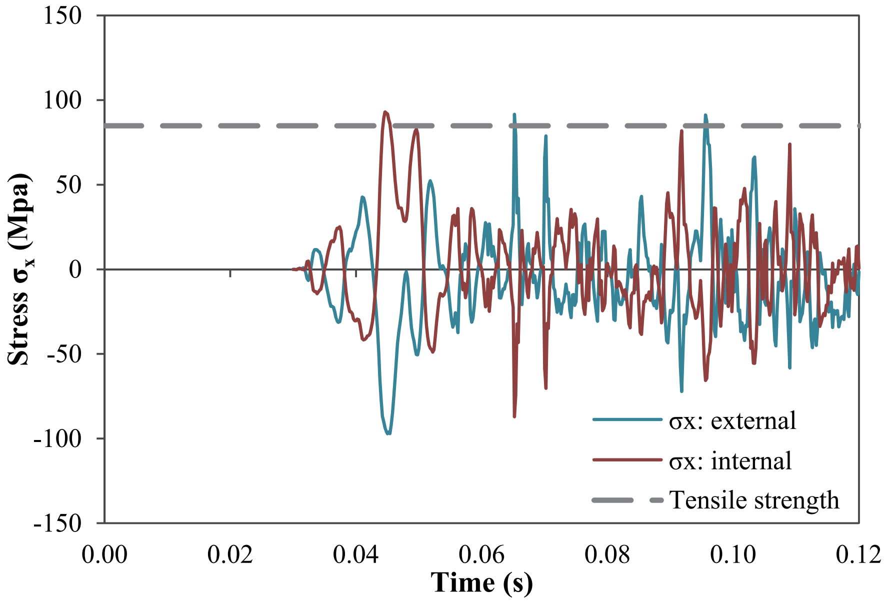

a. stress component σ_x.

Figure 8.32: Stress time histories at the external and internal extreme fibres of the AG panel centre (Cont'd…).

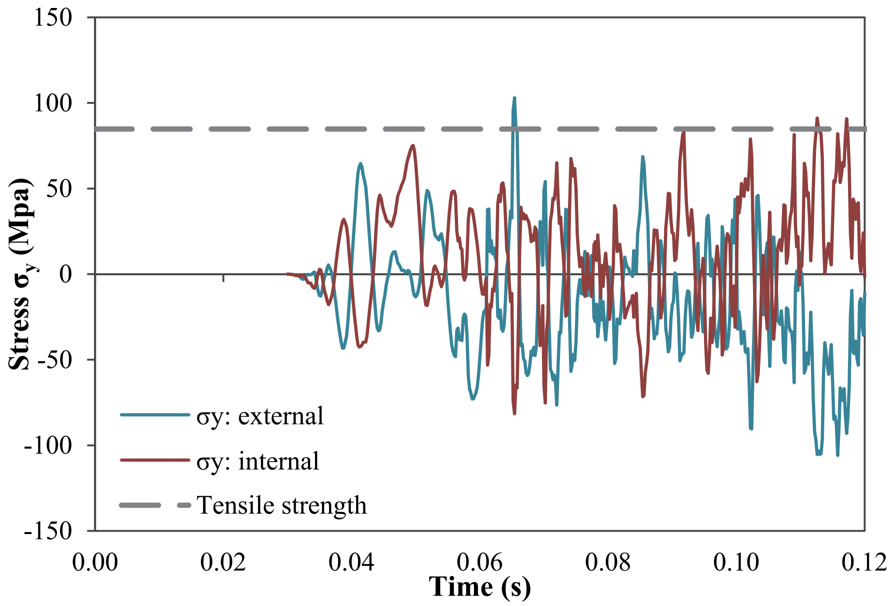

b. stress component σ_y.

Figure 8.32: Stress time histories at the external and internal extreme fibres of the AG panel centre.

Table 8.8: Maximum stress values at the AG panel centre.

Stress component	Maximum stress value (MPa)	
	External	Internal
σ_x	91.6	93.0
σ_y	103.0	91.2

8.5 Summary

This chapter provides several applications of the proposed modelling approach in this thesis for both static and dynamic analysis of LG structures. The wide range of application examples studied here is aimed at demonstrating the significant potential of this work in providing simple laminated shell elements which are computationally efficient and accurate, and which allow nonlinear analysis involving geometric and material nonlinearities. In the last case study, the proposed volume-pressure control algorithm is also employed in the simulation of the enclosed gas pressure in double glazing.

CHAPTER 9

Conclusions

9.1 Summary

The work presented in this thesis is motivated by the need for an efficient numerical modelling approach for the analysis of laminated glass structures. Even though the LG has been widely used in building construction owing to its aesthetic appearance and safety benefits, its behaviour under loading is complicated, which is characterised by: (1) a significant material mismatch between the glass and the PVB, (2) an alternating stiff/soft stacking sequence, (3) geometric nonlinearity owing to the large slenderness, (4) the sensitivity to load duration and temperature, (5) the complicated fracture mechanism of glass, and (6) the nonlinear material properties of PVB at large strains.

Focusing on the pre-cracking stage of LG, this research has proposed multi-layer shell elements specific to laminations with an alternating stiff/soft lay-up, which are applied to the simulation of LG structures. In the following sections, some of the major achievements in this research work are highlighted.

9.1.1 Lock-free monolithic shell elements

Reissner-Mindlin shell finite elements usually suffer from locking, where the element is unable to generate lower-order strain fields owing to the existence of some higher-order polluting strain terms. The hierarchic optimisation approach proposed by Izzuddin (2007), as an assumed strain method, overcomes locking by enhancing conforming strains with hierarchic *corrective* strains, and mathematical optimisation is performed towards *objective* low-order strain fields, as afforded by the element DOFs. This approach not only alleviates shear and membrane locking, but also addresses locking arising from element distortion. The order of the corrective strain field is not capped to a prescribed distribution but can attain any hierarchic order, which results in families of hierarchically optimised elements.

In this research, some modifications have been made to the hierarchic optimisation procedure for the 9-noded shell element (Izzuddin, 2007). Firstly, an additional objective transverse shear strain mode is introduced to the assumed strain modes, which is required to achieve the correct rank of the local stiffness. Secondly, a modification of the hierarchic strain modes is proposed to enable the 9-noded element to pass constant strain patch tests. In addition, the hierarchic optimisation approach is extended to a 6-noded triangular shell element, with the further consideration of the requirements of spatial isotropy. The local formulation of the 6-noded triangular shell element is framed within the zero-macrospin co-rotational system, which upgrades it to geometric nonlinear analysis with relative ease.

The performance of the quadrilateral and the triangular monolithic shell elements has been investigated with extensive numerical tests, with the outcomes summarised as follows:

- All the optimised quadrilateral and triangular elements with different hierarchic orders pass all fundamental element tests, including the zero energy mode tests, the constant strain patch tests and the isotropic element tests.
- The optimised elements exhibit a significant relief of shear locking and membrane locking with good convergence rates. Nevertheless, the optimised elements that do not employ corrective hierarchic strain modes in the optimisation (H2O9 and H2O6) result in degraded performance for curved shell problems compared to elements with hierarchic correction, which highlights the importance of the inclusion of higher-order strain modes in the optimisation.
- For the same hierarchic correction order, the objective alternative yields superior results than the corrective alternative in terms of both accuracy and convergence rate,

with the objective alternative based on third order hierarchic optimisation (H3O9 and H3O6 elements) exhibiting both accuracy and efficiency.

- The H3O9 and H3O6 elements also have comparable or even better accuracy than the mixed elements based on the MITC formulations, mainly due to effective relief of distortion locking.

9.1.2 Lamination model with an alternating stiff/soft lay-up

A three-layered sandwich shell model is first proposed in this research work, which is characterised by the following features:

- A zigzag function that assumes identical rotations in face sheets is added to the Reissner-Mindlin plate theory to consider the zigzag effect in displacements, which effectively captures the sectional warping for both symmetric and asymmetric lay-ups with only one zigzag mode.

- A piecewise linear-constant-linear through-thickness distribution of the transverse shear strain is assumed, which is specifically suitable for sandwich layer-ups.

- Each layer of the sandwich shell is regarded as a pseudo monolithic shell and employs available kinematics and constitutive relationships. The governing equations of the laminated shell are derived with the employment of the virtual work principle.

The effectiveness and efficiency of the proposed zigzag function for the sandwich shell is illustrated with a 1D cantilever example. The adequacy of the assumed discrete transverse shear strain distribution has also been demonstrated in comparison with the results of models with continuous transverse shear stress distributions. In addition, the proposed zigzag function outweighs the MZZF in asymmetrically laminated cases, which inspired the use of similar assumptions on layer rotations in the development of generalised multi-layered shell model.

The three-layered shell model is then extended to a generalised multi-layered shell model with an alternate (stiff/soft/…) layer-up scheme, which has the following features:

- A set of zigzag displacement modes are employed in the planar displacements, the number of which is dependent on the number of soft layers. These zigzag displacement modes are defined such that all stiff layers are assumed to rotate at the same angle while the soft layers may have different rotations.

- The through-thickness transverse shear strain is assumed such that all internal layers have constant values through the layer thickness while the external ones utilise a linear distribution with zero values at the top and bottom of the plate.

Similar to the three-layered case, a 1D cantilever example has been used to stress the accuracy of the zigzag displacement set and the assumed transverse shear strain distribution. The results show that the proposed multi-layered shell model is both accurate and efficient.

9.1.3 Laminated shell elements

The proposed lamination model can be readily incorporated into the co-rotational monolithic shell elements. In order to eliminate the need for co-rotational transformations for the additional zigzag displacement parameters, a 2D curvilinear shell system is proposed for the direct definition of these parameters, such that a simple and fixed transformation of these additional parameters to their counterparts in the local element system holds throughout the analysis.

The benefits of the 2D curvilinear shell system can be summarised as follows:

- With the associated additional zigzag parameters defined in this shell coordinate system, continuity of the zigzag fields is ensured.

- The element response associated with the zigzag parameters can be evaluated via a fixed linear kinematic transformation between the shell and local element systems rather than a varying nonlinear co-rotational transformation, which enhances the computational efficiency of the geometric nonlinear analysis of sandwich shells.

- The shell coordinate system is also useful to provide the orientation of material fibres in relation to the local element coordinate system when composite materials are considered.

The proposed multi-layer shell modelling approach has been incorporated into the 9-noded and 6-noded co-rotational shell elements, and the element performance in the simulation of sandwich and laminated plates and shells with an alternating stiff/soft lay-up has been verified with both linear and geometrically nonlinear numerical problems.

9.1.4 Application to laminated glass

The proposed laminated shell elements have been utilised in the simulation of laminated glass. A viscoelastic material model has been implemented to consider the influence of loading rate and temperature on the material properties of PVB. Two LG problems are analysed with the use of the linear viscoelastic material model, the results of which show that:

- Under short-duration loading, the response of the LG can be regarded the same as the response of a monolithic glass pane with the same nominal glass thickness owing to the large shear stiffness generated by PVB.
- Under long-duration loadings, the shear stiffness of PVB becomes quite small, which leads to the response of LG becoming similar to the response of two glass plies layered with no connection.

In order to allow the analysis of insulated glazing, a volume-pressure control algorithm is proposed, which considers the effect of insulated air by assuming a hydrostatic pressure state in the insulated air gap and relating the generated pressure to the relative volume change in the air gap. The algorithm computes the air pressure with the use of the volume and its rate evaluated at the end of the previous step, which eliminates the need to introduce a pressure parameter and hence excludes the coupling between the displacement parameters with the pressure parameter. The accuracy of this volume-pressure control algorithm has been verified with two numerical examples of double glazing. It is shown that for a reasonably small time step, models utilising the proposed volume-pressure control algorithm agree well with solutions by others.

9.1.5 Case studies

Several applications of the proposed laminated shell elements in the modelling of laminated glass structures are demonstrated through example case studies, which consist of a buckling problem, a creep problem, and a blast problem of an insulated curtain wall glazing system. The wide range of numerical examples is used to show the great potential of the proposed shell elements in the estimation of LG behaviour accurately and efficiently.

9.2 Recommendations for future work

In this PhD thesis, novel laminated shell elements have been proposed and applied to the analysis of geometrically nonlinear LG problems. As illustrated in Chapters 7 and 8, the proposed modelling approach for LG provides the capability for many applications which are of importance in LG design and assessment:

- Owing to the good approximation of both displacements and stresses, the laminated shell elements can be used in the practical design of load-resistant LG members, such as columns, beams, roofs and staircases, with almost the same level of simplicity as a monolithic shell model. The proposed volume-pressure algorithm may also be used in the analysis of insulated glazing units.

- Apart from LG structures, the proposed laminated shell elements are also applicable to other structures with an alternating stiff/soft lay-up, such as interior insulation walls and polymer-metal composites.

Notwithstanding, there is room for further improvements towards the modelling of fracture of LG structures under extreme loading conditions such as blast and earthquakes. Potential future research topics in this respect include:

- The modelling of fracture of glass plies. Glass is a brittle material with a limited tensile strength due to random Griffith flaws. The incorporation of an adequate fracture mechanism will allow the initiation and propagation of cracks in glass plies when its tensile strength is exceeded.

- The nonlinear viscoelastic characteristic of PVB. Under extreme loading conditions, the PVB interlayer may be associated with large strains upon the fracture of glass plies, which holds the glass debris in place and withstands further loads.

- The post-cracking cross-sectional behaviour of laminated glass. After the cracking of glass, the glass debris cannot withstand tension but contributes to compression. Therefore, the effective through-thickness displacement modes change during the analysis.

On the algorithmic front, there are also several potential future extensions and improvements of the laminated shell elements developed in this thesis, as follows:

- For the current hierarchic optimisation approach, the objective function is not invariant to the orientation of the element local system. The presented optimised 9-noded and 6-noded elements acquire the characteristic of invariance to nodal ordering either by using a co-rotational system independent of nodal ordering (quadrilateral elements) or by prescribing directions for optimisation (triangular elements). Therefore, an alternative invariant objective function may be developed to enable the optimisation approach with the characteristic of 'spatial isotropy'.

- For the current laminated shell elements, the transverse deformation is not considered, which limits their use within thin-to-moderately thick applications. Further incorporation of zigzag displacements to the transverse displacement may also be considered in the future to extend the applicability to thick plates and shells.

References

Alves de Sousa, Ricardo J, Cardoso, R. P., Fontes Valente, R. A., Yoon, J., Grácio, J. J. & Natal Jorge, R. M. (2006) A new one-point quadrature enhanced assumed strain (EAS) solid-shell element with multiple integration points along thickness—part II: nonlinear applications. *International Journal for Numerical Methods in Engineering.* 67 (2), 160-188.

ANSYS. (2012) Guide, Ansys Mechanical Application User's . Release 14.5. Ansys Inc., Canonsburg, USA.

Arciniega, R. & Reddy, J. (2007) Tensor-based finite element formulation for geometrically nonlinear analysis of shell structures. *Computer Methods in Applied Mechanics and Engineering.* 196 (4), 1048-1073.

ASTM. (2012) Standard practice for determining load resistance of glass in buildings. E1300-12a, West Conshohocken, PA.

Balah, M. & Al-Ghamedy, H. (2002) Finite element formulation of a third order laminated finite rotation shell element. *Computers & Structures.* 80 (26), 1975-1990.

Bathe, K. & Dvorkin, E. (1986) A formulation of general shell elements—the use of mixed interpolation of tensorial components. *International Journal for Numerical Methods in Engineering.* 22 (3), 697-722.

Bathe, K., Lee, P. & Hiller, J. (2003) Towards improving the MITC9 shell element. *Computers & Structures.* 81 (8), 477-489.

Bathe, K., Iosilevich, A. & Chapelle, D. (2000) An evaluation of the MITC shell elements. *Computers & Structures.* 75 (1), 1-30.

Battini, J. & Pacoste, C. (2004) On the choice of local element frame for corotational triangular shell elements. *Communications in Numerical Methods in Engineering.* 20 (10), 819-825.

Behr, R., Minor, J. & Norville, H. (1993) Structural behavior of architectural laminated glass. *Journal of Structural Engineering.* 119 (1), 202-222.

Bennison, S., Jagota, A. & Smith, C. (1999) Fracture of glass/poly (vinyl butyral)(Butacite®) laminates in biaxial flexure. *Journal of the American Ceramic Society.* 82 (7), 1761-1770.

Biolzi, L., Cattaneo, S. & Rosati, G. (2010) Progressive damage and fracture of laminated glass beams. *Construction and Building Materials.* 24 (4), 577-584.

Brischetto, S., Carrera, E. & Demasi, L. (2009) Improved response of unsymmetrically laminated sandwich plates by using zig-zag functions. *Journal of Sandwich Structures and Materials.* 11 (2-3), 257-267.

Bucalem, M. & Bathe, K. (1993) Higher-order MITC general shell elements. *International Journal for Numerical Methods in Engineering.* 36 (21), 3729-3754.

Bucalem, M. L. & da Nóbrega, Selma H Shimura. (2000) A mixed formulation for general triangular isoparametric shell elements based on the degenerated solid approach. *Computers & Structures.* 78 (1), 35-44.

Campello, E., Pimenta, P. & Wriggers, P. (2003) A triangular finite shell element based on a fully nonlinear shell formulation. *Computational Mechanics.* 31 (6), 505-518.

Carrera, E. (2002) Theories and finite elements for multilayered, anisotropic, composite plates and shells. *Archives of Computational Methods in Engineering*. 9(2), 87-140.

Carrera, E. (1997) Cz0 requirements—models for the two dimensional analysis of multilayered structures. *Composite Structures.* 37 (3), 373-383.

Carrera, E. (2003) Theories and finite elements for multilayered plates and shells: a unified compact formulation with numerical assessment and benchmarking. *Archives of Computational Methods in Engineering.* 10 (3), 215-296.

Carrera, E. & Demasi, L. (2002) Classical and advanced multilayered plate elements based upon PVD and RMVT. Part 1: Derivation of finite element matrices. *International Journal for Numerical Methods in Engineering.* 55 (2), 191-231.

Carrera E. (2001) Developments, ideas, and evaluations based upon Reissner's Mixed Variational Theorem in the modeling of multilayered plates and shells. *Applied Mechanics Reviews*. 54(4), 301-329.

Carrera E. (1998) A refined multilayered finite-element model applied to linear and non-linear analysis of sandwich plates. *Composites Science and Technology*. 58(10), 1553-1569.

Carrera E & Krause H. (1998) An investigation of non-linear dynamics of multilayered plates accounting for C 0 z requirements. *Computers & Structures*. 69(4), 473-486.

Carrera E & Parisch H. (1997) An evaluation of geometrical nonlinear effects of thin and moderately thick multilayered composite shells. *Composite Structures*. 40(1), 11-24.

Carrera E. (1997) An improved Reissner-Mindlin-type model for the electromechanical analysis of multilayered plates including piezo-layers. Journal of Intelligent Material Systems and Structures. 8(3), 232-248.

Celigoj, C. (1996) A strain- and displacement-based variational method applied to geometrically nonlinear shells. *International Journal for Numerical Methods in Engineering.* 39 (13), 2231-2248.

Cook, R. D. (1989) *Concepts and applications of finite element analysis.* New York ; Chichester, Wiley.

Crisfield, M. & Moita, G. (1996) A unified co-rotational framework for solids, shells and beams. *International Journal of Solids and Structures.* 33 (20), 2969-2992.

Demasi, L. (2008) 2D, quasi 3D and 3D exact solutions for bending of thick and thin sandwich plates. *Journal of Sandwich Structures and Materials.* 10 (4), 271-310.

Deng, R. & Jin, X. (2010) Numerical Simulation for Blast Analysis of Insulating Glass in a Curtain Wall. *International Journal for Computational Methods in Engineering Science and Mechanics.* 11 (3), 162-171.

Ding, C., Ngo, T., Lumantarna, R., Mendis, P. & Zobec, M. (2014) Investigations of Cavity Pressure Behaviors of Double-Skin Façade Systems Subjected to Blast Loads. *Journal of Performance of Constructed Facilities.*

Doherty, W., Wilson, E. & Taylor, R. (1969) *Stress analysis of axisymmetric solids utilizing higher-order quadrilateral finite elements.* , University of California, Structural Engineering Laboratory.

Du Bois, P., Kolling, S. & Fassnacht, W. (2003) Modelling of safety glass for crash simulation. *Computational Materials Science.* 28 (3), 675-683.

Duser, A., Jagota, A. & Bennison, S. (1999) Analysis of glass/polyvinyl butyral laminates subjected to uniform pressure. *Journal of Engineering Mechanics.* 125 (4), 435-442.

Eberlein, R. & Wriggers, P. (1999) Finite element concepts for finite elastoplastic strains and isotropic stress response in shells: theoretical and computational analysis. *Computer Methods in Applied Mechanics and Engineering.* 171 (3), 243-279.

Eriksson, A. & Pacoste, C. (2002) Element formulation and numerical techniques for stability problems in shells. *Computer Methods in Applied Mechanics and Engineering.* 191 (35), 3775-3810.

Ferreira, A., Fasshauer, G., Batra, R. & Rodrigues, J. (2008) Static deformations and vibration analysis of composite and sandwich plates using a layerwise theory and RBF-PS discretizations with optimal shape parameter. *Composite Structures.* 86 (4), 328-343.

Ferry, J. (1980) *Viscoelastic properties of polymers.* , John Wiley & Sons.

Heppler, G. & Hansen, J. (1986) A Mindlin element for thick and deep shells. *Computer Methods in Applied Mechanics and Engineering.* 54 (1), 21-47.

Hooper, J. (1973) On the bending of architectural laminated glass. *International Journal of Mechanical Sciences.* 15 (4), 309-323.

Hooper, P., Sukhram, R., Blackman, B. & Dear, J. (2012) On the blast resistance of laminated glass. *International Journal of Solids and Structures.* 49 (6), 899-918.

Hu, H., Belouettar, S. & Potier-Ferry, M. (2008) Review and assessment of various theories for modeling sandwich composites. *Composite Structures.* 84 (3), 282-292.

Huang, H. & Hinton, E. (1984) A nine node Lagrangian Mindlin plate element with enhanced shear interpolation. *Engineering Computations.* 1 (4), 369-379.

Hughes, T. J. R., Taylor, R. L. & Kanoknukulchai, W. (1977) A simple and efficient finite element for plate bending. *International Journal for Numerical Methods in Engineering.* 11 (10), 1529-1543.

Izzuddin, B. A. & Lloyd Smith, D. Reissner-Mindlin plate bending elements with shear freedoms, Proc. 9th Int. Conf. on Civil & Struct. Engng. Computing, CC2003, The Netherlands, 2003.

Izzuddin, B. A. (2007) An optimisation approach towards lock-free finite elements. *Proceedings of the Eleventh International Conference on Civil, Structural and Environmental Engineering Computing. Scotland.*

Izzuddin, B. A. (2005) An enhanced co-rotational approach for large displacement analysis of plates. *International Journal for Numerical Methods in Engineering.* 64 (10), 1350-1374.

Izzuddin, B. A. (2006) Co-rotational system definitions for large displacement triangular and quadrilateral shell elements. The Third European Conference on Computational Mechanics Solids, Structures and Coupled Problems in Engineering. Lisbon, Portugal.

Izzuddin, B. A. & Liang, Y. (2015) Bisector and zero-macrospin co-rotational systems for shell elements. *International Journal for Numerical Methods in Engineering*.

Izzuddin, B. A. (1991) *Nonlinear dynamic analysis of framed structures.* PhD Thesis. Imperial College, University of London.

Jang, J. & Pinsky, P. M. (1987) An assumed covariant strain based 9-node shell element. *International Journal for Numerical Methods in Engineering.* 24 (12), 2389-2411.

Jiang, L. & Chernuka, M. (1994) A simple four-noded corotational shell element for arbitrarily large rotations. *Computers & Structures.* 53 (5), 1123-1132.

Jokhio, G. A., & Izzuddin, B. A. (2015) A Dual Super-Element Domain Decomposition Approach for Parallel Nonlinear Finite Element Analysis. *International Journal for Computational Methods in Engineering Science and Mechanics*, (just-accepted), 00-00.

Jokhio, G. A. & Izzuddin, B. A. (2013) Parallelisation of nonlinear structural analysis using dual partition super elements. *Advances in Engineering Software.* 6081-88.

Kapuria, S. & Achary, G. (2004) An efficient higher order zigzag theory for laminated plates subjected to thermal loading. *International Journal of Solids and Structures.* 41 (16), 4661-4684.

Kebari, H. & Cassell, A. (1992) A stabilized 9-node non-linear shell element. *International Journal for Numerical Methods in Engineering.* 35 (1), 37-61.

Kim, D. & Bathe, K. (2009) A triangular six-node shell element. *Computers & Structures.* 87 (23), 1451-1460.

Kim, K., Liu, G. & Han, S. (2005) A resultant 8-node solid-shell element for geometrically nonlinear analysis. *Computational Mechanics.* 35 (5), 315-331.

Kim, K. & Lomboy, G. (2006) A co-rotational quasi-conforming 4-node resultant shell element for large deformation elasto-plastic analysis. *Computer Methods in Applied Mechanics and Engineering.* 195 (44), 6502-6522.

Kim, K., Lomboy, G. & Han, S. (2003) A co-rotational 8-node assumed strain shell element for postbuckling analysis of laminated composite plates and shells. *Computational Mechanics.* 30 (4), 330-342.

Kim, K., Han, S. & Suthasupradit, S. (2007) Geometrically non-linear analysis of laminated composite structures using a 4-node co-rotational shell element with enhanced strains. *International Journal of Non-Linear Mechanics.* 42 (6), 864-881.

Korelc, J. & Wriggers, P. (1997) Improved enhanced strain four-node element with Taylor expansion of the shape functions. *International Journal for Numerical Methods in Engineering.* 40 (3), 407-421.

Kulikov, G. & Plotnikova, S. (2006) Geometrically exact assumed stress–strain multilayered solid-shell elements based on the 3D analytical integration. *Computers & Structures.* 84 (19), 1275-1287.

Larcher, M., Solomos, G., Casadei, F. & Gebbeken, N. (2012) Experimental and numerical investigations of laminated glass subjected to blast loading. *International Journal of Impact Engineering.* 39 (1), 42-50.

Le, T., Battini, J. & Hjiaj, M. (2014) Corotational formulation for nonlinear dynamics of beams with arbitrary thin-walled open cross-sections. *Computers & Structures*. 134, 112-127.

Lee, P. & Bathe, K. (2010) The quadratic MITC plate and MITC shell elements in plate bending. *Advances in Engineering Software.* 41 (5), 712-728.

Lee, P. & Bathe, K. (2004) Development of MITC isotropic triangular shell finite elements. *Computers & Structures.* 82 (11), 945-962.

Lekhnitskii, S. (1935) Strength calculation of composite beams. *Vestnik Inzhen i Tekhnikov.*

Li, Z. X., Izzuddin, B. A. & Vu-Quoc, L. (2008) A 9-node co-rotational quadrilateral shell element. *Computational Mechanics.* 42 (6), 873-884.

Li, Z. X., Liu, Y. F., Izzuddin, B. A. & Vu-Quoc, L. (2011) A stabilized co-rotational curved quadrilateral composite shell element. *International Journal for Numerical Methods in Engineering.* 86 (8), 975-999.

Li, Z., Xiang, Y., Izzuddin, B. A., Vu-Quoc, L., Zhuo, X. & Zhang, C. (2015) A 6-node co-rotational triangular elasto-plastic shell element. *Computational Mechanics.* , 1-23.

Li, Z. & Vu-Quoc, L. (2007) An efficient co-rotational formulation for curved triangular shell element. *International Journal for Numerical Methods in Engineering.* 72 (9), 1029-1062.

Li, Z., Zhuo, X., Vu-Quoc, L., Izzuddin, B. A. & Wei, H. (2013) A four-node corotational quadrilateral elastoplastic shell element using vectorial rotational variables. *International Journal for Numerical Methods in Engineering.* 95 (3), 181-211.

Lindberg, G., Olson, M. & Cowper, G. (1969) New developments in the finite element analysis of shells. *Quarterly Bulletin of the Division of Mechanical Engineering and the National Aeronautical Establishment.* 4, 1-38.

Linden, M., Minor, J. & Vallabhan, C. (1984) Evaluation of laterally loaded laminated glass units by theory and experiment. *Glass Research and Testing Laboratory, Texas Tech University, Lubbock.*

Macneal, R. H. (1982) Derivation of element stiffness matrices by assumed strain distributions. *Nuclear Engineering and Design.* 70 (1), 3-12.

Macneal, R. H. & Harder, R. L. (1985) A proposed standard set of problems to test finite element accuracy. *Finite Elements in Analysis and Design.* 1 (1), 3-20.

Malkus, D. S. & Hughes, T. J. (1978) Mixed finite element methods—reduced and selective integration techniques: a unification of concepts. *Computer Methods in Applied Mechanics and Engineering.* 15 (1), 63-81.

Maple. (2012) Maple user manual. Version 16.00, Maplesoft, Waterloo, Canada.

Minor, J. & Reznik, P. (1990) Failure strengths of laminated glass. *Journal of Structural Engineering.* 116 (4), 1030-1039.

Murakami, H. (1986) Laminated composite plate theory with improved in-plane responses. *Journal of Applied Mechanics.* 53 (3), 661-666.

Nawar, M., Salim, H., Lusk, B. & Kiger, S. (2013) Numerical Simulation and Verification of Curtain Wall Systems under Shock Pressure. *Practice Periodical on Structural Design and Construction.* 19 (2), 04014008.

Norachan, P., Suthasupradit, S. & Kim, K. (2012) A co-rotational 8-node degenerated thin-walled element with assumed natural strain and enhanced assumed strain. *Finite Elements in Analysis and Design.* 50, 70-85.

Norville, H., King, K. & Swofford, J. (1998) Behavior and strength of laminated glass. *Journal of Engineering Mechanics.* 124 (1), 46-53.

Pagano, N. (1970) Exact solutions for rectangular bidirectional composites and sandwich plates. *Journal of Composite Materials.* 4 (1), 20-34.

Panasz, P. & Wisniewski, K. (2008) Nine-node shell elements with 6 dofs/node based on two-level approximations. Part I: Theory and linear tests. *Finite Elements in Analysis and Design.* 44 (12), 784-796.

Pandit, M. K., Sheikh, A. H. & Singh, B. N. (2008) An improved higher order zigzag theory for the static analysis of laminated sandwich plate with soft core. *Finite Elements in Analysis and Design.* 44 (9), 602-610.

Pandit, M., Sheikh, A. & Singh, B. (2009) Analysis of laminated sandwich plates based on an improved higher order zigzag theory. *Journal of Sandwich Structures and Materials*.

Pandya, B. & Kant, T. (1988) Higher-order shear deformable theories for flexure of sandwich plates—finite element evaluations. *International Journal of Solids and Structures.* 24 (12), 1267-1286.

Peng, Y., Yang, J., Deck, C. & Willinger, R. (2013) Finite element modeling of crash test behavior for windshield laminated glass. *International Journal of Impact Engineering.* 57, 27-35.

Pugh, E., Hinton, E. & Zienkiewicz, O. (1978) A study of quadrilateral plate bending elements with 'reduced' integration. *International Journal for Numerical Methods in Engineering.* 12 (7), 1059-1079.

Pyttel, T., Liebertz, H. & Cai, J. (2011) Failure criterion for laminated glass under impact loading and its application in finite element simulation. *International Journal of Impact Engineering.* 38 (4), 252-263.

Rankin, C. (1998) On choice of best possible corotational element frame. *Modeling and Simulation Based Engineering.* 1, 772-777.

Rankin, C. & Brogan, F. (1986) An element independent corotational procedure for the treatment of large rotations. *Journal of Pressure Vessel Technology.* 108 (2), 165-174.

Reddy, J. (2004) *Mechanics of laminated composite plates and shells: theory and analysis.* , CRC press.

Sansour, C. & Kollmann, F. (2000) Families of 4-node and 9-node finite elements for a finite deformation shell theory. An assesment of hybrid stress, hybrid strain and enhanced strain elements. *Computational Mechanics.* 24 (6), 435-447.

Sedef, M., Samur, E. & Basdogan, C. (2006) Real-time finite-element simulation of linear viscoelastic tissue behavior based on experimental data. *Computer Graphics and Applications, IEEE.* 26 (6), 58-68.

Seica, M. V., Krynski, M., Walker, M. & Packer, J. A. (2010) Analysis of dynamic response of architectural glazing subject to blast loading. *Journal of Architectural Engineering.* 17 (2), 59-74.

Sharifi, P. & Popov, E. (1973) Nonlinear finite element analysis of sandwich shells of revolution. *AIAA Journal.* 11 (5), 715-722.

Shaw, M. & MacKnight, W. (2005) *Introduction to polymer viscoelasticity.* , John Wiley & Sons.

Simo, J., Armero, F. & Taylor, R. (1993) Improved versions of assumed enhanced strain tri-linear elements for 3D finite deformation problems. *Computer Methods in Applied Mechanics and Engineering.* 110 (3), 359-386.

Simo, J. C. & Rifai, M. (1990) A class of mixed assumed strain methods and the method of incompatible modes. *International Journal for Numerical Methods in Engineering.* 29 (8), 1595-1638.

Smith, C. (1968) Large deflections of circular sandwich plates. *AIAA Journal.* 6 (4), 721-723.

Srinivas, S. & Rao, A. (1970) Bending, vibration and buckling of simply supported thick orthotropic rectangular plates and laminates. *International Journal of Solids and Structures.* 6 (11), 1463-1481.

Stolarski, H. & Belytschko, T. (1982) Membrane locking and reduced integration for curved elements. *Journal of Applied Mechanics.* 49 (1), 172-176.

Sun, D., Andrieux, F., Ockewitz, A., Klamser, H. & Hogenmüller, J. (2005) Modelling of the failure behaviour of windscreens and component tests. *5th European LS-DYNA Users Conference.* pp.26.

Tessler, A. & Hughes, T. (1983) An improved treatment of transverse shear in the Mindlin-type four-node quadrilateral element. *Computer Methods in Applied Mechanics and Engineering.* 39 (3), 311-335.

Tessler, A. & Hughes, T. J. (1985) A three-node Mindlin plate element with improved transverse shear. *Computer Methods in Applied Mechanics and Engineering.* 50 (1), 71-101.

Thai, C., Ferreira, A., Carrera, E. & Nguyen-Xuan, H. (2013) Isogeometric analysis of laminated composite and sandwich plates using a layerwise deformation theory. *Composite Structures.* 104, 196-214.

Timmel, M., Kolling, S., Osterrieder, P. & Du Bois, P. (2007) A finite element model for impact simulation with laminated glass. *International Journal of Impact Engineering.* 34 (8), 1465-1478.

Timoshenko, S. (1940) *Theory of plates and shells.* New York, McGraw-Hill.

Toledano, A. & Murakami, H. (1987) A high-order laminated plate theory with improved in-plane responses. *International Journal of Solids and Structures.* 23 (1), 111-131.

Vallabhan, C., Das, Y., Magdi, M., Asik, M. & Bailey, J. (1993) Analysis of laminated glass units. *Journal of Structural Engineering.* 119 (5), 1572-1585.

Vallabhan, C., Das, Y. & Ramasamudra, M. (1992) Properties of PVB interlayer used in laminated glass. *Journal of Materials in Civil Engineering.* 4 (1), 71-76.

Vallabhan, C., Minor, J. & Nagalla, S. (1987) Stresses in layered glass units and monolithic glass plates. *Journal of Structural Engineering.* 113 (1), 36-43.

Wagner, M. & Müller, R. (2010) Nonlinear Dynamic Finite Element Analysis of Blast Loaded Curtain Walls. *Structures Congress 2010.* , ASCE. pp.2090-2100.

Weggel, D. C., Zapata, B. J. & Kiefer, M. J. (2007) Properties and dynamic behavior of glass curtain walls with split screw spline mullions. *Journal of Structural Engineering.* 133 (10), 1415-1425.

Wei, J., Shetty, M. & Dharani, L. (2006) Stress characteristics of a laminated architectural glazing subjected to blast loading. *Computers & Structures.* 84 (10), 699-707.

Wisniewski, K. & Panasz, P. (2013) Two improvements in formulation of nine-node element MITC9. *International Journal for Numerical Methods in Engineering.* 93 (6), 612-634.

Xu, J., Li, Y., Liu, B., Zhu, M. & Ge, D. (2011) Experimental study on mechanical behavior of PVB laminated glass under quasi-static and dynamic loadings. *Composites Part B: Engineering.* 42 (2), 302-308.

Zenkert, D. & Industrifond, N. (1997) *The handbook of sandwich construction.* , Engineering Materials Advisory Services Limited (EMAS).

Zienkiewicz, O. & Taylor, R. (2000) *The finite element method: Solid mechanics.* Butterworth-Heinemann.

Zienkiewicz, O., Taylor, R. & Too, J. (1971) Reduced integration technique in general analysis of plates and shells. *International Journal for Numerical Methods in Engineering.* 3 (2), 275-290.

Zolghadr Jahromi, H. (2014) *Energy consistent nonlinear dynamic contact analysis of structures.* PhD Thesis. Imperial College London.

Appendix A: Global-to-Local Displacement Transformations for 6-Noded Shell Element

The required first derivatives for the 6-noded triangular element are obtained from (3.61) and (3.47):

$$\frac{\partial \mathbf{t}_{i,m}}{\partial \mathbf{d}_{k,n}} = \delta_{ik} \mathbf{R}_m \begin{Bmatrix} \delta_{1n} \\ \delta_{2n} \\ \delta_{3n} \end{Bmatrix} + \frac{\partial \mathbf{R}_m}{\partial \mathbf{d}_{k,n}} \left(\mathbf{d}_i + \mathbf{v}_i^o \right) \quad \left(\text{i and k} = 1 \to 6, \quad \text{m and n} = 1 \to 3 \right) \tag{A1}$$

$$\frac{\partial \mathbf{t}_{i,m}}{\partial \overline{\mathbf{n}}_{k,n}} = 0 \quad \left(\text{i and k} = 1 \to 6,\ \text{m} = 1 \to 3,\ \text{n} = 1 \to 2 \right) \tag{A2}$$

$$\frac{\partial \overline{\mathbf{r}}_{i,m}}{\partial \mathbf{d}_{k,n}} = \frac{\partial \overline{\mathbf{R}}_m}{\partial \mathbf{d}_{k,n}} \mathbf{n}_i \quad \left(\text{i and k} = 1 \to 6,\ \text{m} = 1 \to 2,\ \text{n} = 1 \to 3 \right) \tag{A3}$$

$$\frac{\partial \overline{\mathbf{r}}_{i,m}}{\partial \overline{\mathbf{n}}_{k,n}} = \overline{\mathbf{R}}_m \frac{\partial \mathbf{n}_i}{\partial \overline{\mathbf{n}}_{k,n}} \quad \left(\text{i and k} = 1 \to 6,\ \text{m and n} = 1 \to 2 \right) \tag{A4}$$

The associated first derivatives of $(\mathbf{c}_x, \mathbf{c}_y, \mathbf{c}_z)$ with respect to global translational DOFs are given as follows:

$$\frac{\partial \mathbf{c}_x}{\partial \mathbf{d}_{i,n}} = \frac{\mathbf{I} - \mathbf{c}_x \mathbf{c}_x^T}{\left| \mathbf{c}'_x + \mathbf{c}'^n_y \right|} \left(\frac{\partial \mathbf{c}'_x}{\partial \mathbf{d}_{i,n}} + \frac{\partial \mathbf{c}'^n_y}{\partial \mathbf{d}_{i,n}} \right) \tag{A5}$$

$$\frac{\partial \mathbf{c}'_x}{\partial \mathbf{d}_{i,n}} = a_{x1} (\delta_{2i} - \delta_{1i}) \begin{Bmatrix} \delta_{1n} \\ \delta_{2n} \\ \delta_{3n} \end{Bmatrix} \tag{A6}$$

$$\frac{\partial \mathbf{c}'^n_y}{\partial \mathbf{d}_{i,n}} = \frac{\partial \mathbf{c}'_y}{\partial \mathbf{d}_{i,n}} \times \mathbf{c}_z + \mathbf{c}'_y \times \frac{\partial \mathbf{c}_z}{\partial \mathbf{d}_{i,n}} \tag{A7}$$

$$\frac{\partial \mathbf{c}'_y}{\partial \mathbf{d}_{i,n}} = \left[a_{y1} (\delta_{2i} - \delta_{1i}) + a_{y2} (\delta_{3i} - \delta_{2i}) \right] \begin{Bmatrix} \delta_{1n} \\ \delta_{2n} \\ \delta_{3n} \end{Bmatrix} \tag{A8}$$

$$\frac{\partial \mathbf{c}_{\mathrm{z}}}{\partial \mathbf{d}_{\mathrm{i,n}}} = \frac{\mathbf{I} - \mathbf{c}_{\mathrm{z}}\mathbf{c}_{\mathrm{z}}^{\mathrm{T}}}{\left|\mathbf{v}_{12} \times \mathbf{v}_{23}\right|}\left[(\delta_{2\mathrm{i}} - \delta_{1\mathrm{i}})\begin{Bmatrix}\delta_{1\mathrm{n}} \\ \delta_{2\mathrm{n}} \\ \delta_{3\mathrm{n}}\end{Bmatrix} \times \mathbf{v}_{23} + (\delta_{3\mathrm{i}} - \delta_{2\mathrm{i}})\mathbf{v}_{12} \times \begin{Bmatrix}\delta_{1\mathrm{n}} \\ \delta_{2\mathrm{n}} \\ \delta_{3\mathrm{n}}\end{Bmatrix}\right] \tag{A9}$$

$$\frac{\partial \mathbf{c}_{\mathrm{y}}}{\partial \mathbf{d}_{\mathrm{i,n}}} = \frac{\partial \mathbf{c}_{\mathrm{z}}}{\partial \mathbf{d}_{\mathrm{i,n}}} \times \mathbf{c}_{\mathrm{x}} + \mathbf{c}_{\mathrm{z}} \times \frac{\partial \mathbf{c}_{\mathrm{x}}}{\partial \mathbf{d}_{\mathrm{i,n}}} \tag{A10}$$

Second partial derivatives of ($\mathbf{c}_{\mathrm{x}}, \mathbf{c}_{\mathrm{y}}, \mathbf{c}_{\mathrm{z}}$) with respect to global translational DOFs can be similarly derived. It is emphasised that the resulting local tangent stiffness matrix is symmetric, since the triad ($\mathbf{c}_{\mathrm{x}}, \mathbf{c}_{\mathrm{y}}, \mathbf{c}_{\mathrm{z}}$) is explicitly related to the global translational DOFs, leading to explicit relationships between the local and global DOFs.

Appendix B: Mixed Formulations of Reissner-Mindlin Shell Elements Based on MITC9 and MITC6 Elements

Herein, the local kinematics of curved Reissner-Mindlin shell elements based on the MITC formulations for 9-noded quadrilateral and 6-noded triangular elements, MITC9 (Bathe et al., 2003) and MITC6 (Lee & Bathe, 2004), are briefly introduced.

The general MITC formulation procedure can be summarised as follows:

(i) Evaluate Green strains directly from displacement fields at a set of prescribed tying points (see Figures B.1-B.2 for the typing point positions of a 9-noded shell element, MITC9, and a 6-noded shell element, MITC6, respectively).

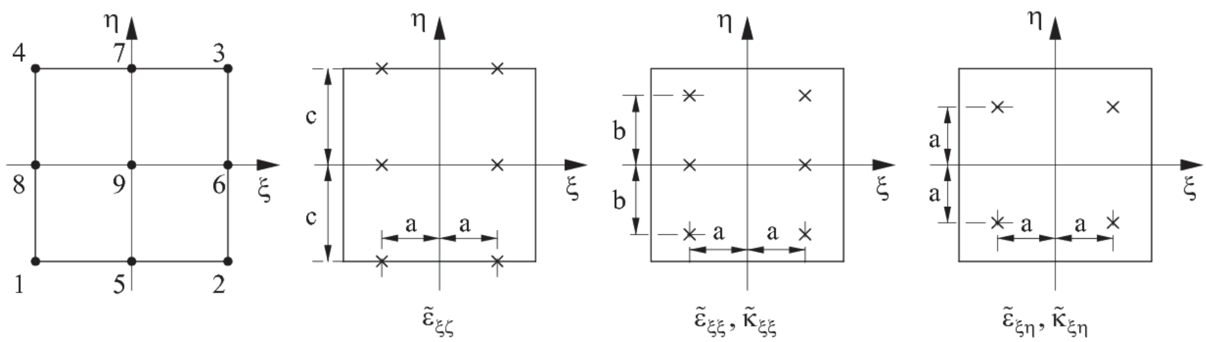

Figure B.1: Positions of tying points for MITC9 element ($a = 1/\sqrt{3}$, $b = \sqrt{3/5}$, and $c = 1$) (Bathe et al., 2003).

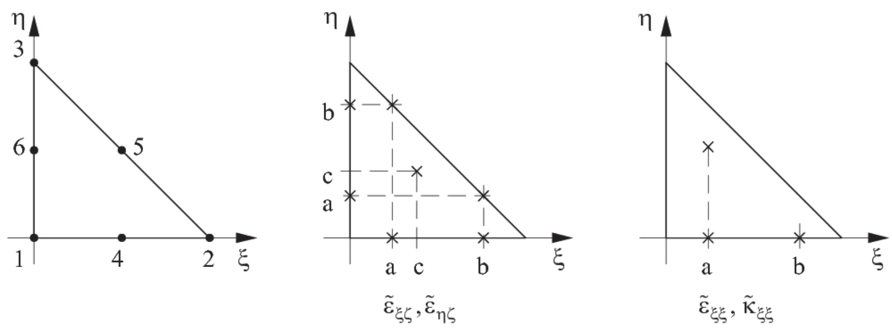

Figure B.2: Positions of tying points for MITC6 element ($a = \frac{1}{2} - \frac{1}{2\sqrt{3}}$, $b = \frac{1}{2} + \frac{1}{2\sqrt{3}}$, $c = \frac{1}{3}$) (Kim & Bathe, 2009).

(ii) Transform the extracted Green strains into corresponding covariant strain components using (B1):

$$\boldsymbol{\varepsilon}_2 = \mathbf{J}^{\mathrm{T}}\,\mathbf{E}_2\mathbf{J} \tag{B1}$$

where $\mathbf{E}_2$ is the Green strain tensor in terms of Cartesian coordinates; $\boldsymbol{\varepsilon}_2$ is the covariant strain tensor; and $\mathbf{J}$ is the Jacobian matrix, which is given by (3.66).

(iii) Interpolate covariant strain fields with the use of the extracted covariant strains:

$$\varepsilon_{\mathrm{rs}}^{\mathrm{AS}}(\xi, \eta, \zeta) = \mathbf{H}_{\mathrm{rs}}\boldsymbol{\varepsilon}_{\mathrm{rs,T}}^{\mathrm{DI}} \tag{B2}$$

where $\mathrm{r, s} = (\xi, \eta, \zeta)$; the superscripts 'AS' and 'DI' refer respectively to the assumed strain distribution and the distribution obtained directly from displacement fields; $\mathbf{H}_{\mathrm{rs}}$ is a row vector of interpolation functions associated with the tying points; $\boldsymbol{\varepsilon}_{\mathrm{rs,T}}^{\mathrm{DI}}$ consists of the covariant strain values extracted at the tying points.

(iv) Transform the assumed covariant strain fields to the corresponding Green strain fields in terms of real coordinates, obtained from:

$$\mathbf{E}_2^{\mathrm{AS}} = \mathbf{J}^{-\mathrm{T}}\boldsymbol{\varepsilon}_2^{\mathrm{AS}}\mathbf{J}^{-1} \tag{B3}$$

(v) Replace displacement-based strains with the assumed strain distributions obtained from (iv) in the element formulation.

The MITC9 (Bathe et al., 2003) quadrilateral shell element performs well, but it does not pass the patch test for irregular element shapes due to the varying basis used for sampling and mapping covariant strains, which can be resolved by using a constant Jacobian matrix evaluated at the element centre (Wisniewski & Panasz, 2013). This is equivalent to replacing (B1) and (B3) with:

$$\boldsymbol{\varepsilon}_2 = \mathbf{J}_{\mathrm{C}}^{\mathrm{T}}\,\mathbf{E}_2\mathbf{J}_{\mathrm{C}} \tag{B4}$$

$$\mathbf{E}_2^{\mathrm{AS}} = \mathbf{J}_{\mathrm{C}}^{-\mathrm{T}}\boldsymbol{\varepsilon}_2^{\mathrm{AS}}\mathbf{J}_{\mathrm{C}}^{-1} \tag{B5}$$

where $\mathbf{J}_C$ is the Jacobian matrix evaluated at the element centre ($\xi = 0, \eta = 0$). Similarly, the MITC6 (Lee & Bathe, 2004) triangular shell element is enhanced with the same method (Kim & Bathe, 2009), where $\mathbf{J}_C$ is evaluated at ($\xi = 1/3$, $\eta = 1/3$).

In this work, 9-noded Reissner-Mindlin shell elements are established based on the original MITC9 (Bathe et al. , 2003) and the improved MITC9is (Wisniewski & Panasz, 2013) local formulations. Although Wisniewski and Panasz also proposed another modified element 'MITC9i' (Wisniewski & Panasz, 2013), where further amendments on the element shape functions are made to allow for element distortion, nonlinear equations require to be solved to determine the additional parameters describing the element distortion. Therefore, MITC9i is not considered in this work due to increased computational demands. Similarly, a local formulation of the 6-noded Reissner-Mindlin shell element is established based on the MITC6 (Kim & Bathe, 2009) element.

Before employing the tying schemes for the element formulation, further assumptions are made that the element is shallow and thin, so that the natural coordinate axis ζ is taken to have an identical orientation to the local z-axis, and the transverse normal strain ε_z is ignored. Accordingly, the Jacobian matrix is simplified to:

$$\mathbf{J} = \begin{bmatrix} \dfrac{\partial x}{\partial \xi} & \dfrac{\partial x}{\partial \eta} & 0 \\ \dfrac{\partial y}{\partial \xi} & \dfrac{\partial y}{\partial \eta} & 0 \\ 0 & 0 & \dfrac{h}{2} \end{bmatrix} \tag{B6}$$

where h is the shell thickness. This simplification enables decoupled relationships between real strains and covariant strains, with each set of the generalised real strains related to their covariant counterparts only, which are expressed thus as:

$$\begin{bmatrix} \varepsilon_{\xi\xi} & \varepsilon_{\xi\eta} \\ \varepsilon_{\xi\eta} & \varepsilon_{\eta\eta} \end{bmatrix} = \mathbf{J}_p^T \begin{bmatrix} \varepsilon_x & \dfrac{1}{2}\gamma_{xy} \\ \dfrac{1}{2}\gamma_{xy} & \varepsilon_y \end{bmatrix} \mathbf{J}_p \tag{B7}$$

$$\begin{bmatrix} \kappa_{\xi\xi} & \kappa_{\xi\eta} \\ \kappa_{\xi\eta} & \kappa_{\eta\eta} \end{bmatrix} = \mathbf{J}_p^T \begin{bmatrix} \kappa_x & \frac{1}{2}\kappa_{xy} \\ \frac{1}{2}\kappa_{xy} & \kappa_y \end{bmatrix} \mathbf{J}_p \tag{B8}$$

$$\begin{Bmatrix} \varepsilon_{\xi\zeta} \\ \varepsilon_{\eta\zeta} \end{Bmatrix} = \frac{t}{2}\mathbf{J}_p^T \begin{Bmatrix} \frac{1}{2}\gamma_{xz} \\ \frac{1}{2}\gamma_{yz} \end{Bmatrix} \tag{B9}$$

where $\mathbf{J}_p$ is a sub-matrix of $\mathbf{J}$:

$$\mathbf{J}_p = \begin{bmatrix} \frac{\partial x}{\partial \xi} & \frac{\partial x}{\partial \eta} \\ \frac{\partial y}{\partial \xi} & \frac{\partial y}{\partial \eta} \end{bmatrix} \tag{B10}$$

By using (B7)-(B9) and evaluating $\mathbf{J}_p$ at the element centroid, the strains at each tying point are transformed to the covariant strains, which are then used in mapping the assumed covariant strain fields. The positions of the tying points for the MITC9 and MITC6 elements are shown in respectively Figures B.1 - B.2, where the associated interpolation functions for the covariant strains can be found elsewhere (Lee & Bathe, 2004; Bathe et al., 2003). Once the distribution of the covariant strain fields is obtained, these are transformed back to real assumed strains in the local co-rotational system, and these are then used in the formulation of the local response of the 6-noded and 9-noded curved shell elements.

In this thesis, the acronyms ‘MITC9*’ and ‘MITC9is*’ are used for the amended 9-noded Reissner-Mindlin elements based on respectively the MITC9 (Bathe et al., 2003) and the MITC9is (Wisniewski & Panasz, 2013) formulations, and the acronym ‘MITC6*’ is used for the amended 6-noded element based on the MITC6 (Kim & Bathe, 2009) formulation.

Appendix C: Parameters of Zigzag Functions of Sandwich Model

Explicit expressions of $\hat{a}_i^{(k)}$ and $\hat{b}_i^{(k)}$ (i =3,4) in (5.1)-(5.2) are given by:

$$\hat{a}_3^{(1)} = \frac{1}{h_1} - \frac{(h_1 - h_3)(h_1 + 3h_2 + h_3)}{(h_1 + h_2 + h_3)^3} \tag{C1}$$

$$\hat{a}_3^{(2)} = -\frac{(h_1 - h_3)(h_1 + 3h_2 + h_3)}{(h_1 + h_2 + h_3)^3} \tag{C2}$$

$$\hat{a}_3^{(3)} = -\frac{1}{h_3} - \frac{(h_1 - h_3)(h_1 + 3h_2 + h_3)}{(h_1 + h_2 + h_3)^3} \tag{C3}$$

$$\hat{b}_3^{(1)} = \hat{b}_3^{(3)} = \frac{h_1 h_3 + (h_2 + h_3)^2}{2h_1(h_1 + h_2 + h_3)} \tag{C4}$$

$$\hat{b}_3^{(2)} = \frac{h_1 + h_3}{2(h_1 + h_2 + h_3)} \tag{C5}$$

$$\hat{a}_4^{(1)} = \hat{a}_4^{(3)} = -\frac{h_2^2 + 3h_1h_2 + 6h_1h_3 + 3h_2h_3}{(h_1 + h_2 + h_3)^3} \tag{C6}$$

$$\hat{a}_4^{(2)} = \frac{1}{h_2} - \frac{h_2^2 + 3h_1h_2 + 6h_1h_3 + 3h_2h_3}{(h_1 + h_2 + h_3)^3} \tag{C7}$$

$$\hat{b}_4^{(1)} = -\frac{h_2 + 2h_3}{2(h_1 + h_2 + h_3)} \tag{C8}$$

$$\hat{b}_4^{(2)} = -\frac{h_1^2 + 2h_3^2}{2h_2(h_1 + h_2 + h_3)} \tag{C9}$$

$$\hat{b}_4^{(3)} = -\frac{2h_1 + h_2}{2(h_1 + h_2 + h_3)} \tag{C10}$$

For symmetric cross-sections, the above equations are simplified to:

$$\hat{a}_3^{(1)} = -\hat{a}_3^{(3)} = \frac{1}{h_1}, \quad \hat{a}_3^{(2)} = 0 \tag{C11}$$

$$\hat{b}_3^{(1)} = \hat{b}_3^{(3)} = \frac{2h_1^2 + h_2^2 + 2h_1h_2}{2h_1\left(2h_1 + h_2\right)}, \quad \hat{b}_3^{(2)} = \frac{h_1}{2h_1 + h_2} \tag{C12}$$

$$\hat{a}_4^{(1)} = \hat{a}_4^{(3)} = -\frac{6h_1^2 + h_2^2 + 6h_1h_2}{\left(2h_1 + h_2\right)^3}, \quad \hat{a}_4^{(2)} = \frac{1}{h_2} - \frac{6h_1^2 + h_2^2 + 6h_1h_2}{\left(2h_1 + h_2\right)^3} \tag{C13}$$

$$\hat{b}_4^{(1)} = -\hat{b}_4^{(3)} = -\frac{1}{2}, \quad \hat{b}_4^{(2)} = 0 \tag{C14}$$

Appendix D: Linear Viscoelastic Model for 2D Shell Elements

In order to apply the viscoelastic material model described in Section 7.2 to 2D elements, the zero value constraint on the transverse normal stress σ_{33} needs to be imposed, which yields a transverse normal strain ε_{33}^{n+1} expressed as:

$$\varepsilon_{33}^{n+1} = \frac{\hat{b}}{\hat{a}}\left(\varepsilon_{11}^{n+1} + \varepsilon_{22}^{n+1}\right) - \frac{\hat{c}}{\hat{a}} \tag{D1}$$

in which:

$$\hat{a} = \frac{4}{3}G_\infty + K + \frac{4}{3}\sum_{j=1}^{N_M} G_j A_j, \quad \hat{b} = \frac{2}{3}G_\infty - K + \frac{2}{3}\sum_{j=1}^{N_M} G_j A_j \tag{D2}$$

$$\hat{c} = \sum_{j=1}^{N_M} G_j A_j \left[\frac{2}{3}\left(\varepsilon_{11}^{n} + \varepsilon_{22}^{n}\right) - \frac{4}{3}\varepsilon_{33}^{n}\right] + \sum_{j=1}^{N_M} e^{-\frac{\Delta t}{\tau_j}} h_{j,33}^{n} \tag{D3}$$

By substituting (D1) into (7.9)-(7.10), (7.13) is obtained with the matrices $\mathbf{C}_{v,p}^{n+1}$ and $\mathbf{C}_{v,s}^{n+1}$ expressed as:

$$\mathbf{C}_{v,p}^{n+1} = \begin{bmatrix} \frac{(\hat{a}+\hat{b})(\hat{a}-\hat{b})}{\hat{a}} & -\frac{\hat{b}(\hat{a}+\hat{b})}{\hat{a}} & 0 \\ -\frac{\hat{b}(\hat{a}+\hat{b})}{\hat{a}} & \frac{(\hat{a}+\hat{b})(\hat{a}-\hat{b})}{\hat{a}} & 0 \\ 0 & 0 & \hat{d} \end{bmatrix}, \quad \mathbf{C}_{v,s}^{n+1} = \begin{bmatrix} \hat{d} & 0 \\ 0 & \hat{d} \end{bmatrix} \tag{D4}$$

with:

$$\hat{d} = G_\infty + \sum_{j=1}^{N_M} G_j A_j \tag{D5}$$

where A_j is given in (7.6).

The stress vectors $\boldsymbol{\sigma}_{hist,p}$ and $\boldsymbol{\sigma}_{hist,s}$ are then derived as:

$$\boldsymbol{\sigma}_{hist,p} = \frac{\hat{b}\,\hat{c}}{\hat{a}}\begin{Bmatrix}1\\1\\0\end{Bmatrix} - \sum_{j=1}^{N_M} G_j A_j \left[\begin{array}{ccc|c} \frac{4}{3} & -\frac{2}{3} & -\frac{2}{3} & 0\\ -\frac{2}{3} & \frac{4}{3} & -\frac{2}{3} & 0\\ \hline 0 & 0 & 0 & 1 \end{array}\right]\begin{Bmatrix}\varepsilon_{11}^{n}\\ \varepsilon_{22}^{n}\\ \varepsilon_{33}^{n}\\ \gamma_{12}^{n}\end{Bmatrix} + \sum_{j=1}^{N_M} e^{-\frac{\Delta t}{\tau_j}}\begin{Bmatrix}h_{j,11}^{n}\\ h_{j,22}^{n}\\ h_{j,12}^{n}\end{Bmatrix} \tag{D6}$$

$$\boldsymbol{\sigma}_{hist,s} = -\sum_{j=1}^{N_M} G_j A_j \begin{Bmatrix}\gamma_{13}^{n}\\ \gamma_{23}^{n}\end{Bmatrix} + \sum_{j=1}^{N_M} e^{-\frac{\Delta t}{\tau_j}}\begin{Bmatrix}h_{j,13}^{n}\\ h_{j,23}^{n}\end{Bmatrix} \tag{D7}$$

Appendix E: Effective Thickness of Laminated Glass for Analysis of Deflection and Stresses (ASCE E1300-12a X9)

Appendix X9 of ASCE E1300-12a provides engineering formulae for calculating the effective thickness of LG. Two different effective laminate thickness values are determined for a specific case: (1) an effective thickness, $h_{ef;w}$, for use in calculations of laminate deflection, and (2) an effective laminate thickness, $h_{1,e,\sigma}$, for use in calculations of LG stress. These effective thickness values can be used with standard engineering formulae or finite element methods for calculating both deflection and glass stress of laminates subjected to load. The method applies to 2-ply laminates fabricated from both equal and unequal thickness glass plies.

The shear transfer coefficient, Γ, is a measure of the transfer of shear stresses across the interlayer, which is defined as:

$$\Gamma = \frac{1}{1 + 9.6 \dfrac{E I_s h_v}{G h_s^2 a^2}} \tag{E1}$$

with:

$$I_s = h_1 h_{s;2}^2 + h_2 h_{s;1}^2 \tag{E2}$$

$$h_{s;1} = \frac{h_s h_1}{h_1 + h_2}, \quad h_{s;2} = \frac{h_s h_2}{h_1 + h_2} \tag{E3}$$

$$h_s = 0.5(h_1 + h_2) + h_v \tag{E4}$$

where h_v is the interlayer thickness; h_1 and h_2 are the minimum thicknesses of the two glass plies; E is glass Young’s modulus; a is the smallest in-plane dimension of bending of the laminate plate; and G is the interlayer complex shear modulus.

For calculations of laminate deflection, the laminate effective thickness is given by:

$$h_{ef;w} = \sqrt[3]{h_1^3 + h_2^3 + 12\Gamma I_s} \tag{E5}$$

For calculations of maximum glass bending stress, the laminate effective thicknesses are given by:

$$h_{1;ef;\sigma} = \sqrt{\frac{h_{ef;w}^3}{h_1 + 2\Gamma h_{s;2}}}, \quad h_{2;ef;\sigma} = \sqrt{\frac{h_{ef;w}^3}{h_2 + 2\Gamma h_{s;1}}} \tag{E6}$$